Phase-Field Methods for Deformation Processes in Lithium-Ion Batteries

vom Fachbereich Maschinenbau und Verfahrenstechnik
der Technischen Universität Kaiserslautern
zur Verleihung des akademischen Grades
Doktor-Ingenieur (Dr.-Ing.)
genehmigte Dissertation

von
M.Sc. Tobias Hofmann
aus Augsburg

Hauptreferent:	Priv.-Doz. Dr. Heiko Andrä
Korreferenten:	Prof. Dr.-Ing. Ralf Müller
	Prof. Dr. Arnulf Latz
Vorsitzender:	Prof. Dr.-Ing. Tilmann Beck
Dekan:	Prof. Dr.-Ing. Jörg Seewig

Tag der Einreichung:	28. August 2017
Tag der mündlichen Prüfung:	08. Januar 2018

D 386

Herausgeber

Lehrstuhl für Technische Mechanik
Technische Universität Kaiserslautern
Gottlieb-Daimler-Straße
Postfach 3049
67653 Kaiserslautern

Ich danke der „Prof. Dr. Hans Georg und Liselotte Hahn Stiftung“ für die finanzielle Unterstützung bei der Drucklegung.

Druck

Technische Universität Kaiserslautern
Hauptabteilung 5/ Bau-Technik-Energie
Abteilung 5.6 Foto-Repro-Druck

ISBN 978-3-942695-15-2

Vorwort

Als ich im Sommer 2013 zum Vorstellungsgespräch am Fraunhofer ITWM unterwegs war, zuckelte ich zweifelnd über eine Stunde lang mit der S-Bahn von Mannheim durch den Pfälzer Wald bis nach Kaiserslautern. Doch schon auf der Rückfahrt wenige Stunden später hatte ich ein gutes Gefühl für das Team in der Abteilung Strömungs- und Materialsimulation gewonnen. Der Schritt von der theoretischen in die angewandte Mathematik hat sich gelohnt.

Ich möchte mich zuerst bei meinen beiden Professoren und Doktorvätern Priv.-Doz. Dr. Heiko Andrä und Prof. Dr.-Ing. Ralf Müller für die teilweise konträren Perspektiven aus Mathematik und Mechanik bedanken. Weiterhin danke ich Prof. Dr. Arnulf Latz für sein Fachwissen zur elektro-chemischen Modellierung und Prof. Dr.-Ing. Tilmann Beck für die Übernahme des Prüfungsvorsitzes. Die Finanzierung der Promotionsstelle wurde durch das *Fraunhofer High Performance Center for Simulation- and Software-Based Innovation* ermöglicht.

Danke an alle Kollegen der Abteilung SMS, insbesondere Jochen und Matthias, für die spannenden fachlichen Diskussionen. Danke an Sebastian fürs Korrekturlesen, sowie an meine Doktoranden-Kollegen für den Hut und an meine (ehemaligen) Zimmerkollegen Janis und Jonathan für Abwechslung im Alltag. Für den Blick über den naturwissenschaftlichen Tellerrand danke an den Unichor Haste Töne und das Ukulelenorchester u'kl. Danke auch an das Stockacher Hüttenteam für die Ablenkung vor der Disputation bei Skifahren, Schnitzel und Spielen (... der Bass muss laut sein).

Zuletzt danke ich meinen Eltern und Geschwistern für ihre immerwährende Unterstützung sowie meiner Tante für die frühzeitige Einführung in die Pfälzer Sprache und Kultur. Diese Arbeit ist meinen verstorbenen Großeltern gewidmet, die immer an mich geglaubt haben und mich zu jedem weiteren Schritt im Studium ermutigt haben.

Kaiserslautern, Januar 2018 Tobias Hofmann

> *Wir müssen unbedingt Raum für Zweifel lassen, sonst gibt es keinen Fortschritt, kein Dazulernen. Man kann nichts Neues herausfinden, wenn man nicht vorher eine Frage stellt.*
>
> — Richard Feynman, 1918-1988, Safeknacker, Bongospieler, Nobelpreisträger

Kurzfassung

Wiederaufladbare Lithium-Ionen-Batterien stellen heutzutage eine unverzichtbare Komponente in elektronischen Geräten und Fahrzeugen dar. Obwohl Elektroden mit Lithium-Ionen aufgrund ihrer hohen Energiedichte sehr verbreitet in der Produktion von Batterien sind, ist in vielen Anwendungsfeldern eine qualitative oder quantitative Vorhersage über die zu erwartende Haltbarkeit und den zu erwartenden Kapazitätsschwund wünschenswert. Die meisten Elektrodenmaterialien zeigen Abnutzungserscheinungen beim Gebrauch. Wenn zum Beispiel hohe Entladeströme an die elektrischen Pole der Batterie angelegt werden, ist die daraus resultierende Diffusion der Lithium-Ionen in der Batterie von Anode zu Kathode nicht schnell genug und es entstehen Konzentrations-Gradienten. Erstens haben diese Gradienten negative Auswirkungen auf die elektrische Spannung, welche die Batterie bereit stellen kann. Außerdem kann es zu unerwünschten chemischen Reaktionen kommen, welche die verwendeten Materialien schädigen oder zerstören oder sich negativ auf die Kontaktflächen auswirken. Schwerwiegender ist der Effekt der unterschiedlichen, unkontrollierten Ausdehnung der Partikel in der Elektrode. Die mechanischen Spannungen innerhalb der Batterie entladen sich möglicherweise in Rissen und das nutzbare Materialvolumen der Batterie wird weiter verringert. Schließlich entsteht durch den elektrischen Widerstand der Bauteile auch Wärme. Durch steigende Temperatur entwickelt sich das physikalische Verhalten der Bauteile möglicherweise negativ, deswegen wird versucht, die Temperatur der Batterie innerhalb festgelegter Schranken zu halten.
Verschiedene Materialien werden für Elektrolyt-Lösungen sowie als Kathoden- oder Anodenmaterial verwendet. Für die meisten Materialien können die elektrochemischen Prozesse hinreichend genau durch gewöhnliche Diffusionsgesetze (für das Lithium-Ionen-Konzentrationsfeld), das Gauß'sche Gesetz (für das elektrische Potential-Feld) und lineare Elastizität (für die Verschiebungen) beschrieben werden. Aber insbesondere im zuletzt häufig benutzten Lithium-Eisen-Phosphat $LiFePO_4$ kann die Diffusion der Lithium-Ionen vom Elektrolyt in das aktive Elektrodenmaterial nicht durch gewöhnliche Diffusionsprozesse beschrieben werden. Während in den meisten Materialien die Diffusion zu einer gleichmäßigen Verteilung der Ionen innerhalb des Materials führt, zeigt Lithium-Eisen-Phosphat eine Teilung in Bereiche mit einer maximalen Konzentration an Lithium-Ionen und Bereiche in denen keine Lithium-Ionen vorhanden sind. Diese Bereiche werden als zwei unterschiedliche Zustände des Materials interpretiert und Phasen genannt, entsprechend zu den physikalischen Phasen fest, flüssig und gasförmig. Sogar ohne angelegten Strom im Gleichgewicht verteilt sich das Lithium nicht gleichmäßig im

verfügbaren Platz. Die Verteilung der Lithium-Ionen im Material kann dann durch zwei verschiedene Phasen beschrieben werden, eine Phase angereichert mit Lithium-Ionen und eine Phase ohne Lithium-Ionen. Der Prozess der Teilung in verschiedene Phasen wird spinodale Entmischung genannt. Die Beschreibung der zeitlichen Entwicklung von Grenzflächen zwischen zwei Phasen wird oft Stefan-Problem genannt und kann mit adaptiven Gittern oder Front-Tracking-Methoden gelöst werden.
Ein anderer Ansatz (genannt Phasenfeldmethode) wird in den Arbeiten von Cahn und Hilliard eingeführt und basiert auf einer thermodynamischen Herleitung mittels nichtkonvexer Helmholtz-Energie-Funktionale. In einer allgemeinen Phasenfeldmethode wird die Grenze zwischen zwei Phasen diskretisiert und ein feines räumliches Netz verwendet. Insbesondere in Phasenfeldmethoden für diffusive Prozesse nennt man die dazugehörige nichtlineare partielle Differentialgleichung vierter Ordnung Cahn-Hilliard-Gleichung. Während bisherige Formulierungen beschränkt sind auf die Beschreibung von Diffusion in reinem Elektrodenmaterial, wird in dieser Arbeit eine Kopplung zwischen Diffusion und Gauß'schem Gesetz in Elektrolyt und beiden Elektroden definiert. Viele Formulierungen verzichten auch auf das Auflösen einer komplexen Mikrostruktur in den Elektroden und erwägen stattdessen Argumente der Homogenisierung.
In Kapitel 1 wird eine kurze Einführung in den Umfang dieser Arbeit gegeben. Es wird ein kurzer Überblick über die Geschichte der Batterien gegeben und die Längenskalen, sowieso die chemischen, physikalischen und mechanischen Effekte erklärt, sowie das Konzept der Phasenseparation. Die Verwendung numerischer Simulation für die virtuelle Optimierung von Batterien wird motiviert. Die Phasenseparation in Batteriematerialien und mechanische Effekte in Batterien werden erklärt.
In Kapitel 2 wird das elektro-chemo-mechanische Modell für eine Lithium-Ionen-Batterie auf der Mikroskala eingeführt. Zuerst werden grundsätzliche Begriffe für Phasenfeldmethoden und lineare Elastizität erklärt. Danach wird ein Modell einer Batterie mit aufgelöster Mikrostruktur in den Elektroden definiert. Dieses Modell umfasst die Diffusion der Lithium-Ionen in den Elektroden und im Elektrolyt sowie das entstehende elektrische Feld. In diesem Modell wird zusätzlich zu normaler Diffusion auch die Phasenseparation in Lithium-Eisen-Phosphat modelliert. Außerdem wird die Ausdehnung der Elektroden und die dabei entstehende mechanische Spannung berechnet. An den Grenzflächen zwischen Elektrode und Elektrolyte werden Übergangsbedingungen für die Lithium-Ionen formuliert, die so genannten Butler-Volmer-Bedingungen. Diese beschreiben die Einlagerung der Lithium-Ionen aus dem flüssigen Elektrolyt in das feste Elektrodenmaterial hinein. Ein gewöhnlicher Anwendungsfall des Modells ist das einmalige Laden oder Entladen einer Batterie, wobei die Lithium-Ionen von einer der beiden Elektroden über den Elektrolyt in die andere Elektrode diffundieren.
In Kapitel 3 werden zwei verschiedene numerische Methoden zur Lösung des elektrochemischen Modells definiert und erklärt. Beide Methoden basieren auf der räumlichen Diskretisierung mit einem regelmäßigen Voxel-Gitter und einer darauf aufbauenden Finite-Volumen-Methode. Außerdem wird ein adaptiver Zeitintegrations-Algorithmus ver-

wendet, der kleine Zeitschritte während der Ausbildung und Umlagerung der Phasengrenzen verwendet und möglichst große Zeitschritte während des Wachstums der Phasen und der Bewegung der Phasengrenzen. Außerdem wird das mechanische Modell für die Ausdehnung der Batterieelektrode in beiden Methoden identisch gelöst.
Die erste Methode verwendet das Newton-Verfahren und kann genutzt werden, um das elektro-chemische Modell zu diskretisieren und zu lösen. Die Jacobi-Matrix wird hergeleitet und ein gedämpftes Newton-Verfahren für die Lösung der nichtlinearen Gleichungen eingeführt. Das entstehende lineare Gleichungssystem wird mit einem direkten Löser invertiert für die Berechnung der Korrekturschritte. Dieses Verfahren ist sehr stabil und wird deswegen oft verwendet. Es ist jedoch nicht leistungsfähig genug, um das Verhalten auf komplizierten Mikrostrukturen in drei Dimensionen zu berechnen.
Die zweite Methode verwendet Ansätze aus der Gebietszerlegung und der Fourierintegration, um den numerischen Aufwand stark zu reduzieren. Dafür muss jedoch das Modell an manchen Stellen vereinfacht werden. In jedem der einzelnen Gebiete der Batterie werden die dazugehörigen partiellen Differentialgleichungen mit Fourier-Methoden integriert. Ein Finite-Differenzen-Schema wird erklärt und die Integration von periodischen linearen Differentialoperatoren im Fourier-Raum wird definiert. Die Lösung von periodischen Poisson-, Diffusions, und Cahn-Hilliard-Gleichungen wird hergeleitet. Diese Methode wird dann erweitert zu einer Lösungen von linearen Anfangs-Randwert-Problemen mittels einer Immersed-Interface-Methode (IIM). In dieser Formulierung kann auf die Aufstellung der Jacobi-Matrix sowie einen direkten Löser des Gleichungssystem verzichtet werden. Dadurch ist das Verfahren leistungsfähig genug, um das Verhalten in komplizierten dreidimensionalen Mikrostrukturen zu berechnen.
In Kapitel 4 werden die beiden Methoden für zahlreiche Anwendungen verwendet. Zuerst werden Eigenschaften der Phasenfeldmethode untersucht. Eine Abschätzung für eine Mindestgröße für die Kondensation von reinen Phasengebieten wird berechnet. Außerdem werden analytische Eigenschaften wie die Dicke der Grenzflächenschicht und die damit verbundene Grenzflächenenergie hergeleitet. Die Konvergenz der Fourier-Integrationsverfahren wird gezeigt für die verschiedenen Gleichungstypen. Danach wird die Generierung von dreidimensionalen Kugelpackungen diskutiert. Das dazugehörige elastische Problem kann nur korrekt gestellt werden durch die Anwendung einer Beschichtung. Die Interface-Ränder werden in der Umgebung so verändert, dass alle Teilgebiete Lipschitz-Gebiete werden und die Regularität der Lösungen sichergestellt ist. Beschichtungsalgorithmen werden definiert und deren Eigenschaften an Simulationen validiert. Anschließend wird das elektro-chemische Modell anhand verschiedener Beispiele in ein oder zwei Dimensionen betrachtet. Die spinodale Entmischung und der Aufbau zweier Phasenregionen in einer Kathodenstruktur werden gezeigt. Verschiedene Modelle für die Butler-Volmer-Bedingungen werden evaluiert. Außerdem wird die Auswirkung der Phasenseparation auf die Zellspannung untersucht, sowie verschiedene Partikelgrößen und -formen in der Kathodenmikrostruktur verglichen. Abschließend wird das elektro-chemo-mechanische Modell in ein, zwei oder drei Dimensionen betrachtet. Die Wirkung

der Phasenseparation auf die Zellspannung unter Berücksichtigung von mechanischen Spannungen wird untersucht sowie der Einfluss vorhandener mechanischer Spannungen auf die Phasenseparation. Die Leistungsfähigkeit des Gebietszerlegungsalgorithmus wird durch Beispiele mit dreidimensionalen Kugelpackungen bewiesen.

Abstract

Today lithium-ion batteries form an indispensable component for electronic devices or electric vehicles. Even though lithium-ion electrodes are very versatile in battery production due to their high energy density, the diverse fields of application require the prediction of lifetime and capacity fade. A lot of electrode materials show degradation during usage. If a large current is applied to the poles of the battery during discharge, the diffusion of lithium ions inside the battery from the anode to the cathode is not fast enough and concentration gradients arise. Those gradients affect the cell potential and decrease the voltage range that the battery can supply. Furthermore, chemical reactions may occur which damage or destroy the materials in the battery or the interface between them. Even more severe is the irregular, uncontrolled expansion of electrode particles. The mechanical stresses inside the battery may result in fracture and the active electrode material may be decreased. The resistance of the battery is increased and more heat is generated. By this, the material properties are affected in a negative way. Therefore it is important to keep the battery temperature inside a certain range.
Different materials have been used for an electrolyte as well as for the cathode and the anode. In a lot of them, the electrochemical processes can be accurately described by Fickian diffusion for the lithium ion concentration field and the Gaussian law for the electric potential field. But especially in the popular cathode material lithium iron phosphate ($LiFePO_4$, LFP), the diffusion of the lithium ions from the electrolyte into the active material cannot be modelled by a regular diffusion equation. While in a lot of materials the diffusion leads to a uniform ion distribution inside the material, for LFP a separation into areas with a maximum concentration of lithium ions and areas where no lithium ions are present [34, 154, 21, 85]. Even without applied current, the lithium enriched areas do not diffuse. The distribution of the lithium ions inside the material can then be described by two different phases, one phase enriched with lithium ions and one phase devoid of lithium ions. The process of separation into different phases is called spinodal decomposition. The problem of describing the movement of the boundaries between both phases is often called a Stefan problem [2, 55] and can be approached by adaptive meshes and front-tracking methods [95].
Another approach called phase-field method is introduced in the works of Cahn and Hilliard [14] and is based on a thermodynamical approach involving a non-convex Helmholtz energy functional. In a general phase-field method, the boundary between two phases is discretized and a fine regular spatial mesh is used [74]. Phase-field methods have

been applied for the solution of displacive problems such as the phase transformation between austenite and martensite [97, 98] or mechanical fracture processes [108, 75].
In phase-field models for diffusive processes, the constituent fourth-order nonlinear partial differential equation is called the Cahn-Hilliard equation. Recent formulations for lithium iron phosphate particles can be found in [1, 11, 122, 5]. While those models are restricted to simulations of electrode material, the model presented in this thesis describes diffusion and electric potentials in both electrodes and the electrolyte. There are simulations for the charging of electrode material for different spherical [140, 149], ellipsoidal nanoparticles [66, 82] or more complex single particle microstructures [127, 24]. The macroscopic charge-discharge behaviour of porous electrodes [30, 46, 45, 106, 87] and a focus on effects like hysteresis [32] are explained without resolving a microstructure but using arguments of homogenization or particle size [129].
In Chapter 2 an electro-chemo-mechanical model for the simulation of a lithium-ion battery on the microscale is given. The model is valid for a porous microstructure for both electrode domains. They can be generated by software or given by imaging. Several physical processes are described, including the transport of lithium ions inside each electrode and the intercalation from and into the liquid electrolyte and the combined transport of lithium ions and electrons in the liquid electrolyte. Furthermore, the electric field is modelled by a Laplace equation. The expansion of battery material is described by a chemical strain associated with the corresponding lithium ion concentration inside the electrode material. In anode and electrolyte, the mathematical model for the movement of the lithium ions is given by a classical diffusion equation with while in the cathode a model is given for the description of phase separation phenomena.
Section 2.2 deduces the multiphysics model. In Subsection 2.2.2, the governing equations are derived and the associated chemical potentials are given for anode, electrolyte and cathode. The formulation with a chemical potential in (2.15),(2.20), and (2.27) supports the dynamic analysis of charging and discharging of the battery in Section 4.1. The focus on consistent coupling conditions in (2.23) is important. Models with one-way coupling exist but their validity is diminished. Different models for the exchange current density have been introduced as Model A in (2.33) and Model B in (2.34) and compared in Subsection 4.4.2. While usually Model B is well-known and used, its validity is questionable for cathode materials showing phase separation. The interface current is channelled mainly through the phase interface region. Model A gives a better description. For the diffusion equation and the Poisson equation, both the homogeneous Neumann boundary condition may be justified as well as periodic boundary conditions. In the elastic model, periodic boundary conditions without macroscopic displacements have been prescribed.
In Chapter 3 different numerical methods are applied to the numerical solution of partial differential equations. A regular voxel mesh, a finite volume method and an implicit Euler scheme as introduced in [79] is used for the discretization of the microscale model

on a cuboid domain. It is applied for both logarithmic (see [62]) and polynomial phase-field potentials.
The numerical simulation of phase separation requires very different sized time steps [149]. During the phase initiation, small time steps in the range of microseconds are required. As soon as stable phases emerge, the time step can be enlarged again. In this work, an adaptive time step algorithm is presented in combination with a damped Newton scheme in Subsection 3.2.4 and demonstrated in Subsection 4.4.1.
The coupled electro-chemical model for the electrolyte (2.15) is decoupled. This requires rewriting of both the governing equations and the Butler-Volmer interface conditions. The decoupled model is given as (3.35) and (3.36). The logarithmic phase-field potential in (2.26) is replaced by the best polynomial approximation in (3.40). The Dirichlet boundary condition on the electric potential in (2.37) is replaced by a pure Neumann boundary condition in (3.42). Dirichlet boundary conditions require the application of a penalty method in the discretization. Their abundance simplifies the numerical solution. In 3.3.5 a fully decoupled algorithm is given that enables the parallel solution of the equations in the different domains. The information exchange is given by means of the Butler-Volmer interface currents.
The numerical solution of the Poisson equation and the diffusion equation in Section 3.4 by Fourier integration gives higher-order integration schemes for the periodic formulations in (3.69) and (3.71). On complex domains, first-order schemes are achieved by the immersed interface method in (3.77) and in (3.84). In space, finite difference approximations are applied, while in time, Gauss-Legendre methods are used. The higher-order convergence is demonstrated for the periodic Poisson equation in Subsection 4.2.1 and for the periodic diffusion equation in Subsection 4.2.2. For the Poisson equation in complex domains, the first-order discretization is compared to the second-order discretization given in [141]. All these convergence studies are performed by comparison with analytic, manufactured solutions.
While second-order time integration methods are mentioned for the Cahn-Hilliard equation in Subsubsection 4.2.5.7, the work is focused on the application of a semi-implicit first-order discretization in (3.86). The preconditioner in (3.94) reduces the number of iterations for the iterative solution of the problem as demonstrated in Subsubsection 4.2.5.2. The immersed interface is then applied to this equation and numerical first-order convergence is shown by comparison with a numerical reference solution in Subsubsection 4.2.5.1. Although not applied later in the electro-chemical model, surface-wetting can be included as demonstrated in Subsubsection 4.2.5.5. Neumann boundary conditions are applied to a porous microstructure in Subsubsection 4.2.5.6. These are later replaced by Butler-Volmer interface conditions in the domain decomposition algorithm.
In Section 4.3 the generation of microstructures composed of spherical packings is discussed. It is shown that the elastic properties of such microstructures are singular for grid refinement and not suitable for the prediction of internal stresses in Subsection 4.3.1.

Subsection 4.3.2 introduces a mathematical model for the description of an additional coating on the spherical particles in order to give a well-posed elastic problem. Subsections 4.3.4 and 4.3.4 define two such coatings analytically. The volume fraction is derived dependent on the uncoated microstructure. The validity of the coating is then proven in 4.3.6. Using this, the coated microstructures can be applied for tests in Section 4.5.
In Section 4.4 several numerical tests show the electrochemical processes during the charging of a phase-separating cathode material. Between SOC 0.13 and 0.9, the cathode material undergoes phase separation into lithium-poor and lithium-rich phases in Subsection 4.4.1. Both lithium-rich and lithium-poor phase are shown to be present at the particle surface opposed to the core-shell model [5], where a spherically symmetric model predicts that either one of the phases is present at the particle surface. In Subsection 4.4.3 the electric potential difference at cathode-electrolyte interface is investigated. A discontinuity is observed as soon as the lithium-rich phase is initiated. During phase separation, a voltage plateau is observed. Size and shape of the cathode microstructure are shown to affect the emergence of lithium-rich phases in Subsection 4.4.4. Subsection 4.4.5 shows that the lithium-rich phases can grow independently in a complex microstructure.
In Section 4.5 the electro-chemo-mechanical model is applied. The equilibrium concentration in lithium-rich and lithium-poor phase is affected as well as the cell voltage in Subsection 4.5.1. Also, the emergence of lithium-rich phases is enforced by local eigenstrains in Subsection 4.5.3. For a cathode consisting of several spherical particles, the particles are charged one after another in Subsection 4.5.5. The maximum stress invariants show periodicity. For several spherical packings as a cathode microstructure, the maximum stress invariants are calculated during a charge cycle and compared to each other in Subsection 4.5.6.

Contents

Chapter 1

Introduction

In this short first chapter, an introduction to the topic of the thesis is given. A motivation for the numerical simulation and virtual optimization of phase separation and mechanical effects in lithium-ion batteries is given in Section 1.1. Then Section 1.2 reviews the invention and the history of batteries and sets the current development and issues into proper context. Section 1.3 introduces and defines length scales and the chemical, physical and mechanical effects in a battery. In Section 1.4, specific materials in battery development are discussed that show phase-separation effects during usage. The mechanics of these materials can not be described with classical models. Section 1.6 defines the scope of the thesis and gives an outline for the chapters.

1.1 Motivation

Today lithium-ion batteries form an indispensable component for electronic devices or electric vehicles. Even though lithium-ion electrodes are very versatile in battery production due to their high energy density, the diverse fields of application require the prediction of lifetime and capacity fade. A lot of electrode materials show degradation during usage. If a large current is applied to the poles of the battery during discharge, the diffusion of lithium ions inside the battery from the anode to the cathode is not fast enough and concentration gradients arise.

1.2 History of batteries

At the end of the 18^{th} century, Alessandro Volta invented the voltaic pile, see Figure 1.1 (a), which was the first electrical battery providing a continuous direct current. Together with Luigi Galvani, he discovered that alternating piles of the metals copper and zinc separated by a cloth soaked in sulfuric acid results in an electric potential [115]. Different electrochemical potentials result in chemical reactions of the involved materials, the emergence of ions and an electric current of electrons.
These first battery cells were so-called primary battery cells. They can be used once after assembly as the electrochemical processes taking place in the electrodes and the

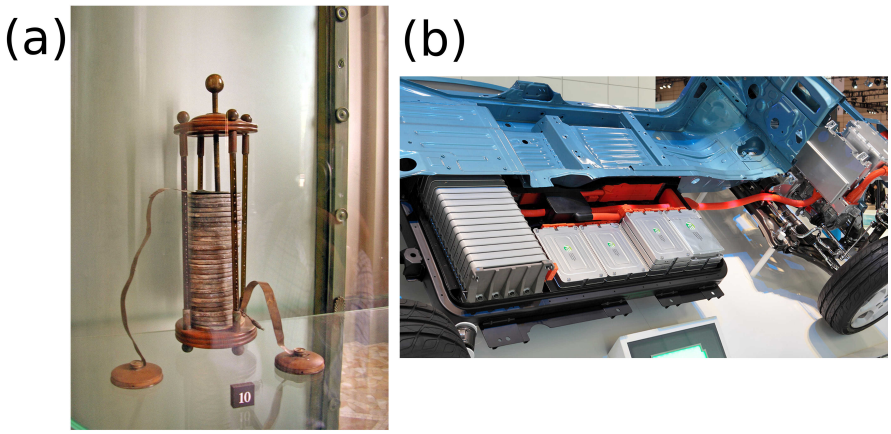

Figure 1.1: (a) Voltaic pile built of several discs of different metals. Positive and negative pole can be seen attached to the pile [51]. (b) Battery system in an electric car. A lot of battery cells are connected and accomodated in the underfloor of the car [130].

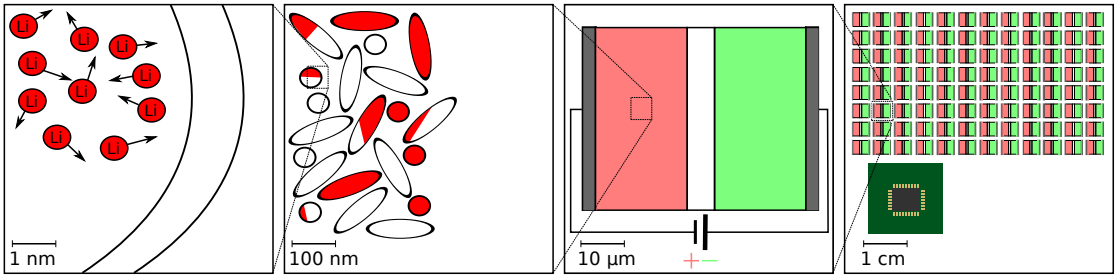

Figure 1.2: Length scales in a lithium-ion battery. Shown are the nano scale, the micro scale, the meso scale and the macro scale.

electrolyte are usually irreversible. The development of lead-acid batteries piloted the ascent of rechargeable or secondary battery cells. They are designed to be used multiple times. The electrochemical processes are partly or totally reversible. This is achieved by the application of an electric potential that is reverse to the electric potential provided by the battery during usage [29].
Since then a lot of different materials have been used. In electric cars such as the Nissan Leaf, see Figure 1.1 (b), modern lithium-ion batteries provide current and move the car hundreds of kilometres.

1.3 Modern lithium-ion batteries

In this section, a short overview over the different length scales and structures of a lithium ion battery is given. Figure 1.2 shows on different length scales the physical phenomena that are to be explained on this scale.
First, Figure 1.2 shows the nanoscale. Processes occurring inside the battery are described by the movements of lithium ions and electrons and their interaction with the crystal lattice of the electrode material. The electromagnetic force and the Maxwell equations are used together with individual motion equations of each discrete entity. Usually, these approaches are restricted to a certain region of the battery, either inside the electrode, the electrolyte or at the solid-electrolyte-interface. The crystal lattice of an electrode is structurally resolved by individual atoms. The interaction between lithium ions and the crystal lattice in either anode or cathode is called intercalation or lithiation. A popular numerical approach is the discrete element method that describes the movement of ions or electrons by their interaction potentials.
Next, Figure 1.1 shows the microscale. Here a continuum argument gives governing equations for the diffusive flux of lithium ions as well as the electrons. The behaviour of the material is described by thermodynamical principle [102]. The composition of each electrode is described by a fully resolved porous microstructure. A lithium ion concentration field replaces the description by the individual motion of lithium ions, the electric potential field replaces the individual motion of electrons and the atomistic forces on the crystal lattice are replaced by a mechanical stress force. In some materials, the restructuring of the lithium ions inside the crystal structure of the electrode material gives rise to large strains [10]. From experiments, it is known that the stresses related to these strains can cause mechanical damage effects in materials including lithium tin oxide [16], lithium manganese oxide [66], lithium titanate oxide [19] and lithium iron phosphate [23]. The mechanical stresses arising in a porous electrode made of lithium manganese oxide have been numerically simulated with a model based on diffusive dilute solution theory [128].
Then, Figure 1.1 shows the so-called mesoscale. Here, a complete battery cell is included, consisting of the two separate electrodes, anode and cathode, that are placed in a liquid electrolyte solution. The electrodes are connected to respective current collectors that eventually represent the positive and negative poles for direct current. On this scale, appropriate and reasonable boundary conditions have to be given to set the usage of the battery into an applicable context. The electrochemical processes derived for the microscale may only be valid for certain temperature ranges. Therefore, a model representing this effect is required [78].
Lastly, on the macroscale, a battery system is given. It is composed of several battery cells and a battery management, here depicted as a microchip. Complex boundary conditions are applied to provide efficient and stable supply depending on the use case.

Usual concerns involve the storage security, heat loss, macroscopic expansion, cyclic fatigue and ageing [137].
A battery system is by its nature on the brink of being chemically unstable. It is supposed to contain the maximum of energy while minimizing volume, that is, a large energy density in $\mathrm{J\,m^{-3}}$ is desired. Some use cases, for example, an acceleration process or going up slopes, require high power and therefore create large heat loss, requiring thermal design for fast heat dissipation. Other use cases in low-temperature environments may require the ability to fastly heat the battery system up to a certain temperature range. Multi-physics or multi-body simulations try to combine individual solutions for subsystems in order to predict the behaviour of the whole system. In [48], the battery system is interacting with other systems like the chassis of the vehicle or the engine by their response.

1.4 Phase-separating materials and phase-field methods

Different materials have been used for an electrolyte as well as for the cathode and the anode. In a lot of them, the electrochemical processes can be accurately described by Fickian diffusion for the lithium ion concentration field and the Gaussian law for the electric potential field. But especially in the popular cathode material lithium iron phosphate ($LiFePO_4$, LFP), the diffusion of the lithium ions from the electrolyte into the active material cannot be modelled by a regular diffusion equation. While in a lot of materials the diffusion leads to a uniform ion distribution inside the material, for LFP a separation into areas with a maximum concentration of lithium ions and areas where no lithium ions are present [34, 154, 21, 85]. Even without applied current, the lithium enriched areas do not diffuse. The distribution of the lithium ions inside the material can then be described by two different phases, one phase enriched with lithium ions and one phase devoid of lithium ions. The process of separation into different phases is called spinodal decomposition. The problem of describing the movement of the boundaries between both phases is often called a Stefan problem [2, 55] and can be approached by adaptive meshes and front-tracking methods [95].
Another approach called phase-field method is introduced in the works of Cahn and Hilliard [14] and is based on a thermodynamical approach involving a non-convex Helmholtz energy functional. In a general phase-field method, the boundary between two phases is discretized and a fine regular spatial mesh is used [74]. Phase-field methods have been applied for the solution of displacive problems such as the phase transformation between austenite and martensite [97, 98] or mechanical fracture processes [108, 75].
In phase-field models for diffusive processes, the constituent fourth-order nonlinear partial differential equation is called the Cahn-Hilliard equation. Recent formulations for lithium iron phosphate particles can be found in [1, 11, 122, 5]. While those models are restricted to simulations of electrode material, the model presented in this thesis

describes diffusion and electric potentials in both electrodes and the electrolyte. There are simulations for the charging of electrode material for different spherical [140, 149], ellipsoidal nanoparticles [66, 82] or more complex single particle microstructures [127, 24]. The macroscopic charge-discharge behaviour of porous electrodes [30, 46, 45, 106, 87] and a focus on effects like hysteresis [32] are explained without resolving a microstructure but using arguments of homogenization or particle size [129].

1.5 State of the art

An established model for the electro-chemical processes in a lithium-ion battery has first been presented by Newman in a general context [103].
Measurements are either ex-situ or in-situ. A measurement is called ex-situ if it is performed without application of a current without the usage of the cell. Several details are important. The process of preparing the specimen for the imaging device may change for example the temperature of the battery cell and is, therefore, a source of error. More important, dynamic chemical processes in the specimen progress to equilibrium after the cell is taken from the current source and therefore it has to be assumed that only equilibrium states may be measured. "In situ" is conducting the measurement on a battery cell during its usage. Depending on how often and how fast a detailed image can be processed it allows for the description of dynamic processes and validation of time-dependent models.
In-situ methods are important as ex-situ methods only provide measurements in equilibrium and may not be able to document intermittent states [114]. In-situ measurements prove the existence of two phases in LFP using X-ray diffraction spectroscopy [90], X-ray absorption spectroscopy [27], transmission electron microscopy [63, 114, 89], or nanoparticle powder diffraction [152, 119]. Dependent on the charge rate[1] the phase separation may be suppressed for large charge rates [153]. Analytic properties of phase-field methods can be applied to predict suppression of phase separation in nanoparticles.
A general description of lithium ion diffusion by a diffusion equation with varying, but positive diffusion coefficients is possible [12]. Especially for LFP, experimental evidence shows the more complex thermo-dynamical behaviour resulting in phase transformation and the separation into lithium-rich phases $LiFePO_4$ and lithium-poor phases $FePO_4$. The lithium ions reside on fixed places inside the crystal lattice, a process called intercalation [136]. The intercalation of lithium ions into the electrode material is also usually connected to mechanical stresses inside the porous microstructure. For some electrode materials like silicon, volumetric expansions of over 300 % have been observed [65, 93]. Therefore, finite strain models have been introduced. For some materials, complex material models have been proposed including hyperelasticity [94] or plasticity (for LiSi [83]). In-situ measurements show coupling between intercalation and mechanical strains for

[1] The charge rate gives a measure of the speed of charging or discharging a battery.

LFP [147]. In [4] the interface kinetics from electrolyte over carbon coating is explained by the description of the crystal lattice of LFP. Transmission electron microscopy is used in [126] and compared to scanning transmission X-ray microscopy on LFP. They identify LFP particles in phase-separated state and also provide methods to find particle overlap in the imaging and account for it.
Different mathematical models have been established for the simulation of phase separation in LFP cathodes across several scales. Non-dimensionalization has been presented [3] and several upscaling methods are discussed based on the dimensionless description. Also, a dimensionless Damköhler number has been introduced that describes the ratio between the diffusivity and the charging rate. The interaction between particles has been studied on an agglomerate of many different sized spherical particles [105]. It is shown that during de-lithiation, most of the particles are either de-lithiated or still lithiated. Also, it is noted that the charge rate decides whether large particles get de-lithiated first or if the de-lithiation process is size-independent. Two-scale models have been developed [26] that connect the particle or crystal scale to the cell or cathode scale. It is noted that on the cell scale effects across several particles can be observed. The memory effect of relaxation to equilibrium is studied for different charge rates and alternating charging and discharging in [43, 44]. Fully resolved three-dimensional battery model has been introduced [67] for the numerical simulation of the charging process of a Lithium-Cobalt-Oxide cathode ($LiCoO_2$, LCO). LCO is a non-phase-separating material and the diffusion of the cathode material is modelled with a constant diffusion coefficient.
The Cahn-Hilliard equation has been introduced to describe effects like nucleation, Ostwald ripening [77] in order to model interfaces and spinodal decomposition in binary alloys [13, 14]. Since then, it has been also applied to model Stokes flow [113], two-phase-flows [120, 100], volume reconstruction [85] and battery modeling [5, 62]. The two-phase lithium intercalation model has been generalized to several different phases [52][2]. The surface wetting effect in the Cahn-Hilliard equation has been investigated in numerical models for cathode materials [125].
Several models have been proposed for the deformation of electrode materials. For small strain models, isotropic linear elastic models have been introduced [150]. The mechanical effects on LFP during intercalation have also been simulated for simple microstructures. Isotropic linear-elastic model has been applied and several galvanostatic and potentiostatic simulation have been performed [123]. It is observed that the maximum stress develops in the interfacial region. Also, anisotropic models to analyse stress evolution on the cell scale have been presented [18, 64]. It has been shown that the strain energy depends on the charge rate. Mesoscopic models have been used to calculate the stress in

[2] Appendix B presents a possible extension to the model presented in this work in order to include several different phases.

battery electrodes [18]. The coupling between elastic effects and intercalation has been investigated [7].
For the spatial discretization of diffusion problems, finite-volume methods have proven to be useful and flexible [109, 61]. A uniform regular cell grid is used and thus a finite-volume scheme on cell-centered voxels is identical to a finite-difference scheme [92]. Recently some research has been focused on the use of multigrid methods for the numerical efficient solution of Cahn-Hilliard equations in periodic domains [121, 91] or general phase-field methods [84]. Another popular approach for spatial discretization is the usage of the convolution property of a discrete Fourier transform for the application of linear differential operators [28, 146, 124]. A lot of work is focused on the optimized and parallel computation of the discrete Fourier transform [49]. While explicit time discretizations are often favoured for their easy implementation, their applicability is diminished by the restriction on time step size. On the other hand, an implicit discretization requires the assembly and inversion of a matrix which is both costly in memory and computation time. To resolve this, a semi-implicit discretization has been introduced [40, 42] which is unconditionally stable [20]. This requires the approximation of logarithmic chemical potentials by polynomials [68]. Since then it has been applied to a variety of problems [86, 71, 81]. It enables a semi-explicit scheme for the Cahn-Hilliard equation in arbitrary complex domains. On regular voxel grids, the application of a discrete differential operator under periodic boundary conditions onto a function can be rewritten as a convolution with another function [15].
Preconditioners for the fast solution of periodic Cahn-Hilliard problems have been applied [8]. Different numerical approaches on different scales from atomistic models up to multi-system simulations e.g. in COMSOL or SimuLink have been compared and investigated [111]. Phase-field models on periodic domains have been extensively studied and solved with methods using fast Fourier transformation [110, 118]. Problems on electrode particles with constant Butler-Volmer currents have been simulated with higher-order schemes due to the fourth-order Cahn-Hilliard equation in order to make use of larger time steps [149, 26]. However, the highly nonlinear interface conditions in combination require small time-steps regardless of the convergence order of the scheme used. Even though unconditionally stable semi-implicit backwards schemes have successfully been derived and proved for the simple elliptic equations and Cahn-Hilliard equations in [42], they are not capable of implementing nonlinear interface conditions.
In order to improve the stable semi-implicit method for complex domains in two and three dimensions, the immersed interface method method [88] is applied in this work. This method was proposed for elliptic equations in heterogeneous materials with discontinuous constant coefficients [142]. Later it was extended to elasticity [116], crack jumps [143] and currently the Cahn-Hilliard equation [60]. It can also be applied to embed and discretize arbitrarily shaped domains into larger encompassing cuboid domains. It is part of the family of immersed boundary methods [107], but instead of modifying the governing equations and adding additional terms, the solution field is extended arbitrarily onto the

embedded domain. Then the jumps of the unknowns along the boundary are discretized and the jump variables are introduced as additional unknowns. The resulting linear system is solved iteratively by a Schur complement method [135].

1.6 Scope and outline

In Chapter 2 a model describing electrical, chemical and mechanical processes in a lithium-ion battery on the microscale during charging and discharging is presented. First, a short introduction into phase-field methods and linear elasticity are described. Then the electro-chemical model for a battery with porous microstructure is introduced and coupling terms to mechanical processes are given. A phase-field model for phase separation especially in the cathode material LFP is defined. Interface conditions for the transmission problem are given between the different domains. The model consists of several Poisson equations, diffusion equations and the Cahn-Hilliard equation.
In Chapter 3 numerical methods are introduced. A finite volume method on a regular voxel mesh and adaptive time integration are defined. This allows for small time steps during initiation of phase-separation and reconfigurations and large time steps during stable movement of phase-interfaces and accelerates the numerical solution. Also, the discretization and solution of the mechanical model are shown. Two different methods for the solution of the electro-chemical model are defined. The first method solves the system of nonlinear equations given by the discretization of the partial differential equations. The Jacobian is derived and a damped Newton algorithm is used for the solution of the nonlinear system. The second method simplifies the model and applies a domain decomposition. Then the immersed interface method is used in combination with Fourier methods for differentiation. A finite difference scheme is introduced and the integration of periodic linear operators in Fourier space is defined. Finally, the immersed interface method is applied for the Poisson equation, the diffusion equation and the Cahn-Hilliard equation.
In Chapter 4 different numerical tests are presented. First, the properties of the applied phase-field potentials are analysed. Then the numerical convergence of the introduced methods is demonstrated on several examples. The generation of microstructures consisting of periodic spherical packings is discussed. Next, the electro-chemical model is investigated in different applications in microstructures in 1D and 2D. Finally different porous microstructure in 3D are considered and the electro-chemo-mechanical model is investigated.
In Chapter 5 a short summary is given and an outlook to future work is discussed.
Appendices A and B describe two other applications of phase-field methods. Appendix A shows examples for the solidification of materials, while Appendix B shows examples for the decomposition of multiphase composites. Both are a generalization to the Cahn-Hilliard model presented in this work.

Chapter 2

Electro-chemo-mechanical model

In this chapter, the model involving physical, chemical and mechanical properties is presented. A charge process of a lithium-ion battery is modeled on the microscale as an initial boundary value problem with several partial differential equations. As an initial state, a discharged battery is used that is charged over a time period ranging from several seconds up to an hour. The speed at which this charge process happens is called C-rate. It is later defined precisely.
Section 2.1 defines notation and fundamentals for phase-field methods and linear elasticity. In Section 2.2 the governing equations and all interface, boundary and initial conditions for the involved variables are derived.

2.1 Fundamentals

Subsection 2.1.1 introduces basic notation and ideas from phase-field methods. Subsection 2.1.2 gives a short introduction in the theory of elastic displacement and defines notation and variables.

2.1.1 Phase-field methods

Some materials can attain different physical phases, where each phase possesses specific physical properties. As an example, the three well-known phases of the material water H_2O are ice, liquid water or vapour. The example of an ice cube in liquid water is used for this subsection. The occurence of the different phases may depend on physical properties such as temperature or density. Especially in water also induced nucleation is possible, this is the usual origin for snowflakes. If two phases coexist, the boundary between their domains is called a phase interface. Figure 2.1 (a) shows two different phases in their respective domains Ω_0 and Ω_1 and the phase interface between them is called Γ.
For example, it is possible to describe the physical behavior of the material in each of the domains with a partial differential equation, stationary or time-dependent. Additionally, interface conditions on the phase interface can be posed. If the phase interface evolves

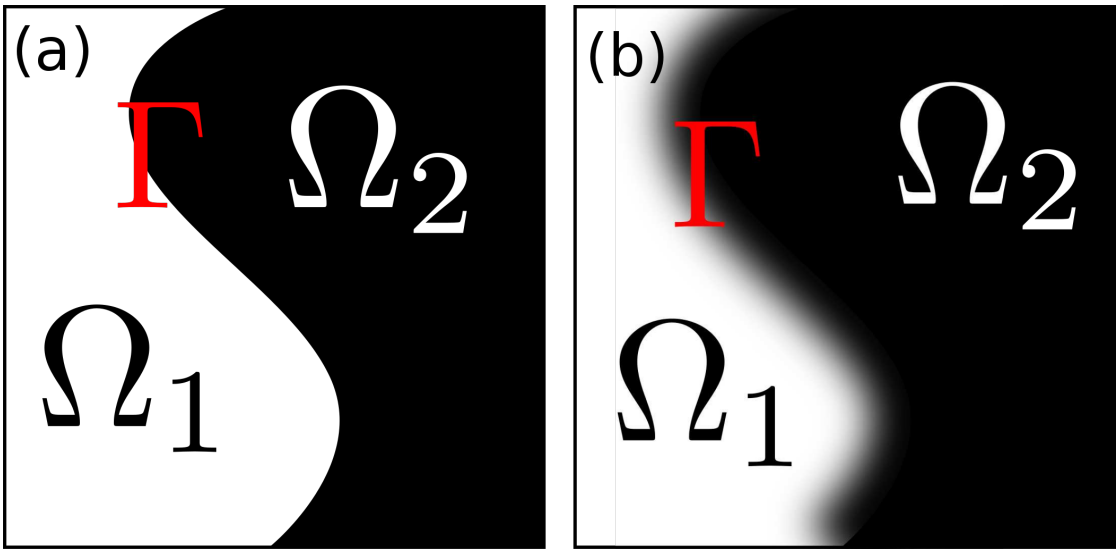

Figure 2.1: (a) Two different phases, symbolized by black and white and a sharp interface between them. (b) A smoothed interface as it is used in a phase-field method.

with time, this problem is called a Stefan problem. Mathematically, it represents a free boundary problem.
Phase-field methods are a class of mathematical models to describe and solve these problems. An auxiliary field called phase-field p is introduced that can attain different discrete values which are associated with the different phases of the material, in terms of the example the discrete values $p_1 = 0$ for liquid water and $p_2 = 1$ for solid ice. Also, p may attain other values. As a function, p is usually assumed to be a smooth function of some degree, e.g., $C^2(\Omega)$ or $C^4(\Omega)$. The phase interface Γ is then given as the contour value for $p = 0.5$. Values of p in the domain (p_1, p_2) can then be interpreted in two different ways: From a mathematical point of view it is possible to interpret a phase-field method as a smooth relaxation of a free boundary problem. From a physical point of view it is possible to interpret the domain where $p \in (p_1, p_2)$ as the region, where neither discrete phase may be attributed to this region, i.e., a mixture of both phases exists there.
Next a short overview to the equations involved in phase-field method is given. For a general introduction, see [14] or more recently [53]. Given a phase-field parameter p and the discrete values representing pure phases p_1 and p_2. Assume a non-convex free energy $F_0(p)$ with minima at p_1 and p_2. Superposition with an additional gradient term $||\nabla p||^2$ with the scalar values α and β gives the total energy

$$F(p(\boldsymbol{x}, t), \nabla p) = \alpha F_0(p(\boldsymbol{x}, t)) + \frac{\beta}{2}||\nabla p(\boldsymbol{x}, t)||^2. \tag{2.1}$$

A chemical potential μ is then defined as the variational derivative of this energy,

$$\begin{aligned}\mu(\boldsymbol{x},t) &= \frac{\delta F(p(\boldsymbol{x},t),\nabla p)}{\delta p(\boldsymbol{x},t)} = \frac{\partial F(p)}{\partial p} - \nabla\cdot\frac{\partial F(\nabla p)}{\partial \nabla p} = \\ &= \alpha F_0'(p(\boldsymbol{x},t)) - \frac{\beta}{2}2\nabla\cdot(\nabla p(\boldsymbol{x},t)) = \alpha F_0'(p(\boldsymbol{x},t)) - \beta\Delta p(\boldsymbol{x},t).\end{aligned} \tag{2.2}$$

Now an additional balance equation is used to define a time evolution of the phase-field parameter. For a diffusive process the conservation of mass is used, e.g.

$$\partial_t p(\boldsymbol{x},t) = \operatorname{div}\left(\boldsymbol{D}(\boldsymbol{x},t)\nabla\mu(\boldsymbol{x},t)\right), \tag{2.3}$$

where $\boldsymbol{D}(\boldsymbol{x},t)$ is an arbitrary tensor defining the diffusivity. For the proposed chemical potential $\mu(\boldsymbol{x},t)$, this results in a fourth-order partial differential equation for the phase-field parameter $p(\boldsymbol{x},t)$

$$\partial_t p(\boldsymbol{x},t) = \operatorname{div}\left(\boldsymbol{D}(\boldsymbol{x},t)\nabla\left(\alpha F_0'(p(\boldsymbol{x},t)) - \beta\Delta p(\boldsymbol{x},t)\right)\right). \tag{2.4}$$

This equation is called Cahn-Hilliard equation.

2.1.2 Linear elasticity

In this subsection, a short introduction to linear elastic models for small displacements in three dimensions is presented. For a more comprehensive and general introduction the reader is referred to [56].
The difference between a reference configuration $\boldsymbol{X} \in \mathbb{R}^3$ and a deformed or current configuration $\boldsymbol{x} \in \mathbb{R}^3$ is called displacement vector $\boldsymbol{u} \in \mathbb{R}^3$,

$$\boldsymbol{u} = \boldsymbol{x} - \boldsymbol{X}. \tag{2.5}$$

Its gradient is $\nabla\boldsymbol{u} \in \mathbb{R}^{3\times3}$. The symmetric part of $\nabla\boldsymbol{u}$ is called (linearized) strain,

$$\boldsymbol{\varepsilon} = \frac{1}{2}(\nabla\boldsymbol{u} + \nabla\boldsymbol{u}^T), \tag{2.6}$$

and may be described due to symmetry as a vector $\boldsymbol{\varepsilon} \in \mathbb{R}^6$. This is called Voigt-Notation. If $u_{i,j} = \partial_j u_i$, the components are then

$$\boldsymbol{\varepsilon} = \left(u_{1,1},\quad u_{2,2},\quad u_{3,3},\quad u_{2,3}+u_{3,2},\quad u_{1,3}+u_{3,1},\quad u_{1,2}+u_{2,1}\right)^T. \tag{2.7}$$

The same holds for the mechanical stress $\sigma \in \mathbb{R}^{3\times3} \cong \mathbb{R}^6$. In the context of linear elasticity, the stress is given by the application of a linear operator, the stiffness tensor $\mathbb{C} \in \mathbb{R}^{3\times3\times3\times3} \cong \mathbb{R}^{6\times6}$ on the strain $\boldsymbol{\varepsilon}$,

$$\boldsymbol{\sigma} = \mathbb{C} : \boldsymbol{\varepsilon}. \tag{2.8}$$

Name	Character	Value	Unit
Concentration	$c(\boldsymbol{x}, t)$	-	$\mathrm{mol\,l^{-1}}$
Potential	$\phi(\boldsymbol{x}, t)$	-	V
Deformation	$\boldsymbol{u}(\boldsymbol{x}, t)$	-	cm
Electric current	$i_{\mathrm{se}}(\boldsymbol{x}, t)$	-	$\mathrm{A\,cm^{-2}}$
Lithium ion flux	$f_{\mathrm{se}}(\boldsymbol{x}, t)$	-	$\mathrm{mol\,cm^{-2}\,s^{-1}}$
Strain	$\boldsymbol{\varepsilon}(\boldsymbol{x}, t)$	-	1
Stress	$\boldsymbol{\sigma}(\boldsymbol{x}, t)$	-	GPa
Universal gas constant	R	8.314	$\mathrm{J\,mol^{-1}\,K^{-1}}$
Temperature	T	300	K
Faraday constant	F	96485	$\mathrm{A\,s\,mol^{-1}}$

Table 2.1: Definition of symbols and constants.

For linear isotropic elastic materials two material parameters are used to define $\mathbb{C}$, the Lamé constants λ and μ. The stress is then given as

$$\boldsymbol{\sigma} = \lambda \operatorname{Tr}(\boldsymbol{\varepsilon})\boldsymbol{I} + 2\mu\boldsymbol{\varepsilon}. \tag{2.9}$$

For a solid body the static equilibrium equation under volume forces f is given as

$$0 = \operatorname{div}\boldsymbol{\sigma} + f. \tag{2.10}$$

A linear isotropic elastic material may also be described by the two parameters Young's modulus E and Poisson's ratio ν. In this case, the Lamé constants are given as

$$\lambda = \frac{E\nu}{(1+\nu)(1-2\nu)} \quad \mu = \frac{E}{2(1+\nu)}. \tag{2.11}$$

The governing equations for a linear isotropic elastic material (disregarding boundary conditions) are then

$$\begin{aligned} \boldsymbol{\varepsilon} &= \frac{1}{2}(\nabla\boldsymbol{u} + \nabla\boldsymbol{u}^T) \\ \boldsymbol{\sigma} &= \lambda \operatorname{Tr}(\boldsymbol{\varepsilon})\boldsymbol{I} + 2\mu\boldsymbol{\varepsilon}, \\ 0 &= \operatorname{div}\boldsymbol{\sigma} + f. \end{aligned} \tag{2.12}$$

In the next section, a battery model with corresponding linear isotropic elastic models is introduced referencing the introduced model in each domain.

2.2 Battery model

In this section, the equations for a lithium-ion battery model on the microscale are presented. The mathematical model involves the scalar fields concentration c, the electric

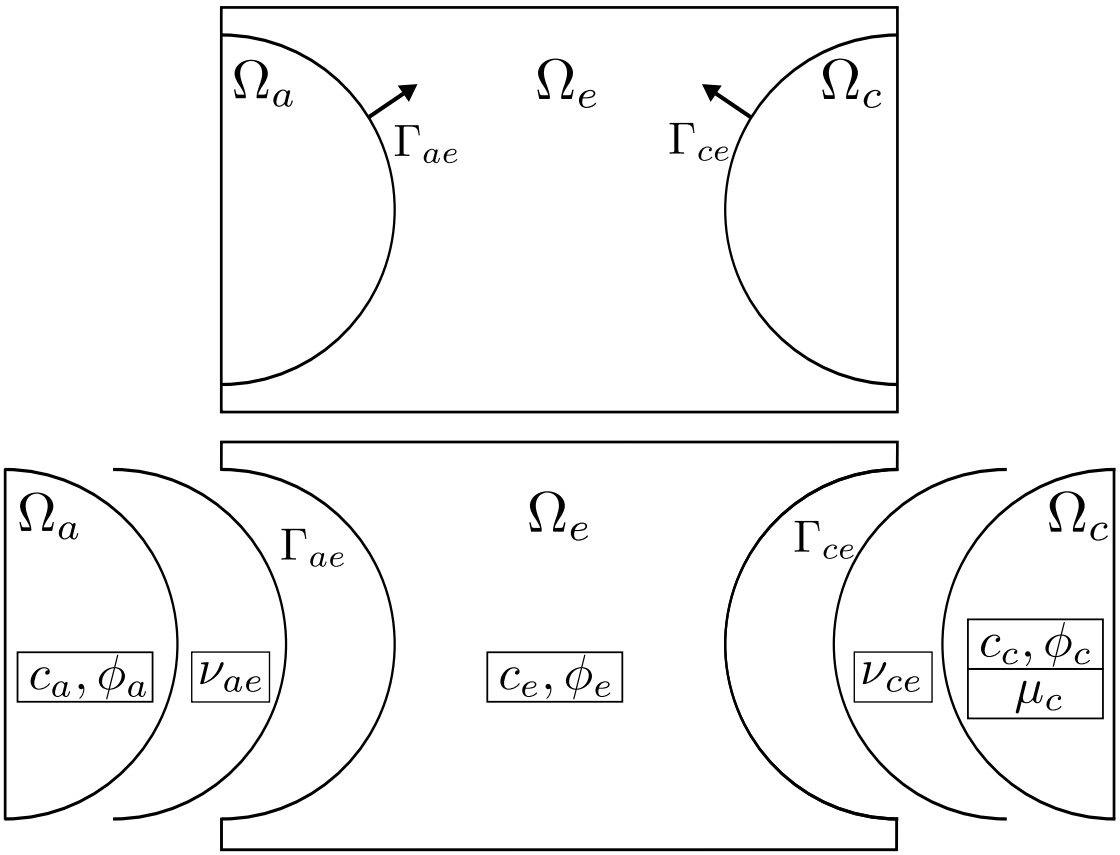

Figure 2.2: Decomposition of a battery cell into anode Ω_a, electrolyte Ω_e, cathode Ω_c and the interfaces Γ_{ae} and Γ_{ce}.

potential ϕ, the chemical potential μ and the vector field displacement $\boldsymbol{u}$. The movement of electrons and the charging of a battery is connected to the local concentration c and diffusion of positive lithium ions Li^+. The electric field ϕ is connected to the current provided by the battery during usage. The lithium ion intercalation into electrode material results in local displacement $\boldsymbol{u}$ of the electrodes. Table 2.1 defines symbols and physical constants.
First the spatial domains are introduced in Subsection 2.2.1. Then the governing equations are derived in Subsection 2.2.2. Additional conditions are given on the interfaces (Subsection 2.2.3) and boundaries of the domain (Subsection 2.2.4). Initial conditions close the mathematical model in Subsection 2.2.5. Finally, a summary of the electro-chemo-mechanical model is given in Subsection 2.2.6.

2.2.1 Domain

A cuboid domain $\Omega = (0, L_1) \times (0, L_2) \times (0, L_3) \subset \mathbb{R}^3$ denotes the microstructure of a battery cell and consists of the two solid electrodes, anode Ω_a and cathode Ω_c, and the liquid electrolyte Ω_e, i.e., $\Omega = \Omega_a \cup \Omega_e \cup \Omega_c$. A porous separator domain is not included in the model. The union $\Omega_s = \Omega_a \cup \Omega_c$ is called the solid domain. Figure 2.2 shows a two-dimensional representation and also introduces a domain decomposition with interfaces Γ_{ae}, Γ_{ce}, and $\Gamma_{\mathrm{se}} = \Gamma_{ae} \cup \Gamma_{ce}$.
A time-dependent problem is posed on the domain $T = (0, t_0)$. The following subsections define partial differential equations for the concentration field $c(\boldsymbol{x}, t)$, the electric potential field $\phi(\boldsymbol{x}, t)$, the displacement $\boldsymbol{u}(\boldsymbol{x}, t)$, and the interface current $i_{\mathrm{se}}(\boldsymbol{x}, t)$. For concentration, electric potential and displacement, governing equations are given on each of the three domains $\Omega_{a,T} = \Omega_a \times T$, $\Omega_{e,T} = \Omega_e \times T$, and $\Omega_{c,T} = \Omega_c \times T$. Additionally define $\Omega_T = \Omega \times T$.
The interface currents are defined on $\Gamma_{\mathrm{ae,T}} = \Gamma_{\mathrm{ae}} \times T$, $\Gamma_{\mathrm{ce,T}} = \Gamma_{\mathrm{ce}} \times T$ with $\Gamma_{\mathrm{se,T}} = \Gamma_{\mathrm{se}} \times T$. In this context, the trace operator γ_0 is introduced that gives the trace of a scalar field defined on $\Omega_{i,T}$ with $i \in \{a, c, e\}$ onto $\Gamma_{\mathrm{se,T}}$.

$$\gamma_{ce,c} : \begin{cases} \Omega_{c,T} & \to \Gamma_{ce,T} \\ c_c(\boldsymbol{x}, t) & \mapsto c_{ce,c}(\boldsymbol{x}, t) = \lim\limits_{\Omega_c \ni \tilde{x} \to x \in \Gamma_{\mathrm{ce}}} c_c(\tilde{x}, t). \end{cases} \tag{2.13}$$

Similar projections $\gamma_{ce,e}$, $\gamma_{ae,a}$, and $\gamma_{ae,e}$ are defined for the other parts of the domains and fields $c_{ce,e}$, $c_{ae,a}$, and $c_{ae,e}$ are deduced. The lithium ion concentration $c_{se,s}$ is defined as $(c_{ce,c}, c_{ae,a})$ on the side of the electrode and corresponding as $c_{se,e}$ as $(c_{ce,e}, c_{ae,e})$ on the side of the electrolyte. In general $c_{se,s} \neq c_{se,e}$, i.e., there is no continuous extension of c_s and c_e across Γ_{se}. The fields ϕ_c,ϕ_e,ϕ_a are extended in the same way to functions $\phi_{se,s}$ and $\phi_{se,e}$.

2.2.2 Governing equations

In this subsection, the transport equations in the electrolyte domain Ω_e, the anode domain Ω_a, and the cathode domain Ω_c are introduced separately.

2.2.2.1 Electrolyte

The transport equations for ion concentration c_e and the electric potential ϕ_e in an electrolyte, see [79], are considered as

$$\begin{aligned} \partial_t c_e - \operatorname{div}\left[D_e \nabla c_e - \frac{t_+}{F}\left(\kappa_e \nabla \phi - \kappa \frac{t_+ - 1}{F}\left(\frac{\partial \mu_e}{\partial c} \right) \nabla c_e \right) \right] &= 0, \\ - \operatorname{div}\left[\kappa_e \frac{t_+ - 1}{F}\left(\frac{\partial \mu_e}{\partial c} \right) \nabla c_e + \kappa_e \nabla \phi_e \right] &= 0. \end{aligned} \tag{2.14}$$

Name	Character	Unit	Anode	Electrolyte	Cathode
Diffusivity	D	$\mathrm{cm^2\,s^{-1}}$	10^{-10}	$1.27 \cdot 10^{-7}$	10^{-10}
Conductivity	κ	$\mathrm{A\,V^{-1}\,cm^{-1}}$	10	0.0038	10
Reference pot,	$\bar{U}$	V	0	$\times$	3.42
Max. Li-ion conc.	$c_{\max}$	$\mathrm{mol\,l^{-1}}$	20	$\times$	20
Li. transf. nr.	t_+	1	$\times$	0.2	$\times$
Young's modulus	E	GPa	10	0.1	10
Poisson's ratio	ν	1	0.3	0	0.3
Partial molar vol.	θ	$\mathrm{cm^3\,mol^{-1}}$	3.497	0	3.497
Mixing enthalpy	q	$\mathrm{J\,mol^{-1}}$	$\times$	$\times$	0.118
Initial conc.	c_0	$\mathrm{mol\,l^{-1}}$	$0.99c_{\max,\mathrm{c}}$	$0.06c_{\max,\mathrm{c}}$	$0.01c_{\max,\mathrm{c}}$

Table 2.2: Material parameters partially taken from [58, 79, 148, 151].

Table 2.2 gives numerical values for the electrolyte diffusion coefficient D_e, the electrolyte conductivity κ_e, the lithium transference number t_+, and the Faraday constant F. A logarithmically scaled chemical potential $\mu_e(c_e) = RT \log \frac{c_e}{c_{\max}}$[1] is used to rewrite (2.14). Table 2.2 gives numerical values for the ideal gas constant R and the temperature T. The transport equations are then

$$\begin{aligned} \partial_t c_e - \operatorname{div}\left[\left(\frac{D_e}{RT}c_e + \frac{\kappa_e t_+(t_+-1)}{F^2}\right)\nabla\mu_e(c_e) + \frac{\kappa_e t_+}{F}\nabla\phi_e\right] = 0, \\ -\operatorname{div}\left[\kappa_e\frac{(t_+-1)}{F}\nabla\mu_e(c_e) + \kappa_e\nabla\phi_e\right] = 0. \end{aligned} \tag{2.15}$$

The model for the electrolyte displacement is given in (2.12) with the Young's modulus E and Poisson's ratio ν given in Table 2.2.

2.2.2.2 Anode

An electrochemical model for the transport of lithium ions inside electrode material is taken from [79] as

$$\partial_t c_a + \operatorname{div}\left[D(c_a)\nabla\mu_a(c_a)\right] = 0. \tag{2.16}$$

The anode diffusion coefficient $D(c_a)$ is chosen depending on the local lithium ion concentration c as

$$D(c_a) = \frac{D_a}{RT}c_a\left(1 - \frac{c_a}{c_{\max,\mathrm{a}}}\right) \tag{2.17}$$

[1] Table 2.2 does not give a value for a maximum lithium ion concentration in the electrolyte. The initial concentration in the electrolyte may be used for the formulation with a chemical potential μ_e.

The solid diffusion coefficient D_a is smaller than in the electrolyte as diffusive processes in the solid material are slower than in the liquid electrolyte.
The chemical potential is given as a sum of both chemical and elastic parts,

$$\mu_a = \mu_{ch}(c_a) + \mu_{\text{el}}(\sigma_a) = RT \log \frac{c_a}{c_{\text{max,a}} - c_a} + \frac{\theta_a}{3}\text{tr}(\sigma_a). \tag{2.18}$$

It is derived from a convex Helmholtz energy assuming a maximum solid concentration $c_{\text{max,a}}$ depending on the material [149, 151].
Additionally, the Poisson equation for an electric potential ϕ_a inside the electrode is considered as

$$-\text{ div } (\kappa_a \nabla \phi_a) = 0. \tag{2.19}$$

This gives the governing equations for the electrochemical model in the anode as

$$\begin{aligned} \partial_t c_a + \text{div } \left[\frac{D_a}{RT} c_a \left(1 - \frac{c_a}{c_{\text{max,a}}} \right) \nabla \mu_a(c_a) \right] &= 0, \\ -\text{ div } (\kappa_a \nabla \phi_a) &= 0. \end{aligned} \tag{2.20}$$

The stress-strain relationship model presented in this work is based on a linear-elastic model introduced in [151] and applied in [128]. The strain $\boldsymbol{\varepsilon}$ is modified to include a chemical part, $\boldsymbol{\varepsilon}_{\text{el}} := \boldsymbol{\varepsilon} - \boldsymbol{\varepsilon}_{\text{ch}}$. The chemical strain is a linear function of the concentration as

$$\boldsymbol{\varepsilon}_{\text{ch}} = \frac{\theta}{3} c \boldsymbol{I}, \tag{2.21}$$

where θ is the partial molar volume given in Table 2.2. Model (2.12) is then modified to

$$\begin{aligned} \boldsymbol{\varepsilon}_{\text{el}} &= \frac{1}{2}(\nabla \boldsymbol{u} + \nabla \boldsymbol{u}^T) - \frac{\theta}{3} c \boldsymbol{I}, \\ \boldsymbol{\sigma} &= \lambda \,\text{Tr}(\boldsymbol{\varepsilon}_{\text{el}}) \boldsymbol{I} + 2\mu \boldsymbol{\varepsilon}_{\text{el}}, \\ 0 &= \text{div}\, \boldsymbol{\sigma}. \end{aligned} \tag{2.22}$$

With those definitions, coupling terms between the electro-chemical model and the elastic model are given as

$$\mu_{\text{el}} = \frac{\theta}{3}\text{tr}(\boldsymbol{\sigma}) \Leftrightarrow \boldsymbol{\varepsilon}_{\text{ch}} = \frac{\theta}{3} c \boldsymbol{I}. \tag{2.23}$$

2.2.2.3 Cathode

In the cathode, a phase-field model for the concentration c_c is considered. The phase-field parameter is here the normalized lithium ion concentration $p = \frac{c}{c_{\text{max,c}}}$. In [66, 5, 148], the free energy is assumed as

$$F_0(p) = p\log p + (1-p)\log(1-p) + \frac{q}{RT}p(1-p). \tag{2.24}$$

Table 2.2 gives the enthalpy of mixing q. The first term is related to a diffusion potential based on one-body terms in a Hamiltonian of the crystalline structure in active material. The second term results from a mean-field approximation of two-body interaction terms in the Hamiltonian. The phase interface between lithium-rich phase and lithium-poor phase is related to misfits in the crystal structure. Therefore, a penalty term involving a norm of the gradient of the phase-field parameter is added to the free energy to receive

$$F(p, \nabla p) = \alpha L_0^2 \frac{G}{L} F_0(p) + \frac{\beta G L}{2} (\nabla p)^2 . \tag{2.25}$$

Table 2.2 gives the reference length L_0. Here the parameters G and L are used to describe the phase-field model. They represent energy density and the width of the interface region, respectively. Additionally α and β are dimensionless scalar parameters. From (2.25), the chemical potential μ is now given as the variational derivative by

$$\frac{\mu(c_c)}{RT} = \alpha L_0^2 \frac{G}{L} F_0'(\frac{c_c}{c_{\max,c}}) - \beta G L \Delta \left(\frac{c_c}{c_{\max,c}} \right). \tag{2.26}$$

Combining (2.16) and (2.26), the equations governing the lithium ion concentration c_c, the electric potential ϕ_c and the chemical potential μ are given by

$$\begin{aligned} \partial_t c &= \operatorname{div}\left[\frac{D_c}{RT} c_c \left(1 - \frac{c_c}{c_{\max,c}} \right) \nabla \mu \right], \\ 0 &= -\operatorname{div}(\kappa_c \nabla \phi_c), \\ \mu &= RT\alpha L_0^2 \frac{G}{L} F_0'(\frac{c_c}{c_{\max,c}}) - RT\beta G L \Delta \left(\frac{c_c}{c_{\max,c}} \right). \end{aligned} \tag{2.27}$$

Here the chemical potential μ is introduced with a third equation as an additional unknown. The elastic model for the cathode is chosen identical to (2.22) as

$$\begin{aligned} \boldsymbol{\varepsilon}_{\mathrm{el}} &= \frac{1}{2}(\nabla \boldsymbol{u} + \nabla \boldsymbol{u}^T) - \frac{\theta}{3} c \boldsymbol{I}, \\ \boldsymbol{\sigma} &= \lambda \operatorname{Tr}(\boldsymbol{\varepsilon}_{\mathrm{el}}) \boldsymbol{I} + 2\mu \boldsymbol{\varepsilon}_{\mathrm{el}}, \\ 0 &= \operatorname{div} \boldsymbol{\sigma}. \end{aligned} \tag{2.28}$$

2.2.3 Interface conditions

The domains Γ_{ae} and Γ_{ce} in Figure 2.2 are both part of the electrode domain and the electrolyte domain. They act as inner boundaries between electrode and electrolyte and are called interface boundaries. In order to close the partial differential equations given in their respective domain, this subsection will define transmission conditions.

One way for this is to resolve the porous structure of the electrode surface atomistically. The crystal structure is exposed to the liquid electrolyte and surface reactions take place that change the chemical reaction rates. In order to simplify this complex conditions, usually Butler-Volmer interface conditions are applied [80]. They result from an up-scaling argument. This homogenization allows to describe the chemical intercalation reaction on the electrode surface as a simple transmission conditions while still solving correctly for electric potential and lithium ion concentration. However, this comes at the price of the possibility of a jump in both of these variables. Therefore, the concentration field and the electric potential field are both usually not continuous across the electrode-electrolyte interface in a microscale model as it is presented here.
The Butler-Volmer interface electric current i_{se} is defined as

$$i_{\mathrm{se}} = i_0(c_{se,s}, c_{se,e}) \sinh\left(\frac{F}{2RT}\eta\right). \tag{2.29}$$

The hyperbolic function is a result of the approximation of chemical reaction rates. The transmission of electrons and lithium ions happens in such way that no charges are built up. For this reasons, the negative electric current resulting from the electrons corresponds to the charge transfer resulting from the lithium ions. A corresponding interface concentration flux is therefore defined as

$$f_{\mathrm{se}} = \frac{i_{\mathrm{se}}}{F}. \tag{2.30}$$

The Nernst overpotential η is the difference between the electrochemical potentials on both sides of the particle surface and is given as

$$\eta = \phi_{se,s} - \phi_{se,e} - U_0(c_{se,s}) \tag{2.31}$$

The open circuit potential $U_0(c_{se,s})$ is the difference of the chemical potential at the particle surface divided by the Faraday constant and the reference potential $\bar{U}_s$,

$$U_0 = \frac{\mu_{se,s}}{F} - \bar{U}_s, \tag{2.32}$$

where U_s is either $\bar{U}_a$ or $\bar{U}_c$, depending on the electrode. They are given in Table 2.2.
The function i_0 is called the exchange current density. In [80] the exchange current density is derived as

$$i_0(c_{se,s}, c_{se,e}) = 2k\sqrt{c_{se,e}c_{se,s}\frac{c_{\max}}{2}} \qquad \text{(Model A)}, \tag{2.33}$$

while in [103] another function is given as

$$i_0(c_{se,s}, c_{se,e}) = 2k\sqrt{c_{se,e}c_{se,s}(c_{\max} - c_{se,s})} \qquad \text{(Model B)}. \tag{2.34}$$

Although the Model B (Newman) is more commonly employed, Model A has been derived from first principles of thermodynamics in [80]. Both are considered and compared to each other in Subsection 4.4.2.
The electric current i_{se} is used to define a Neumann boundary condition for the Poisson equations for the electric potential while the concentration flux f_{se} is used to define a Neumann boundary conditions for the diffusion equations of the lithium ion concentration. The Faraday constant F acts as a coupling factor. As the lithium ions carry a positive charge, the concentration flux is coupled to the electric current.
The interface conditions on the solid-electrolyte interface are

$$\begin{aligned} f_{\text{se}} =& \boldsymbol{n} \cdot \left(\frac{D_s}{RT} c_{se,s} \left(1 - \frac{c_{se,s}}{c_{\max,\text{s}}} \right) \nabla \mu_{se,s} \right), \\ i_{\text{se}} =& \boldsymbol{n} \cdot (\kappa_s \nabla \phi_{se,s}), \\ f_{\text{se}} =& - \boldsymbol{n} \cdot \left(\left(\frac{D_e}{RT} c_{se,e} + \frac{\kappa_e t_+ (t_+ - 1)}{F^2} \right) \nabla \mu_{se,e} + \frac{\kappa_e t_+}{F} \nabla \phi_{se,e} \right), \\ i_{\text{se}} =& - \boldsymbol{n} \cdot \left(\frac{\kappa_e (t_+ - 1)}{F} \nabla \mu_{se,e} + \kappa_e \nabla \phi_{se,e} \right), \end{aligned} \tag{2.35}$$

where the material parameters $\cdot_s$ denoted with index s represent material parameters from either anode or cathode, depending on the corresponding flux on either anode-electrolyte or cathode-electrolyte interface. The normal vector $\boldsymbol{n}$ is assumed to point from the solid domain to the electrolyte domain, see Figure 2.2. The resulting transmission problem is fully coupled in all three domains. Both concentration and electric potential are involved in a nonlinear Robin condition.

2.2.4 Boundary conditions

Since the battery cell is placed in an enclosed housing, no concentration flux over the boundaries Γ_a, Γ_c and Γ_e is possible. Therefore, the boundary conditions for the concentration c are homogeneous Neumann conditions, i.e.,

$$\begin{aligned} \boldsymbol{n} \cdot \left(\frac{D_s}{RT} c_{se,s} \left(1 - \frac{c_{se,s}}{c_{\max,\text{s}}} \right) \nabla \mu_{se,s} \right) = 0, \quad (\boldsymbol{x}, t) \in \Gamma_{s,T}, \\ - \boldsymbol{n} \cdot \left(\left(\frac{D_e}{RT} c_{se,e} + \frac{\kappa_e t_+ (t_+ - 1)}{F^2} \right) \nabla \mu_{se,e} + \frac{\kappa_e t_+}{F} \nabla \phi_{se,e} \right) = 0, \quad (\boldsymbol{x}, t) \in \Gamma_{e,T}. \end{aligned} \tag{2.36}$$

The electric potential is set to zero along the anode boundary Γ_a,

$$\phi_a(\boldsymbol{x}, t) = 0, \quad (\boldsymbol{x}, t) \in \Gamma_{a,T}. \tag{2.37}$$

It is also possible to include a varying electric potential along the anode boundary. In the presented model it is fixed in order to simplify the model description. A possible

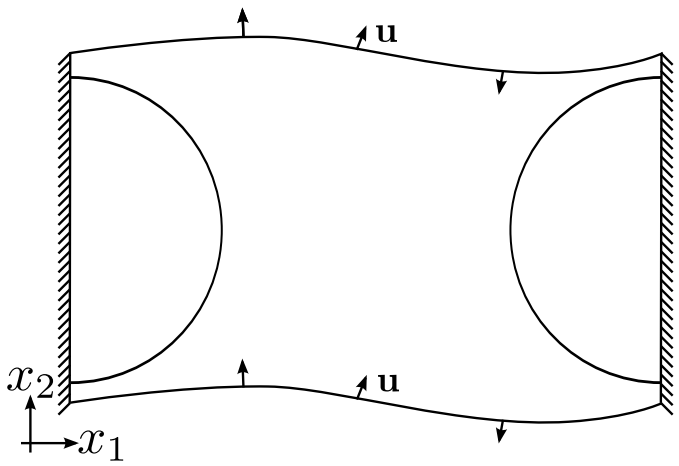

Figure 2.3: Boundary conditions for the mechanical model. The displacements are locked in the x_1 dimension. In the x_2 and x_3 dimension periodic displacements are used.

extension includes a discretized model for current collectors that allows for variation of the electric potential on Γ_a. This may be important if the microstructures consists of several disconnected particles.
The parameter C-rate is used to define meaningful charging boundary conditions. It is defined as quotient of charging current and battery capacity and usually specified in the unit per hour, $\frac{1}{3600s} = \frac{1}{h}$. C-rate 1 defines a charging current i_{in} such that it takes one hour to charge the battery cell from empty to full state of charge. On the cathode boundary Γ_c a constant current density i_{in} is applied such that a particular C-rate is achieved,

$$\kappa_c \nabla \phi_c(\boldsymbol{x}, t) = i_{\text{in}}, \quad (\boldsymbol{x}, t) \in \Gamma_{c,T}. \tag{2.38}$$

The boundary Γ_e containing the electrolyte is isolating for the electric current,

$$\left(\frac{D_e}{RT} c_e + \frac{\kappa_e t_+ (t_+ - 1)}{F^2} \right) \nabla \mu_e + \frac{\kappa_e t_+}{F} \nabla \phi_e = 0, \quad (\boldsymbol{x}, t) \in \Gamma_{e,T}. \tag{2.39}$$

For the chemical potential μ in the cathode material, cf. (2.27), an additional boundary condition on the cathode domain boundary $\Gamma_c \cup \Gamma_{ce,c}$ is needed. The applied boundary condition corresponds to neither strong wetting nor strong dewetting,

$$\boldsymbol{n} \cdot \nabla c_c = 0, \quad (\boldsymbol{x}, t) \in (\Gamma_c \cup \Gamma_{ce}) \times T. \tag{2.40}$$

In the mechanical model, the boundary conditions depend on the spatial dimension, see Figure 2.3. In the first dimension, the simulation domain represents a battery electrode

which ends at the current collectors. The domain is spatially locked and the displacement is zero. In the second and third dimension, the microstructure is assumed to be periodic. In those dimensions, the microstructure is interpreted as a representative volume element. Additionally, no macroscopic displacement is assumed. Therefore, the displacements are periodic and identical on opposite sites. The boundary conditions are then

$$\begin{aligned} \boldsymbol{u}(\boldsymbol{x},t) &= \boldsymbol{u}(\boldsymbol{x}+L_1\boldsymbol{e}_1,t) = 0, && (\boldsymbol{x},t),(\boldsymbol{x}+L_1\boldsymbol{e}_1,t) \in \Omega_T, \\ \boldsymbol{u}(\boldsymbol{x},t) &= \boldsymbol{u}(\boldsymbol{x}+L_i\boldsymbol{e}_i,t), && (\boldsymbol{x},t),(\boldsymbol{x}+L_i\boldsymbol{e}_i,t) \in \Omega_T, i \in \{2,3\}. \end{aligned} \tag{2.41}$$

In the case of vanishing elastic parameters for the electrolyte, both electrodes are fixed at their interface to the current collectors Γ_s and fulfill a no-stress boundary condition $\operatorname{div}\boldsymbol{\sigma} = 0$ on the interface to the electrolyte Γ_{se}.

2.2.5 Initial conditions

If not stated otherwise, the initial lithium ion concentration in the respective domains is prescribed as

$$\begin{aligned} c(\boldsymbol{x},0) &= c_{0,a}, && \boldsymbol{x} \in \Omega_a, \\ c(\boldsymbol{x},0) &= c_{0,e}, && \boldsymbol{x} \in \Omega_e, \\ c(\boldsymbol{x},0) &= c_{0,c}, && \boldsymbol{x} \in \Omega_c, \end{aligned} \tag{2.42}$$

with $c_{0,a}, c_{0,e}, c_{0,c} \in \mathbb{R}^+$. This is a static equilibrium state as no concentration gradient in each of the domains is present. It corresponds to a state of charge $\frac{c_{0,a}}{c_{\text{max,a}}}$ in the anode and $\frac{c_{0,c}}{c_{\text{max,c}}}$ in the cathode. The displacement is zero in the initial state, $\boldsymbol{u} = \boldsymbol{0}$ for $\boldsymbol{x} \in \Omega$. It is possible to calculate consistent initial values for the electric potential and the particle surface currents as

$$\begin{aligned} \phi(\boldsymbol{x},0) &= \phi_0(\boldsymbol{x}), && \boldsymbol{x} \in \Omega, \\ i_{\text{se}}(\boldsymbol{x},0) &= i_{\text{se},0}(\boldsymbol{x}), && \boldsymbol{x} \in \Gamma_{\text{se}}, \end{aligned} \tag{2.43}$$

which solve their respective governing static equations.

2.2.6 Summary

The governing equations introduced in this section are for the electrolyte domain Ω_e

$$
\begin{aligned}
\mu(\boldsymbol{x},t) &= RT\log\frac{c(\boldsymbol{x},t)}{c_{\max,\mathrm{c}}},\\
\partial_t c(\boldsymbol{x},t) &= \operatorname{div}\left[\left(\frac{D_e}{RT}c(\boldsymbol{x},t)+\frac{\kappa_e t_+(t_+-1)}{F^2}\right)\nabla\mu(\boldsymbol{x},t)+\frac{\kappa_e t_+}{F}\nabla\phi(\boldsymbol{x},t)\right],\\
0 &= -\operatorname{div}\left[\frac{\kappa_e(t_+-1)}{F}\nabla\mu(\boldsymbol{x},t)+\kappa_e\nabla\phi(\boldsymbol{x},t)\right],\\
\boldsymbol{\varepsilon}(\boldsymbol{x},t) &= \frac{1}{2}(\nabla\boldsymbol{u}(\boldsymbol{x},t)+\nabla\boldsymbol{u}(\boldsymbol{x},t)^T),\\
\boldsymbol{\sigma}(\boldsymbol{x},t) &= \lambda_e\operatorname{Tr}(\boldsymbol{\varepsilon}(\boldsymbol{x},t))\boldsymbol{I}+2\mu_e\boldsymbol{\varepsilon}(\boldsymbol{x},t),\\
0 &= \operatorname{div}\boldsymbol{\sigma}(\boldsymbol{x},t),\quad (\boldsymbol{x},t)\in\Omega_{e,T},
\end{aligned}
\tag{2.44}
$$

for the anode domain Ω_a

$$
\begin{aligned}
\mu(\boldsymbol{x},t) &= RT\log\frac{c(\boldsymbol{x},t)}{c_{\max,\mathrm{a}}-c_a}+\frac{\theta}{3}\operatorname{Tr}(\boldsymbol{\sigma}(\boldsymbol{x},t)),\\
\partial_t c(\boldsymbol{x},t) &= \operatorname{div}\left[\frac{D_a}{RT}c(\boldsymbol{x},t)\left(1-\frac{c(\boldsymbol{x},t)}{c_{\max,\mathrm{a}}}\right)\nabla\mu(\boldsymbol{x},t)\right],\\
0 &= -\operatorname{div}\left[\kappa_a\nabla\phi(\boldsymbol{x},t)\right],\\
\boldsymbol{\varepsilon}_{\mathrm{el}}(\boldsymbol{x},t) &= \frac{1}{2}(\nabla\boldsymbol{u}(\boldsymbol{x},t)+\nabla\boldsymbol{u}(\boldsymbol{x},t)^T)-\frac{\theta_a}{3}c(\boldsymbol{x},t)\boldsymbol{I},\\
\boldsymbol{\sigma}(\boldsymbol{x},t) &= \lambda_a\operatorname{Tr}(\boldsymbol{\varepsilon}_{\mathrm{el}}(\boldsymbol{x},t))\boldsymbol{I}+2\mu_a\boldsymbol{\varepsilon}_{\mathrm{el}}(\boldsymbol{x},t),\\
0 &= \operatorname{div}\boldsymbol{\sigma}(\boldsymbol{x},t),\quad (\boldsymbol{x},t)\in\Omega_{a,T},
\end{aligned}
\tag{2.45}
$$

for the cathode domain Ω_c

$$
\begin{aligned}
\mu(\boldsymbol{x},t) &= RT\alpha L_0^2\frac{G}{L}\left[\log\left(\frac{c(\boldsymbol{x},t)}{c_{\max,\mathrm{c}}-c(\boldsymbol{x},t)}\right)+\frac{\theta}{RTc_{\max,\mathrm{c}}}(c_{\max,\mathrm{c}}-c(\boldsymbol{x},t))\right]\\
&\quad - RT\beta GL\Delta\left(\frac{c(\boldsymbol{x},t)}{c_{\max,\mathrm{c}}}\right)+\frac{\theta}{3}\operatorname{Tr}(\boldsymbol{\sigma}(\boldsymbol{x},t)),\\
\partial_t c(\boldsymbol{x},t) &= \operatorname{div}\left[\frac{D_c}{RT}c(\boldsymbol{x},t)\left(1-\frac{c(\boldsymbol{x},t)}{c_{\max,\mathrm{c}}}\right)\nabla\mu(\boldsymbol{x},t)\right],\\
0 &= -\operatorname{div}\left(\kappa_c\nabla\phi(\boldsymbol{x},t)\right),\\
\boldsymbol{\varepsilon}_{\mathrm{el}}(\boldsymbol{x},t) &= \frac{1}{2}(\nabla\boldsymbol{u}(\boldsymbol{x},t)+\nabla\boldsymbol{u}(\boldsymbol{x},t)^T)-\frac{\theta_c}{3}c(\boldsymbol{x},t)\boldsymbol{I},\\
\boldsymbol{\sigma}(\boldsymbol{x},t) &= \lambda_c\operatorname{Tr}(\boldsymbol{\varepsilon}_{\mathrm{el}})\boldsymbol{I}+2\mu_c\boldsymbol{\varepsilon}_{\mathrm{el}},\\
0 &= \operatorname{div}\boldsymbol{\sigma}(\boldsymbol{x},t),\quad (\boldsymbol{x},t)\in\Omega_{c,T}.
\end{aligned}
\tag{2.46}
$$

These equations define fields c, ϕ and $\boldsymbol{u}$ in $\Omega \times T$. For the initial boundary value problem, the interface and boundary conditions are on the solid-electrolyte domain Γ_{se}

$$\begin{aligned}
i_{\mathrm{se}}(\boldsymbol{x},t) =& 2k\sqrt{c_{se,e}(\boldsymbol{x},t)c_{se,s}(\boldsymbol{x},t)\frac{c_{\max,\mathrm{s}}}{2}} \\
&\times \sinh\left(\frac{F}{2RT}\left(\phi_{se,s}(\boldsymbol{x},t) - \phi_{se,e}(\boldsymbol{x},t) - \frac{\mu_{se,s}(\boldsymbol{x},t)}{F} - \bar{U}_s\right)\right), \\
f_{\mathrm{se}}(\boldsymbol{x},t) =& \frac{i_{\mathrm{se}}(\boldsymbol{x},t)}{F}, \\
f_{\mathrm{se}}(\boldsymbol{x},t) =& \boldsymbol{n}\cdot\left(\frac{D_s}{RT}c_{se,s}(\boldsymbol{x},t)\left(1-\frac{c_{se,s}(\boldsymbol{x},t)}{c_{\max,\mathrm{s}}}\right)\nabla\mu_{se,s}(\boldsymbol{x},t)\right), \\
i_{\mathrm{se}}(\boldsymbol{x},t) =& \boldsymbol{n}\cdot(\kappa_s\nabla\phi_{se,s}(\boldsymbol{x},t)), \\
f_{\mathrm{se}}(\boldsymbol{x},t) =& -\boldsymbol{n}\cdot\left(\left(\frac{D_e}{RT}c_{se,e}(\boldsymbol{x},t) + \frac{\kappa_e t_+(t_+-1)}{F^2}\right)\nabla\mu_{se,e}(\boldsymbol{x},t) + \frac{\kappa_e t_+}{F}\nabla\phi_{se,e}(\boldsymbol{x},t)\right), \\
i_{\mathrm{se}}(\boldsymbol{x},t) =& -\boldsymbol{n}\cdot\left(\frac{\kappa_e(t_+-1)}{F}\nabla\mu_{se,e}(\boldsymbol{x},t) + \kappa_e\nabla\phi_{se,e}(\boldsymbol{x},t)\right), \\
&(\boldsymbol{x},t)\in\Gamma_{e,T},
\end{aligned} \tag{2.47}$$

on the boundary Γ_a,

$$\begin{aligned}
0 &= \boldsymbol{n}\cdot\left(\frac{D_a}{RT}c(\boldsymbol{x},t)\left(1-\frac{c(\boldsymbol{x},t)}{c_{\max,\mathrm{a}}}\right)\nabla\mu(\boldsymbol{x},t))\right), \\
0 &= \phi(\boldsymbol{x},t), \\
0 &= \boldsymbol{u}(\boldsymbol{x},t), (\boldsymbol{x},t)\in\Gamma_{a,T},
\end{aligned} \tag{2.48}$$

on the boundary Γ_c,

$$\begin{aligned}
0 =& \boldsymbol{n}\cdot\left(\frac{D_c}{RT}c(\boldsymbol{x},t)\left(1-\frac{c(\boldsymbol{x},t)}{c_{\max,\mathrm{c}}}\right)\nabla\mu(\boldsymbol{x},t))\right), \\
i_{\mathrm{in}}(\boldsymbol{x},t) =& \boldsymbol{n}\cdot(\kappa_c\nabla\phi(\boldsymbol{x},t)), \\
0 =& \boldsymbol{u}(\boldsymbol{x},t), (\boldsymbol{x},t)\in\Gamma_{c,T},
\end{aligned} \tag{2.49}$$

and on the boundary Γ_e

$$
\begin{aligned}
0 &= \boldsymbol{n} \cdot \left(\left(\frac{D_e}{RT} c(\boldsymbol{x},t) + \frac{\kappa_e t_+ (t_+ - 1)}{F^2} \right) \nabla \mu(\boldsymbol{x},t) + \frac{\kappa_e t_+}{F} \nabla \phi(\boldsymbol{x},t) \right), \\
0 &= \boldsymbol{n} \cdot \left(\frac{\kappa_e (t_+ - 1)}{F} \nabla \mu(\boldsymbol{x},t) + \kappa_e \nabla \phi(\boldsymbol{x},t) \right), \\
\boldsymbol{u}(\boldsymbol{x},t) &= \begin{cases} 0, & x_1 = 0, \\ \boldsymbol{u}(\boldsymbol{x} + L_i \boldsymbol{e}_i, t), & x_i = 0, i \in \{2,3\}, \end{cases} \quad (\boldsymbol{x},t) \in \Gamma_{e,T}.
\end{aligned} \tag{2.50}
$$

The sufficient initial conditions are

$$
\begin{aligned}
c(\boldsymbol{x},0) &= c_{0,a}, \qquad \boldsymbol{x} \in \Omega_a, \\
c(\boldsymbol{x},0) &= c_{0,e}, \qquad \boldsymbol{x} \in \Omega_e, \\
c(\boldsymbol{x},0) &= c_{0,c}, \qquad \boldsymbol{x} \in \Omega_c.
\end{aligned} \tag{2.51}
$$

Chapter 3

Numerical methods

In this chapter, different numerical methods for the solution of the electro-chemical model are defined. Two different methods are used for the solution of the electrochemical model. First an overview of both methods and a comparison is given in Section 3.1. Mathematical fundamentals are defined in Section 3.2. A domain decomposition (DD) algorithm is introduced in Section 3.3. The immersed interface method (IIM) is defined for the Poisson and the diffusion equation in Section 3.4 as well as for the Cahn-Hilliard equation in Section 3.5.

3.1 Overview

The Newton algorithm (NWT) is explained in Section 3.2. NWT applies established numerical methods. DD builds upon Subsections 3.2.1, 3.2.2 and 3.2.3. It is defined in Section 3.3 and uses the IIM as deduced in Sections 3.4 and 3.5. DD applies several new numerical methods .

3.1.1 Newton algorithm (NWT)

A regular voxel mesh discretization is introduced as well as a finite-volume scheme for the spatial discretization and an first-order implicit Euler method for time-integration. The mechanical model for the displacement $\boldsymbol{u}$ is solved decoupled from the electro-chemical model for the concentration c and the electric potential ϕ, cf. (2.2.6). The lack of interface conditions allows for the application of established fast solvers based on Fourier preconditioners [141]. Convergence for the whole electro-chemo-mechanical model is reached by iterating over the coupling variables hydrostatic stress and lithium ion concentration.
The system of non-linear equations resulting from the discretization of the electro-chemical model is linearized. The Neumann boundary conditions are resolved naturally by the finite-volume scheme. The Dirichlet boundary conditions are integrated by a penalty method. The Jacobian matrix is assembled and the system of linear equations is solved by Gaussian elimination [131]. A damped Newton solver with adaptive time steps is used.

NWT	DD
Assembly of a Jacobian matrix	No Jacobian matrix
Convergence of the large system depends on phase-field domain	Fast phase-field problem calculated separately
Destruction of structural block information	Block solution
Direct linear solver	Iterative linear solver
Logarithmic phase-field potential	Polynomial phase-field potential
Concentration-dependent diffusion coefficient	Constant diffusion coefficient
Correct solution of the phase-field potential	Approximation to the phase-field potential

Table 3.1: Comparison of the two different numerical methods

3.1.2 Domain decomposition algorithm (DD)

First the governing equations of the electro-chemical model are separated into six smaller initial-boundary-value-problems (IBVPs). The focus is on the coupling of those six different IBVPs in anode, cathode and electrolyte for both lithium ion concentration and electric potential. The coupling by the non-linear Butler-Volmer equations is solved by iteration. The convergence order of the domain decomposition algorithm is one.
Next the immersed interface method (IIM) is introduced for the Poisson equation[1], the diffusion equation[2], and the Cahn-Hilliard equation[3]. For the solution finite difference stencils and implicit Runge-Kutta schemes are applied. Methods with convergence order two, four and six are defined for the periodic Poisson equation and the periodic diffusion equation. For the periodic Cahn-Hilliard equation a method with convergence order two is defined. The convergence order of the IIM is one [88].

3.1.3 Comparison

Table 3.1 compares the two different numerical methods.
NWT uses the Gaussian elimination which does not take the structural information of the matrix entries into account. The block system resulting from the discretization of the diffusion equation and the Poisson equation is not used for a faster or more robust

[1]This concerns the electric potential in anode, electrolyte and cathode.
[2]This concerns the lithium ion concentration in anode and electrolyte.
[3]This concerns the lithium ion concentration in the cathode.

solution. The numerical solution for a given microstructure with $N = O(N_x^3)$ volume degrees of freedom and $N_{IF} = O(N_x^2)$ interface degrees of freedom requires the solution of a system of linear equations with $N + N + N_{IF} = 2N + N_{IF}$ degrees of freedom and bandwidth $O(N_x^2)$ due to the connectivity of the finite volume cells. The simulation of three-dimensional microstructures is numerically expensive. An adaptive time integration method in combination with a direct linear solver gives a robust, but slow algorithm which is not fast enough for the solution of large three-dimensional microstructures, both in terms of CPU time and memory usage. A multi-grid method for a linear solver [133] may benefit from the regular voxel discretization. DD uses the block structures to its advantage. A Schur complement converts the linear system to a system with N_{IF} unknowns which is then solved by an iterative stabilized biconjugate gradient solver [9].
NWT solves the logarithmic phase-field potential fully-implicit. No additional error is introduced. In DD, the bulk energy of the phase-field potential is approximated by a polynomial potential splitted into a concave and a convex part and integrated semi-implicitly. The time integration is stable, but an additional error is introduced. A preconditioner reduces the numerical condition of the matrix and the convergence rate is independent of the spatial discretization width.

3.2 Fundamentals

In this section, established mathematical methods for the numerical solution of partial differential equations are introduced. First, a regular voxel mesh discretization is defined in Subsection 3.2.1. Simple time integration methods are introduced in Subsection 3.2.2. Next, a first-order finite-volume discretization of the electro-chemical model is explained in Subsection 3.2.3 resulting in a system of non-linear equations. The Jacobian matrix and a damped Newton algorithm with adapative time step size is given in Subsection 3.2.4. The Fourier transform is defined and applied for the solution of the elastic sub-problem in Subsection 3.2.5.

3.2.1 Regular voxel mesh

Regular voxel meshes enable the use of acquired microstructure information by computer tomography without the need for a meshing. Additionally, they are well suited for phase-field methods as the origin of phase interfaces is not known before. Their numerical stability is independent of an angle criterion as it may appear for isoparametric finite elements [92]. Therefore, an equally spaced mesh is applied.
Given a cuboid domain $\Omega = (0, L_1) \times (0, L_2) \times (0, L_3)$. A regular spatial grid in Ω is defined by $x_{1,i} = (i - 0.5)h$, $x_{2,j} = (j - 0.5)h$ and $x_{3,k} = (k - 0.5)h$. Here $1 \leq i \leq N_1$, $1 \leq j \leq N_2$, $1 \leq k \leq N_3$, N_1, N_2, N_3 positive integers and $h = \frac{L_i}{N_i}$ for all $i \in 1, 2, 3$. Then the grid Ω_h is given by

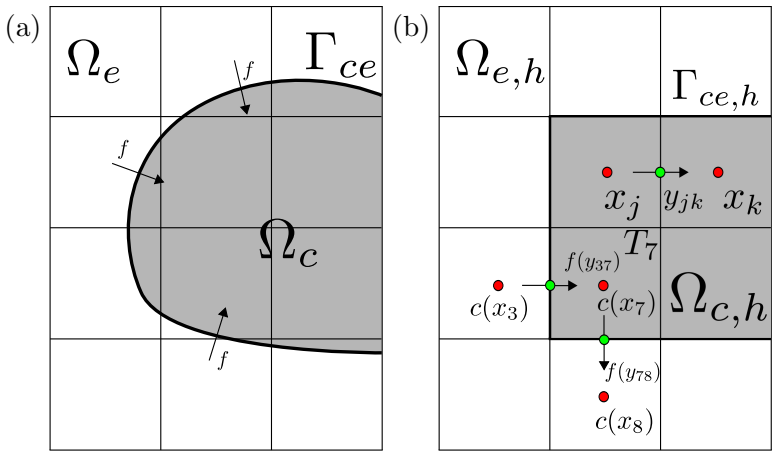

Figure 3.1: (a) A continuous structure depicting the cathode-electrolyte interface in a battery. (b) A discretization of the structure into finite volume cells.

$$\Omega_h = \{(x_{1,i}, x_{2,j}, x_{3,k}) \in \Omega | 1 \leq i \leq N_1, 1 \leq j \leq N_2, 1 \leq k \leq N_3\}. \tag{3.1}$$

Each element $\boldsymbol{x} \in \Omega_h$ is the center of a cuboid grid cell with volume h^3. A function space $V_h = \{f : \Omega_h \to \mathbb{R}\}$ is introduced. Finite difference operators [70] are introduced as

$$\begin{aligned} u_h^{\pm i} &:= u_h^{\pm i}(x) = u_h(x \pm he_i), \quad e_i := (\delta_{i1}, \delta_{i2}, \delta_{i3}), \quad i = 1, 2, 3 \\ D_{x_i}^+ u_h &:= \frac{u_h^{+i} - u_h}{h}, \quad D_{x_i}^- u_h := \frac{u_h - u_h^{-i}}{h}, \end{aligned} \tag{3.2}$$

The introduced operators are periodic such that

$$u_h(x \pm he_i) := u_h(x \pm he_i \mp L_i), \quad \text{if } x \pm he_i \notin \Omega_h. \tag{3.3}$$

The discrete second-order operator Δ_h on Ω_h of the Laplacian operator Δ is introduced (by Einstein summation notation) as

$$\Delta_h u_h := D_{x_i}^+ D_{x_i}^- u_h, \quad \boldsymbol{x} \in \Omega_h \tag{3.4}$$

with periodic boundary conditions as well as a unity operator $I_h u_h := u_h$.
Meshes $\Omega_{i,h} = \Omega_i \cap \Omega_h$ are defined for $i \in \{a, e, c\}$.
Figure 3.1 shows Ω_h and a shifted mesh Σ_h (for simplification in two dimensions). The shifted mesh Σ_h on Ω is defined by

$$\begin{aligned}\Sigma_h \coloneqq &\{\boldsymbol{y} \in \mathbb{R}^3 | y_1 = ih, y_2 = jh - \frac{1}{2}, y_3 = kh - \frac{1}{2}, 0 \leq i \leq N_1, 1 \leq j \leq N_2, 1 \leq k \leq N_3\} \cup \\ &\{\boldsymbol{y} \in \mathbb{R}^3 | y_1 = ih - \frac{1}{2}, y_2 = jh, y_3 = kh - \frac{1}{2}, 1 \leq i \leq N_1, 0 \leq j \leq N_2, 1 \leq k \leq N_3\} \cup \\ &\{\boldsymbol{y} \in \mathbb{R}^3 | y_1 = ih - \frac{1}{2}, y_2 = jh - \frac{1}{2}, y_3 = kh, 1 \leq i \leq N_1, 1 \leq j \leq N_2, 0 \leq k \leq N_3\}\end{aligned} \tag{3.5}$$

From now on, an arbitrary point in Ω_h is denoted by a single index i as $\boldsymbol{x}_i \in \Omega$. Similar, an arbitrary point in Σ_h is denoted as $\boldsymbol{y}_i$.
Now a partition of Σ_h into different meshes is defined. Figure 3.1 (a) shows a continuous structure depicting the cathode-electrolyte interface in a battery. The electrolyte domain Ω_e and the cathode domain Ω_c coincide at the interface domain Γ_{ce}. The concentration flux f flows into the cathode particle. Figure 3.1 (b) shows a discretization of the structure into finite volume cells with a mesh $\Omega_h = \{\boldsymbol{x}_i\}$ in the cell centers (red) and a shifted mesh $\Sigma_h = \{\boldsymbol{y}_i\}$ on the edges of the cells (green).
The components $c_i = c(\boldsymbol{x}_i)$ of a function c_h discretize the lithium ion concentration. Components $f_{jk} = f(\boldsymbol{y}_{jk})$ of a function f discretize the normal component of the concentration flux. Also a notation relating elements of Σ_h to elements of Ω_h is established. The mesh Σ_h is the union of several meshes $\Sigma_{i,h}$ for $i \in \{a, c, e\}$ and $\Gamma_{i,h}$ for $i \in \{ae, ce, a, e, c\}$. A mesh point $\boldsymbol{y}_{jk}$ is considered an element of $\Sigma_{i,h}$, if it lies on the edge between two cells T_j and T_k with center points $\boldsymbol{x}_j$ and $\boldsymbol{x}_k$ being elements of the $\Omega_{i,h}$,

$$\Sigma_{i,h} = \{\boldsymbol{y}_{jk} \in \Sigma_h | \boldsymbol{x}_j, \boldsymbol{x}_k \in \Omega_{i,h}\} \quad \text{for} \quad i \in \{a, c, e\}. \tag{3.6}$$

Mesh points $\boldsymbol{y}_{jk}$ on edges between two cells T_j and T_k with $\boldsymbol{x}_j$ being an element of a discrete solid domain $\Omega_{a,h} \cup \Omega_{c,h}$ and $\boldsymbol{x}_k$ being an element of the discrete electrolyte domain $\Omega_{e,h}$ are considered elements of domain $\Gamma_{ae,h}$,

$$\begin{aligned}\Gamma_{ae,h} &= \{\boldsymbol{y}_{jk} \in \Sigma_h | \boldsymbol{x}_j \in \Omega_{a,h}, \boldsymbol{x}_k \in \Omega_{e,h}\}, \\ \Gamma_{ce,h} &= \{\boldsymbol{y}_{jk} \in \Sigma_h | \boldsymbol{x}_j \in \Omega_{c,h}, \boldsymbol{x}_k \in \Omega_{e,h}\}.\end{aligned} \tag{3.7}$$

The remaining mesh points $\boldsymbol{y}_{jk}$ are elements of $\Gamma_{i,h}$ for $i \in \{a, c, e\}$ as they lie on the boundary of Ω.
Each cell center $\boldsymbol{x}_j$ in Ω_h is now related to facet centers $\boldsymbol{y}_{jk}$ in Σ_h.

3.2.2 Time integration

Given a time-dependent equation with a differential operator $\mathcal{L}$

$$\partial_t c(\boldsymbol{x}, t) = \mathcal{L}(c(\boldsymbol{x}, t)), \tag{3.8}$$

and a time step $\tau > 0$, define

$$\hat{c} = c(\boldsymbol{x}, t+\tau), \quad \check{c} = c(\boldsymbol{x}, t-\tau). \tag{3.9}$$

Explicit (forwards) and implicit (backwards) Euler time integration schemes are then defined as

$$\partial_t c \approx c_t = \frac{\hat{c} - c}{\tau}, \quad \partial_t c \approx c_{\bar{t}} = \frac{c - \check{c}}{\tau}. \tag{3.10}$$

Used in the differential equation (3.8), the explicit Euler method gives

$$\hat{c} = c + \tau \mathcal{L}(c). \tag{3.11}$$

while implicit Euler gives

$$(I - \tau\mathcal{L})(c) = \check{c}. \tag{3.12}$$

Both are consistent with convergence order one. The explicit Euler is stable under the CFL-condition, the implicit Euler is unconditionally stable [39].

3.2.3 Finite volume method

The governing equations in (2.2.2) are now discretized depending on two functions $\boldsymbol{f}$ and $\boldsymbol{i}$ called the concentration flux and the electrical current. The discretization is demonstrated by the diffusion equation in the anode, but respective steps are taken for the remaining diffusion equations, the Laplace equations for the electric potential and the equation for the chemical potential μ in the cathode.
Let $\bar{c}$ be a solution for the lithium ion concentration in Eq. (2.45), τ the current time step size and $t > \tau$ a fixed time. Then $c = \bar{c}(\boldsymbol{x}, t)$ is called the current solution and $\check{c} = \bar{c}(\boldsymbol{x}, t-\tau)$ is called the previous solution. Integration of the diffusion equation in Eq. (2.45) over $[t-\tau, t]$ gives

$$\begin{aligned} 0 &= \int_{t-\tau}^{t} \partial_t \bar{c} \mathrm{dt} - \int_{t-\tau}^{t} \operatorname{div}\left(\frac{D_a}{RT}\bar{c}\left(1 - \frac{\bar{c}}{c_{\max,\mathrm{a}}}\right)\nabla\mu_a(\bar{c})\right)\mathrm{dt} = \\ &= c - \check{c} - \tau \operatorname{div}\left(\frac{D_a}{RT} c\left(1 - \frac{c}{c_{\max,\mathrm{a}}}\right)\nabla\mu_a(c)\right) + O(\tau). \end{aligned} \tag{3.13}$$

Now an integral in space over Ω is discretized into cubic cells T_j surrounding mesh points $\boldsymbol{x}_j \in \Omega_h$. With the divergence theorem, the volume integrals are converted into surface integrals over normal components (denoted by dS). Given c_h and $c_{h,j} \coloneqq c_h(\boldsymbol{x}_j)$, it is

$$
\begin{aligned}
0 &= \int_{T_j} (c - \check{c}) dV - \tau \int_{T_j} \operatorname{div} \left(\frac{D_a}{RT} c \left(1 - \frac{c}{c_{\max,\mathrm{a}}} \right) \nabla \mu_a(c) \right) dV + O(\tau) \Leftrightarrow \\
0 &= \int_{T_j} (c - \check{c}) dV - \tau \int_{\partial T_j} \left(\frac{D_a}{RT} c \left(1 - \frac{c}{c_{\max,\mathrm{a}}} \right) \nabla \mu_a(c) \right) dS + O(\tau) \Leftrightarrow \\
0 &= h^3 (c_{h,j} - \check{c}_{h,j}) - h^2 \tau \sum_{\boldsymbol{y}_{jk} \in \Sigma_h} f_{jk} + O(h + \tau) \quad \forall x_j \in \Omega_h.
\end{aligned} \tag{3.14}
$$

The normal component of $\boldsymbol{f}$ between two cells T_j and T_k is approximated first order by

$$
\begin{aligned}
\boldsymbol{n} \cdot \boldsymbol{f}_{jk} &= \boldsymbol{n} \cdot \frac{D_a}{RT} c \left(1 - \frac{c}{c_{\max,\mathrm{a}}} \right) \nabla \mu_a(c) = \\
&= \frac{D_a}{RT} \frac{c_{h,j} + c_{h,k}}{2} \left(1 - \frac{c_{h,j} + c_{h,k}}{2 c_{\max,\mathrm{a}}} \right) \frac{\mu_a(c_{h,j}) - \mu_a(c_{h,k})}{h} + O(h) \\
&\quad \text{if } \boldsymbol{f}_{jk} \in \Sigma_{a,h},
\end{aligned} \tag{3.15}
$$

if they are the same domain such that $\boldsymbol{y}_{jk} \in \Sigma_{a,h}$.
Next, the remaining discrete fluxes $\boldsymbol{f}$ for $\boldsymbol{y}_{jk}$ on $\Gamma_{i,h}$ for $i \in \{ae, ce, a, c, e\}$ are defined. The cell-wise constant projection of c_h and ϕ_h defines a continuous extension of lithium ion concentration and electric potential onto $\Gamma_{ae,h}$ and $\Gamma_{ce,h}$. If $\boldsymbol{x}_j \in \Omega_{a,h}$ and $\boldsymbol{x}_k \in \Omega_{e,h}$ the normal component of the discrete flux $\boldsymbol{f}_{jk}$ between the cells T_j and T_k is approximated with Eq. (2.29) and Eq. (2.31) as

$$
\boldsymbol{n} \cdot \boldsymbol{f}_{jk} = \frac{1}{F} i_0(c_{h,j}, c_{h,k}) \sinh \left(\frac{F}{2RT} \eta(\phi_{h,j}, \phi_{h,k}, \mu_{h,j}) \right) + O(h + \tau), \tag{3.16}
$$

and respectively for $\Omega_{a,h}$ and $\Omega_{e,h}$.
The remaining components $\boldsymbol{f}_{jk}$ of the discretized concentration flux $\boldsymbol{f}$ are zero for $\boldsymbol{y}_{jk} \in \Gamma_{a,h} \cup \Gamma_{e,h} \cup \Gamma_{c,h}$ according to the boundary conditions in Eq. (2.36). The components $\boldsymbol{i}_{jk}$ of the discretized electrical current $\boldsymbol{i}$ are zero for $\boldsymbol{y}_{jk} \in \Gamma_{e,h}$ according to Eq. (2.39) and identical to $\boldsymbol{i}_{\mathrm{in}}$ for $\boldsymbol{y}_{jk} \in \Gamma_{c,h}$ according to Eq. (2.38). For $\boldsymbol{y}_{jk} \in \Gamma_{a,h}$, components $\boldsymbol{i}_{jk}$ are set such that the Dirichlet boundary condition in Eq. (2.37) is fulfilled. Finally, the components defining the gradient of the lithium ion concentration ∇c in Eq. (2.27) for the chemical potential μ in the cathode are also set according to the surface wetting boundary condition in Eq. (2.40).
The initial conditions in (2.42) are evaluated at $\boldsymbol{x}_j \in \Omega_h$ to get the initial configuration c_h at time $t = 0$ as

$$
c_{h,j} = c_0(\boldsymbol{x}_j), \quad \boldsymbol{x}_j \in \Omega_h. \tag{3.17}
$$

```
step ← 0;
t ← 0;
while true do
    SOC ← Calculate state of charge;
    if SOC> SOC̄ then Finish simulation;
    u_0 ← ŭ;
    for k = 1 ... do
        if k > k_max then
            τ ← τ/2;
            Restart time step;
        end if
        e ← Calculate error of u_{k−1};
        if e < ϵ then
            u ← u_{k−1};
        else
            f, J ← Calculate residuum and Jacobian from u_{k−1};
            d ← Calculate search direction from J and f;
            u_k ← Calculate new Newton iterate of u_{k−1} and d (Line search);
        end if
    end for
    t ← t + τ ;
    step ← step + 1;
    if step-lastDampedStep > N_trust then τ ← min(τ_max,2τ); ;
end while
```

Algorithm 1: Time-adaptive damped Newton-Raphson scheme

3.2.4 Linearization and adaptive algorithm

The discrete non-linear system of equations is now solved with a damped Newton-Raphson algorithm using adaptive time steps. The system can be written as

$$\begin{aligned} 0 &= h^3(c_{h,j} - \check{c}_{h,j}) - h^2\tau \sum_{\boldsymbol{y}_{jk}\in\Sigma_h} \boldsymbol{n}\cdot\boldsymbol{f}_{jk}(c_h,\phi_h), \quad && \forall \boldsymbol{x}_j \in \Omega_h, \\ 0 &= -h^2 \sum_{\boldsymbol{y}_{jk}\in\Sigma_h} \boldsymbol{n}\cdot\boldsymbol{i}_{jk}(c_h,\phi_h), && \forall \boldsymbol{x}_j \in \Omega_h, \\ \boldsymbol{n}\cdot\boldsymbol{i}_{jk} &= i_0(c_{h,j},c_{h,k})\sinh\left(\frac{F}{2RT}\eta(\phi_{h,j},\phi_{h,k},\check{\mu}_{h,k})\right), && \forall \boldsymbol{y}_{jk} \in \Gamma_{se,h}. \end{aligned} \tag{3.18}$$

The discretization of the equation for the chemical potential μ is an explicit expression in c_h. Therefore, μ is eliminated from the equations. Define $N_{ae} = |\Gamma_{ae,h}|$, $N_{ce} = |\Gamma_{ce,h}|$

Data: Current Newton iterate u_{k-1}, search direction d, current residual error e
Result: New Newton iterate u_k
for $l = 1..$ **do**
  $u_{k,l} \leftarrow u_{k-1} - \omega_{l-1} d$;
  Project concentration in $u_{k,l}$ to feasible domain;
  $\overline{e} \leftarrow$ Calculate new error of $u_{k,l}$;
  if $\overline{e} < e$ **then**
    $u_k = u_{k,l}$;
    Return;
  else if $\omega > \omega_{min}$ **then**
    lastDampedStep $\leftarrow$ step;
    $\omega_l \leftarrow \omega_{l-1}\sigma$;
  else if $\tau > \tau_{min}$ **then**
    $\tau \leftarrow \frac{\tau}{2}$;
    Restart time step;
  end if
end for

Algorithm 2: Line search in the adaptive damped Newton-Raphson scheme.

and $N_{\text{se}} = N_{ae} + N_{ce}$. The discrete system in Eq. (3.18) involves N equations given by the discrete diffusion equation, N equations given by the discrete Laplace equation and N_{se} equations given by the equation defining the particle surface flux. Then the number of degrees of freedom of the equation system is $N_{DoF} = N + N + N_{\text{se}}$.
Eq. (3.18) is written as $f(\boldsymbol{z}) = 0$. Then $\boldsymbol{z} \in \mathbb{R}^{N_{\text{DoF}}}$ is the solution vector defined as $\boldsymbol{z} = (c_h; \phi_h; i_h) \in \mathbb{R}^{N_{\text{DoF}}}$. Introducing terms of a general nonlinear equation solver, $f = f(\boldsymbol{z})$ is the residuum and $J = Df(\boldsymbol{z}) \in \mathbb{R}^{N_{\text{DoF}} \times N_{\text{DoF}}}$ is the Jacobian matrix of the system. The Newton direction vector $\boldsymbol{d} \in \mathbb{R}^{N_{\text{DoF}}}$ is the solution to the system of linear equations given by $J\boldsymbol{d} = \boldsymbol{f}$.
Algorithm 1 defines a time-adaptive damped Newton-Raphson scheme. In line 18, a line search is applied that is given by Algorithm 2. The index k denotes the current Newton iteration. The index l denotes the current line search iteration. The error e corresponds to discrete L^2-norms for the grid functions c_h, ϕ_h and i_h and is calculated as

$$e = ||f||_2 = \sqrt{h^3 \sum_{j=1}^{N} c_{h,j}^2} + \sqrt{h^3 \sum_{j=1}^{N} \phi_{h,j}^2} + \sqrt{h^2 \sum_{j=1}^{N_{\text{se}}} i_{h,j}^2}. \tag{3.19}$$

The line search in Algorithm 2 ensures global linear convergence and local quadratic convergence [104]. If a lot of sequential undamped Newton iterations are accepted, the time step is enlarged. Corresponding, the time step is reduced if the Newton iteration

Name	Symbol	Value
Number of undamped steps until time step is doubled	N_{trust}	10
Maximum state of charge	$\overline{SOC}$	0.99
Error criterion	ϵ	10^{-10}
Maximum number of Newton iterations	$k_{\max}$	20
Reduction factor in the line search algorithm	σ	$\frac{1}{2}$
Initial line search step size	ω_0	1
Minimum line search step size	$\omega_{\min}$	10^{-3}
Minimum time step size	$\tau_{\min}$	10^{-6}
Maximum time step size	$\tau_{\max}$	$\frac{t_0}{100}$

Table 3.2: Parameters for the time integration scheme.

takes too many steps. Table 3.2 defines the parameters used in the solver. Possible extensions include an arc-length scheme for finding an optimum time step size [25].
An iteration on a smaller system of nonlinear equations with size $N_{\text{steady}} := N + N_{\text{se}}$ given by the equations in ϕ_h and i_{jk} is used in a first iteration step to establish consistent values for the electric potential and the particle surface current. For this iteration an undamped Newton algorithm is applied. The electric potential ϕ_h is initialized on $\Omega_{a,h}$, $\Omega_{e,h}$ and $\Omega_{c,h}$ with the values 0, $\bar{U}_a$ and $\bar{U}_a + \bar{U}_c$, respectively. The particle surface current i_{jk} on $\Gamma_{ae,h}$ and $\Gamma_{ce,h}$ is initialized with values proportional to the boundary current density i_{in}.
This concludes the description of the Newton algorithm including the assembly of the Jacobian.

3.2.5 Numerical solution of the elasticity problem

Let $\Omega = (0, 2\pi)^3$ and $f \in C^\infty(\Omega)$. The continuous Fourier transform and its inverse are defined as

$$\tilde{f}(\xi) = (2\pi)^{-\frac{3}{2}} \int_0^{2\pi} f(x) e^{-i\xi x} \mathrm{dx}, \quad f(x) = (2\pi)^{-\frac{3}{2}} \int_0^{2\pi} \tilde{f}(\xi) e^{i\xi x} \mathrm{d}\xi. \tag{3.20}$$

Let $N_1, N_2, N_3 \in \mathbb{N}$, $N = N_1 N_2 N_3$ and Ω_h an equally spaced grid discretization of Ω as introduced in Subsection 3.2.1. Let $v \in \mathbb{R}^N$. The discrete Fourier transform and its inverse are defined as

$$\begin{aligned}\tilde{v}_k &= \frac{(2\pi)^{-\frac{3}{2}}}{h^3} \sum_{\boldsymbol{x}_j \in \Omega_h} \exp\left(-i\boldsymbol{\xi}_k \boldsymbol{x}_j\right) v_j, \qquad \boldsymbol{x}_j \in \Omega_h, \\ v_j &= \frac{(2\pi)^{-\frac{3}{2}}}{h^3} \sum_{\boldsymbol{\xi}_k \in \Omega_h} \exp\left(i\boldsymbol{\xi}_k \boldsymbol{x}_j\right) \tilde{v}_k, \qquad \boldsymbol{\xi}_k \in \Omega_h.\end{aligned} \tag{3.21}$$

The function mapping the vector v to the vector $\tilde{v}$ is called the (discrete) Fourier transform $\mathcal{F}_h(\cdot)$, the inverse function mapping $\tilde{v}$ to v ic called inverse (discrete) Fourier transform $\mathcal{F}_h^{-1}(\cdot)$.
In [69] it is shown that the Fourier transform of the convolution of the function $f, g \in C^\infty(\Omega)$ is given by the product of the Fourier transforms. Similar for the discrete Fourier transform, it holds

$$\begin{aligned}\mathcal{F}_h(f * g) &= \mathcal{F}_h\left(\int_{\mathbb{R}} f(\tau) g(\cdot - \tau) d\tau\right) = \mathcal{F}_h(f) \cdot \mathcal{F}_h(g) \\ \Rightarrow f * g &= \mathcal{F}_h^{-1}\left(\mathcal{F}_h(f) \cdot \mathcal{F}_h(g)\right).\end{aligned} \tag{3.22}$$

This is used in [96] for an efficient iterative solution of a linear-elastic heterogeneous problem. The approach does not require the assembly of a stiffness matrix. With the convolution property the Fourier transform is used as a preconditioner. The derivation of the method, the numerical convergence, and optimization methods by the appplication of a conjugate gradient solver have been established in recent works [99, 117].
The stress-strain relationship for the linear elastic problem in 2.2.6 can be written as

$$\boldsymbol{\sigma}(\boldsymbol{x}, t) = \mathbb{C}(\boldsymbol{x}) : \boldsymbol{\varepsilon}_{\mathrm{el}}(\boldsymbol{x}, t), \quad (\boldsymbol{x}, t) \in \Omega \times T. \tag{3.23}$$

The stiffness tensor $\mathbb{C}$ is heterogeneous in this formulation. It varies depending on the linear-elastic coefficients for the different domains anode, electrolyte, and cathode. The zero displacement boundary condition is enforced by duplication of the domain. While the original domain was $\Omega = (0, L_1) \times (0, L_2) \times (0, L_3)$, the enlarged domain is $\Omega_2 = (0, 2L_1) \times (0, L_2) \times (0, L_3)$. A projection of the stiffness tensor defined on Ω is then given by mirroring as

$$\begin{cases} \mathbb{C}(\boldsymbol{x}), & x_1 < L_1, \\ \mathbb{C}(2L_1 - x_1, x_2, x_3), & x_1 > L_1. \end{cases}. \tag{3.24}$$

By an argument of symmetry, the zero displacement boundary condition is then recovered for the symmetric solution $u(\boldsymbol{x}, t) \in \Omega_2 \times (0, t_0)$. The periodic boundary conditions will be naturally incorporated into the discretization. The resulting elasticity problem is periodic in all three dimensions.

The governing equations are solved by the introduction of a reference material with linear-elastic material parameters (E_0, ν_0) and stiffness matrix $\mathbb{C}_0$. The solution to the stress field is divided into a homogenenous solution and a stress deviation field called polarization,

$$\boldsymbol{\tau}(\boldsymbol{x}, t) = (\mathbb{C}(\boldsymbol{x}) - \mathbb{C}_0) : \boldsymbol{\varepsilon}_{\mathrm{el}}(\boldsymbol{x}, t). \tag{3.25}$$

A constant coefficient operator $\mathcal{L}_0 = \nabla^{\mathrm{sym}} G_0 \mathrm{div}$ that depends only on $\mathbb{C}_0$ is introduced in [96]. The Green operator G_0 is associated with the reference material $\mathbb{C}_0$. By application of the operator $\mathcal{L}_0$, the following equation is received,

$$\boldsymbol{\varepsilon}_{\mathrm{el}}(\boldsymbol{x}, t) = E - \mathcal{L}_0 * \boldsymbol{\tau}(\boldsymbol{x}, t), \tag{3.26}$$

where E is the macroscopic strain. Together an equation for the elastic strain $\boldsymbol{\varepsilon}_{\mathrm{el}}$ is given as

$$\boldsymbol{\varepsilon}_{\mathrm{el}}(\boldsymbol{x}, t) = E - \mathcal{L}_0 * (\mathbb{C}(\boldsymbol{x}) - \mathbb{C}_0) : \boldsymbol{\varepsilon}_{\mathrm{el}}(\boldsymbol{x}, t) \tag{3.27}$$

This equation is discretized for each time step on the regular voxel mesh Ω_h and solved with a fixed-point iteration,

$$\boldsymbol{\varepsilon}_{\mathrm{el},h,j+1} = E - \mathcal{L}_{0,h} * (\mathbb{C}(\boldsymbol{x}_h) - \mathbb{C}_0) : \boldsymbol{\varepsilon}_{\mathrm{el},h,j} \tag{3.28}$$

with $\boldsymbol{\varepsilon}_{\mathrm{el}h,0} = 0$. The fixed-point iteration converges because the operator $\mathcal{L}_0$ is contractive. The convolution is carried out in Fourier space as defined in (3.22).
The coupling conditions are given in (2.23) as

$$\mu_{\mathrm{el}} = \frac{\theta}{3}\mathrm{tr}(\sigma) \Leftrightarrow \boldsymbol{\varepsilon}_{\mathrm{ch}} = \frac{\theta}{3} c\mathbf{I} \tag{3.29}$$

The numerical solution of the coupling between the electro-chemical model and the mechanical model is done by iteration. Given an iterate of the hydrostatic stress, the solution to the electro-chemical model is calculated. Then the iterate for the the concentration is used for the solution of the mechanical model. This iteration is continued until convergence is reached. The solution of the mechanical model adds an additional iteration loop.

3.3 Domain decomposition

In this section, a domain decomposition algorithm for the electro-chemical model is explained. First the governing equations in the electrolyte are decoupled in Subsection 3.3.1. Then the Cahn-Hilliard equation is simplified in Subsection 3.3.2. A method for the solution of the Poisson equation with mixed boundary conditions is given in Subsection 3.3.3 and the Butler-Volmer conditions are used for the unique solution of the

Poisson equation in Subsection 3.3.4. The algorithm combining the methods is given in Subsection 3.3.5.

3.3.1 Diffusion and electrostatic equation in the electrolyte domain

In the electrode domains, the governing equations for concentration and electrolyte are decoupled, see (2.20). However, in the electrolyte domain Ω_e, the governing equations for the concentration c_e and the electric potential ϕ_e are coupled, see (2.15). In this paragraph, the system of equations is decoupled and written as a triangular system. Section 2.2.2 introduces the following equations for the electrolyte domain Ω_e,

$$\partial_t c_e - \operatorname{div}\left[\left(D_e + \frac{RT\kappa_e t_+(t_+-1)}{F^2 c_e}\right)\nabla c_e + \frac{\kappa_e t_+}{F}\nabla\phi_e\right] = 0, \tag{3.30a}$$

$$-\operatorname{div}\boldsymbol{j} = -\operatorname{div}\left[\frac{RT\kappa_e(t_+-1)}{Fc_e}\nabla c_e + \kappa_e\nabla\phi_e\right] = 0. \tag{3.30b}$$

$$\tag{3.30c}$$

The electric current $\boldsymbol{j}$ in (3.30b) is a linear combination of the gradient of the concentration c_e and the electric field ϕ_e. Rearrangement of (3.30a) gives

$$\begin{aligned}\partial_t c_e &= \operatorname{div}\left(D_e\nabla c_e\right) + \operatorname{div}\left(\frac{RT\kappa_e t_+(t_+-1)}{F^2 c_e}\nabla c_e + \frac{\kappa_e t_+}{F}\nabla\phi_e\right)\\ &= \operatorname{div}\left(D_e\nabla c_e\right) + \frac{t_+}{F}\operatorname{div}\left(\frac{RT\kappa_e(t_+-1)}{Fc_e}\nabla c_e + \kappa_e\nabla\phi_e\right)\\ &= \operatorname{div}\left(D_e\nabla c_e\right) + \frac{t_+}{F}\operatorname{div}\boldsymbol{j}\\ &= \operatorname{div}\left(D_e\nabla c_e\right).\end{aligned} \tag{3.31}$$

Observe that (3.31) only depends on the concentration c_e, but not on the electric field ϕ_e. This allows to rewrite (3.30b) and solve for ϕ_e as

$$\operatorname{div}\left(\kappa_e\nabla\phi_e\right) = -\operatorname{div}\left(\frac{RT\kappa_e(t_+-1)}{Fc_e}\nabla c_e\right) \tag{3.32}$$

with a right-hand side that is given as a differential operator of the concentration c_e. Next, a decoupled description of the interface conditions on the electrolyte is presented. Here i_{se} is used for both interface conditions on the anode-electrolyte interface Γ_{ae} and the cathode-electrolyte interface Γ_{ce}. They are posed in (2.2.3) as

$$\begin{aligned}\boldsymbol{n}\cdot\left[\left(D_e + \frac{RT\kappa_e t_+(t_+-1)}{F^2 c_e}\right)\nabla c_e + \frac{\kappa_e t_+}{F}\nabla\phi_e\right] &= \frac{1}{F}i_{\mathrm{se}}\\ \boldsymbol{n}\cdot\left[-\frac{RT\kappa_e(t_+-1)}{Fc_e}\nabla c_e - \kappa_e\nabla\phi_e\right] &= i_{\mathrm{se}}\end{aligned} \tag{3.33}$$

The interface current i_{se} depends nonlinearly on the concentration and the electric potential. A system of linear equations in the normal components of concentration gradient $\nabla_n c_e$ and of electric potential gradient $\nabla_n \phi_e$ is given as

$$\begin{aligned}
\begin{pmatrix} D_e + \frac{RT\kappa_e t_+(t_+-1)}{F^2 c_e} & \frac{\kappa_e t_+}{F} \\ -\frac{RT\kappa_e(t_+-1)}{F c_e} & -\kappa_e \end{pmatrix} \begin{pmatrix} \nabla_n c_e \\ \nabla_n \phi_e \end{pmatrix} &= \begin{pmatrix} \frac{1}{F} \\ 1 \end{pmatrix} i_{\mathrm{se}}, \\
\begin{pmatrix} D_e & 0 \\ \frac{RT\kappa_e(t_+-1)}{F c_e} & \kappa_e \end{pmatrix} \begin{pmatrix} \nabla_n c_e \\ \nabla_n \phi_e \end{pmatrix} &= \begin{pmatrix} \frac{1+t_+}{F} \\ -1 \end{pmatrix} i_{\mathrm{se}}, \\
\begin{pmatrix} D_e & 0 \\ 0 & \kappa_e \end{pmatrix} \begin{pmatrix} \nabla_n c_e \\ \nabla_n \phi_e \end{pmatrix} &= \begin{pmatrix} \frac{1+t_+}{F} \\ -1 - \frac{RT\kappa_e(t_+-1)(1+t_+)}{D_e F^2 c} \end{pmatrix} i_{\mathrm{se}}.
\end{aligned} \tag{3.34}$$

As a result of this derivation, the following equations are received for the diffusion in the electrolyte,

$$\begin{aligned}
\frac{\partial}{\partial t} c_e(\boldsymbol{x}, t) &= \operatorname{div}\left(D_e \nabla c_e(\boldsymbol{x}, t)\right), && (\boldsymbol{x}, t) \in \Omega_e \times (0, t_0), \\
\boldsymbol{n} \cdot D_e c_e(\boldsymbol{x}, t) &= \frac{1 + t_+}{F} i_{\mathrm{se}}, && (\boldsymbol{x}, t) \in \Gamma_{\mathrm{se}} \quad t \in (0, t_0). \\
\boldsymbol{n} \cdot D_e c_e(\boldsymbol{x}, t) &= 0, && (\boldsymbol{x}, t) \in \Gamma_e \quad t \in (0, t_0), \\
c_e(\boldsymbol{x}, 0) &= c_0(\boldsymbol{x}) && \boldsymbol{x} \in \Omega_e,
\end{aligned} \tag{3.35}$$

and the electric potential in the electrolyte,

$$\begin{aligned}
\operatorname{div}\left(\kappa_e \nabla \phi_e(\boldsymbol{x}, t)\right) &= -\operatorname{div}\left(\frac{RT\kappa_e(t_+ - 1)}{F c_e(\boldsymbol{x}, t)} \nabla c_e(\boldsymbol{x}, t)\right), && (\boldsymbol{x}, t) \in \Omega_e \times (0, t_0), \\
\boldsymbol{n} \cdot \kappa_e \nabla \phi_e(\boldsymbol{x}, t) &= -1 - \frac{RT\kappa_e(t_+ - 1)(1 + t_+)}{D_e F^2 c_e(\boldsymbol{x}, t)} i_{\mathrm{se}}, && (\boldsymbol{x}, t) \in \Gamma_{\mathrm{se}} \times (0, t_0), \\
\boldsymbol{n} \cdot \kappa_e \nabla \phi_e(\boldsymbol{x}, t) &= 0, && (\boldsymbol{x}, t) \in \Gamma_0 \times (0, t_0).
\end{aligned} \tag{3.36}$$

Compare (3.35) and (3.36) to the equations (2.44) and (2.50). The previously coupled equations are now decoupled and can be solved consecutively.

3.3.2 Cathode diffusion equation

Although the logarithmic double-well potential presented in 2.2.2 is derived from first thermodynamic principle, diffusive phase-field models are also applied with a polynomial double-well potential. Figure 3.2 shows different options for the choice of a chemical potential. The following paragraph defines a polynomial potential with the same equilibrium values as the logarithmic potential.

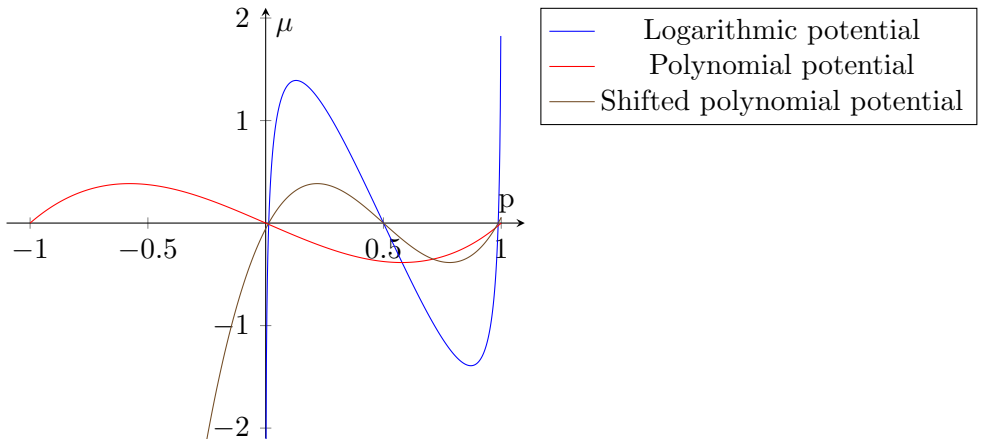

Figure 3.2: Comparison of different chemical potentials.

The potential $\mu(p) = \log \frac{p}{1-p} + q(1-2p)$ has equilibrium values $p_1 = 0.013$ and $p_2 = 0.987$. The polynomial chemical potential $\mu^*(p) = p^3 - p$ has equilibrium values $p_1^* = -1$ and $p_2^* = 1$. A linear map correlating the equilibrium values is then given as

$$f : p \mapsto \frac{p_2^* - p_1^*}{p_2 - p_1} p + \frac{p_1^* p_2 - p_2^* p_1}{p_2 - p_1}. \tag{3.37}$$

Given the values of p_1^* and p_2^* and the fact that $p_1 + p_2 = 1$ (due to symmetry) this simplifies to

$$f : p \mapsto \frac{2p - 1}{p_2 - p_1}. \tag{3.38}$$

The resulting shifted chemical potential $\mu^*(f(p))$ is shown in Figure 3.2. It has the same equilibrium phase-field parameters as the original chemical potential. While a logarithmic potential is defined in $(0, 1)$, the substitute chemical potential $\mu^*(f(p))$ is defined on $\mathbb{R}$.
The double-well potential (2.24) compares to the approximation as

$$\begin{aligned} F_0(p) &= p \log p + (1-p) \log (1-p) + \frac{q}{RT} p(1-p), \\ F_0^*(p) &= \frac{1}{4} \left(\frac{2p-1}{p_2 - p_1} + 1 \right)^2 \left(\frac{2p-1}{p_2 - p_1} - 1 \right)^2. \end{aligned} \tag{3.39}$$

Additionally the diffusion coefficient D in (2.27) depends on the concentration. Each occurence of the concentration c_c in the diffusion coefficient is approximated by half of maximum lithium ion concentration, $c_c \approx \frac{c_{\max,c}}{2}$,

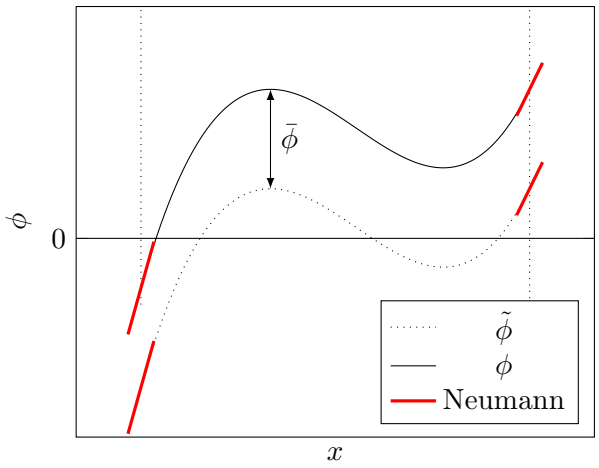

Figure 3.3: Solution decomposition for a pure Neumann elliptic problem.

$$\begin{aligned} \frac{\partial}{\partial t}c &= \operatorname{div}\left(\frac{D_0}{RT}\frac{c_{\max,\mathrm{c}}}{4}\nabla\mu\right), \\ \mu &= RT\alpha L_0^2\frac{G}{L}F_0^{*\prime}\left(\frac{c_c}{c_{\max,\mathrm{c}}}\right) - RT\beta GL\Delta\left(\frac{c_c}{c_{\max,\mathrm{c}}}\right). \end{aligned} \tag{3.40}$$

Compare (3.40) to (2.27).

3.3.3 Electrostatic equations with mixed boundary conditions

This paragraph replaces the mixed nonlinear boundary conditions in the equation for the electric potential with pure Neumann boundary conditions. The boundary conditions for the electrostatic field in the anode are

$$\begin{aligned} \boldsymbol{n}\cdot\nabla\phi(\boldsymbol{x},t) &= i_{\mathrm{se}}(\boldsymbol{x},t), && (\boldsymbol{x},t)\in\Gamma_{ae}\times(0,t_0), \\ \phi(\boldsymbol{x},t) &= 0, && (\boldsymbol{x},t)\in\Gamma_a\times(0,t_0). \end{aligned} \tag{3.41}$$

Assume that the normal component of the gradient $\boldsymbol{n}\cdot\nabla\phi$ is known on Γ_a. For the benefit of this paragraph, assume that i_{se} is defined on $\Gamma_{ae+a} := \Gamma_{ae}\cup\Gamma_a$. Then the boundary condition

$$\boldsymbol{n}\cdot\nabla\phi(\boldsymbol{x},t) = i_{\mathrm{se}}(\boldsymbol{x},t), \quad (\boldsymbol{x},t)\in\Gamma_{ae+a}\times(0,t_0) \tag{3.42}$$

is not enough to define a unique solution for the electric potential. With a reference point $x_0\in\Gamma_{ae+a}$ given by

$$\phi(\boldsymbol{x}_0,t) = \phi_0 \tag{3.43}$$

the solution ϕ is unique, as the set of different solutions $\{\tilde{\phi}\}$ to (3.42) can be characterized: If $\tilde{\phi}_1$ and $\tilde{\phi}_2$ are both solutions to (3.42), then it holds $\tilde{\phi}_1 - \tilde{\phi}_2 = K$ with $K \in \mathbb{R}$. A unique solution $\tilde{\phi}$ to (3.42) is defined by the addition of a mean-free condition,

$$\int_{\Omega_a} \tilde{\phi}(\boldsymbol{x}, t) \mathrm{d}\boldsymbol{x} = 0. \tag{3.44}$$

The solution ϕ can then be recovered with (3.43) as

$$\phi(\boldsymbol{x}, t) = \tilde{\phi}(\boldsymbol{x}, t) - \tilde{\phi}(\boldsymbol{x}_0, t) + \phi_0. \tag{3.45}$$

Figure 3.3 explains the concept of a unique, mean-free solution $\tilde{\phi}$ and the shift $\bar{\phi}$.
As a result of the high conductivity κ of the current collector material and the electrode material, the current $\kappa_a \nabla \phi$ along both current collector boundaries Γ_a and Γ_c is assumed to be constant[4]. In a galvanostatic loadcase, this allows to reduce the Dirichlet condition on Γ_a from the electric potential equations in the anode to an arbitrary single point $x_0 \in \Gamma_a$. The reference potential of the anode is set to $\phi_0 = 0$. For the electrolyte material and the cathode material, the reference values for the electric potential will be determined by the interface conditions in the next subsection.
Summarizing, the electric potentials ϕ_a, ϕ_e and ϕ_c are split into their mean-free part $\tilde{\phi}_i$ for $i \in \{a, e, c\}$ and a scalar value $\bar{\phi}_i \in \mathbb{R}$ for $i \in \{a, e, c\}$ that relates to the reference potential in (3.42) called electric potential offset such that holds

$$\phi_i = \tilde{\phi}_i + \bar{\phi}_i \text{ for } i \in \{a, e, c\}. \tag{3.46}$$

3.3.4 Butler-Volmer interface conditions

In this paragraph the electric potential offsets $\bar{\phi}_i$ are derived. The mean-free solutions of the electric potentials $\tilde{\phi}_i$ for $i \in \{a, e, c\}$ and the concentrations c_i for $i \in \{a, e, c\}$ are assumed as given.
The Butler-Volmer interface currents $i_{\mathrm{se}} = i_{\mathrm{se}}(\eta)$ are monotonically increasing in the overpotential η as $\eta = \phi_s - \phi_e - \mu(c_s)$ and $\partial_\eta i_{\mathrm{se}}(\eta) > 0$. An integral interface condition can be given for galvanostatic loadcases on the anode-electrolyte interface,

$$I_0 = \int_{\Gamma_{\mathrm{ae}}} i_{\mathrm{ae}}(c_a, c_e, \phi_a, \tilde{\phi}_e + \bar{\phi}_e) \mathrm{dS}, \tag{3.47}$$

Here the constant I_0 is the total current applied to the battery cell. It can be calculated dependent on the C-rate of the problem. The electric potential offset $\bar{\phi}_e$ is then calculated by a Newton algorithm on the scalar function $r(\bar{\phi}_e)$ and its derivative $r'(\bar{\phi}_e)$,

[4] This is only valid if the electrode domain is connected.

$$
\begin{aligned}
r(\bar{\phi}_e) &= \int_{\Gamma_{\mathrm{ae}}} i_{\mathrm{ae}}(c_a, c_e, \phi_a, \tilde{\phi}_e + \bar{\phi}_e)\mathrm{dS} - I_0, \\
r'(\bar{\phi}_e) &= \int_{\Gamma_{\mathrm{ae}}} \partial_{\phi_e} i_{\mathrm{ae}}(c_a, c_e, \phi_a, \tilde{\phi}_e + \bar{\phi}_e)\mathrm{dS}.
\end{aligned} \tag{3.48}
$$

As ν_{se} is monotonic in the overpotential η, so is the integral in $r(\bar{\phi}_e)$. Therefore, the Newton algorithm

$$
\bar{\phi}_e^0 = 0, \quad \bar{\phi}_e^{k+1} = \bar{\phi}_e^k - \frac{r(\bar{\phi}_e^k)}{r'(\bar{\phi}_e^k)}, \tag{3.49}
$$

is known to converge to a unique solution $\bar{\phi}_e$. Similarly, the electric potential offset in the cathode $\bar{\phi}_c$ is received with the cathode-electrolyte interface condition.

3.3.5 Algorithm

Data: Old concentration $\check{c}$
Result: New concentration c, electric potentials ϕ and interface currents f

for $i = 1..$ **do**
- $\tilde{\phi}_a \leftarrow$ IIM(i_{se}) ;
- $\tilde{\phi}_e \leftarrow$ IIM(c_e,i_{se});
- $\tilde{\phi}_c \leftarrow$ IIM(i_{se});
- $\bar{\phi}_a \leftarrow$ Boundary conditions;
- $\bar{\phi}_e \leftarrow$ Newton(c,ϕ_a,$\tilde{\phi}_e$) + Interface conditions;
- $\bar{\phi}_c \leftarrow$ Newton(c,ϕ_e,$\tilde{\phi}_c$) + Interface conditions;
- $\phi \leftarrow \tilde{\phi} + \bar{\phi}$;
- $i_{\mathrm{se}} \leftarrow$ ButlerVolmer(c,ϕ);
- $c_a \leftarrow$ IIM($\check{c}_a$,i_{se}) ;
- $c_e \leftarrow$ IIM($\check{c}_e$,i_{se});
- $c_c \leftarrow$ IIM($\check{c}_c$,i_{se});
- Calculate the error e;
- **if** $e < TOL$ **then**
  - Return;

end for

Algorithm 3: Domain decomposition algorithm

The domain decomposition algorithm presented in this section separates the electrochemical model into a series of boundary value problems of elliptic and parabolic type

with linear Neumann boundary conditions and a series of scalar equations for the electric potential offsets. The following problems are solved in the given order. An iteration starts with the iteration counter $j = 0$. As an initial value, the new values for the concentration c and the Butler-Volmer interface currents i_{se} are copied from the last time step.

1. The mean-free electric potential in the anode $\tilde{\phi}_{a,j+1}$ is calculated by a Poisson equation. This equation depends on the Butler-Volmer currents $i_{\mathrm{se},j}$.

$$\begin{aligned} -\mathrm{div}\left(\kappa_a \nabla \tilde{\phi}_{a,j+1}\right) &= 0, && \text{in } \Omega_a, \\ \kappa_a \nabla_n \tilde{\phi}_{a,j+1} &= i_0, && \text{on } \Gamma_a, \\ \kappa_a \nabla_n \tilde{\phi}_{a,j+1} &= i_{\mathrm{ae},j}, && \text{on } \Gamma_{ae}, \\ \int_{\Omega_a} \tilde{\phi}_{a,j+1} \mathrm{dS} &= 0. \end{aligned} \tag{3.50}$$

2. The mean-free electric potential in the electrolyte $\tilde{\phi}_{e,j+1}$ is calculated by a Poisson equation. This equation depends on the Butler-Volmer currents $i_{\mathrm{se},j}$ and the concentration in the electrolyte $c_{e,j}$.

$$\begin{aligned} -\mathrm{div}\left(\kappa_e \nabla \tilde{\phi}_{e,j+1}\right) &= \mathrm{div}\left(\frac{RT\kappa_e(t_+ - 1)}{F c_{e,j}} \nabla c_{e,j}\right), && \text{in } \Omega_e, \\ \kappa_e \nabla_n \tilde{\phi}_{e,j+1} &= 0, && \text{on } \Gamma_e., \\ \kappa_e \nabla_n \tilde{\phi}_{e,j+1} &= \left(-1 - \frac{RT(t_+ - 1)(1 + t_+)}{D_e F^2 c_{e,j}}\right) i_{\mathrm{se},j}, && \text{on } \Gamma_{\mathrm{se}}, \\ \int_{\Omega_e} \tilde{\phi}_{e,j+1} \mathrm{dS} &= 0. \end{aligned} \tag{3.51}$$

3. The mean-free electric potential in the cathode $\tilde{\phi}_{c,j+1}$ is calculated by a Poisson equation. This equation depends on the Butler-Volmer currents $i_{\mathrm{se},j}$.

$$\begin{aligned} -\mathrm{div}\left(\kappa_c \nabla \tilde{\phi}_{c,j+1}\right) &= 0, && \text{in } \Omega_c, \\ \boldsymbol{n} \cdot \kappa_c \nabla \tilde{\phi}_{c,j+1} &= i_0, && \text{on } \Gamma_c, \\ \boldsymbol{n} \cdot \kappa_c \nabla \tilde{\phi}_{c,j+1} &= i_{\mathrm{ce},j}, && \text{on } \Gamma_{ce}, \\ \int_{\Omega_c} \tilde{\phi}_{c,j+1} \mathrm{dS} &= 0. \end{aligned} \tag{3.52}$$

4. The electric potential offset in the anode $\bar{\phi}_{a,j+1}$ is determined by the Dirichlet condition on the anode.

$$\bar{\phi}_{a,j+1} = -\tilde{\phi}_{a,j+1}(\boldsymbol{x}_0). \tag{3.53}$$

5. The electric potential offset in the electrolyte $\bar{\phi}_{e,j+1}$ and the electric field in the electrolyte $\phi_{e,j+1}$ are calculated by the Butler-Volmer interface condition.

$$\begin{aligned} \int_{\Gamma_{ae}} i_{ae}(c_{a,j}, c_{e,j}, \phi_{a,j}, \tilde{\phi}_{e,j+1} + \bar{\phi}_{e,j+1})\mathrm{dS} = I_0, \\ \phi_{e,j+1} = \tilde{\phi}_{e,j+1} + \bar{\phi}_{e,j+1}. \end{aligned} \tag{3.54}$$

6. The electric potential offset in the cathode $\bar{\phi}_{c,j+1}$ and the electric field in the cathode $\phi_{c,j+1}$ are calculated by the Butler-Volmer interface condition.

$$\begin{aligned} \int_{\Gamma_{ce}} i_{ce}(c_{c,j}, c_{e,j}, \tilde{\phi}_{c,j+1} + \bar{\phi}_{c,j+1}, \phi_{e,j+1})\mathrm{dS} = I_0, \\ \phi_{c,j+1} = \tilde{\phi}_{c,j+1} + \bar{\phi}_{c,j+1}. \end{aligned} \tag{3.55}$$

7. The Butler-Volmer interface currents $i_{ae,j+1}$ are calculated.

$$\begin{aligned} i_{\mathrm{ae},j+1} &= i_{ae}(c_{c,j}, c_{e,j}, \phi_{a,j+1}, \phi_{e,j+1}), \\ i_{\mathrm{ce},j+1} &= i_{ce}(c_{c,j}, c_{e,j}, \phi_{c,j+1}, \phi_{e,j+1}). \end{aligned} \tag{3.56}$$

8. The concentration in the anode is calculated by the diffusion equation in the anode. This equation depends on the Butler-Volmer interface currents $i_{\mathrm{ae},j+1}$.

$$\begin{aligned} \frac{\partial}{\partial t} c_{a,j+1} &= \mathrm{div}\,(D_a \nabla c_{a,j+1}), && \text{in } \Omega_a, \\ D_a \nabla_n c_{a,j+1} &= \frac{1}{F} i_0, && \text{on } \Gamma_a, \\ D_a \nabla_n c_{a,j+1} &= \frac{1}{F} i_{\mathrm{ae},j+1}, && \text{on } \Gamma_{ae}. \end{aligned} \tag{3.57}$$

9. The concentration in the electrolyte is calculated by the diffusion equation in the electrolyte. This equation depends on the Butler-Volmer interface currents $i_{\mathrm{ae},j+1}$ and $i_{\mathrm{ce},j+1}$.

$$\begin{aligned}
\frac{\partial}{\partial t} c_{e,j+1} &= \operatorname{div}\left(D_e \nabla c_{e,j+1}\right), && \text{in } \Omega_e, \\
D_e \nabla_n c_{e,j+1} &= 0, && \text{on } \Gamma_e, \\
D_e \nabla_n c_{e,j+1} &= \frac{1+t_+}{F} i_{\mathrm{ae},j+1}, && \text{on } \Gamma_{ae}, \\
D_e \nabla_n c_{e,j+1} &= \frac{1+t_+}{F} i_{\mathrm{ce},j+1}, && \text{on } \Gamma_{ce}.
\end{aligned} \tag{3.58}$$

10. The concentration in the cathode is calculated by the Cahn-Hilliard equation in the cathode. This equation depends on the Butler-Volmer interface currents $i_{\mathrm{ce},j+1}$.

$$\begin{aligned}
\frac{\partial}{\partial t} c_{c,j+1} &= \operatorname{div}\left(\frac{D_0}{RT}\frac{c_{\max,\mathrm{c}}}{4}\nabla \mu_{c,j+1}\right), && \text{in } \Omega_c, \\
\frac{1}{RT}\mu_{c,j+1} &= \alpha L_0^2 \frac{G}{L} F_0^{*\prime}\left(\frac{c_{c,j+1}}{c_{\max,\mathrm{c}}}\right) - \beta G L \Delta\left(\frac{c_{c,j+1}}{c_{\max,\mathrm{c}}}\right), && \text{in } \Omega_c, \\
\boldsymbol{n} \cdot \frac{D_0}{RT}\frac{c_{\max,\mathrm{c}}}{4}\nabla \mu_{c,j+1} &= \frac{1}{F} i_0, && \text{on } \Gamma_c, \\
\boldsymbol{n} \cdot \frac{D_0}{RT}\frac{c_{\max,\mathrm{c}}}{4}\nabla \mu_{c,j+1} &= \frac{1}{F} i_{\mathrm{ce},j+1}, && \text{on } \Gamma_{ce}, \\
\boldsymbol{n} \cdot \nabla c_{c,j+1} &= 0, && \text{on } \Gamma_c \cup \Gamma_{ce}.
\end{aligned} \tag{3.59}$$

The resulting Algorithm 3 shows the iterative process. Each of the problems denoted with IIM is solved with an IIM as introduced in the following sections with pure Neumann conditions.

3.4 Poisson equation and diffusion equation

In this section, fast solution methods for the Poisson equation and the diffusion equation are discussed. First the differentiation and integration of a function represented by Fourier polynoms is explained in Subsection 3.4.1. Then methods for the solution of the periodic Poisson equation in Subsection 3.4.2 and the periodic diffusion equation in Subsection 3.4.3 are defined. Finally, the immersed interface method is defined in Subsection 3.4.4.

3.4.1 Representation by a trigonometric basis

The first spatial discretization is based on the projection of a periodic function $f : \Omega \mapsto \mathbb{R}$ with $|\Omega| = L$ to a finite N-dimensional space spanned by Fourier polynomials

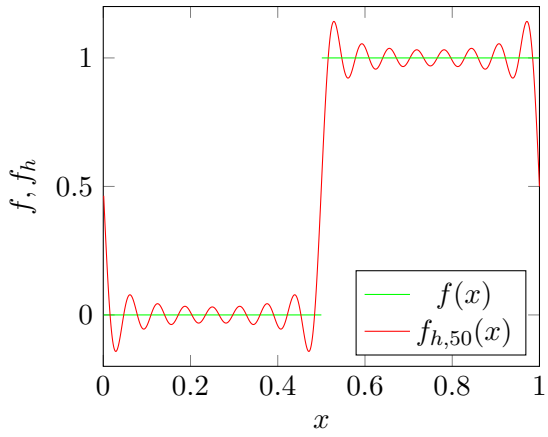

Figure 3.4: Fourier representation of a square wave and Gibbs overshoot

$\exp\left(\frac{2\pi}{L} imx\right)$ with $m \in \{1, \ldots, N\}$. According to this representation, the Fourier coefficients are often called frequencies. If the function f represents the amplitude of a wave function depending on the position, the Fourier coefficients represents the wave amplitude depending on the frequency. The vector ξ with the entries $\xi_m = \frac{2\pi}{L}m$ is called the discrete wave vector.
The error of the Fourier representation descreases larger than any polynomial in the gridwidth h for infinitely smooth functions. This is often called spectral accuracy. Given the approximation f_N with Fourier polynomials as defined in (3.21),

$$f_N(x) = \sqrt{\frac{L}{2\pi}} \sum_{m=1}^{N} \exp\left(i\xi_m x\right)\tilde{v}_m, \tag{3.60}$$

it holds $f(x) = f_N(x) + O(h^N)$ if $f \in C^\infty(\Omega)$. An approximation to the spatial derivative of f can then be calculated as

$$\partial_x f(x) = \partial_x f_N + O(h^N) = \sqrt{\frac{L}{2\pi}} \sum_{m=1}^{N} i\xi_m \exp\left(i\xi_m x\right)\tilde{v}_m + O(h^N). \tag{3.61}$$

Summarizing the process of differentiation by Fourier transforms with the previously introduced notation it can be written

$$\partial_x f_N = \mathcal{F}_h^{-1}\left(i\xi \cdot \mathcal{F}_h\left(f_N\right)\right). \tag{3.62}$$

The vector $i\xi$ is multiplied component-wise with the frequency vector. This simple equation is the foundation of Fourier-based differentiation and integration. It is easy to derive a similar equation [132] for an indefinite integral of f,

$$\int_0^x f_N(x')dx' = \mathcal{F}_h^{-1}\left(\frac{1}{i\xi}\cdot\mathcal{F}_h\left(f_N\right)\right) + C. \tag{3.63}$$

The second derivative is given by

$$\partial_x^2 f_N = \mathcal{F}_h^{-1}\left(-\xi^2\cdot\mathcal{F}_h\left(f_N\right)\right). \tag{3.64}$$

If non-smooth functions are differentiated with this approach, the representation does not converge uniformly [59]. Figure 3.4 shows a non-smooth square wave function $f : [0,1] \to \mathbb{R}$

$$f(x) = \begin{cases} 0 & x \leq 0.5 \\ 1 & x > 0.5 \end{cases} \tag{3.65}$$

and its representation in the finite Fourier space for $N = 50$. The oscillations around non-continuities are called Gibbs phenomenon [50]. The overshoot from the correct function value does not vanish with increasing N. The approached finite limit is derived analytically in [155]. In the presented case it is approximately 0.0894. This problem is relevant for the application of Fourier transforms for differentiation or integration of discrete discontinuous functions. While the convergence rate for the derivatives of smooth functions has been shown to be of spectral accuracy, for discontinuous functions unwanted oscillations are introduced. For the correct application of the IIM, uniform convergence of the derivatives is needed. For this reason another way to use Fourier transforms for the calculation of derivatives is introduced.

3.4.2 Solution of the periodic Poisson equation

A similar way to apply Fourier methods for the differentiation and integration of functions is now defined. Central finite differences are applied to approximate the second spatial derivative. On a regular periodic spatial grid, the application of a second order stencil is given as

$$\begin{aligned} D^2 f_N(x) &= \frac{f_N(x^-) - 2f_N(x) + f_N(x^+)}{h^2} \\ &= \sum_{m=1}^{N} \frac{\exp\left(i\xi_m\left(x-h\right)\right) - 2\exp\left(i\xi_m x\right) + \exp\left(i\xi_m\left(x+h\right)\right)}{h^2}\tilde{v}_m \\ &= \sum_{m=1}^{N} \frac{\left(2\cos\xi_m - 2\right)}{h^2}\exp\left(i\xi_m x\right)\tilde{v}_m. \\ D^2 f_N(x) &= \mathcal{F}_h^{-1}\left(\frac{\left(2\cos\xi - 2\right)}{h^2}\cdot\mathcal{F}_h\left(f_N\right)\right) \end{aligned} \tag{3.66}$$

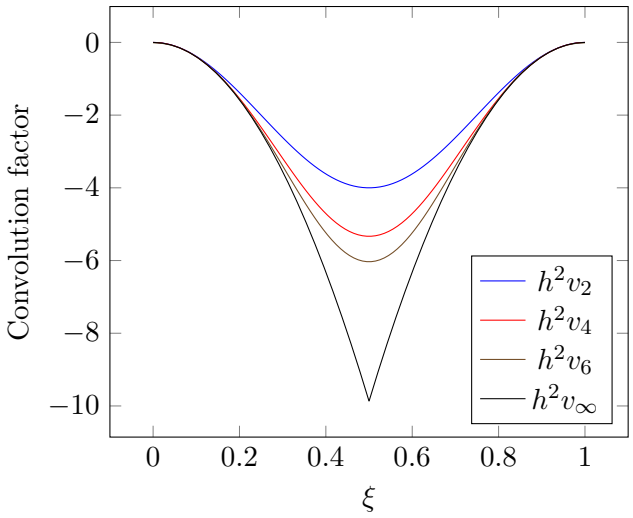

Figure 3.5: Convolution vectors for Fourier derivation methods

Compare this result to (3.64). The discrete vector involved in this equation $v_2 = \frac{(2\cos\xi - 2)}{h^2}$ is called the convolution vector. Remembering (3.22), this vector is the Fourier transform of the central difference stencil in real space of second order. Central difference stencils can be derived of arbitrary even order [47][5]. The following approximations can be derived for second, fourth and sixth order. Additionally the convolution vector for the previously introduced continuous approximation is given.

$$\begin{aligned} h^2v_2 &= 2\cos\xi - 2, \\ h^2v_4 &= -\frac{1}{6}\cos 2\xi + \frac{8}{3}\cos 2\xi - \frac{5}{2}, \\ h^2v_6 &= \frac{1}{90}\cos 3\xi - \frac{3}{10}\cos 2\xi + 3\cos\xi - \frac{49}{18}, \\ h^2v_\infty &= \begin{cases} -4\pi^2(\xi^2), & x \leq 0.5, \\ -4\pi^2(1-\xi^2), & x > 0.5. \end{cases} \end{aligned} \tag{3.67}$$

In Figure 3.5 the vectors are plotted. It can be seen that the convolution vectors for the central difference of higher order approximate the convolution vector for the continuous interpolation. This fits the expectation that the error of a central difference approximation converges to zero for higher approximation order.

[5]They are given for example by the coefficients of the Taylor series around $x_0 = 1$ of $x^d \log(x)^k$, where k is the order of the derivative.

Both differentiation and integration of periodic functions can be realized by a transform to Fourier space, a multiplication with a convolution vector v and an inverse Fourier transform. It holds

$$\Delta_h(f_h) \approx \mathcal{F}_h^{-1}\left(\tilde{\Delta}_h \mathcal{F}_h\left(f_h\right)\right) \quad \Delta_h^{-1}(f_h) \approx \mathcal{F}_h^{-1}\left(\tilde{\Delta}_h^{-1} \mathcal{F}_h\left(f_h\right)\right) \tag{3.68}$$

With this, an arbitrary even-order discrete linear differential operator can be applied. The solution of a corresponding system of linear equations is straight-forward and can be explicitly calculated in one step for a problem with constant coefficients.
The order of consistency of the introduced stencils is now verified on a simple analytical example. Let $\Omega = (0, L_1) \times (0, L_2) \times (0, L_3)$ a cuboid domain with boundary $\Gamma = \partial\Omega$. The boundary value problem for the periodic Poisson equation is given as

$$\begin{aligned} -\Delta\phi(\boldsymbol{x}) &= f(\boldsymbol{x}), & \boldsymbol{x} &\in \Omega, \\ \phi(\boldsymbol{x}) &= \phi(\boldsymbol{x} + L_i\boldsymbol{e}_i), & \boldsymbol{x}, \boldsymbol{x} + L_i\boldsymbol{e}_i &\in \Gamma, \\ \boldsymbol{n} \cdot \nabla\phi(\boldsymbol{x}) &= -\boldsymbol{n} \cdot \nabla\phi(\boldsymbol{x} + L_i\boldsymbol{e}_i), & \boldsymbol{x}, \boldsymbol{x} + L_i\boldsymbol{e}_i &\in \Gamma. \end{aligned} \tag{3.69}$$

These boundary conditions are called periodic boundary conditions as every solution can be periodically extended to a C^1-solution in $\mathbb{R}^3$ by periodic extension in all three Cartesian dimensions such that $\phi(\boldsymbol{x}, t) \coloneqq \phi(x_1 + i_1 L_1, x_2 + i_2 L_2, x_3 + i_2 L_2, t)$ with $i_j \in \mathbb{Z}$ and $x_j + i_j L_j \in \Omega$ for $j \in \{1, 2, 3\}$. The function $f \in C^2(\Omega)$ is called the right-hand side. Given a discretization on the regular mesh Ω_h and the convolution vector , the solution is given as

$$-\Delta_h\phi_h = f_h \quad \Rightarrow \quad \phi_h = \mathcal{F}_h^{-1}\left(-\frac{1}{v_2}\mathcal{F}_h\left(f_h\right)\right). \tag{3.70}$$

Similarly to the previous subsection, the problem is not unique and the uniqueness has to be assured by an arbitrary additional condition (e.g. mean-free integral).

3.4.3 Solution of the periodic diffusion equation

In this paragraph, implicit time integration methods for ordinary differential equations are applied to a partial differential equation that has been discretized in space. Consider the periodic diffusion equation

$$\begin{aligned} \partial_t c(\boldsymbol{x}, t) &= \Delta c(\boldsymbol{x}, t) & (\boldsymbol{x}, t) &\in \Omega \times T, \\ c(\boldsymbol{x}, t) &= c(\boldsymbol{x} + L_i\boldsymbol{e}_i, t), & \boldsymbol{x}, \boldsymbol{x} + L_i\boldsymbol{e}_i &\in \Gamma, t \in T \\ \boldsymbol{n} \cdot \nabla c(\boldsymbol{x}, t) &= -\boldsymbol{n} \cdot \nabla c(\boldsymbol{x} + L_i\boldsymbol{e}_i, t), & \boldsymbol{x}, \boldsymbol{x} + L_i\boldsymbol{e}_i &\in \Gamma, t \in T. \end{aligned} \tag{3.71}$$

discretized in space,

$\frac{1}{2}$	$\frac{1}{2}$
	1

$\frac{1}{2} - \frac{1}{6}\sqrt{3}$	$\frac{1}{4}$	$\frac{1}{4} - \frac{1}{6}\sqrt{3}$
$\frac{1}{2} + \frac{1}{6}\sqrt{3}$	$\frac{1}{4} + \frac{1}{6}\sqrt{3}$	$\frac{1}{4}$
	$\frac{1}{2}$	$\frac{1}{2}$

$\frac{1}{2} - \frac{1}{10}\sqrt{15}$	$\frac{5}{36}$	$\frac{2}{9} - \frac{1}{15}\sqrt{15}$	$\frac{5}{36} - \frac{1}{30}\sqrt{15}$
$\frac{1}{2}$	$\frac{5}{36} + \frac{1}{24}\sqrt{15}$	$\frac{2}{9}$	$\frac{5}{36} - \frac{1}{24}\sqrt{15}$
$\frac{1}{2} + \frac{1}{10}\sqrt{15}$	$\frac{5}{36} + \frac{1}{30}\sqrt{15}$	$\frac{2}{9} + \frac{1}{15}\sqrt{15}$	$\frac{5}{36}$
	$\frac{5}{18}$	$\frac{4}{9}$	$\frac{5}{18}$

Table 3.3: Butcher tableaus for the Gauss-Legendre methods of order two, four and six. Given are the values b_i, a_{ij} and d_j.

$$\begin{aligned} \partial_t c_h(t) &= \Delta_h c_h(t), \quad c_h(t) \in \mathbb{R}^N, \\ c_h(0) &= c_{h,0}, \quad c_0 \in \mathbb{R}^N. \end{aligned} \tag{3.72}$$

With Ω_h a regular mesh as introduced before. For the time integration different implicit Runge-Kutta methods are used. A general Runge-Kutta time-integration method is given as

$$\begin{aligned} c_h &= \check{c} + \tau \sum_{l=1}^{s} b_l k_l \\ k_i &= \Delta_h \left(\check{c}_h + \tau \sum_{j=1}^{s} a_{ij} k_j \right) \end{aligned} \tag{3.73}$$

A comprehensive overview and introduction to different Runge-Kutta time-integration methods is available in [33], [54]. Here the Gauss-Legendre methods are applied as they are A-stable and can be used for the time-integration of stiff differential equations. Table 3.3 shows Butcher tableaus for the Gauss-Legendre methods of order two, four and six. According to [139], the stability functions are Padé approximations to the matrix exponential $\exp \tau\Delta_h$. For the introduced methods, they are

$$\begin{aligned} (2 - L)c_h &= (2 + L)\check{c}_h, \\ (12 - 6L + L^2)c_h &= (12 + 6L + L^2)\check{c}_h, \\ (120 - 60L + 12L^2 - L^3)c_h &= (120 + 60L + 12L^2 + L^3)\check{c}_h, \end{aligned} \tag{3.74}$$

where $L = \tau\Delta_h$. Given this description, the next time step can be explicitly calculated as $c_h = A\check{c}_h = \frac{2+L}{2-L}\check{c}_h$ in the first method. The application of such a fractional operator is done straight-forward by point-wise application of the convolution vector. For the operator A now follows

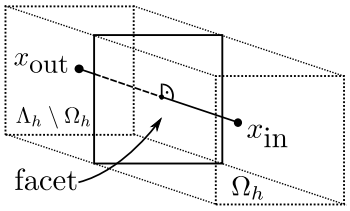

Figure 3.6: Grid cell centers $x_{\text{in}} \in \Lambda_h$ and $x_{\text{out}} \in \Omega_h \setminus \Lambda_h$. Boundary conditions are applied across the facet perpendicular to the line connecting both x_{in} and x_{out}.

$$A = \frac{2+L}{2-L} = \frac{2+\tau\Delta_h}{2-\tau\Delta_h} \quad \Rightarrow \quad \tilde{A} = \frac{2+\tau v_2}{2-\tau v_2}. \tag{3.75}$$

Using this

$$c_h = \mathcal{F}_h^{-1}\left(\frac{2+\tau v_2}{2-\tau v_2}\mathcal{F}_h\left(\check{c}_h\right)\right) \tag{3.76}$$

is the solution for the diffusion equation at the next time step.

3.4.4 Immersed interface method

Previously, periodic equations are considered. Now a solution of

$$\begin{aligned} -\Delta\phi(\boldsymbol{x}) &= f(\boldsymbol{x}), \qquad \boldsymbol{x} \in \Lambda, \\ \boldsymbol{n}\cdot\nabla\phi(\boldsymbol{x}) &= i(\boldsymbol{x}), \qquad \boldsymbol{x} \in \partial\Lambda, \end{aligned} \tag{3.77}$$

where $\Lambda \subset \Omega = (0, L_1) \times (0, L_2) \times (0, L_3)$, is given. The regular mesh Ω_h is applied and the variable ϕ_h is defined on Ω_h but may be discontinuous at $\partial\Lambda$. Additionally $\Lambda_h \coloneqq \Lambda \cap \Omega_h$. An extended equation system introduces additional variables for the discontinuous jumps across $\partial\Lambda$ [142].
A finite difference matrix $D \in \mathbb{R}^{N_{\text{IF}} \times N}$ and its transpose $\Psi = D^T$ are used to enforce the boundary conditions while still maintaining a valid solution of the differential equation inside the domain Ω_h[6].
Figure 3.6 introduces a pair of points $(x_{\text{in}}, x_{\text{out}}) \in \Lambda_h \times (\Omega_h \setminus \Lambda_h)$. Now, if an ordered set $I \subset \Lambda_h \times (\Omega_h \setminus \Lambda_h)$ of pairs of points with $|I| = N_{\text{IF}}$ is given, a finite difference matrix $D \in \mathbb{R}^{N_{\text{IF}} \times N}$ is defined as

[6] This is similar to solution methods where the solution is decomposed into a homogeneous and an inhomogeneous part.

$$D_{ij} = \begin{cases} \frac{1}{h} & \text{if } I_{i,1} = \boldsymbol{x}_j \in \Lambda_h, \\ -\frac{1}{h} & \text{if } I_{i,2} = \boldsymbol{x}_j \in \Omega_h \setminus \Lambda_h, \\ 0 & \text{else.} \end{cases} \tag{3.78}$$

Discrete Neumann boundary conditions can be enforced with this formulation with first order consistency[7] by incorporating correctional body forces g_h as

$$\begin{pmatrix} -\Delta_h & \Psi \end{pmatrix} \begin{pmatrix} \phi_h \\ g_h \end{pmatrix} = f_h. \tag{3.79}$$

The equations defining the jump conditions are given as

$$\begin{pmatrix} D & I_h \end{pmatrix} \begin{pmatrix} \phi_h \\ g_h \end{pmatrix} = i_h. \tag{3.80}$$

Therefore, the system of linear equations is

$$\begin{pmatrix} -\Delta_h & \Psi \\ D & I_h \end{pmatrix} \begin{pmatrix} \phi_h \\ g_h \end{pmatrix} = \begin{pmatrix} f_h \\ i_h \end{pmatrix}. \tag{3.81}$$

This linear system has $N + N_{\mathrm{IF}}$ unknowns. By linear transformation (Uzawa algorithm or Schur complement [135]) the following equation for g_h is obtained,

$$(I + D\Delta_h^{-1}\Psi)g_h = i_h + D\Delta_h^{-1} f_h, \tag{3.82}$$

and by this the solution is

$$\phi_h = -\Delta_h^{-1}(f_h - \Psi i_h). \tag{3.83}$$

This linear equation can be solved with an iterative algorithm such as conjugate gradient[9]. Similar considerations lead to a solution for the diffusion equation,

$$\begin{aligned} \partial_t c(\boldsymbol{x}, t) &= \Delta c(\boldsymbol{x}, t), & (\boldsymbol{x}, t) &\in \Lambda \times T, \\ \boldsymbol{n} \cdot \nabla c(\boldsymbol{x}, t) &= f(\boldsymbol{x}, t), & (\boldsymbol{x}, t) &\in \partial\Lambda \times T, \\ c(\boldsymbol{x}, 0) &= c_0, & \boldsymbol{x} &\in \Lambda. \end{aligned} \tag{3.84}$$

The same interpolation matrices D and Ψ can be applied for the pure Neumann boundary problem after the spatial discretization with mesh Ω_h and discretization in time with time step size τ.

[7] For higher convergence orders, other pairs of D and Ψ are required, see [142].

3.5 Cahn-Hilliard equation

In this section, fast solution methods for the Cahn-Hilliard equation are discussed. First, a first-order method for the periodic Cahn-Hilliard equation is presented in Subsection 3.5.1. Then the immersed interface method is given in Subsection 3.5.2. The solution of the linear system is accelerated by a preconditioner in Subsection 3.5.3. Finally, a second-order method for the periodic Cahn-Hilliard equation is presented in Subsection 3.5.4.

3.5.1 Solution of the periodic Cahn-Hilliard equation

The periodic Cahn-Hilliard equation is written as a system of two second-order partial differential equations [14]. The equations for the non-dimensional phase-field parameter $p : \Omega \times T \mapsto \mathbb{R}$ and a non-dimensional chemical potential $\mu : \Omega \times T \mapsto \mathbb{R}$ are

$$\begin{aligned}
\partial_t p(\boldsymbol{x},t) &= G\Delta\mu(\boldsymbol{x},t), && (\boldsymbol{x},t) \in \Omega \times T,\\
\mu(\boldsymbol{x},t) &= \frac{1}{L}\left(p(\boldsymbol{x},t)^3 - p(\boldsymbol{x},t)\right) + L\Delta p(\boldsymbol{x},t), && (\boldsymbol{x},t) \in \Omega \times T,\\
\boldsymbol{n}\cdot\nabla p(\boldsymbol{x},t) &= \boldsymbol{n}\cdot\nabla p(\boldsymbol{x}+L_i,t), && \boldsymbol{x},\boldsymbol{x}+L_i\boldsymbol{e}_i \in \Gamma,\\
\boldsymbol{n}\cdot\nabla \mu(\boldsymbol{x},t) &= \boldsymbol{n}\cdot\nabla \mu(\boldsymbol{x}+L_i,t), && \boldsymbol{x},\boldsymbol{x}+L_i\boldsymbol{e}_i \in \Gamma.\\
p(\boldsymbol{x},0) &= p_0, && \text{in } \Omega, t=0.
\end{aligned} \tag{3.85}$$

The bulk potential $p^3 - p$ is split into the convex and concave parts of the corresponding energy $F(p)$. The part p^3 is integrated semi-implicitly as $\check{p}^2 p$, the part $-p$ is integrated explicitly as $\check{p}$. With this linearization it is assured that the enthalpy of the associated physical system is declining and the solution for the phase-field parameter does not diverge [71], [42]. For the spatial discretization the regular mesh Ω_h is chosen again. The system of linear equations of size $2N$ for the unknowns p_h and μ_h is then given by

$$\begin{pmatrix} L\Delta_h - \frac{1}{L}\check{p}_h^2 & I_h \\ I_h & -\tau G\Delta_h \end{pmatrix} \begin{pmatrix} p_h \\ \mu_h \end{pmatrix} = \begin{pmatrix} -\frac{1}{L}\check{p}_h \\ \check{p}_h \end{pmatrix}. \tag{3.86}$$

Now a unconditionally gradient stable discretization of the Cahn-Hilliard equation system is defined that requires only one solution of a system of linear equations for each time step. Compare this to a Newton-Raphson scheme that would require several assemblies of the Jacobian matrix and the solution of several system of linear equationss to obtain the Newton correction steps.

3.5.2 Immersed interface method

Previously, periodic equations are considered. Now a solution of

$$
\begin{aligned}
\partial_t p(\boldsymbol{x},t) &= G\Delta\mu(\boldsymbol{x},t), && (\boldsymbol{x},t)\in\Lambda\times T,\\
\mu(\boldsymbol{x},t) &= \frac{1}{L}\left(p(\boldsymbol{x},t)^3 - p(\boldsymbol{x},t)\right) + L\Delta p(\boldsymbol{x},t), && (\boldsymbol{x},t)\in\Lambda\times T,\\
\boldsymbol{n}\cdot\nabla\mu(\boldsymbol{x},t) &= r_\mu(\boldsymbol{x},t), && (\boldsymbol{x},t)\in\partial\Lambda\times T,\\
\boldsymbol{n}\cdot\nabla p(\boldsymbol{x},t) &= r_p(\boldsymbol{x},t), && (\boldsymbol{x},t)\in\partial\Lambda\times T,\\
p(\boldsymbol{x},0) &= p_0, && (\boldsymbol{x},t)\in\Lambda\times\{0\},
\end{aligned}
\tag{3.87}
$$

where $\Lambda\subset\Omega=(0,L_1)\times(0,L_2)\times(0,L_3)$ is given.
In Subsection 3.4.4, matrices D and Φ are introduced. For the Cahn-Hilliard equation this yields

$$
\begin{pmatrix}
L\Delta-\frac{1}{L}\check{p}^2 & I_h & -L\Psi & 0\\
I_h & -\tau G\Delta & 0 & \tau G\Psi\\
D & 0 & I_h & 0\\
0 & D & 0 & I_h
\end{pmatrix}
\begin{pmatrix} p\\ \mu\\ g_p\\ g_\mu \end{pmatrix}
=
\begin{pmatrix} -\frac{1}{L}\check{p}\\ \check{p}\\ r_p\\ r_\mu \end{pmatrix}.
\tag{3.88}
$$

The chemical potential μ is now eliminated from the system as

$$
\begin{pmatrix}
I_h+\tau GL\Delta\Delta-\tau\frac{G}{L}\Delta\check{p}^2 & -\tau GL\Delta\Psi & \tau G\Psi\\
D & I & 0\\
-LD\Delta+\frac{1}{L}D\check{p}^2 & LD\Psi & I
\end{pmatrix}
\begin{pmatrix} p\\ g_p\\ g_\mu \end{pmatrix}
=
\begin{pmatrix} \check{p}+\tau\frac{G}{L}\Delta\check{p}\\ r_p\\ r_\mu+D\frac{1}{L}\check{p} \end{pmatrix}
\tag{3.89}
$$

The system can be written shortly by using the symbols defined in Table 3.4

$$
\begin{pmatrix} A_E & \Psi_E\\ D_E & I_E \end{pmatrix}
\begin{pmatrix} p\\ g \end{pmatrix}
=
\begin{pmatrix} r_1\\ r_2 \end{pmatrix},
\tag{3.90}
$$

This linear system has $N+2N_{\mathrm{IF}}$ unknowns. Again, the Uzawa algorithm leads to the simplified equation system

$$
(I_E - D_E A_E^{-1}\Psi_E)g = r_2 - D_E A_E^{-1} r_1.
\tag{3.91}
$$

After the jump variables g are calculated, the phase-field parameter solution p is received as

$$
p = A_E^{-1}(r_1 - \Psi_E g).
\tag{3.92}
$$

The linear operator in (3.91) is non-symmetric and therefore a stabilized bi-conjugate gradient method [9] is chosen.

Symbol	A_E	Ψ_E	
Operator	$\left(I_h + \tau GL\Delta_h\Delta_h - \tau\frac{G}{L}\Delta_h\check{p}^2\right)$	$\begin{pmatrix}-\tau GL\Delta_h\Psi & \tau G\Psi\end{pmatrix}$	
Symbol	D_E	I_E	
Operator	$\begin{pmatrix} D \\ -LD\Delta_h \end{pmatrix}$	$\begin{pmatrix} I & 0 \\ LD\Psi & I \end{pmatrix}$	
Symbol	r_1	r_2	g
Operator	$\left(\check{p} + \tau\frac{G}{L}\Delta\check{p}\right)$	$\begin{pmatrix} r_p \\ r_\mu + D\frac{1}{L}\check{p} \end{pmatrix}$	$\begin{pmatrix} g_p \\ g_\mu \end{pmatrix}$

Table 3.4: Abbreviation of linear operators

3.5.3 Preconditioner

The Fourier representation of the discrete Laplace operator Δ_h^{-1} has been introduced. However, for the discrete operator A_E^{-1} no Fourier representation is easily available because it is not a operator with constant coefficients,

$$A_E = I_h + \tau GL\Delta_h\Delta_h - \tau\frac{G}{L}\Delta_h\check{p}^2. \tag{3.93}$$

The vector $\check{p}^2$ is not a constant coefficient. It is possible to give a Fourier representation of

$$A_{E0} = I_h + \tau GL\Delta_h\Delta_h - \tau\frac{G}{L}\bar{p}^2\Delta_h, \tag{3.94}$$

because the value $\bar{p}^2$ is a constant coefficient. The operator A_{E0} is defined as a preconditioner to accelerate the convergence of the inner iterative algorithm [42], [41]. Instead of solving the system of linear equations $A_E u_h = y$, the system of linear equations

$$A_{E0}^{-1}A_E = A_{E0}^{-1}y, \tag{3.95}$$

is solved. A practical preconditioner has to fulfill two conditions. First, the inversion of a preconditioner must be faster than the inversion of the original matrix in order to simplify the calculation. Second, it has to reduce the condition of the system matrix significantly, cond $A_{E0}^{-1}A_E \ll$ cond A_E. The operator A_E depends on the spatial grid width h. A preconditioner may also resolve the dependence of the matrix condition number on the spatial gridwidth h. The homogenization parameter $\bar{p}^2$ is chosen as the arithmetic mean of $\check{p}^2$. The inverse of A_{E0} is easily available with the presented Fourier methods. The second qualifying property, the reduction of the condition number of the pre-conditioned system is studied in 4.2.5.2.

3.5.4 Second-order time integration of the Cahn-Hilliard equation

The previously presented time integration methods guarantee higher-order convergence for the Poisson equation and the diffusion equation. A higher-order integration scheme for the Cahn-Hilliard equation is more complicated to derive as the non-linearity has to be treated in a special way such that the convergence order is not lost. In [35] it is shown that the solution to the Cahn-Hilliard is smooth, if the initial data is smooth up to a certain degree. Several methods have been proposed [42, 57] for a second-order time integration. In [17] it is noted that it is not only important to achieve the consistency order but also to preserve stability regarding the energy of the system.
In [57] a predictor-corrector method is proposed in order to receive a second-order scheme. An interpolation to the chemical potential $\mu(p)$ is introduced as $\mu^0(q,r)$,

$$\begin{aligned} \mu(p) &= p^3 - p \\ \mu^0(q,r) &= \frac{(q+r)(q^2+r^2-2)}{4}. \end{aligned} \tag{3.96}$$

Given a discretization on the regular mesh Ω_h of periodic Cahn-Hilliard equation in (3.85), the method is defined with an intermediate solution $p_{\frac{1}{2}}$

$$\begin{aligned} (2+\tau GL\Delta_h^2)p_{\frac{1}{2}} &= (2-\tau GL)\check{c} + \frac{2\tau G}{L}\Delta_h \mu_{\text{bulk}}(\check{p}) \\ (2+\tau GL\Delta_h^2)p_h &= (2-\tau GL)\check{c} + \frac{2\tau G}{L}\Delta_h \mu^0_{\text{bulk}}(\check{p}, p_{\frac{1}{2}}) \end{aligned} \tag{3.97}$$

The operator $(2+\tau GL\Delta_h^2)$ has a Fourier representation and the integration can be carried out without an iterative algorithm.

Chapter 4

Examples and applications

In this chapter, the introduced numerical models are applied. In Section 4.1, different properties of a phase-field method are analyzed. Section 4.2 establishes the numerical convergence of the fast solvers and the immersed interface method. In Section 4.3, the generation of spherical packing microstructures is discussed. In Section 4.4, the focus is on the electro-chemical model. Finally, Section 4.5 applies a fully-coupled electro-chemo-mechanical model and analyzes complex 3D microstructures.

4.1 Properties of phase-field methods

In this section, different phase-field potentials are analyzed. First properties of the logarithmic phase-field potential are analytically derived in Subsection 4.1.1. Then the formation of a phase-separated state in a polynomial phase-field is investigated in Subsection 4.1.2. The energy of different states is approximated in Subsectiosn 4.1.3 and 4.1.4 and compared to a numerical simulation in Subsection 4.1.5.

4.1.1 Analysis of the logarithmic phase-field potential

An alternative representation of the chemical phase-field potential μ is derived in terms of the interface width L and the interface energy density G as presented in [118].
With the free energy F_0 in (2.24) and the mixing enthalpy q given in Table 2.2, the minima of the free energy can be derived from the equation $F_0'(p) = 0$ as $p_1 \approx 0.013$ and $p_2 \approx 0.987$. The corresponding equilibrium concentrations are $c_1 \approx 0.013 c_{\max,\mathrm{c}}$ and $c_2 = c_{\max,\mathrm{c}} - c_1 \approx 0.987 c_{\max,\mathrm{c}}$. A shifted free energy $\Delta F_0(p) = F_0(p) - F_0(p_1)$ allows to define the activation energy needed during a phase-transformation between the equilibrium states p_1 and p_2 as an integral. The coefficients in (2.25) can be identified with corresponding values given in [148] as

$$\alpha L_0^2 \frac{G}{L} = 1, \quad \beta G L = \frac{\kappa}{L_0^2 c_{\max,\mathrm{c}} N_A R T}. \tag{4.1}$$

With this and the use of the Euler-Lagrange equations, the phase-field interface energy and length G and L are calculated as

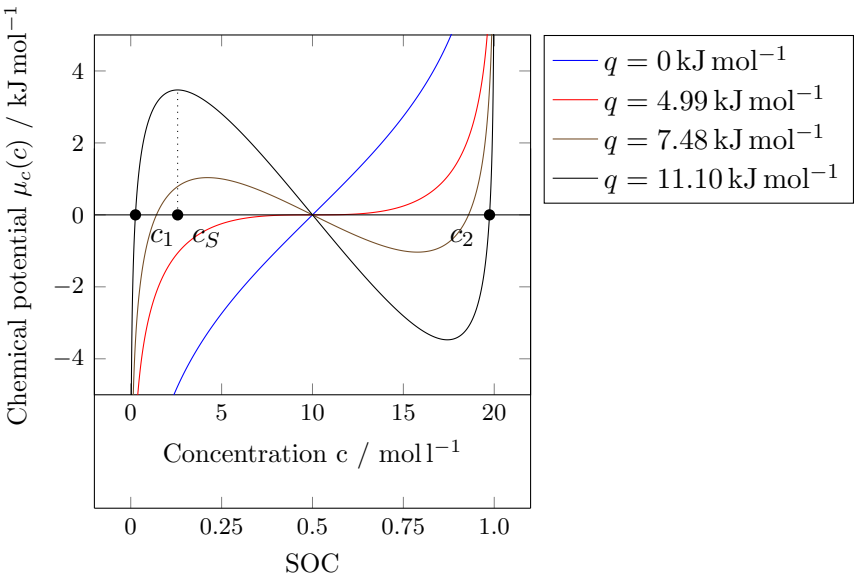

Figure 4.1: Bulk chemical potential $\mu_c(c)$ for different values of the phase-field enthalpy q. Equilibrium concentrations c_1 and c_2 and maximizing concentration c_S are depicted for the value $q = 11.10\,\mathrm{kJ\,mol^{-1}}$.

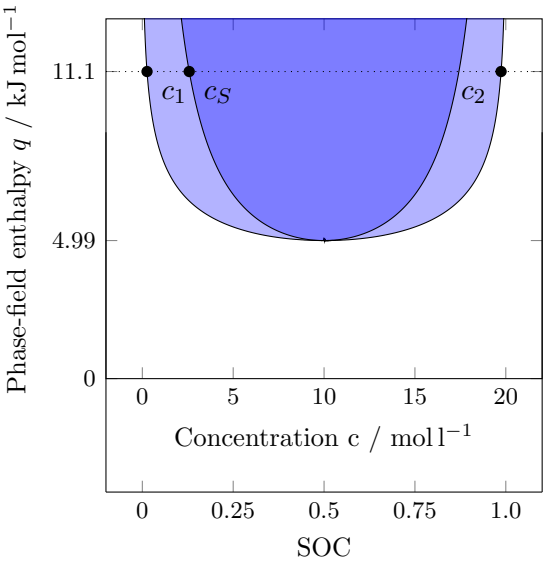

Figure 4.2: The phase diagram with curves denoting the equilibrium concentrations c_1 and c_2 (outer) and the point of spontaneous spinodal decomposition c_S (inner).

$$
\begin{aligned}
G &= \frac{1}{L_0}\sqrt{2\frac{\kappa}{L_0^2 c_{\max,\mathrm{c}} N_A RT}}\int_{p_1}^{p_2}\sqrt{\Delta F_0(p)}dp \approx 2.09\cdot 10^{-7}\mathrm{cm}^{-1},\\
L &= L_0(p_2-p_1)\sqrt{\frac{\kappa}{2L_0^2 c_{\max,\mathrm{c}} N_A RT\Delta F_0(0.5)}} \approx 3.33\cdot 10^{-7}\mathrm{cm}.
\end{aligned}
\tag{4.2}
$$

The free energy F_0 is non-dimensional in this formulation. See (2.26) where the chemical potential is given in terms of RT. Therefore, the unit of G is cm^{-1}. The scalar parameters α and β are deduced as

$$
\alpha \approx 1.593\cdot 10^{-14}, \quad \beta \approx 1.444\cdot 10^{10} \tag{4.3}
$$

The application of a phase-field method requires a fine discretization of the interface width. From the interface width being $L = 3.3$ nm, it can be concluded that the spatial discretization size should not be larger than $h \approx 1$ nm. With this grid size the interface between the different phases is at least resolved with three voxels.
Figure 4.1 shows the influence of the mixing enthalpy parameter q in (2.26) on the bulk chemical potential,

$$
\mu_{c,\mathrm{bulk}}(c) = F_0'(p) = RT\log\frac{c}{c_{\max,\mathrm{c}}-c} + q\left(1-2\frac{c}{c_{\max,\mathrm{c}}}\right). \tag{4.4}
$$

For a value of $q < q_{\mathrm{crit}} = 4.99\mathrm{kJ\,mol}^{-1}$ the chemical potential is monotonic [149]. There are no extrema and no phase separation will occur. For $q > q_{\mathrm{crit}}$ two stable phases exist with equilibrium concentrations given by the root marks. An over-saturated SOC between the equilibrium concentration $c_1 \approx 0.013 c_{\max,\mathrm{c}}$ and the concentration $c_S \approx 0.12 c_{\max,\mathrm{c}}$, where F_0' attains a local maximum, gives rise to a spinodal decomposition. The value c_S is given by

$$
\frac{\partial^2}{\partial p^2}F_0\left(\frac{c_S}{c_{\max,\mathrm{c}}}\right) = 0. \tag{4.5}
$$

In this domain, small perturbations lead to phase separation into a lithium-poor phase with concentration c_1 and a lithium-rich phase with concentration $c_2 = c_{\max,\mathrm{c}} - c_1$. Figure 4.2 shows the regions where spontaneous spinodal decomposition is possible (light blue) and where spinodal decomposition is inevitable (dark blue), depending on both the SOC and the phase field enthalpy. A dotted line indicates the value $q = 11.10\,\mathrm{kJ\,mol}^{-1}$.

4.1.2 Phase-field energy

A polynomial double-well potential is analyzed for characteristic length scales of the phase separation. The energy content of two different states is approximated. The first state is a spatially homogenous state where the concentration is constant in space. The

second is a state where the available mass is concentrated in a single spherical particle and an equilbrium interface between enriched phase and devoid phase is built.
Let F_0^* a bulk energy density and F_1^* a gradient energy density,

$$\begin{aligned} F_0^* &= \frac{1}{4}(p-1)^2(p+1)^2, \\ F_1^* &= \frac{1}{2}||\nabla p||^2. \end{aligned} \tag{4.6}$$

The total energy density F is then the sum of both densities

$$F = \alpha F_0^* + \beta F_1^* \tag{4.7}$$

and the total energy in the domain is defined as the spatial integral,

$$E = \int_\Omega F(\boldsymbol{x})\mathrm{d}\boldsymbol{x}. \tag{4.8}$$

Instead of parameters α and β, the energy is written with interface energy G and interface length L. Again, the Euler-Lagrange equations are applied. The result is $\alpha = 3\frac{G}{L}$ and $\beta = \frac{3}{8}GL$. The Cahn-Hilliard equation is then given as

$$\partial_t p(\boldsymbol{x},t) = -\frac{3}{2}GL\Delta\Delta p(\boldsymbol{x},t) + 3\frac{G}{L}\Delta(p^3(\boldsymbol{x},t)) - p(\boldsymbol{x},t)). \tag{4.9}$$

In $\Omega = \mathbb{R}$ an equilibrium solution to this equation is given as $p(x) = \tanh\frac{x}{L}$. With $\partial_x \tanh x = 1 - \tanh^2 x$,

$$\begin{aligned} &-\frac{3}{2}GL\Delta\Delta\left(\tanh\frac{x}{L}\right) + 3\frac{G}{L}\Delta\left[\left(\tanh\frac{x}{L}\right)^3 - \left(\tanh\frac{x}{L}\right)\right] \\ &= 3\frac{G}{L}\Delta\left(-\frac{L^2}{2}\Delta\left(\tanh\frac{x}{L}\right) + \tanh^3\frac{x}{L} - \tanh\frac{x}{L}\right) \\ &= 3\frac{G}{L}\Delta\left(-\frac{L}{2}\partial_x\left(1-\tanh^2\frac{x}{L}\right) + \tanh^3\frac{x}{L} - \tanh\frac{x}{L}\right) \\ &= 3\frac{G}{L}\Delta\left(\frac{1}{2}\left(2\tanh\frac{x}{L}\left(1-\tanh^2\frac{x}{L}\right)\right) + \tanh^3\frac{x}{L} - \tanh\frac{x}{L}\right) \\ &= 3\frac{G}{L}\Delta\left(\tanh\frac{x}{L}\left(1-\tanh^2\frac{x}{L}\right) + \tanh^3\frac{x}{L} - \tanh\frac{x}{L}\right) \\ &= 3\frac{G}{L}\Delta\left(\tanh\frac{x}{L} - \tanh^3\frac{x}{L} + \tanh^3\frac{x}{L} - \tanh\frac{x}{L}\right) \\ &= 3\frac{G}{L}\Delta\left(0\right) = 0, \end{aligned} \tag{4.10}$$

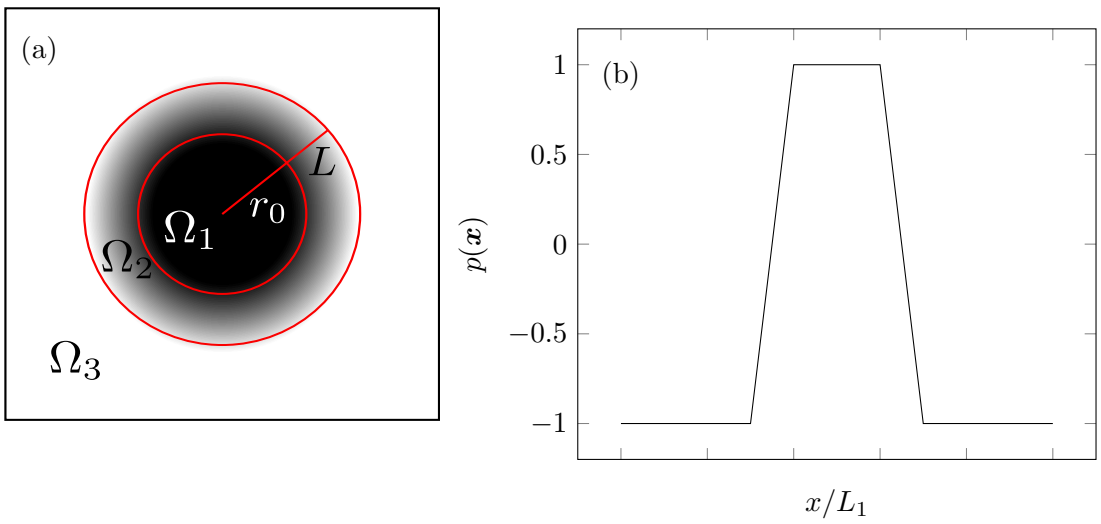

Figure 4.3: (a) A box domain with a phase-field droplet in domain Ω_1 where $p = 1$ with radius r_0 and the interfacial domain Ω_2 with interface width L. Domain Ω_3 denotes the region where $p = -1$. (b) A plot of the phase-field along a line through the center of the droplet.

and therefore $\partial_t p(\boldsymbol{x}, t) = 0$ and $p(x) = \tanh \frac{x}{L}$ is an equilibrium solution. In bounded domains or for more-dimensional domains, there is no such simple solution, although series evolution formulas can be derived [138].

4.1.3 Spherical particle

Let $\Omega = (0, L_1)^2$. Figure 4.3 (a) defines a circular region with $p(\boldsymbol{x}) = 1$ at the center $\boldsymbol{x}_0 = (L_1/2, L_1/2)$. Figure 4.3 (b) shows a line plot of the phase-field along a line through the center of the droplet. Polar coordinates at the center $\boldsymbol{x}_0$ are introduced as $r = ||\boldsymbol{x} - \boldsymbol{x}_0||$ and $\tan \lambda = \frac{x_2}{x_1}$. Three domains are distinguished as

$$\begin{aligned} \Omega_1 &= \{(r, \lambda) \in \Omega | r < r_0\}, \\ \Omega_2 &= \{(r, \lambda) \in \Omega | r_0 < r < r_0 + L\}, \\ \Omega_3 &= \Omega \setminus (\Omega_1 \cup \Omega_2). \end{aligned} \tag{4.11}$$

The areas of the domains are

$$
\begin{aligned}
|\Omega_1| &= \pi r_0^2, \\
|\Omega_2| &= \int_{r_0}^{r_0+L} r \mathrm{d}r\mathrm{d}\lambda = \pi((r_0+L)^2 - r_0^2) = \pi L(L+2r_0), \\
|\Omega_3| &= L_1^2 - \pi(r_0+L)^2.
\end{aligned} \tag{4.12}
$$

The phase-field parameter $p(r,\lambda)$ is then given as

$$
p(r,\lambda) = p(r) = \begin{cases} 1, & \text{for } (r,\lambda) \in \Omega_1, \\ 1 - 2\frac{r-r_0}{L}, & \text{for } (r,\lambda) \in \Omega_2, \\ -1, & \text{for } (r,\lambda) \in \Omega_3. \end{cases} \tag{4.13}
$$

The phase interface has length L as it changes from 1 to -1 in length L. The gradient is given as $||\nabla p|| = \frac{2}{L}$ in the interface domain. Both F_0^* and F_1^* are zero in Ω_1 and Ω_3. The energy in Ω_2 is calculated as

$$
\begin{aligned}
\int_{\Omega_2} F_0^*(r)\mathrm{d}r\mathrm{d}\lambda &= 2\pi\alpha \int_{r_0}^{r_0+L} \frac{1}{4} r(p(\boldsymbol{x})-1)^2(p(\boldsymbol{x})+1)^2 \mathrm{d}r \\
&= 2\pi\alpha \cdot \int_{r_0}^{r_0+L} \frac{1}{4} r(1 - 2\frac{r-r_0}{L} - 1)^2(1 - 2\frac{r-r_0}{L} + 1)^2 \mathrm{d}r \\
&= 2\pi\alpha \cdot \frac{1}{15} L(2r_0 + L).
\end{aligned} \tag{4.14}
$$

The contribution of gradient energy density F_1^* in Ω_2 is calculated as

$$
\begin{aligned}
\int_{\Omega_2} F_1^*(r)\mathrm{d}r\mathrm{d}\lambda &= 2\pi\beta \int_{r_0}^{r_0+L} r \frac{1}{2} ||\nabla p(\boldsymbol{x})||^2 \mathrm{d}r \\
&= 2\pi\beta \int_{r_0}^{r_0+L} r \frac{1}{2} \frac{4}{L^2} \mathrm{d}r = 2\pi\beta \left(\frac{2r_0}{L} + 1 \right).
\end{aligned} \tag{4.15}
$$

Now the total energy by plugging in α and β is given as

$$
\begin{aligned}
E &= 2\pi\alpha \frac{1}{15} L(2r_0 + L) + 2\pi\beta \left(\frac{2r_0}{L} + 1 \right) \\
&= 2\pi 3 \frac{G}{L} \frac{1}{15} L(2r_0 + L) + 2\pi \frac{3}{8} GL \left(\frac{2r_0}{L} + 1 \right) = \frac{23}{20} \pi G(2r_0 + L).
\end{aligned} \tag{4.16}
$$

4.1.4 Equally distributed

The integral of the phase-field over Ω is called mass M. It is given as

$$\begin{aligned} M &= \int_{\Omega} p(\boldsymbol{x})\mathrm{d}\boldsymbol{x} \\ &= \int_{\Omega_1} p(\boldsymbol{x})\mathrm{d}\boldsymbol{x} + \int_{\Omega_2} rp(r,\lambda)\mathrm{d}r\mathrm{d}\theta + \int_{\Omega_3} p(\boldsymbol{x})\mathrm{d}\boldsymbol{x} \\ &= 1 \cdot |\Omega_1| + 2\pi \int_{r_0}^{r_0+L} r\left(1 - 2\frac{r-r_0}{L}\right)\mathrm{d}r + (-1)\cdot|\Omega_3| \\ &= \pi r_0^2 + 2\pi\left(-\frac{L^2}{6}\right) - (L_1^2 - \pi(r_0+L)^2) \\ &= \pi r_0^2 - \frac{\pi}{3}L^2 - L_1^2 + \pi(r_0+L)^2 \end{aligned} \tag{4.17}$$

With this mass, it follows for the equilibrium state of an equally distributed phase-field parameter

$$p(\boldsymbol{x}) = \frac{M}{L_1^2}, \quad ||\nabla p(\boldsymbol{x})|| = 0, \quad \forall \boldsymbol{x} \in \Omega. \tag{4.18}$$

The energy of this configuration depending on M is

$$\begin{aligned} E(r_0) &= \int_{\Omega} F_0^*(\boldsymbol{x})\mathrm{d}\boldsymbol{x} = \frac{\alpha}{4}\int_{\Omega}(p(\boldsymbol{x})-1)^2(p(\boldsymbol{x})+1)^2\mathrm{d}\boldsymbol{x} \\ &= \frac{\alpha}{4}\int_{\Omega}(p(\boldsymbol{x})^2-1)^2\mathrm{d}\boldsymbol{x} = \frac{\alpha}{4}\int_{\Omega}(\frac{M^2}{L_1^4}-1)^2\mathrm{d}\boldsymbol{x} \\ &= \frac{\alpha}{4}L_1^2(\frac{M^2}{L_1^4}-1)^2 = \frac{\alpha}{4L_1^6}(M^2-L_1^4)^2 \\ &= \frac{\alpha}{4L_1^6}((\pi r_0^2 - \frac{\pi}{3}L^2 - L_1^2 + \pi(r_0+L)^2)^2 - L_1^4)^2. \end{aligned} \tag{4.19}$$

The mimimum sustainable radius for phase separation can now be calculated by comparing (4.16) and (4.19),

$$\frac{23}{20}\pi G(2r_0+L) = \frac{3G}{4LL_1^6}((\pi r_0^2 - \frac{\pi}{3}L^2 - L_1^2 + \pi(r_0+L)^2)^2 - L_1^4)^2. \tag{4.20}$$

Table 4.1 gives numerical solutions to this equation for several combinations of L and L_1.

L_1	L	r_0	E
1	0.1	0.147	1.277
2	0.1	0.253	2.191
1	0.05	0.126	1.096
2	0.05	0.212	1.710

Table 4.1: Estimates of the minimum radius for a sustainable stable spherical droplet depending on the size of the domain and the phase-field interface width.

4.1.5 Numerical example

The mesh Ω_h is applied with $N_1 = N_2 = 100$ and $\tau = 0.001$. Algorithm NWT is used for the solution of the system. Choose the domain size $L_1 \in \{1, 2\}$, the phase-field interface width $L \in \{0.05, 0.1\}$ and the radius r_0 of the initial circle $p = 1$ is varied. Only small radii $r_0 \ll L_1$ are valid. Larger radii result in boundary effects that have not been taken into account.
Table 4.1 evaluates the estimate for the minimum sustainable radius in (4.20). Figure 4.4 gives plots for the energy content in equilibrium states. Plotted is the energy content of a spherical-particle state, the energy content of a equally-distributed state and the energy content of the numerical simulation. The numerical simulation validates the estimate of Table 4.1.

4.2 Convergence of fast solvers

In this section, the introduced numerical methods from Sections 3.4 and 3.5 are evaluated. First, the convergence for the periodic Poisson equation is shown in Subsection 4.2.1 and for the diffusion equation in Subsection 4.2.2. This process is repeated for the IIM in Subsections 4.2.3 and 4.2.4. Lastly, the IIM for the Cahn-Hilliard equation is discussed in detail in Subsection 4.2.5.

4.2.1 Convergence for the numerical methods for the periodic Poisson equation

Seven different numerical methods are evaluated. FD2, FD4, and FD6 denote matrix methods. A sparse matrix A is assembled with finite difference stencils of order two, four and six. Then a direct solver is applied to the system of linear equations. In 1D, A is a periodic band-matrix, called Toeplitz matrix [70], while for two and three dimensions it is a band matrix with bandwidth N and N^2, respectively. DFT2, DFT4, and DFT6 denote matrix-free methods. Here the same finite differences stencils are applied. However, the solution of the system of linear equations is done in Fourier space as introduced before.

Dim.	Symbol	Definition
1	ϕ	$e^{\sin(a_1 x)}$
	ϕ_x	$a_1 e^{\sin(a_1 x)} \cos(a_1 x)$
	f	$-a_1^2 e^{\sin(a_1 x)} \left(\sin(a_1 x) - \cos^2(a_1 x)\right)$
	f_x	$a_1^3 e^{\sin(a_1 x)} \cos(a_1 x) \left(-3\sin(a_1 x) + \cos^2(a_1 x) - 1\right)$
2	ϕ	$e^{\sin(a_1 x)+\sin(a_2 y)}$
	ϕ_x	$a_1 \cos(a_1 x) e^{\sin(a_1 x)+\sin(a_2 y)}$
	ϕ_y	$a_2 \cos(a_2 y) e^{\sin(a_1 x)+\sin(a_2 y)}$
	f	$e^{\sin(a_1 x)+\sin(a_2 y)}$ $\times(-a_1^2 \sin(a_1 x) + a_1^2 \cos^2(a_1 x) - a_2^2 \sin(a_2 y) + a_2^2 \cos^2(a_2 y))$
	f_x	$a_1 \cos(a_1 x) e^{\sin(a_1 x)+\sin(a_2 y)}$ $\times \left(-3a_1^2 \sin(a_1 x) + a_1^2 \cos^2(a_1 x) - a_1^2 - a_2^2 \sin(a_2 y) + a_2^2 \cos^2(a_2 y)\right)$
	f_y	$a_2 \cos(a_2 y) e^{\sin(a_1 x)+\sin(a_2 y)}$ $\times \left(-a_1^2 \sin(a_1 x) + a_1^2 \cos^2(a_1 x) - 3a_2^2 \sin(a_2 y) + a_2^2 \cos^2(a_2 y) - a_2^2\right)$
3	ϕ	$e^{\sin(a_1 x)+\sin(a_2 y)+\sin(a_3 z)}$
	ϕ_x	$a_1 \cos(a_1 x) e^{\sin(a_1 x)+\sin(a_2 y)+\sin(a_3 z)}$
	ϕ_y	$a_2 \cos(a_2 y) e^{\sin(a_1 x)+\sin(a_2 y)+\sin(a_3 z)}$
	ϕ_z	$a_3 \cos(a_3 z) e^{\sin(a_1 x)+\sin(a_2 y)+\sin(a_3 z)}$
	f	$e^{\sin(a_1 x)+\sin(a_2 y)+\sin(a_3 z)}(-a_1^2 \sin(a_1 x) + a_1^2 \cos^2(a_1 x) - a_2^2 \sin(a_2 y) + a_2^2 \cos^2(a_2 y) - a_3^2 \sin(a_3 z) + a_3^2 \cos^2(a_3 z))$
	f_x	$a_1 \cos(a_1 x) e^{\sin(a_1 x)+\sin(a_2 y)+\sin(a_3 z)}$ $\times(-3a_1^2 \sin(a_1 x) + a_1^2 \cos^2(a_1 x) - a_1^2 - a_2^2 \sin(a_2 y) + a_2^2 \cos^2(a_2 y) - a_3^2 \sin(a_3 z) + a_3^2 \cos^2(a_3 z))$
	f_y	$a_2 \cos(a_2 y) e^{\sin(a_1 x)+\sin(a_2 y)+\sin(a_3 z)}$ $\times(-a_1^2 \sin(a_1 x) + a_1^2 \cos^2(a_1 x) - 3a_2^2 \sin(a_2 y) + a_2^2 \cos^2(a_2 y) - a_2^2 - a_3^2 \sin(a_3 z) + a_3^2 \cos^2(a_3 z))$
	f_z	$a_3 \cos(a_3 z) e^{\sin(a_1 x)+\sin(a_2 y)+\sin(a_3 z)}$ $\times(-a_1^2 \sin(a_1 x) + a_1^2 \cos^2(a_1 x) - a_2^2 \sin(a_2 y) + a_2^2 \cos^2(a_2 y) - 3a_3^2 \sin(a_3 z) + a_3^2 \cos^2(a_3 z) - a_3^2)$

Table 4.2: Analytic solution for the periodic Poisson equation. Parameter values are $a_1 = 2\pi$, $a_2 = 3\pi$ and $a_3 = 4\pi$.

Dimension	FD2	FD4	FD6	DFT2	DFT4	DFT6	CFT
1	1.98	3.86	5.69	1.97	3.94	5.74	16.35
2	1.98	3.94	5.72	1.99	3.95	5.78	15.43
3	2.09	3.39	5.22	2.05	3.69	5.56	15.30

Table 4.3: Convergence rates for the periodic Poisson equation.

Analytically, the solution of FD2 and DFT2 are supposed to be identical[1]. Numerical cancellation may be an issue for differences between the algorithms. CFT also denotes a matrix-free method. Here the Fourier polynomials are applied for the integration. The Gibbs overshoot does not apply as the functions are infinitely smooth. Concerning numerical effort, the following can be said: The assembly and solution of a linear system (FD2,FD4,FD6) takes more time than a pair of Fourier transforms and a point-wise product of two vectors, matrices or 3D tensors (DFT2,DFT4,DFT6,CFT). Usually it also requires more memory.
In order to receive an analytic solution for the periodic Poisson equation (3.69), the method of manufactured solutions is used. Choose $\Omega = (0, 1)^3$. The functions chosen for the evaluation of the methods have to be periodic, infinitely smooth, and possess non-trivial Fourier-space representation. In [132] a 1D example is introduced by the composition of an exponential function with a trigonometric function. Such a function fulfills all mentioned requirements. Table 4.2 gives the function $\phi(\boldsymbol{x})$ and Figure 4.5 shows the solution in 1D. Given a mesh Ω_h, the error is calculated as the discrete L_2-norm,

$$e = ||\phi_h - \phi||_2 = \sqrt{\frac{1}{N} \sum_{\boldsymbol{x}_h \in \Omega_h} |\phi_h(\boldsymbol{x}_h) - \phi(\boldsymbol{x}_h)|^2}. \tag{4.21}$$

Figure 4.6 shows convergence plots. Additionally each plot denotes three dotted lines that correspond to convergence of order 2, 4 and 6. The matrix-based finite difference method FD and the discrete Fourier method DFT of a specific order are identical. For this reason the plots are expected to overlap for these pairs. As derived before, the CFT has spectral accuracy and therefore the convergence plot is not a line on a logarithmic plot. Additionally, the error decreases below 10^{-16} which is the default accuracy for a double floating point variable on a computer. Table 4.3 gives the convergence rates for the evaluated seven methods. The convergence rates are within expected range. For CFT the linear interpolation gives a high convergence rate.

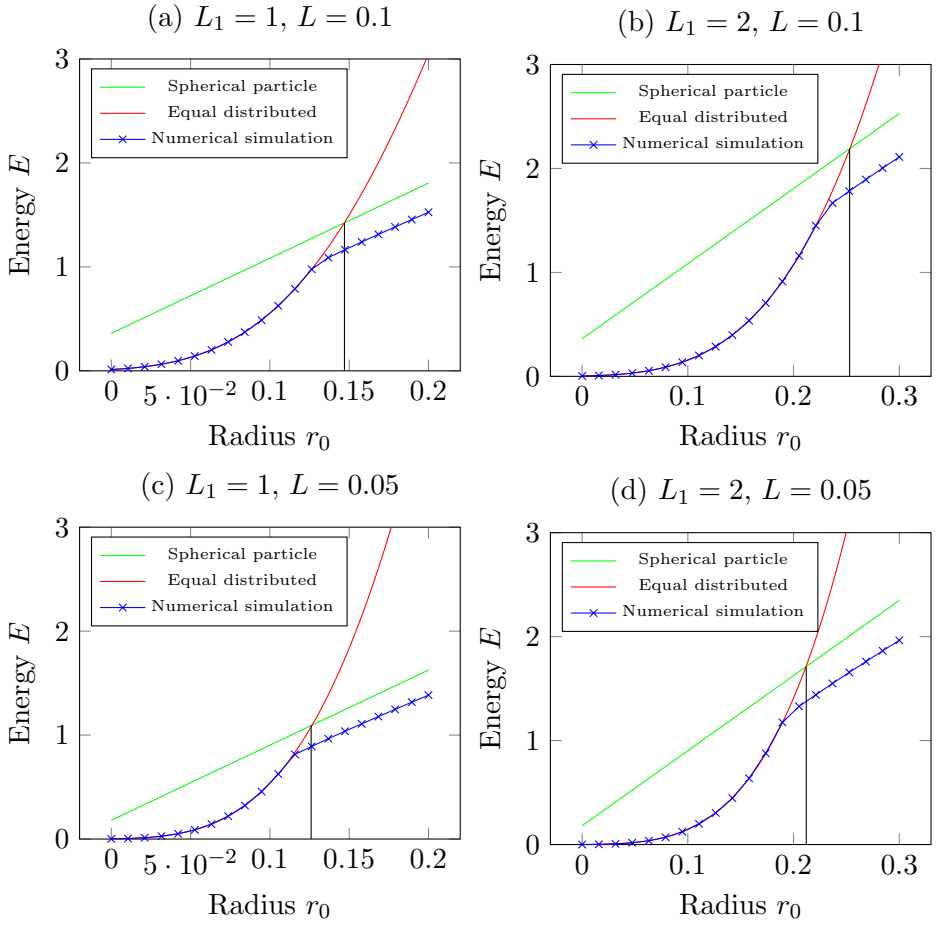

Figure 4.4: The energy content in equilibrium states depending on the size of the containing domain L_1, the phase-field interface width parameter L and the radius of the spherical particle. The analytical estimates for the equally distributed state and the spherical particle state are plotted as well as the numerical results.

Dimension	Solution
1	$e^{-4\pi^2 t} \sin(2\pi x)$
2	$e^{-4\pi^2 t} \sin(2\pi x) \sin(2\pi y)$
3	$e^{-4\pi^2 t} \sin(2\pi x) \sin(2\pi y) \sin(2\pi z)$

Table 4.4: Analytic solutions for the periodic diffusion equation.

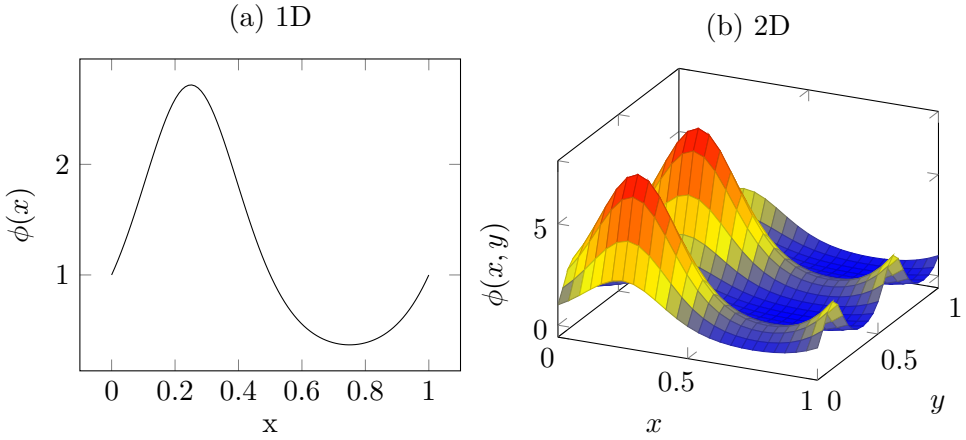

Figure 4.5: Plot of the analytic solution to the periodic Poisson equation.

4.2.2 Convergence for the numerical methods for the periodic diffusion equation

Five different numerical methods are evaluated. FD2 and DFT2 are combined with the second order Runge-Kutta scheme, DFT4 with the fourth order Runge-Kutta and DFT6 and CFT with the sixth order Runge-Kutta scheme.
In order to receive an analytic solution for the periodic diffusion equation (3.71), the method of manufactured solutions is used. Choose $\Omega = (0,1)^3$ and $T = (0, 0.1)$. Table 4.4 gives the function $c(\boldsymbol{x}, t)$ and Figure 4.7 shows the solution in 1D. Given a mesh Ω_h and constant time step τ, the error is calculated as the discrete L_2-Bochner norm,

$$e = ||c_{\tau,h} - c||_2 = \sqrt{\frac{1}{N\frac{|T|}{\tau}} \sum_{i=0}^{\frac{|T|}{\tau}} \sum_{\boldsymbol{x}_h \in \Omega_h} |c_{\tau,h}(\boldsymbol{x}_h, i\tau) - c(\boldsymbol{x}_h, i\tau)|^2}. \tag{4.22}$$

Figures 4.8, 4.9 and 4.10 show convergence plots for the different algorithms for the problem in 1D, 2D and 3D, respectively. It can be seen that in order to decrease the error, both time step size and spatial discretization width have to be decreased by the same amount. For fixed spatial width h and decreasing time step size τ, the spatial discretization error dominates the total error. Vice versa for fixed time step size τ and decreasing spatial width h, the time discretization error dominates the total error. The error plot of the FD2 algorithm conincides nicely as expected with the error of the DFT2. The error of the CFT algorithm is independent of the spatial discretization width and only decreases with smaller time step size τ. The time discretization error dominates

[1]The same holds for FD4 and DFT4 as well as FD6 and DFT6.

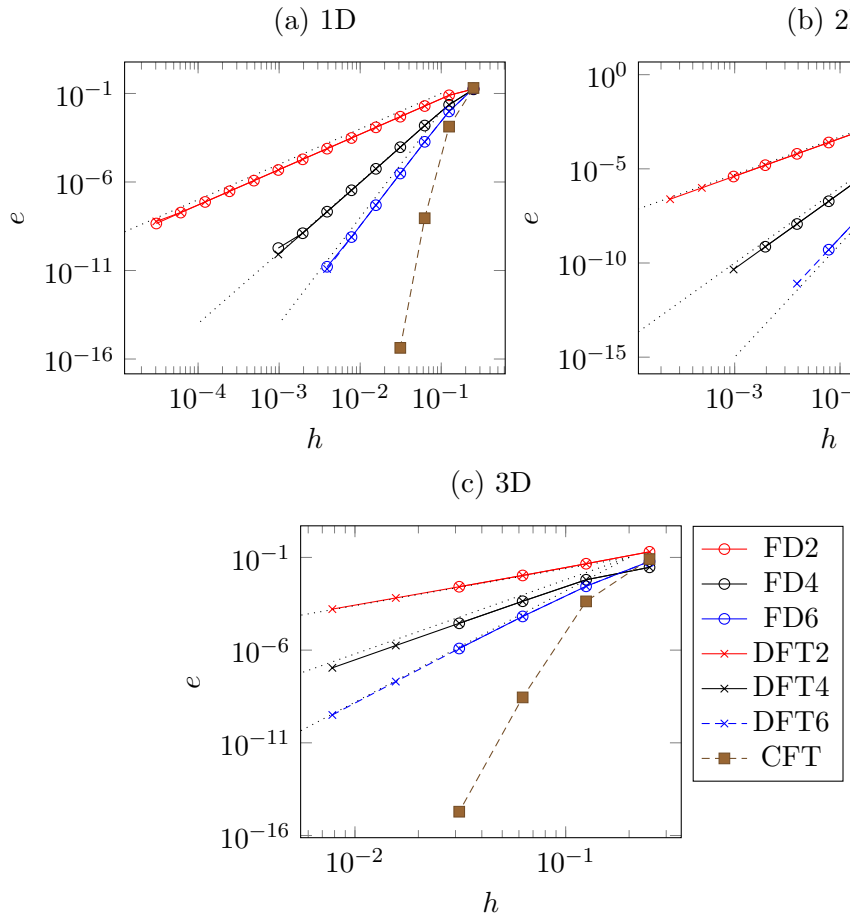

Figure 4.6: Convergence plots for the periodic Poisson equation. Dotted lines show convergence order two, four, and six.

the total error. Table 4.5 gives the convergence rates for the evaluated five methods. The convergence rates are within expected range.

4.2.3 Convergence of the immersed interface method for the Poisson equation

Three different choices for the interpolation matrices D and Ψ are used for the solution of the Poisson equation in a complex domain, see (3.78). The original method *Full* is introduced in [142] and has second order convergence. A second method *Reduced* applies a subset of the original conditions. The third method *Simple* is the one introduced in 3.4.4. The *Simple* method results in a symmetric smaller system in the Uzawa iteration

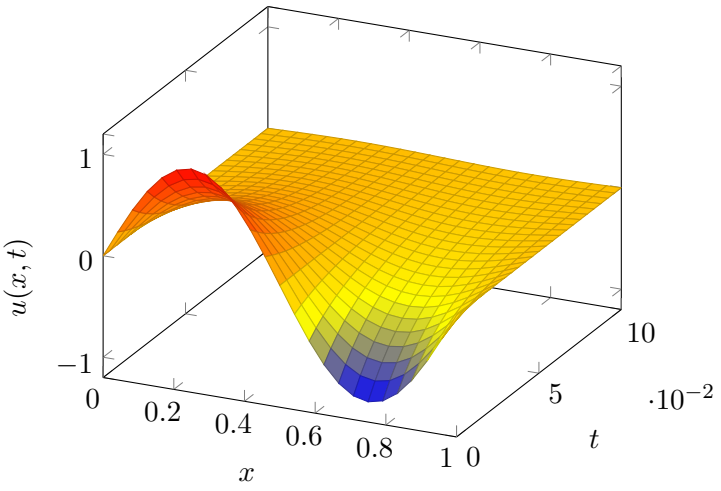

Figure 4.7: Plot of the analytic solution to the periodic diffusion equation in 1D. Contour lines give the binary logarithm of the error.

Dimension	FD2	DFT2	DFT4	DFT6	CFT
1	2.05	2.02	3.98	5.99	5.97
2	1.91	1.94	3.94	5.95	6.03
3	1.97	1.99	3.86	5.59	5.91

Table 4.5: Convergence rates for the periodic diffusion equation.

and allows the usage of an iterative solver for symmetric linear operators such as a conjugate-gradient algorithm instead of the stabilized biconjugate-gradient algorithm.
In order to receive an analytic solution to the Poisson equation (3.77), the method of manufactured solutions is extended. The boundary and initial conditions are assigned such that the manufactured solutions of Table 4.2 coincide inside the domain $\Lambda \subset \Omega = (0,1)^3$. Let

$$\Lambda = \left\{ ||\boldsymbol{x} - \frac{1}{2}|| < r_0 \right\} \subset \Omega, \tag{4.23}$$

with $r_0 = 0.4$. For 1D this is a line, for 2D a disk and for 3D a ball. The boundary $\Gamma = \partial\Omega$ is either just two points, a circle or a sphere.
Given a mesh Ω_h, the number of mesh points scales scales with$1/h^3$ and the number of jump variables scales with $1/h^2$. A biconjugate-gradient solver is used for the iterative solution of the linear system.
Figure 4.12 shows convergence plots and the number of iterations needed in the Schur solver. In 1D and 2D the convergence of the *Full* method and the *Reduced* method is

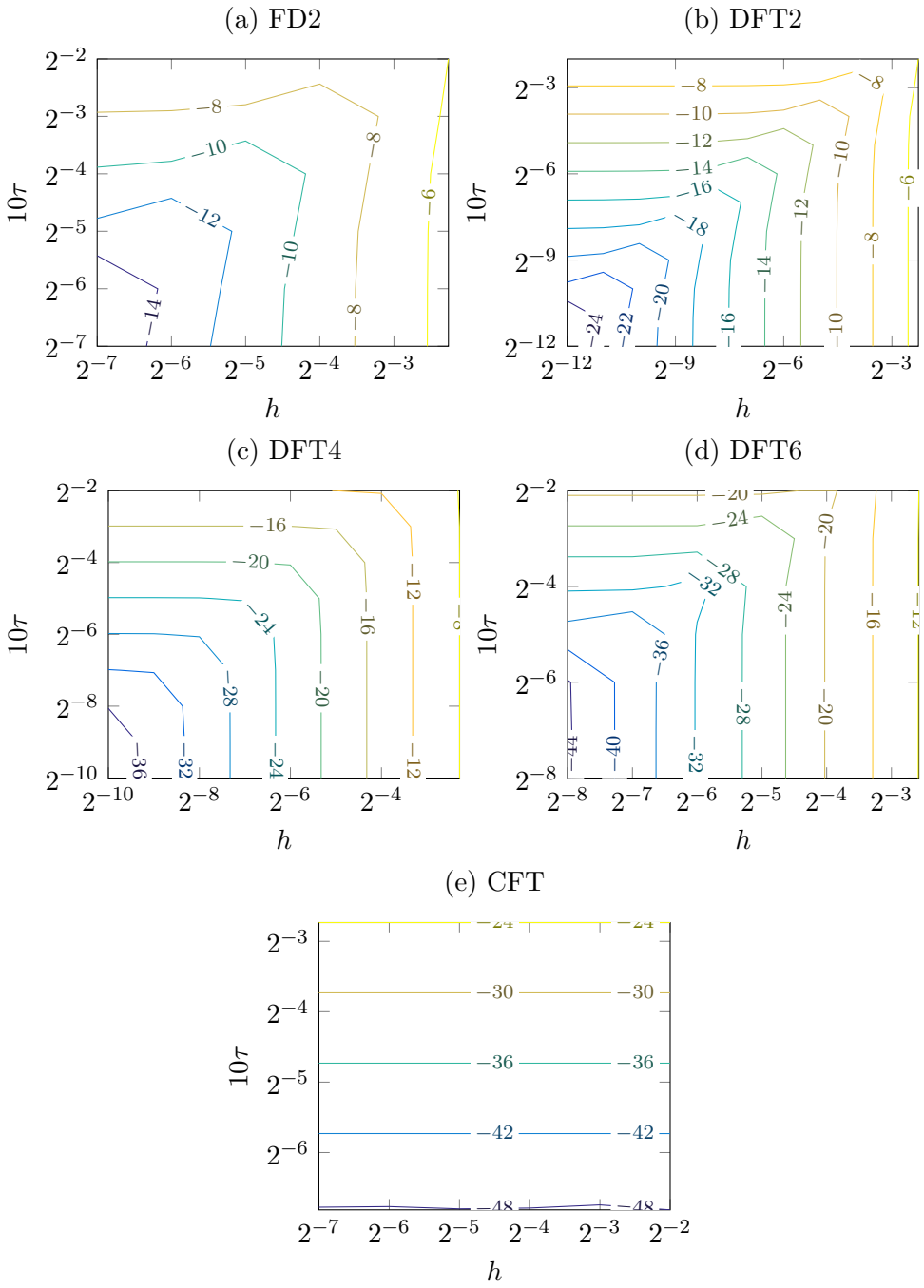

Figure 4.8: Convergence plots for the periodic diffusion equation in 1D. Contour lines give the binary logarithm of the error.

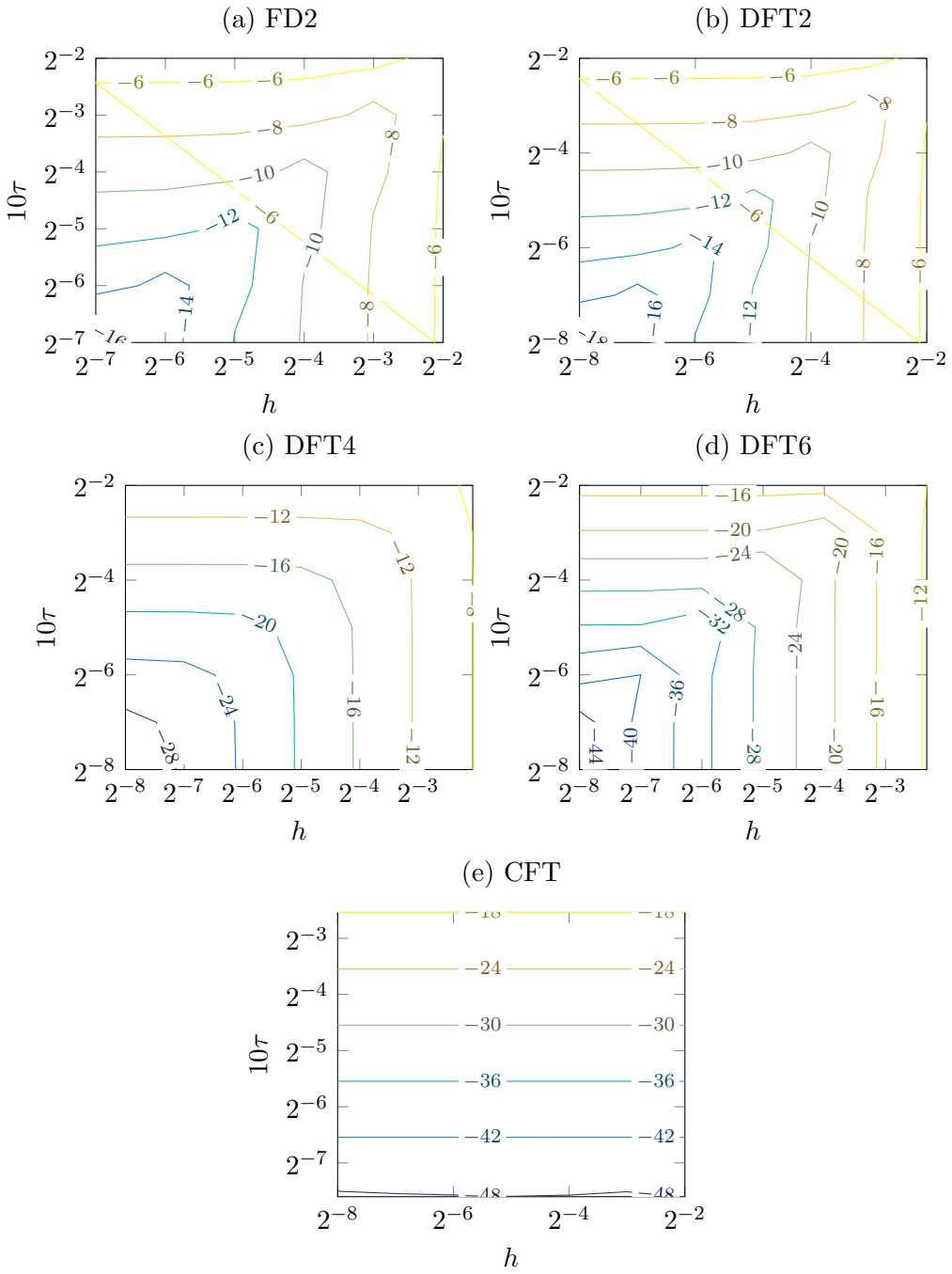

Figure 4.9: Convergence plots for the periodic diffusion equation in 2D. Contour lines give the binary logarithm of the error.

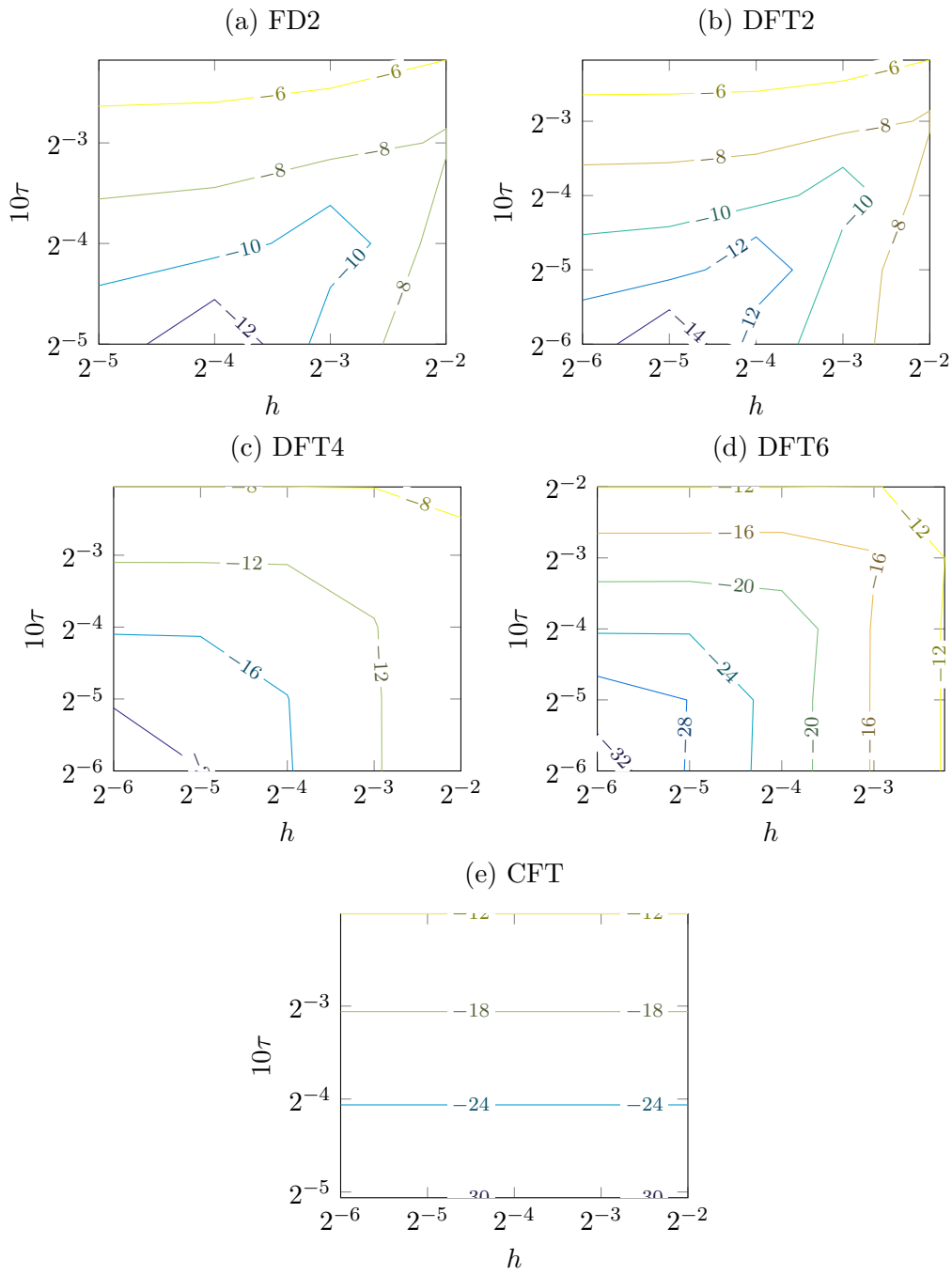

Figure 4.10: Convergence plots for the periodic diffusion equation in 3D. Contour lines give the binary logarithm of the error.

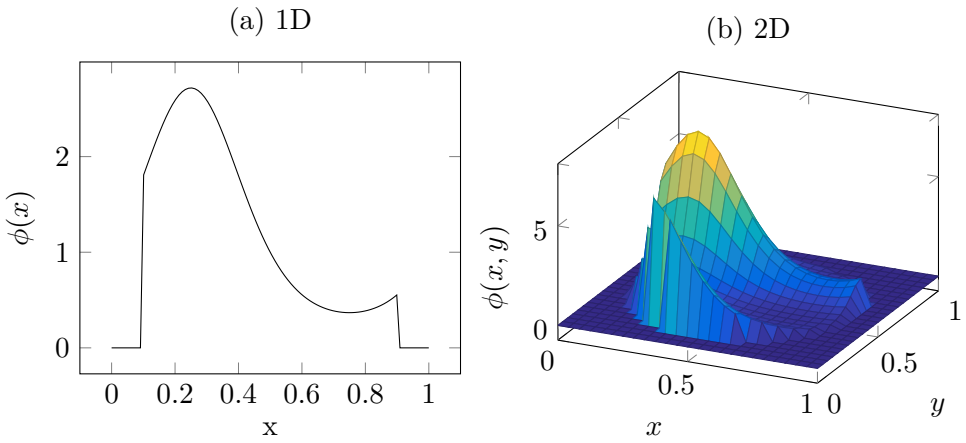

Figure 4.11: Plot of the analytic solution to the Poisson equation in 1D and 2D.

Dimension	Full	Reduced	Simple
1	2.01	2.01	0.96
2	2.23	2.40	1.13
3	1.33	1.52	1.44

Table 4.6: Convergence rates for the Poisson equation.

of order two and the *Simple* method is of order one. In 3D, all methods are of order one[2]. In 1D the number of iterations is independent of the discretization and not shown here[3]. In 2D and 3D the behavior is more interesting. The *Full* method and the *Reduced* method need more iterations than the *Simple* method. The iterations depend on the discretization and increase with finer discretizations. Table 4.6 gives the convergence rates for the different methods.

Dimension	1	2	3
Convergence rate	1.24	1.23	1.22

Table 4.7: Convergence rates for the diffusion equation.

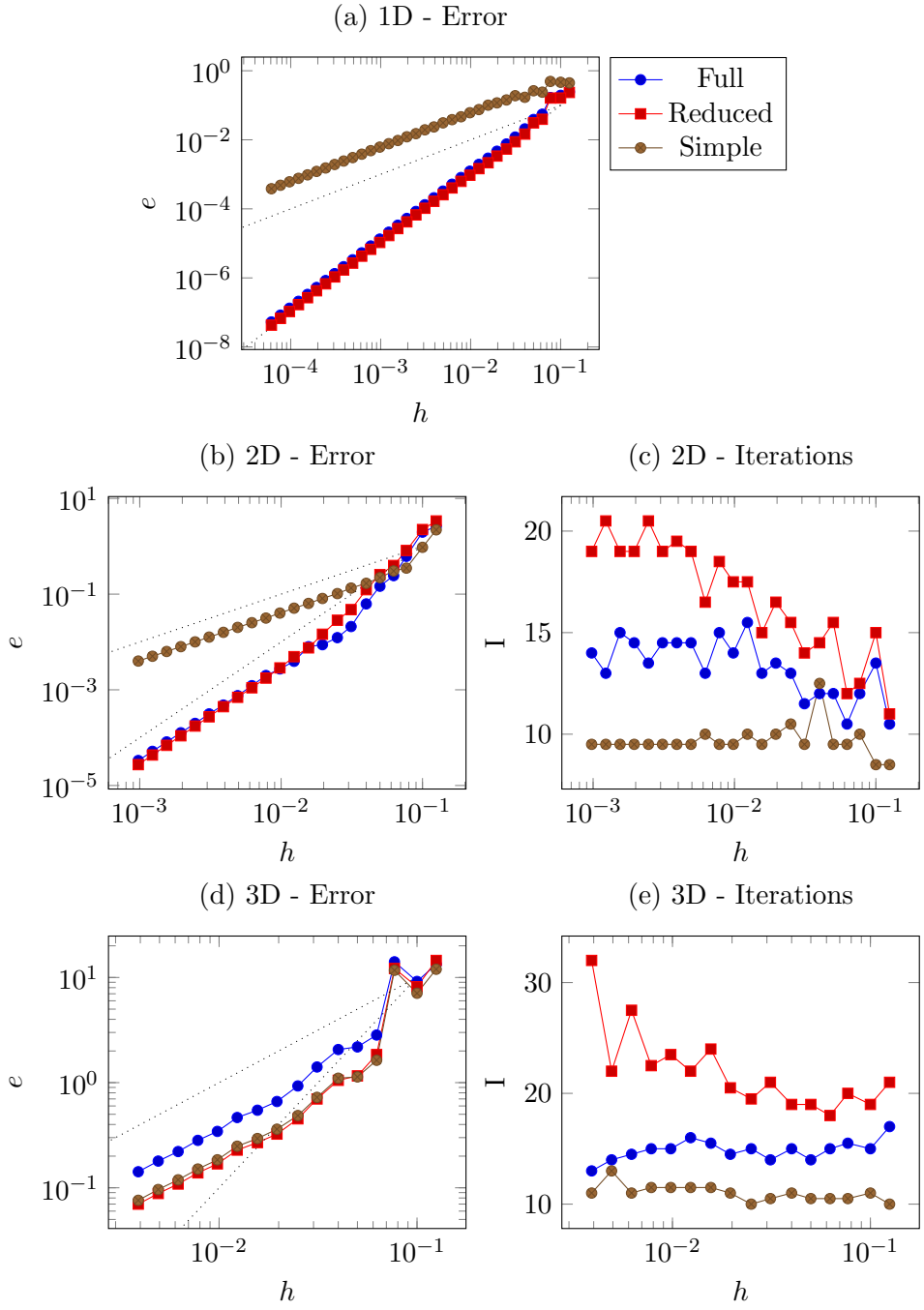

Figure 4.12: Convergence and iterations plots for the Poisson equation. Dotted lines show convergence order one and two.

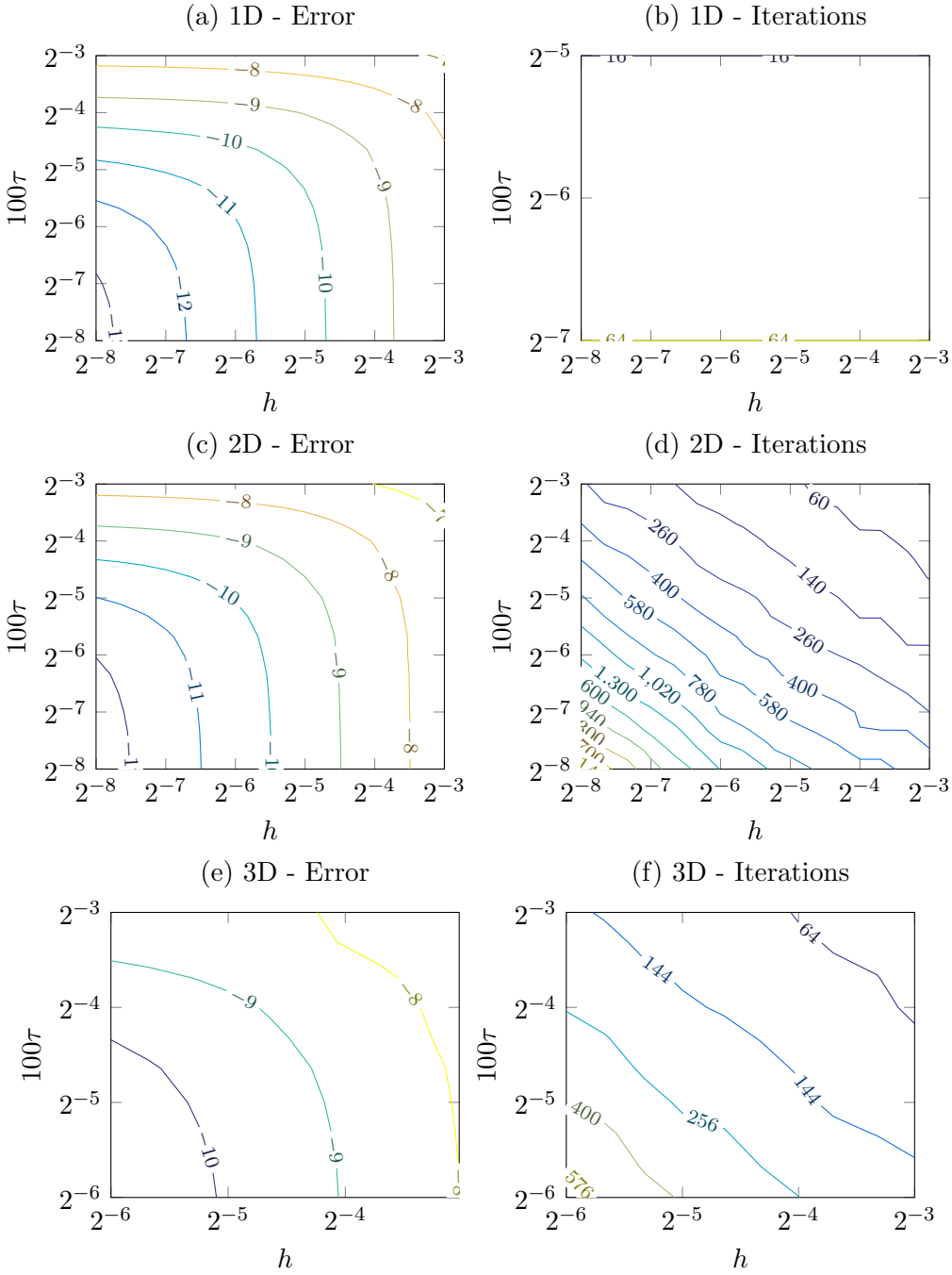

Figure 4.13: Convergence and iteration plots for the diffusion equation.

4.2.4 Convergence of the immersed interface method for the diffusion equation

Only the *Simple* method is now applied. The previously introduced Runge-Kutta methods for the time integration cannot be used with the IIM[4]. The diffusion equation is solved with an implicit Euler scheme.
In order to receive an analytic solution to the diffusion equation (3.77), again the method of manufactured solutions is used and the boundary and initial conditions are assigned such that the manufactured solution of Table 4.4 coincide inside the domain $\Lambda \subset \Omega = (0,1)^3$. Let

$$\Lambda = \left\{ ||\boldsymbol{x} - \frac{1}{2}|| < r_0 \right\} \subset \Omega, \tag{4.24}$$

with $r_0 = 0.4$. The mesh Ω_h and the time domain $T = (0, 0.01)$ are used.
Figure 4.13 shows convergence plots as well as the total number of iterations needed in the Schur solver. Plotted is the sum of all iterations during the time integration. Each simulation test consists of several time steps and in each time step a Schur solver with a certain amount of iterations is called. The number of iterations measures the numerical effort.
In 1D, 2D, and 3D the convergence order for both time and space is one. In 1D the number of iterations is independent of the spatial discretization[5]. In 2D and 3D the contour lines are diagonal. For a fixed product $\tau \cdot h$ the total iteration number is constant.

4.2.5 Convergence of the immersed interface method for the Cahn-Hilliard equation

In this subsection, the IIM is applied for the solution of the Cahn-Hilliard equation (3.87). The numerical convergence is demonstrated in Subsection 4.2.5.1 and the properties of the preconditioner are studied in Subsection 4.2.5.2. The stability of the method for large time steps is investigated in Subsection 4.2.5.3 and effects like spinodal decomposition, see Subsection 4.2.5.4, and surface wetting effects, see Subsection 4.2.5.5, are studied. Grid convergence is studied on a porous microstructure in Subsection 4.2.5.6. Lastly, the properties of the second-order method are examined in Subsection 4.2.5.7.

4.2.5.1 Numerical convergence

As a model problem, the formation of an interfacial region by initialization of two separate phases is numerically simulated. The domain is given as $\Lambda = (0.25, 0.75)$

[2] In 3D the finite-difference stencil has to be adapted to get convergence order two [141].
[3] This is a result of the constant number of jump conditions $N_{\mathrm{IF}} = 2$.
[4] The Runge-Kutta methods apply (3.74) and Ψ and D have to be adapted to this.
[5] Again, this may be the result of the fixed number of interfaces $N_{\mathrm{IF}} = 2$.

2D	N	16	64	256	1024	4096	16384	65536
	$\|\|g\|\|$	8	16	32	64	128	256	512
3D	N	64	512	4096	32768	262144	2097152	
	$\|\|g\|\|$	24	96	384	1536	6144	24576	

Table 4.8: Number of jump variables in comparison to the degress of freedom

with $\Omega = (0, 1)$ and $T = (0, 0.001)$. Interface energy and width are set to academic values, $G = 1$ and $L = 0.1$. A reference solution is calculated with the algorithm NWT. Minimal spatial discretization and time step size are $h_0 = \frac{1}{2^{13}} \approx 1.22 \cdot 10^{-4}$ and $\tau_0 = \frac{|T|}{1024} \approx 9.77 \cdot 10^{-7}$. Figure 4.14 shows the reference solution $p(\boldsymbol{x}, t)$ at different times.
The time step size is varied from $\tau = \frac{|T|}{2} \approx 5 \cdot 10^{-4}$ to $\tau = \frac{|T|}{512} \approx 1.95 \cdot 10^{-6}$, the grid width is varied from $h = \frac{1}{8} = 0.125$ to $h = \frac{1}{4096} \approx 2.44 \cdot 10^{-4}$.
The error is defined as a L_2-Bochner norm

$$e = ||p_{\tau,h} - p_{\text{ref}}||_2 = \sqrt{\frac{1}{N\frac{|T|}{\tau}} \sum_{i=0}^{\frac{|T|}{\tau}} \sum_{\boldsymbol{x}_h \in \Omega_h} |p_{\tau,h}(\boldsymbol{x}_h, i\tau) - p_{\text{ref}}(\boldsymbol{x}_h, i\tau)|^2}. \tag{4.25}$$

Figure 4.15 (a) shows contour lines in a logarithmic error plot. The error decreases with the highest rate if both time step size and spatial grid width are reduced simultaneously. Figure 4.15 (b) shows the convergence for grid width and time step size reduced equally. The error reduces according to $e = O((h+\tau)^{0.85})$, the convergence rate is approximately 0.85.

4.2.5.2 Preconditioner effects

The preconditioner as proposed in 3.5.3 is investigated. The periodic Cahn-Hilliard equation (3.85) is considered and the IIM is not applied. To examine the effect on the condition of the linear system

$$A_E u_h = f \tag{4.26}$$

and on the iteration number of the iterative solver, an examplary problem is posed. In [42] it is suggested to use a conjugate-gradient-squared scheme (CGS) to solve the system of linear equations and to define $\bar{p}^2$ as the arithmetic mean of the vector $\check{p}^2$. In [41] convergence is also proven for $\bar{p}^2$ equal to 1. The condition number of the preconditioned system

$$A_{E0}^{-1} A_E u_h = A_{E0}^{-1} f \tag{4.27}$$

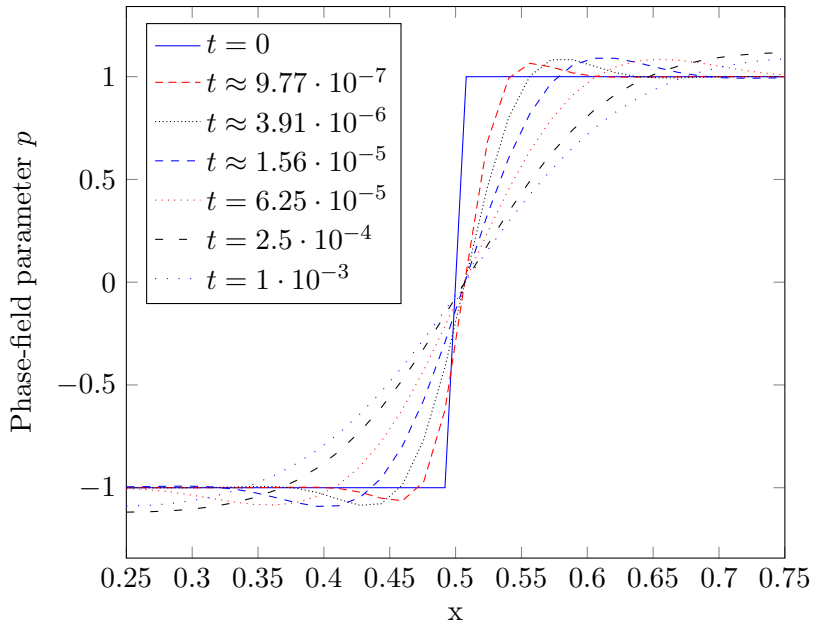

Figure 4.14: Reference solution of the Cahn-Hilliard equation

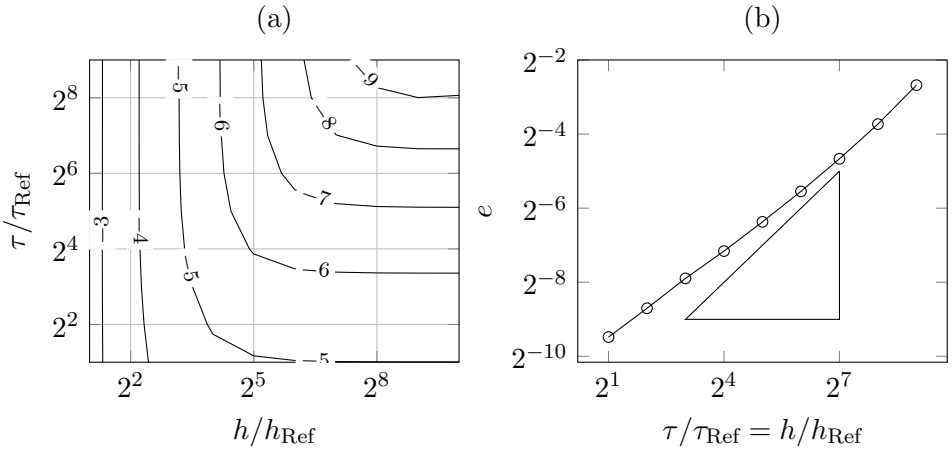

Figure 4.15: (a) Contour lines in a logarithmic error plot. (b) Error for equally reduced grid width and time step size.

N	$\kappa(A_E)$	Iterations	$\kappa(A_{E0}^{-1}A_E)$	Iterations
100	$2.0 \cdot 10^3$	75	$4.6 \cdot 10^0$	4
200	$2.8 \cdot 10^4$	270	$4.5 \cdot 10^0$	3
300	$1.4 \cdot 10^5$	732	$4.5 \cdot 10^0$	3
400	$4.2 \cdot 10^5$	1551	$4.5 \cdot 10^0$	3
500	$1.0 \cdot 10^6$	2724	$4.5 \cdot 10^0$	3
600	$2.1 \cdot 10^6$	3468	$4.5 \cdot 10^0$	3
700	$3.9 \cdot 10^6$	7002	$4.5 \cdot 10^0$	3
800	$6.7 \cdot 10^6$	8437	$4.5 \cdot 10^0$	3
900	$1.1 \cdot 10^7$	9792	$4.5 \cdot 10^0$	3
1000	$1.6 \cdot 10^7$	17399	$4.5 \cdot 10^0$	3

Table 4.9: Preconditioner evaluation for the periodic Cahn-Hilliard equation.

is then smaller than in the original system and independent of the discretization width h.
Set $\Lambda = \Omega = (0,1)$, $G = L = 0.01$, the mesh Ω_h, time step size $\tau = 0.01$ and different spatial discretizations from $N = 100$ to $N = 1000$. The initial distribution is $p(\boldsymbol{x}, 0) = 2x - 1$. The right-hand side vector $f \in \mathbb{R}^N$ is set as $f_i = i^2$.
Table 4.9 shows the results. The second and third column show that the condition number $\kappa(A_E)$ and the iteration number for the solution of (4.26) are large and depend on the discretization width [9]. The fourth and third column show that the condition number of $\kappa(A_{E0}^{-1}A_E)$ and the iteration number for (4.27) are small and independent of the discretization width.

4.2.5.3 Oscillations

The stable approximation in 3.5.1 comes with a price. Although the energy is monotonically decreasing, additional errors are introduced. For large time steps, oscillations during spinodal decomposition and interface formation occur. These effects are independent of spatial discretization. This example investigates the impact of these oscillations compared to the solution achieved by fine time steps.
Set $\Omega = (0,1)$, $\Lambda = (0.25, 0.75)$, $G = L = 0.01$, the mesh Ω_h with $h = 0.01$ and $T = (0,1)$. A reference solution with $\tau = \frac{1}{1000}$ is used and compared to the solution with $\tau \in \{\frac{1}{10}, \frac{1}{20}, \frac{1}{30}, \frac{1}{40}$ or $\frac{1}{50}\}$. The initial phase-field distribution in Λ is set to $p(\boldsymbol{x}, 0) = 4x - 2$. This gives $p(0.25, 0) = -1$ and $p(0.75, 0) = 1$ at the boundary of Ω. No special surface wetting condition or Neumann boundary flux condition are applied, so $r_\mu = r_p = 0$, see (3.87).
Figure 4.16 (a) shows the initial state p_0 inside $\Omega = (0.25, 0.75)$ and the reference solution at $t = 1$. The linear gradient is transformed to two phases of both equilibrium concen-

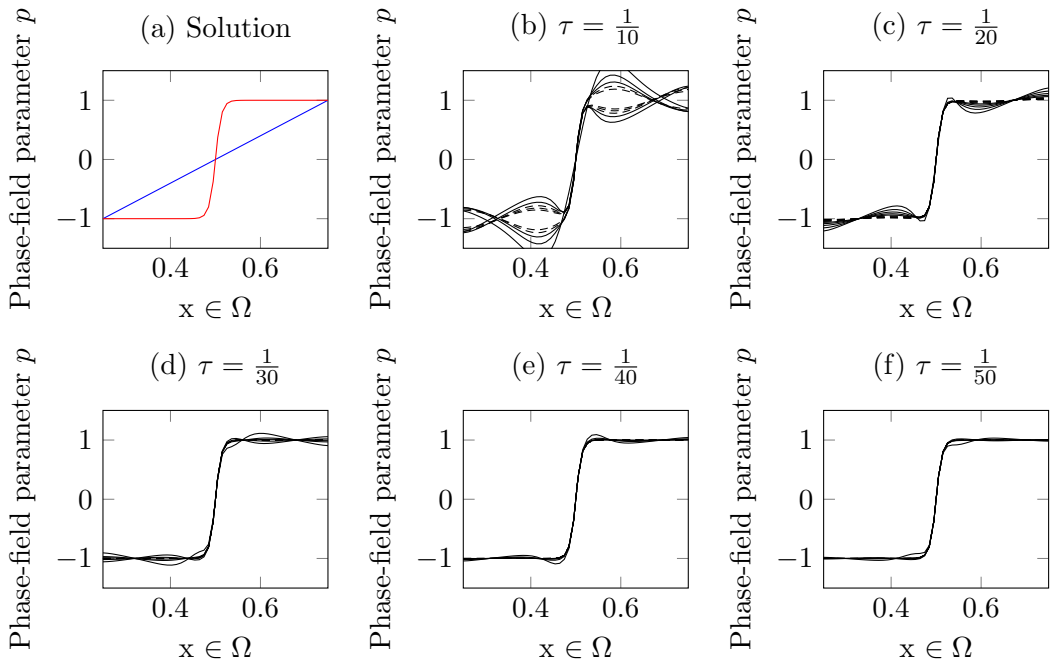

Figure 4.16: Oscillations in a numerical solution to the Cahn-Hilliard equation

tration and a static interface between them. Figure 4.16 (b)-(f) show the evolution of the phase-field around the reference solution at the times $t_i = \frac{i}{10}$, $i \in \{1, \ldots, 10\}$ for the different time step sizes. E.g., Figure 4.16 (b) shows the solutions for the large time step size $\tau = 1/10$. Large oscillations can be observed. The phase-field shows oscillations around the equilibrium solution in Figure 4.16 (a). Figure 4.16 (f) shows the solutions for the small time step size $\tau = 1/50$ and only small oscillations can be observed.

4.2.5.4 Spinodal decomposition

In this example, the effects of spinodal decomposition and Ostwald ripening [76] are investigated. The stable time integration method allows for arbitrary time steps. This is especially interesting as the process of ripening happens on an exponential time scale, i.e., the logarithm of a particle radius depends linearly on the logarithm of the elapsed time. For this example, exponential time step sizes are chosen.
Set $\Omega = (0, 1) \times (0, \frac{\sqrt{3}}{2})$ and $G = L = 0.01$. The domain $\Lambda \subset \Omega$ is characterized by regular star-shaped holes. Figure 4.17 (a) shows the domain Λ in grey. The boundary of Λ is shown in red. The distance between the centers of two stars is 0.25. Each star S is described by the equation

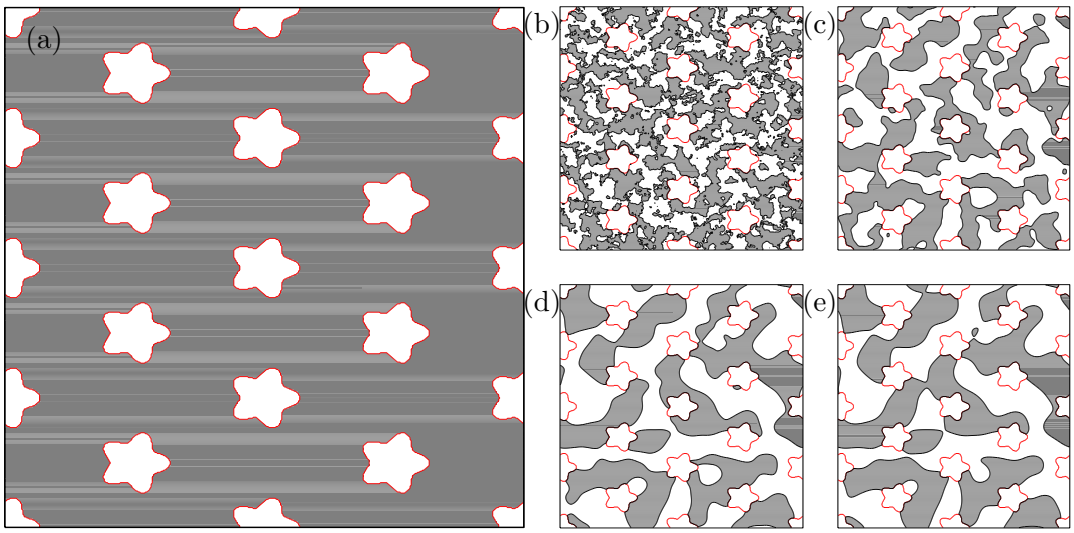

Figure 4.17: (a) Domain Λ with star-shaped holes. (b) - (e) Contour lines for $p = 0$ show the spinodal decomposition for different times.

$$S = \left\{ (x_1, x_2) \in \Omega \middle| ||x|| < 0.05(1 + 0.2 \sin(5\lambda)), \text{ where } \tan\lambda = \frac{x_2}{x_1} \right\}. \tag{4.28}$$

The mesh Ω_h is used with $N_1 = 500$, $N_2 = 433$ and $h = 0.002$. The time domain $(0, 1)$ is discretized into four time steps with different size to get solutions at the times $t \in \{0.001, 0.01, 0.1, 1\}$, that is, $\tau \in \{0.001, 0.009, 0.09, 0.9\}$. The initial state p_0 is chosen randomly from a uniform distribution on $(-1, 1)$ and not shown. No special surface wetting condition or Neumann boundary flux condition are applied, so $r_\mu = r_p = 0$. Figure 4.17 (b) - (e) show the solutions at the different times. In grey regions holds $p > 0$, in white regions holds $p < 0$. The boundary of Λ is in red. In the beginning arbitrary spots show coalescence in Figure 4.17 (b) and (c). Larger phase regions can be seen in Figure 4.17 (d) and (e). The interfaces between different holes then evolve and become shorter between the different holes. By this, they minimize the interface energy.

4.2.5.5 Surface wetting

In this example, the effect of the surface wetting boundary condition r_p is investigated. If $r_p = 0$ the phase interface is orthogonal to the boundary of the domain. The sign of r_p represents if states $p = 1$ and $p = -1$ are either attracted or repelled by the domain boundary[6]. The contact angle is used to describe this property.

[6]Surfaces for water can either be hydrophilic or hydrophobic.

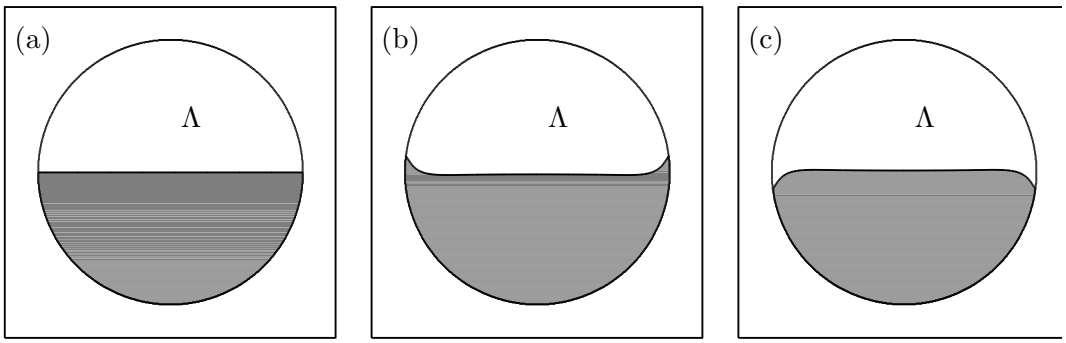

Figure 4.18: (a) Initial state. (b)-(c) State for positive and negative surface wetting.

Set $\Omega = (0,1)^2$, $\Lambda = \{||\boldsymbol{x} - \frac{1}{2}|| < 0.4\}$, $T = (0, 0.1)$ and $G = L = 0.01$. The mesh Ω_h is used with $N_1 = N_2 = 512$, $\tau = 0.01$ and

$$p(\boldsymbol{x}, 0) = \begin{cases} 1 & x_2 < 0.5 \\ -1 & x_2 \geq 0.5 \end{cases}, \tag{4.29}$$

see Figure 4.18 (a). The Neumann boundary condition is set to zero, $r_\mu = 0$, while the surface wetting r_p is chosen from the set $\{50, -50\}$.
Figure 4.18 (b)-(c) show the state for the two different values of r_p at $t = 0.1$. They show contact angles different from orthogonal contact.

4.2.5.6 Phase separation in a porous microstructure

In this example, a 3D example related to the intercalation of lithium-ion batteries is shown. The cathode material is built from a porous microstructure. Then $p(\boldsymbol{x}, t)$ is associated with the lithium ion concentration by the definition in 3.3.2. The boundary conditions define a lithium ion concentration flux into the microstructure.
Set $\Omega = (0, 0.32)^3$ and $G = L = 0.01$. Then Λ consists of several overlapping spheres with diameter 0.15 with $|\Lambda| = \frac{1}{2}|\Omega|$. The spatial discretization $N_1 = N_2 = N_3$ is varied from $N_1 = 32$ up to $N_1 = 512$. Set $T = (0, 1)$, $\tau = 0.01$ and $p(\boldsymbol{x}, 0) = p_{\text{start}} = -1$, associated with an *empty* cathode. No special surface wetting condition is applied, $r_\mu = 0$. The Neumann boundary condition r_μ is set to a constant value such that

$$\begin{aligned} \int_T \int_{\partial\Lambda} r_\mu(\boldsymbol{x}, t) \mathrm{dV dt} &= \int_\Lambda (p_{\text{end}} - p_{\text{start}}) \mathrm{dV}, \\ \Leftrightarrow |T||\partial\Lambda| r_\mu(\boldsymbol{x}, t) &= ((1) - (-1))|\Lambda|, \\ \Leftrightarrow r_\mu(\boldsymbol{x}, t)|\partial\Omega| &= 2|\Lambda|, \\ \Leftrightarrow r_\mu(\boldsymbol{x}, t) &= \frac{2|\Lambda|}{|\partial\Lambda|}. \end{aligned} \tag{4.30}$$

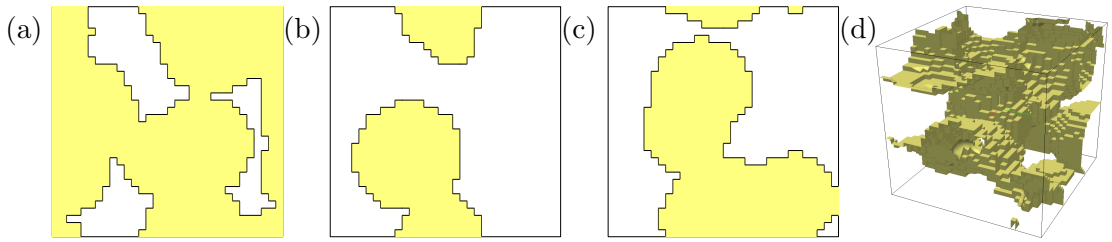

Figure 4.19: 3D porous microstructure. (a) - (c) Slices in XY-direction, XZ-direction and YZ-direction. (d) 3D representation of the structure.

Using this, it is ensured that the average value at time $t = 1$ is $p(\boldsymbol{x}, 1) \approx p_{\text{end}} = 1$. This is associated with a *full* cathode.
Figures 4.19 (a)-(d) show the different slices of the 3D structure along the three Cartesian planes in directions xy, xz and yz. The 3D structure is built of overlapping spheres, randomly and periodically distributed inside the domain. Figures 4.20 (a)-(c) show the same slices of the 3D structure now at time $t = 0.5$. At this point, exactly half of the material has been transformed from lithium-poor to lithium-rich phase. In Figure 4.20 different filled phases can be seen inside the porous structure, some have already merged together in the process of Ostwald ripening. The occurrence of occupied and empty phase-active material next to each other results in mechanical stresses and deformation of the battery material. It is crucial for battery design to predict these occurrence depending on porosity, volume fraction, and geometric composition of the structure.
The error is defined in (4.25). Figure 4.21 shows the numerical convergence rate with a linear slope. Table 4.10 shows numerical details for the simulation. The number of degrees of freedom on the mesh Ω_h is given by N. The number of degrees of freedom on the interfaces is given by $2N_{\text{IF}}$. This is the size of the system of linear equations in (3.91). The column *Inner it.* gives the average number of iterations per solution of (4.27). The column *Outer it.* gives the average number of iterations per solution of (3.91).
The total degrees of freedom of the system $|p_h|$ grow as $O(N_1^3)$, the degrees of freedom in the IIM grow $O(N_1^2)$. This allows for larger discretizations with the same computational effort. The number of inner iterations is independent of the spatial discretization. This fits to the results of 4.2.5.2. The number of outer iterations grows from 11 to 45. Larger numerical effort is required for the solution of (3.91).

4.2.5.7 Second-order time integration

In this example the second-order time integration method in 3.5.4 is evaluated. No IIM is used for this example.

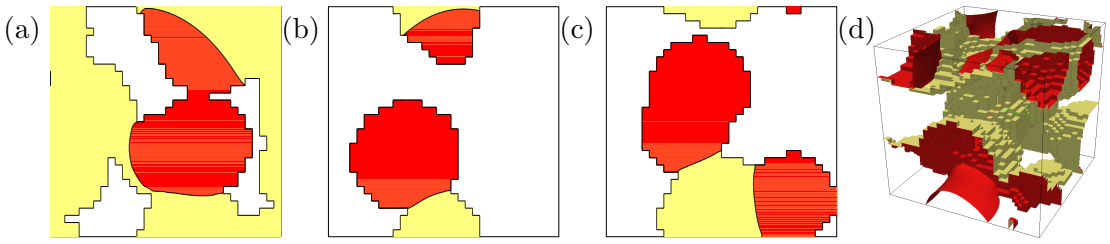

Figure 4.20: Solution in a 3D porous microstructure at $t = 0.5$. (a) - (c) Slices in XY-direction, XZ-direction and YZ-direction. (d) 3D representation of the structure.

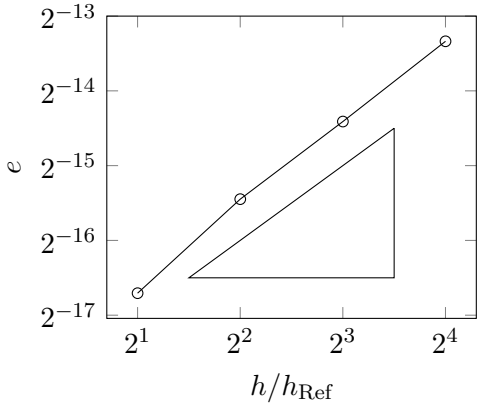

Figure 4.21: Convergence plot for the Cahn-Hilliard equation in 3D

N_1	$N = N_1^3$	$2N_{\text{IF}} = O(N_1^2)$	Inner it.	Outer It.
32	$32^3 = 32\ 768$	12 952	15	11
64	$64^3 = 262\ 144$	51 808	13	16
128	$128^3 = 2\ 097\ 152$	207 232	12	23
256	$256^3 = 16\ 777\ 216$	828 928	15	32
512	$512^3 = 134\ 217\ 728$	3 315 712	13	45

Table 4.10: Iteration numbers for different discretizations.

Example	a	b	c
$c_0(x)$	$\sin(x)$	$\frac{4}{\pi^2}(x-\pi)(\lvert x-\pi\rvert-\pi)$	$\lvert\lvert\frac{2}{\pi}x-1\rvert-2\rvert-1$
$\partial_x c_0(x)$	$\cos(x)$	$\frac{4}{\pi^2}(2\lvert x-\pi\rvert-\pi)$	$\frac{2}{\pi}\operatorname{sign}\left(x-\frac{\pi}{2}\right)\operatorname{sign}\left(x-\frac{3\pi}{2}\right)$
$\partial_x^2 c_0(x)$	$-\sin(x)$	$\frac{8}{\pi^2}\operatorname{sign}(x-\pi)$	0
Smoothness	$C^\infty(\Omega)$	$C^1(\Omega)$	$C^0(\Omega)$

Table 4.11: Three differently smooth initial concentration functions.

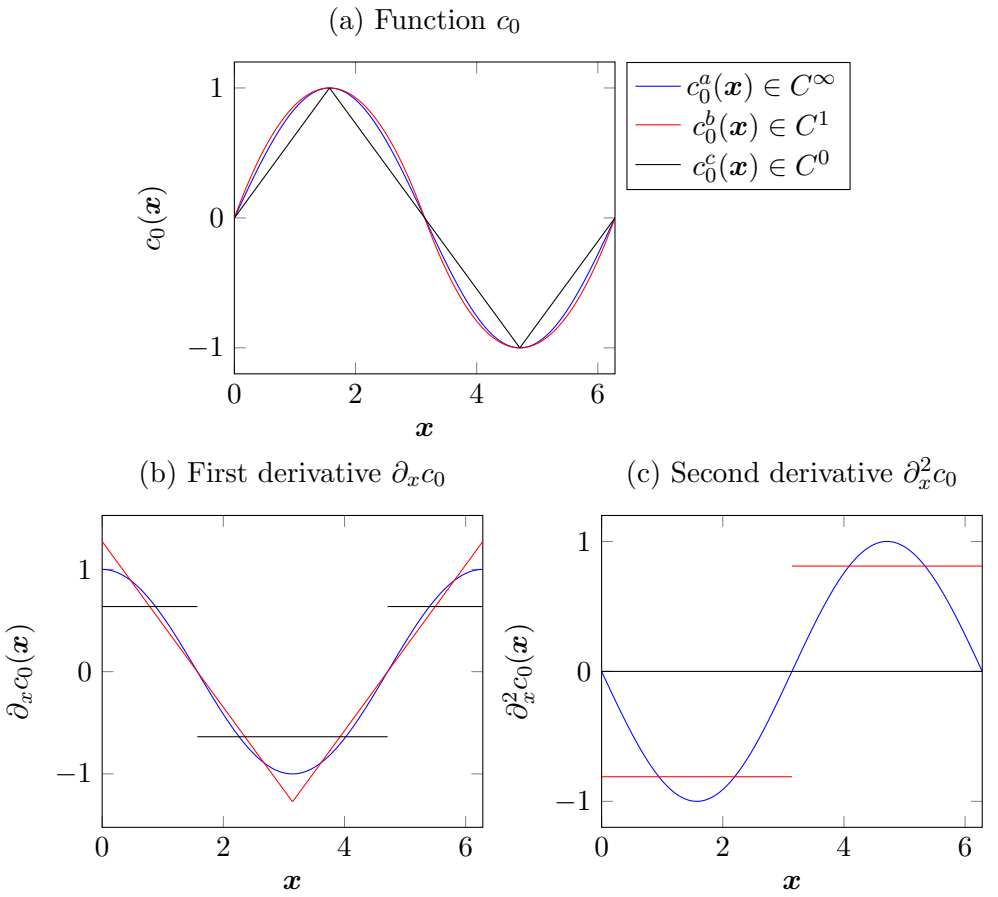

Figure 4.22: Different initial configurations for the Cahn-Hilliard equation and their derivatives.

Set $\Omega = \Lambda = (0, 2\pi)$, $T = (0, 0.1)$, $G = 0.01$, $L = 0.05$. Three different periodic initial configurations c_0^a, c_0^b, c_0^c, with decreasing smoothness are used. Table 4.11 defines the three functions. Figure 4.22 shows a plot of them and their derivatives.
Figure 4.23 shows error plots and Table 4.12 shows the convergence rates. For c_0^a the method gives second-order convergence, while for c_0^b and c_0^c only linear convergence is achieved. The convergence rate of a time integration method depends on the smoothness of the analytic solution to the continuous problem. In [35] the smoothness of the initial data is shown to be sufficient for the smoothness of the solution. Here an example is given where it is required for a smooth solution. The non-smooth initial data $c_0^c(\boldsymbol{x})$ supposedly results in a non-smooth solution $c^c(\boldsymbol{x}, t)$ and second-order convergence is not achieved.

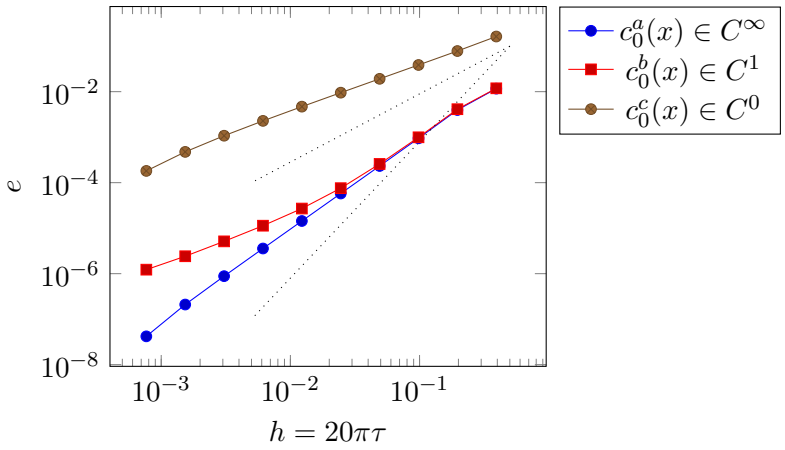

Figure 4.23: Error plot for the Cahn-Hilliard equation with second-order time integration

Initial data	$c_0^a(x) \in C^\infty$	$c_0^b(x) \in C^1$	$c_0^c(x) \in C^0$
Convergence rate	2.02	1.50	1.07

Table 4.12: Convergence rates for the Cahn-Hilliard equation with second-order time integration

4.3 Microstructure generation

In this section, algorithms for the generation and coating of periodic microstructures are introduced. Spherical packings are introduced in Subsection 4.3.1 and an elastic test is given. The concept of coating is defined in Subsection 4.3.2. Then two different coating methods are introduced and analyzed in Subsections 4.3.3 and 4.3.4 and compared in Subsection 4.3.5. Finally the elastic test is repeated with the coated microstructures in Subsection 4.3.6. Lengths are given in nanometers.

4.3.1 Spherical packing

Four different spherical packings are introduced, simple cubic (SC), body centered cubic (BCC), face centered cubic (FCC) and hexagonal close packed (HCP) [37]. The definition of a spherical packing envails the lengths of the unit cell, the radius of the spheres in the unit cells, and the centers of all spheres that have non-empty intersection with this unit cell. This gives an analytical description of the packing.

- SC: Unit cell $[0,1] \times [0,1] \times [0,1]$. Radius $r = \frac{1}{2}$. There are 8 centers of spheres to consider.

Packing	Number of centeres	Center coordinates M_i=(x_M,y_M,z_M)
SC	8	$(0,0,0)$, $(0,0,1)$, $(0,1,0)$, $(0,1,1)$, $(1,0,0)$, $(1,0,1)$, $(1,1,0)$, $(1,1,1)$.
BCC	9	$(0,0,0)$, $(0,0,1)$, $(0,1,0)$, $(0,1,1)$, $(1,0,0)$, $(1,0,1)$, $(1,1,0)$, $(1,1,1)$, $(\frac{1}{2},\frac{1}{2},\frac{1}{2})$.
FCC	14	$(0,0,0)$, $(0,0,1)$, $(0,1,0)$, $(0,1,1)$, $(1,0,0)$, $(1,0,1)$, $(1,1,0)$, $(1,1,1)$, $(\frac{1}{2},\frac{1}{2},0)$, $(\frac{1}{2},\frac{1}{2},1)$, $(\frac{1}{2},0,\frac{1}{2})$, $(\frac{1}{2},1,\frac{1}{2})$, $(0,\frac{1}{2},\frac{1}{2})$, $(1,\frac{1}{2},\frac{1}{2})$.
HCP	14	$(0,0,0)$, $(0,0,\sqrt{\frac{8}{3}})$, $(0,\sqrt{3},0)$, $(0,\sqrt{3},\sqrt{\frac{8}{3}})$, $(1,0,0)$, $(1,0,\sqrt{\frac{8}{3}})$, $(1,\sqrt{3},0)$, $(1,\sqrt{3},\sqrt{\frac{8}{3}})$, $(\frac{1}{2},\frac{\sqrt{3}}{2},0)$, $(\frac{1}{2},\frac{\sqrt{3}}{2},\sqrt{\frac{8}{3}})$, $(\frac{1}{2},\frac{\sqrt{3}}{6},\sqrt{\frac{2}{3}})$, $(\frac{1}{2},\frac{7\sqrt{3}}{6},\sqrt{\frac{2}{3}})$, $(0,\frac{2\sqrt{3}}{6},\sqrt{\frac{2}{3}})$, $(1,\frac{2\sqrt{3}}{6},\sqrt{\frac{2}{3}})$.

Table 4.13: Parameters for the unit cells of spherical packings.

- BCC: Unit cell $[0,1]\times[0,1]\times[0,1]$. Radius $r=\frac{\sqrt{3}}{4}$. There are 9 centers of spheres to consider.
- FCC: Unit cell $[0,1]\times[0,1]\times[0,1]$. Radius $r=\frac{\sqrt{2}}{4}$. There are 14 centers of spheres to consider.
- HCP: Unit cell $[0,1]\times[0,\sqrt{3}]\times[0,\sqrt{\frac{8}{3}}]$. Radius $r=\frac{1}{2}$. There are 14 centers of spheres to consider.

The centers of the spheres are specified in Table 4.13. Figure 4.24 shows the unit cell for the four different spherical packings.
The spherical packings are defined such that the spheres do not overlap. An elastic problem on such spherical packings is ill-posed for the contact points [112]. The numerical solution for the stress does not show uniform convergence for finer discretizations. The analytical solution to an elasticity problem posed with the character of the presented elastic model (isotropic strain) on this domain has a singular value, such as infinitesimal small deformation and an infinite stress maximum [144]. A numerical example is given to show this property and to investigate the maximum stress occuring.
Consider a cathode domain Ω_c consisting of two hemispheres with radius 50 in the domain $\Omega=(0,100)^3$, see Figure 4.25. The centers of the two hemispheres are given as $\boldsymbol{M}_1=(0,50,50)$ and $\boldsymbol{M}_2=(100,50,50)$. The domain Ω_c is then defined as

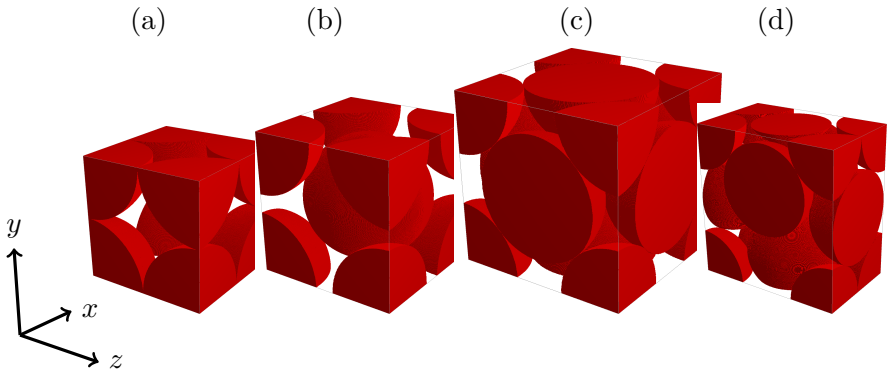

Figure 4.24: Unit cell of uncoated spherical packings. (a) SC. (b) BCC. (c) FCC. (d) HCP.

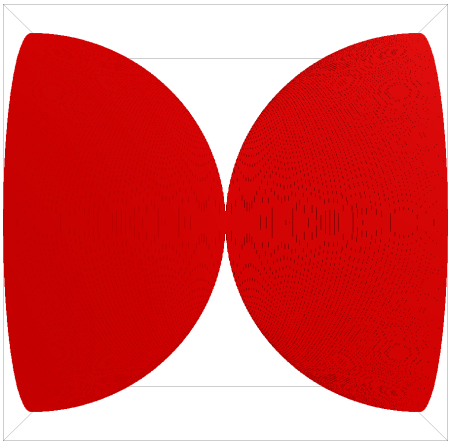

Figure 4.25: Microstructure for computation of elastic stresses

$$\Omega_c = \{||\boldsymbol{x} - \boldsymbol{M}_1|| < r \wedge ||\boldsymbol{x} - \boldsymbol{M}_2|| < r\}\,, \tag{4.31}$$

and $\Omega_e = \Omega \setminus \Omega_c$ is the electrolyte domain. A static elastic problem is considered and the concentration c inside the electrode material is set to the constant value $c(\boldsymbol{x}) = 0.5c_{\mathrm{max,c}}$. The elastic constants in cathode and electrolyte are chosen according to Table 2.2. Periodic boundary conditions are chosen in all three spatial dimensions. The spatial discretization with $N_1 = N_2 = N_3$ is chosen from $N_1 \in \{30, 40, \ldots, 250\}$.
Figure 4.26 (a) shows the resulting von-Mises stress along the line from $\boldsymbol{M}_1$ to $\boldsymbol{M}_2$. The solution for the von-Mises stress does not converge. Figure 4.26 (b) shows the maximum von-Mises stress. A limit value of the maximum von-Mises stress cannot be extrapolated.

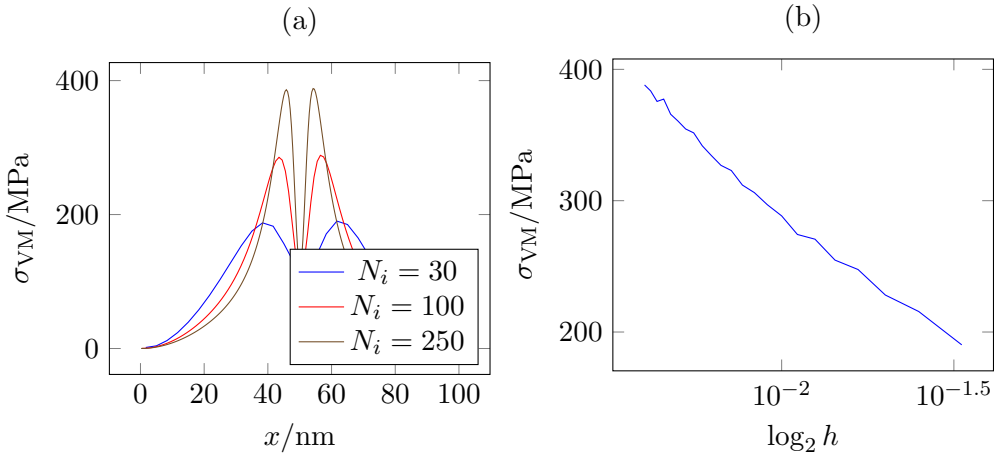

Figure 4.26: von-Mises stress in an uncoated microstructure. (a) Along the line from M_1 to M_2. (b) Maximum von-Mises stress.

4.3.2 Coating algorithms

In order to give a well-posed elastic problem, a coating is introduced that enlarges the domain and gives a smooth surface of the domain Ω_c. Assume a pair of points $P = (\boldsymbol{M}_1, \boldsymbol{M}_2)$ that consists of two centers of spheres with the same radius R touching each other in a point. Therefore, it holds $||\boldsymbol{M}_1 - \boldsymbol{M}_2|| = 2R$.
A local cylindric coordinate system is defined by projection onto (z, r) from the global coordinates $\boldsymbol{x} = (x_1, x_2, x_3)$. The third degree of freedom, the rotational angle around the center axis is neglected due to an assumption of axial symmetry for a coating algorithm. The projection ϕ is then given as

$$\phi : \begin{cases} \mathbb{R}^3 & \to \mathbb{R}^2, \\ \boldsymbol{x} & \mapsto \begin{pmatrix} z \\ r \end{pmatrix} = \begin{pmatrix} (\boldsymbol{x} - \boldsymbol{M}_1) \circ \frac{\boldsymbol{M}_1 - \boldsymbol{M}_2}{||\boldsymbol{M}_1 - \boldsymbol{M}_2||} \\ ||(\boldsymbol{x} - \boldsymbol{M}_1) \times \frac{\boldsymbol{M}_1 - \boldsymbol{M}_2}{||\boldsymbol{M}_1 - \boldsymbol{M}_2||}|| \end{pmatrix}. \end{cases} \tag{4.32}$$

A coating function f is defined as

$$f : \begin{cases} \mathbb{R}^2 & \to \{0, 1\}, \\ \begin{pmatrix} z \\ r \end{pmatrix} & \mapsto f \begin{pmatrix} z \\ r \end{pmatrix}. \end{cases} \tag{4.33}$$

A coating domain is defined as a subset Ω_{coat} of the domain Ω_e and is given as

$$\Omega_{\mathrm{coat}} = \{\boldsymbol{x} \in \Omega_e | f(\phi(\boldsymbol{x})) = 1\}. \tag{4.34}$$

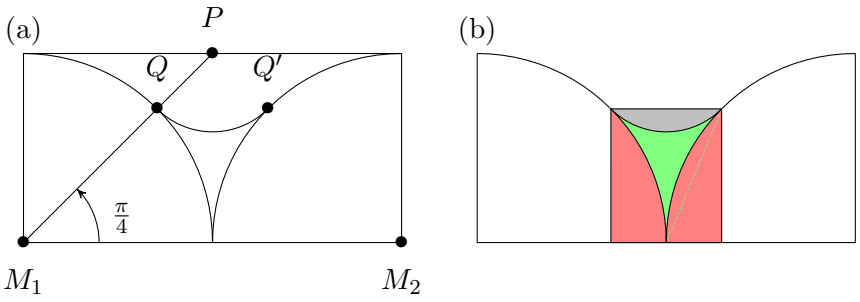

Figure 4.27: (a) Diagram for the derivation of the circle coating. (b) Diagram for the derivation of the volume fraction of the circle coating.

The following properties are required for a valid coating:

- *Bounded coating:* $f(z,r) = 0$ if $(z,r) \notin [0,R] \times [0,2R]$.

  This restricts the coating to a reasonable domain around the contact point.

- *Axial symmetry:* $f(z,r) = f(2R-z,r)\ \forall (z,r) \in [0,R] \times [0,2R]$.

  This ensures that the coating is axially symmetric such that the mapping from the set of center points to the ordered pairs $P = (\boldsymbol{M}_1, \boldsymbol{M}_2)$ is invariant to permutation.

- *Simply connected:* $\Omega_c \cup \Omega_{\text{coat}}$ is simply connected.

  This reflects the basic property of a coating to be adhesive to the surface of the coated domain such that no holes are generated by the coating.

- *Smoothing:* The boundary of $\Omega_c \cup \Omega_{\text{coat}}$ is smooth.

  This should prevent the divergent elastic solution as shown in Figure 4.26.

Next, two different coating functions are defined that fulfill the presented requirements. The analytic description of the coating function f is given as well as the volume fraction of the coating. The geometric derivations are supported by well-known formulas available in standard mathematical handbooks, e.g. [101].

4.3.3 Circle coating

Figure 4.27 (a) depicts the projection domain $[0,2R] \times [0,R]$. The points M_1, M_2, P and Q have local coordinates $(0,0)$, $(2R,0)$, (R,R) and $(\frac{\sqrt{2}}{2}R, \frac{\sqrt{2}}{2}R)$ respectively. Additionally, values $z_l = \frac{\sqrt{2}}{2}R$ and $z_r = \left(2 - \frac{\sqrt{2}}{2}\right) R$ are introduced, the r-coordinates of Q and Q'.
A function $c(r,z) : [0,2R] \times [0,R] \to \mathbb{R}$ is introduced as

$$c(r,z) = (z-R)^2 + (r-R)^2 - (\sqrt{2}-1)^2 R^2 \tag{4.35}$$

The level set $\{c = 0\}$ includes the circle arc going through Q and Q'. The coating function is then

$$f(z,r) = \begin{cases} 0, & \text{if } z < z_l, \\ \theta(c(r,z)), & \text{if } z_l \leqslant z \leqslant z_r, \\ 0, & \text{if } z_r < z, \end{cases} \tag{4.36}$$

where θ is the Heaviside function. This relates to the area under the parabola.
Figure 4.27 (b) introduces several colored domains for the derivation of the volume of the coating domain (green). The volume of the rotational body resulting from the gray segment is now calculated. Guldin's formula gives the volume of a rotational body as $V = 2\pi r_s A$, where A is the area of the rotating shape and r_s the distance of the centroid of it to the rotation axis. The area of a segment and a centroid are given as

$$A(\xi,q) = \frac{q^2}{2}\left(2\xi - \sin(2\xi)\right), \quad d(\xi,q) = \frac{4q\sin^3(\xi)}{3\left(2\xi - \sin(2\xi)\right)}, \tag{4.37}$$

where ξ is the angle and q is the radius of the segment [101]. The value of d gives the distance of the centroid from the radius. The values for angle and radius are $\xi = \frac{\pi}{4}$ and $q = (\sqrt{2}-1)R$, respectively. The distance of the centroid to the rotational axis is then $r_s = R - d(\xi,q)$.
The volume of a spherical cap (red in Figure 4.27) is $V_{\text{Cap}}(q,h) = \frac{\pi h^2}{3}(3q-h)$, where q is the radius and h is the height. Here, $q = r$ and $h = 1 - \cos\left(\frac{\pi}{4}\right)$.
The volume of a cylinder consisting of the colored parts in Figure 4.27 is $V_{\text{Cyl}} = \pi q^2 h$, where q is the radius and h is the height. Here, $h = 2 - 2\cos\left(\frac{\pi}{4}\right)$ and $q = \sin\left(\frac{\pi}{4}\right)$.
The volume of the coating is then given as

$$\begin{aligned} V_{\text{Coating}} &= V_{\text{Cyl}} - V_{\text{Seg}} - 2V_{\text{Cap}} = \\ &= \frac{1}{2}\left(2\sqrt{2}-3\right)(\pi-4)\,\pi R^3 \\ &\approx 0.231346 r^3 \end{aligned} \tag{4.38}$$

4.3.4 Parabola coating

Figure 4.28 depicts the projection domain $[0, 2R] \times [0, R]$. The point Q has coordinates $(R\cos(\alpha), R\sin(\alpha))$. Additionally, values $z_l = R\cos(\alpha)$ and $z_r = R(2 - \cos(\alpha))$ are introduced. The parabola is represented as the level set of the function $p(r,z) = a(z -$

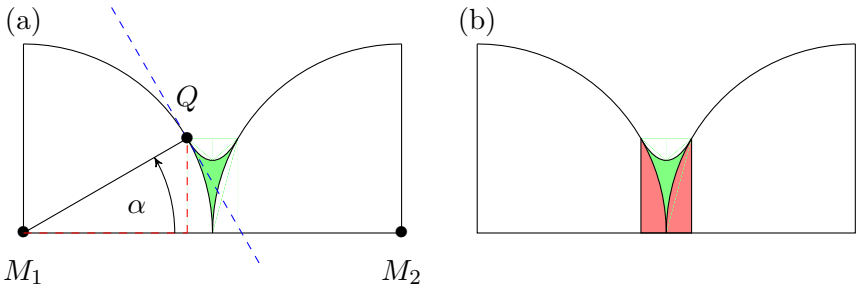

Figure 4.28: (a) Diagram for the derivation of the parabola coating. (b) Diagram for the derivation of the volume fraction of the parabola coating.

$x_s)^2 + b - r$, with $a, b, x_s \in \mathbb{R}$ being the parameters. Then $x_s = R$ due to axial symmetry of M_1 and M_2. Furthermore,

$$R\cos(\alpha) = a(R\sin(\alpha) - R)^2 + b, \tag{4.39a}$$
$$-\cot(\alpha) = 2a(R\sin(\alpha) - R), \tag{4.39b}$$

where (4.39a) results from Q being on the parabola and (4.39b) results from the requirement that the slope is continuous at Q in order to get a C^1-boundary. This gives

$$\begin{aligned} a &= -\frac{\cot(\alpha)}{2(r\cos(\alpha) - r)}, \\ b &= R\sin(\alpha) + \frac{1}{2}R\cot(\alpha)(\cos(\alpha) - 1). \end{aligned} \tag{4.40}$$

The coating function is then

$$f(z,r) = \begin{cases} 0, & \text{if } z < z_l, \\ \theta(p(r,z)), & \text{if } z_l \leqslant z \leqslant z_r, \\ 0, & \text{if } z_r < z, \end{cases} \tag{4.41}$$

where θ is the Heaviside function.
Figure 4.27 (b) introduces several colored domains for the derivation of the volume of the coating domain (green). The volume of the rotational body given by the parabola is given as an integral,

$$V_{\text{Para}} = \pi \int_{z_l}^{z_r} (a(x - x_s)^2 + b)^2 \mathrm{dx}. \tag{4.42}$$

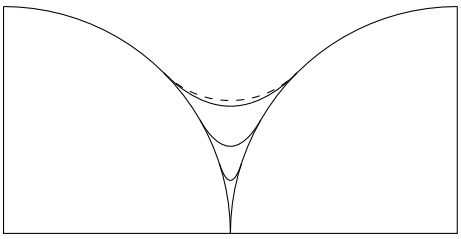

Figure 4.29: Comparison of circle and parabola coating for different angles α.

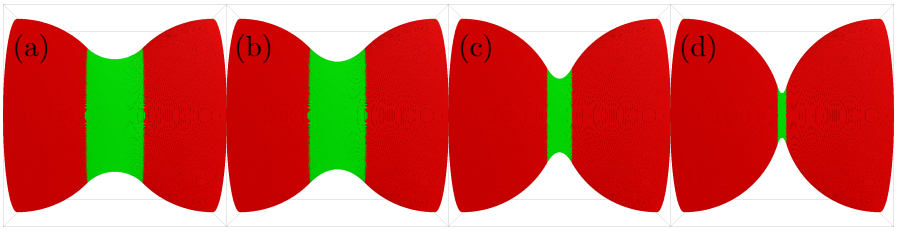

Figure 4.30: Coatings of the elastic test microstructure. (a) Circle coating. (b)-(d) Parabola coating for different angles α.

The volume of the spherical caps V_{Caps} is calculated as shown in the previous subsection. The volume of the coating is then given dependent on the angle α as

$$\begin{aligned} V_{\text{Coating}}(\alpha) &= V_{\text{Para}} - 2V_{\text{Cap}} = \\ &= \frac{16}{15}\pi(6 + 5\cos(\alpha) + \cos(2\alpha)\csc(\alpha)^2 \sin(\frac{\alpha}{2})^6 r^3, \\ V_{\text{Coating}}(\frac{\pi}{4}) &\approx 0.20072 r^3, \\ V_{\text{Coating}}(\frac{\pi}{6}) &\approx 0.0436365 r^3, \\ V_{\text{Coating}}(\frac{\pi}{10}) &\approx 0.00594741 r^3. \end{aligned} \tag{4.43}$$

4.3.5 Comparison of coatings

Figure 4.29 shows the circle coating and the parabola coating for $\alpha \in \{\frac{\pi}{4}, \frac{\pi}{6}, \frac{\pi}{10}\}$. With $\alpha = \frac{\pi}{4}$, the parabola coating uses the same analytic contact points as the circle coating but it has smaller volume fraction. Figure 4.30 shows those four different coatings in a 3D representation. In red the two hemispheres can be seen, in green the coating. Table 4.14 gives numerical values for the volume fraction of the different coatings. Several spatial discretizations are realized and the result is compared to analytical limits. The volume of the sphere itself is in this case $\frac{4\pi}{3}R^3 \approx 4.19R^3$.
Figure 4.31 shows unit cells of coated spherical packings.

Coating function	$N_x = 64$	$N_x = 128$	$N_x = 256$	$N_x = 512$	Analytical sol.
Circle	0.230957	0.230530	0.231510	0.231329	0.231346
Parabola, $\alpha = \frac{\pi}{4}$	0.199219	0.199127	0.200932	0.200720	0.20072
Parabola, $\alpha = \frac{\pi}{6}$	0.042480	0.043365	0.043635	0.043640	0.0436365
Parabola, $\alpha = \frac{\pi}{10}$	0.005615	0.005676	0.005920	0.005932	0.00594741

Table 4.14: Volume fractions as parts of R^3

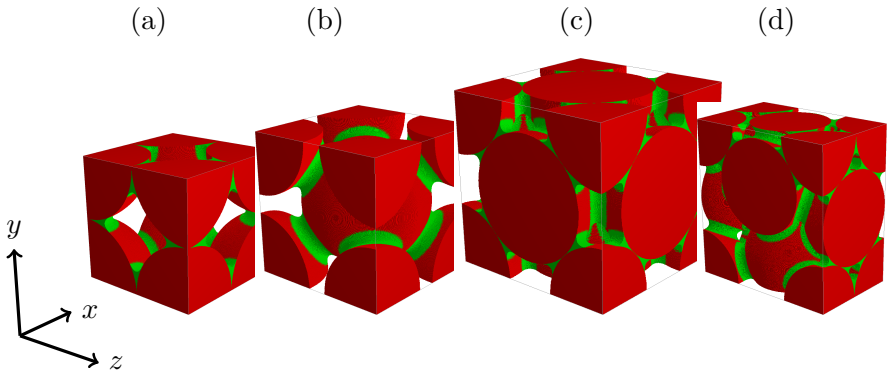

Figure 4.31: Unit cell of coated spherical packings. (a) SC. (b) BCC. (c) FCC. (d) HCP.

4.3.6 Numerical test of the coating

The static elastic test given before is repeated with a coated domain. The parabola coating function is chosen with $\alpha = \frac{\pi}{6}$. The coating is added to the electrode material, $\Omega_c := \Omega_c \cup \Omega_{\text{coat}}$. All other parameters are set to the same values.
Figure 4.32 (a) shows the resulting von-Mises stress along the line from $\boldsymbol{M}_1$ to $\boldsymbol{M}_2$. The solution converges numerically to a limit. Figure 4.32 (b) shows the maximum von-Mises stress in the domain against the spatial discretization width h. For the problem with the coated domain, there is convergence to a value for the maximum von-Mises stress inside the domain.

4.4 Electro-chemical examples

In this section, the algorithm NWT is used for examples of the electro-chemical model in 1D and 2D. The simulation is restricted to short simulation times and high C-rates between 10 and 100 to minimize the computational effort. If not noted otherwise, the material parameters of Table 2.2 are applied as well as Model A, (2.33), for the exchange current density. Lengths are given in nanometers.

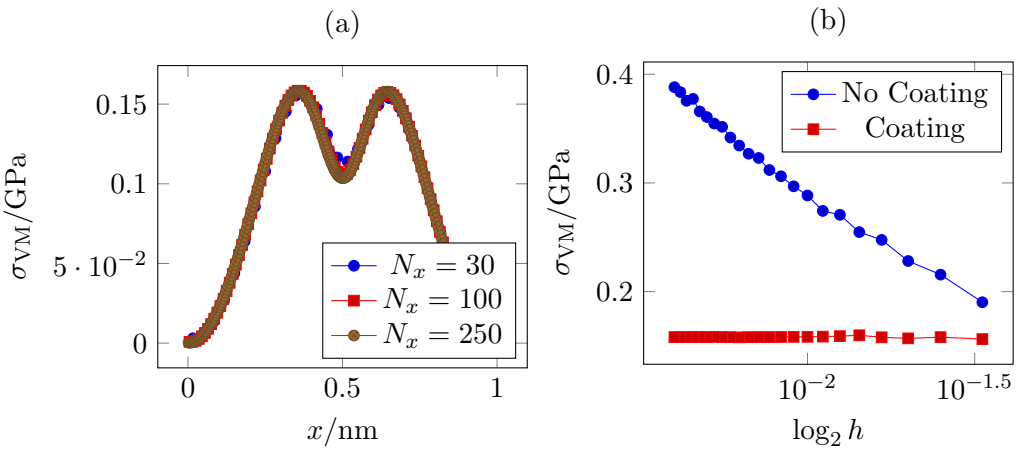

Figure 4.32: von-Mises stress in a coated microstructure. (a) Along the line from M_1 to M_2. (b) Maximum von-Mises stress.

First, the spinodal decomposition in a $LiFePO_4$ cathode is demonstrated in Subsection 4.4.1. Different models for the exchanges current density are compared in Subsection 4.4.2. The cell voltage is analyzed in Subsection 4.4.3 and both size and shape of cathode particles are varied in Subsection 4.4.4. A simulation of a complex microstructure is given in Subsection 4.4.5 and negative C-rates are analyzed in Subsection 4.4.6.

4.4.1 Spinodal decomposition

Set $\Omega = (0, 100)^2$ and $C = 100$. A microstructure with a half-circle cathode is considered, see Figure 4.33. The mesh Ω_h is applied with $N_1 = N_2 = 400$.
Figure 4.34 shows the cathode particle at SOC=0.25. Figure 4.35 shows the lithium ion concentration along the indicated line in Figure 4.34 for different SOC. In the beginning at SOC=0.05 the concentration inside the particle increases uniformly at the surface and in the center of the particle. This is called the bulk state or solid-diffusion state. The diffusivity coefficient inside the solid material is high enough in comparison to the particle radius to distribute the lithium ion flux at the electrode-electrolyte boundary. As soon as SOC=0.12[7] is exceeded, the lithium ions inside the particle separate in lithium-rich and lithium-poor phases. The exact distribution of the phases inside the particle depends on the microstructure, the C-rate, and the parameters used in the phase-field model. While in the bulk state the lithium ion concentration exhibits a radial symmetry inside the circular particle, this symmetry is broken in the phase-separated state in favor of two lithium-rich phases at the surface. At SOC=0.1225 the lithium ion concentration at the surface reaches the maximum equilibrium concentration $c = 0.987 c_{\max,\mathrm{c}}$ and a

[7] Concentration c_S in Figure 4.1

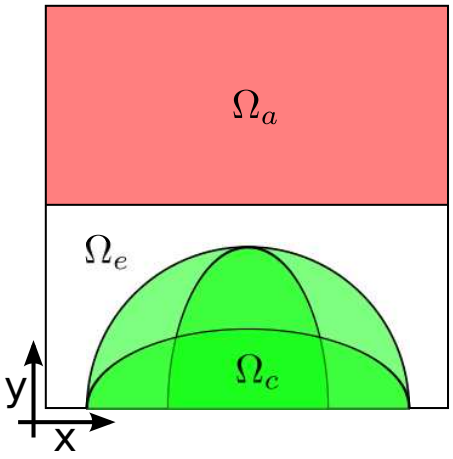

Figure 4.33: Battery microstructure with a half-circle or ellipsoidal cathode in 2D.

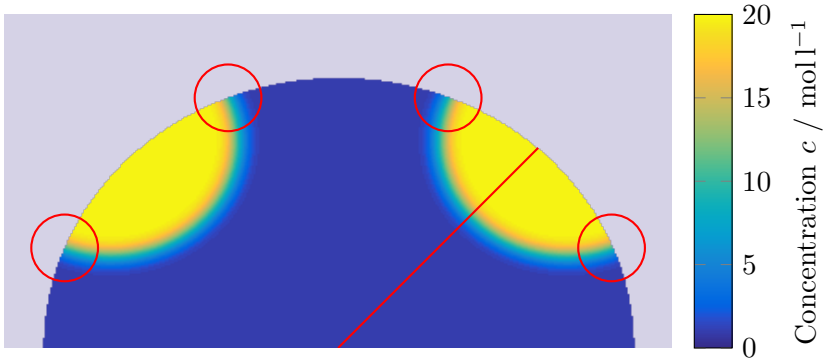

Figure 4.34: Spinodal decomposition in a half-circle cathode particle.

lithium-rich phase is established. Finally at SOC=0.25 the phase-separation is completed and a lithium-poor phase has emerged with the minimum equilibrium concentration $c = 0.013 c_{\max,c}$.

4.4.2 Exchange current densities

In this example, the coexistence of lithium-poor and lithium-rich phase is encouraged by the initial conditions and the resulting Butler-Volmer current density is evaluated. Different models for the exchange current density i_0 are compared.
In spherically symmetric phase-field models [148, 31], the concentration gradient in the electrode material is by definition of the model perpendicular to the surface. The abundance of a concentration gradient along the interface simplifies the choice of a consistent

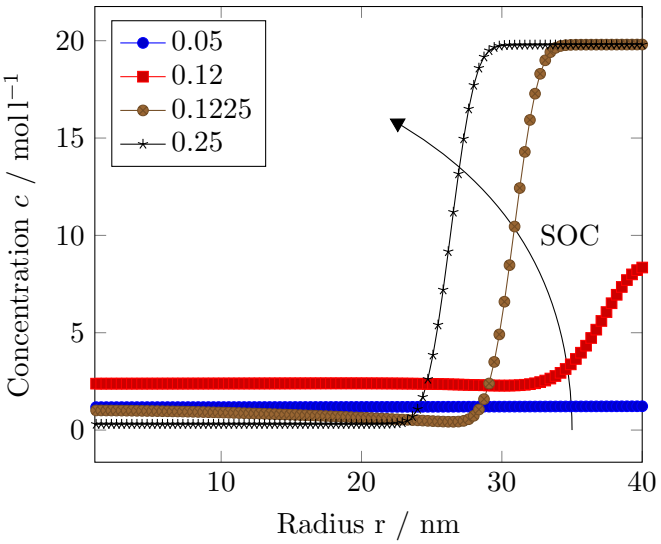

Figure 4.35: Concentration along the indicated line in Figure 4.34 for different SOC.

exchange current density i_0 in the Butler-Volmer equations. In the presented electrochemical model, it is expected that both lithium-rich and lithium-poor phases emerge along the surface of the solid material at the same time. Hence it is also possible that a phase interface region exists along the particle surface. Figure 4.34 shows the phase interface region at the particle surfaces indicated by red circles.
Set $\Omega = (0, 10) \times (0, 100)$ and $C = 100$. A flat layered microstructure is considered, see Figure 4.36. The mesh Ω_h is applied with $N_1 = 40$ and $N_2 = 400$. The initial lithium ion concentration in the cathode is shown in Figure 4.37 (a). Both Model A and B, see (2.33) and (2.34), are used for the simulation as well as different interface lengths L ranging from 3.3 nm to 16.7 nm.
Figure 4.37 (a) shows the lithium ion concentration at SOC=0.5. The center of the phase interface region is at 50 nm. On the left resides a lithium-rich phase, on the right a lithium-poor phase. Figures 4.37 (b)-(c) show the current density i_{se} along the cathode-electrolyte interface. For Model A, the surface current density is large in the lithium-rich phase and rises near the phase interface region. In the lithium-poor phase it is ten times smaller than at the maximum. For Model B, the surface current density is distributed equally to both lithium-rich and lithium-poor phases.
Table 4.15 shows the fraction of the electric current through the phase interface region for different phase-field interface widths L and both exchange current density models. For both models a considerable part of the electrode-electrolyte current flows through the phase interface region.

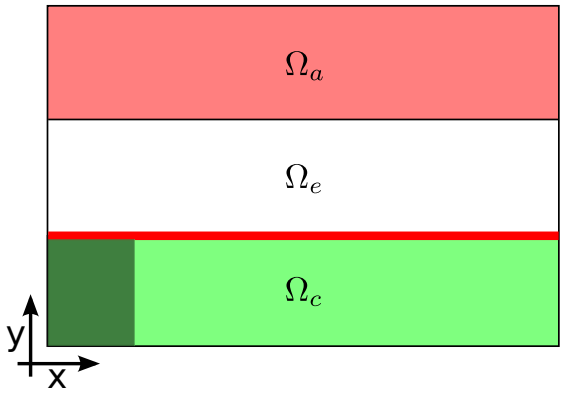

Figure 4.36: Flat three-layer microstructure with phase nucleation region (dark green).

Interface width	16.7	13.3	10.0	6.7	3.3
Model A (2.33)	22.74%	21.28%	16.86%	11.81%	9.44%
Model B (2.34)	36.81%	35.76%	29.83%	22.10%	17.50%

Table 4.15: Fraction of electric current through phase interface region for two different exchange current density models.

4.4.3 Cell voltage

In this example, the influence of the C-rate on the cell voltage is investigated. The cell voltage is defined as the difference of the electric potential between anode and cathode. Due to high conductivity, the electric potential is approximately constant inside each domain. First, the jump $\phi_{se,s} - \phi_{se,e}$ in the electric potential at the solid-electrolyte interfaces will be examined separately for anode and cathode. Then the cell voltage as the sum of both jumps will be discussed later.

4.4.3.1 1D structure

Set $\Omega = (0, 100)$ with $\Omega_a = (0, 40)$, $\Omega_e = (40, 60)$ and $\Omega_c = (60, 100)$ with $C \in \{10, 20, 50, 100\}$ and $N_1 = 400$.
Figure 4.38 (a) shows the potential jump at the anode-electrolyte interface. In an equilibrium state the Nernst overpotential η in (2.31) is zero and the concentration inside the anode particle is constant due to diffusion. The potential jump $\phi_{ae,a} - \phi_{ae,e}$ can be expressed using the logarithmic diffusion potential $\mu_a(c)$ depending on the SOC as

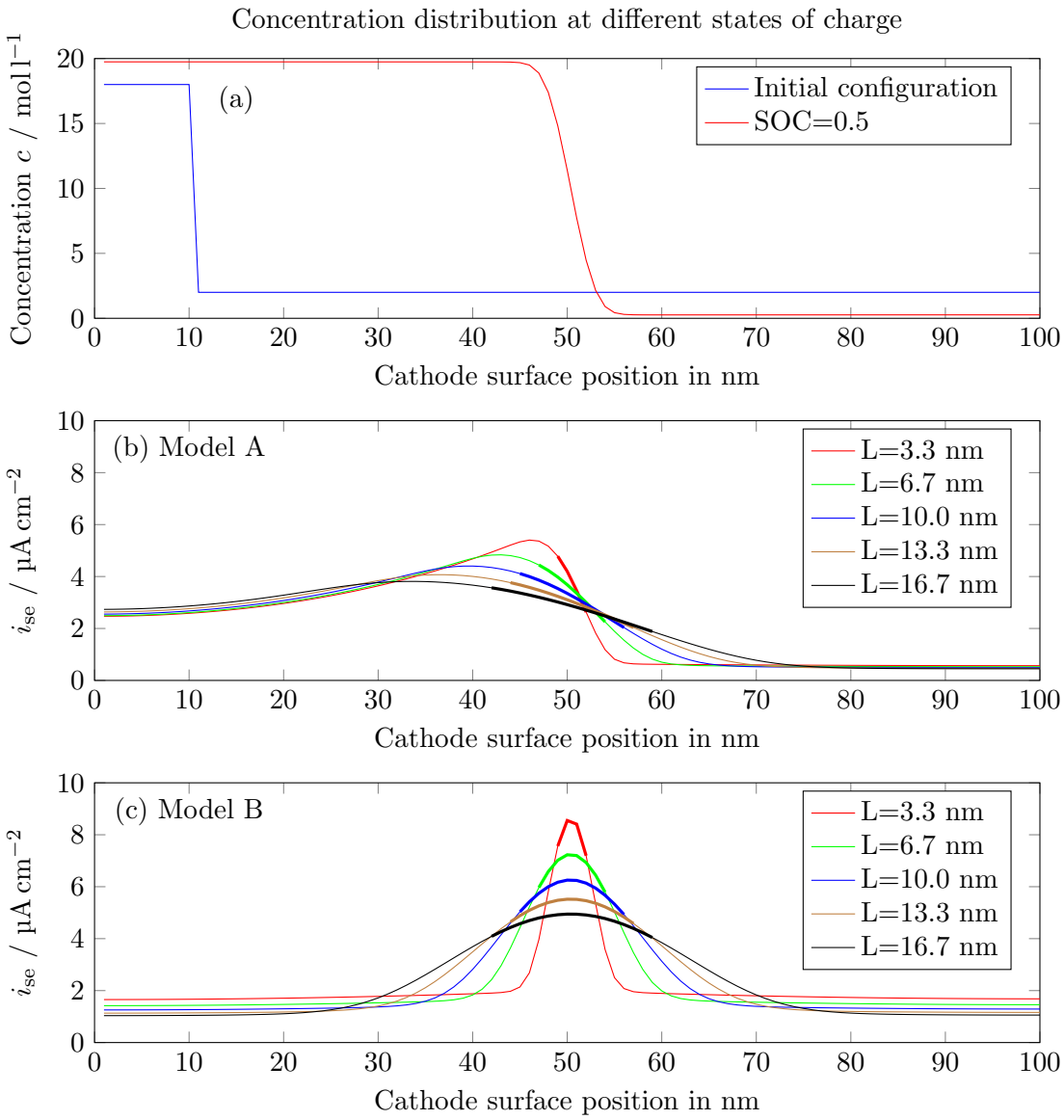

Figure 4.37: (a) Lithium ion concentration in the initial state and for SOC=0.5. (b)-(c) Butler-Volmer current i_{se} along the cathode-electrolyte interface for different phase-field interface lengths L.

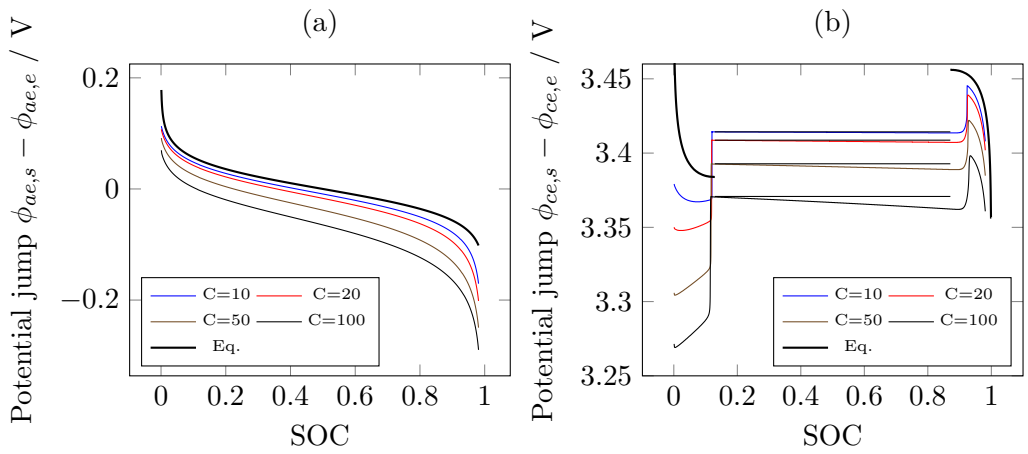

Figure 4.38: (a) Potential jump at the anode-electrolyte interface. (b) Potential jump at the cathode-electrolyte interface.

$$\begin{aligned} \eta &= \phi_{ae,a} - \phi_{ae,e} - \bar{U}_a + \frac{\mu_a(c)}{F} = 0 \\ \Rightarrow \phi_{ae,a} - \phi_{ae,e} &= \bar{U}_a - \frac{\mu_a(c)}{F} = \bar{U}_a - \frac{RT}{F} \log \frac{SOC}{1 - SOC}. \end{aligned} \tag{4.44}$$

Figure 4.38 (a) shows this approximation to the equilibrium state. The voltage curves approach the analytical approximation in (4.44) for smaller C-rates, because the Nernst overpotential η gets smaller. Figure 4.38 (b) shows the potential jump at the cathode-electrolyte interface. The vertical dotted lines show the states of charge that correspond to the spinodal decomposition points. The equilibrium solution for the potential jump $\phi_{ce,c} - \phi_{ce,e}$ at the electrolyte-cathode interface can be derived as

$$\begin{aligned} \eta &= \phi_{ce,c} - \phi_{ce,e} - \bar{U}_c + \frac{\mu_c(c)}{F} = 0 \\ \Rightarrow \phi_{ce,c} - \phi_{ce,e} &= \bar{U}_c - \frac{\mu_c(c)}{F}. \end{aligned} \tag{4.45}$$

Figure 4.38 (b) shows this approximation to the equilibrium state in the bulk state region. For the SOC between spinodal decomposition points another approximation can be given. Given the Maxwell construction and the higher equilibrium concentration $c_2 \approx 0.987 c_{\max,c}$ the resulting plateau electric potential can be calculated. The interface condition in (2.29) is solved for the potential jump $\phi_{ce,c} - \phi_{ce,e}$ at the electrolyte-cathode interface. The chemical potential $\mu_c(c)$ inside the solid at the particle surface is zero in a phase-separated state in equilibrium, so the potential jump is given as

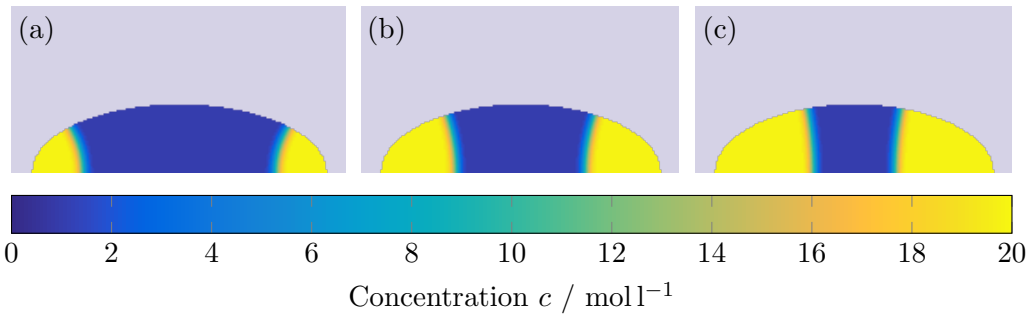

Figure 4.39: (a)-(c) An ellipsoidal particle for SOC $\in \{0.2, 0.4, 0.6\}$.

$$\phi_{ce,c} - \phi_{ce,e} = \bar{U}_c - 2\frac{RT}{F}\,\text{arcsinh}\left(\frac{i_{\text{se}}}{2k\sqrt{c_{e,0}c_2\frac{c_{\max,c}}{2}}}\right). \tag{4.46}$$

This approximation depends on the C-rate. Figure 4.38 (b) shows this approximation to the equilibrium state in the phase-separated region for different C-rates. The transient simulation deviates from the equilibrium solution for larger SOC as the surface concentration rises. The phase-separated state ends when the phase interface collides with the boundary of the cathode particle. The lithium ion concentration is then distributed evenly in the particle and the equilibrium solution for the bulk state is valid again

4.4.3.2 2D structure

Set $\Omega = (0, 100)^2$ with $C \in \{10, 20, 50, 100\}$ and $N_1 = N_2 = 400$. Figure 4.33 introduces structures of different ellipsoidal particles. Choose an ellipsoidal cathode particle with axes 80 nm and 40 nm.
Figure 4.40 (a) shows the potential jump at the cathode-electrolyte interface with equilibrium approximations as derived before. In the previous 1D example, the potential jump decreases with time in the phase-separated state for SOC $\in (0.13, 0.9)$. In the 2D example, the potential jump rises. Figure 4.40 (b) shows the resulting cell voltage. Small discontinuities can be seen if the cathode particle changes from bulk state to phase-separated state and vice versa at SOC 0.12 or 0.9.

4.4.4 Variation of cathode particle size and shape

In this example, the effect of cathode particle size and particle shape on the charging is examined. For transmission problems, the ratio between the size of the interface region Γ_{ce} and the volume of the domain Ω_c is important as well as the shape of the domain

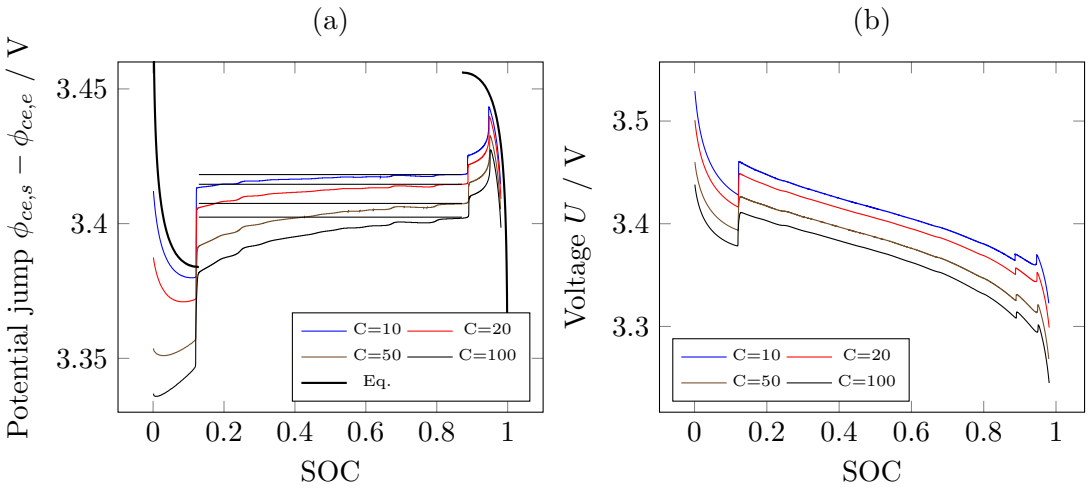

Figure 4.40: (a) Potential jump at the cathode-electrolyte interface. (b) Cell voltage.

Ω_c. The intrinsic length scale of the phase-field model results in a minimum domain size where the phase-separated state can exist, see 4.1.1.

4.4.4.1 Size effects

Set $\Omega = (0, x)^2$ with $x \in \{10, 20, 30, 40, 50\}$, $C = 100$ and $N_1 = N_2 = 200$. The half-circle cathode structure from Figure 4.19 is applied. The resulting diameters of the cathode structure are 8, 16, 24, 32, and 40 nm.
Figure 4.41 shows the cell voltage. For large particles with diameter 40 and 32 nm, the phase separation happens as shown before in 4.4.1. The critical SOC can be found by the voltage discontinuity. This $\mathrm{SOC}_{\mathrm{crit}}$ depends on the particle diameter. The smaller the particle size, the later the phase separation happens. For small particles with diameter 16 and 8 nm, no phase separation happens. The gradients in the lithium ion concentration are dominated by the large interface current[8]. Spikes and additional jumps in the cell voltage result from reorderings of the phases during the intercalation. They depend on the structure and the size of the particle.

4.4.4.2 Shape effects

Set $\Omega = (0, 100)^2$, $C = 100$ and $N_1 = N_2 = 400$. Two different ellipsoidal cathode structures are examined, a flat particle with axes $(a_1, a_2) = (80, 40)$ and a tall particle with axes $(a_1, a_2) = (40, 80)$, see Figure 4.33.

[8] Stochastic fluctuations in the lithium ion concentration may initiate phase separation in nanoparticles, but they are not considered in this work.

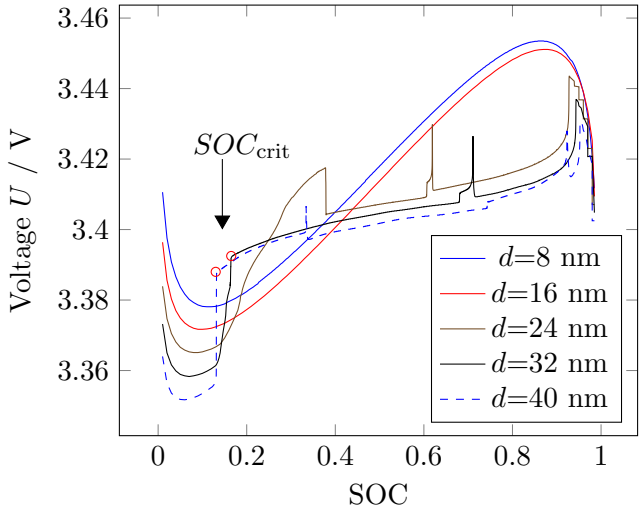

Figure 4.41: Cell voltage for different-sized particles.

Figure 4.42 shows both particles at SOC=0.14 in a phase-separated stage. Starting at the bulk phase, the surface current is constant along Γ_{ce}. For areas with large curvature, the concentration rises faster than for flat edges. Therefore, concentration gradients built up inside the particle at exposed corners. This results in the formation of lithium-rich phases.

4.4.5 Simulation of a complex microstructure

In this example a complex microstructure built from geometric shapes is used. Set $\Omega = (0, 100)^2$, $C = 100$ and $N_1 = N_2 = 400$.
Figures 4.43 (a)-(c) show the lithium ion concentration in the cathode material. The lithium-rich phases evolve at different rates as well as the phase interface. The lithium-rich phase in the middle does not grow. Its growth would cause an increase of the interface energy. The other two lithium-rich phase in the left and right branch grow. Their growth does not increase the interface energy.

4.4.6 Differences between charging and discharging

In this example, the different behavior for charging and discharging is investigated. Set $\Omega = (0, 100)$, $C = \{\pm 1, \pm 2, \pm 5\}$ and $N_1 = 400$.
Figure 4.44 (a) shows the concentration in a 1D cathode structure for $C = \pm 1$ at SOC=0.5. The cathode-electrolyte interface is shown at $x = 0$. For $C = 1$, the lithium-rich phase originates at the cathode-electrolyte interface and an empty cathode particle

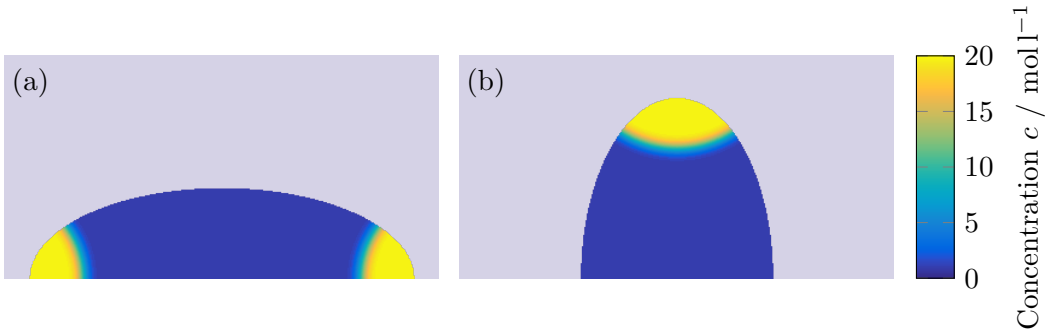

Figure 4.42: Spinodal decomposition in ellipsoidal particles (a) Flat ellipsoidal particle with two lithium-rich phases at both ends at SOC=0.14. (b) Tall ellipsoidal particle with one lithium-rich phase at SOC=0.14.

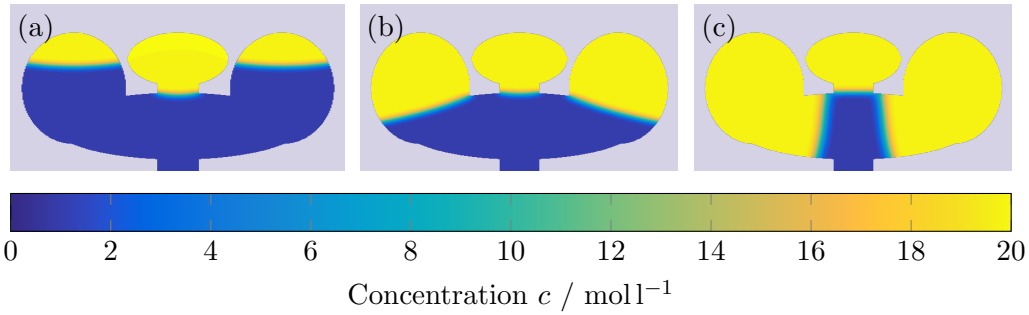

Figure 4.43: (a)-(c) Complex microstructure showing different lithium-rich phases at SOC $\in \{0.28, 0.56, 0.83\}$.

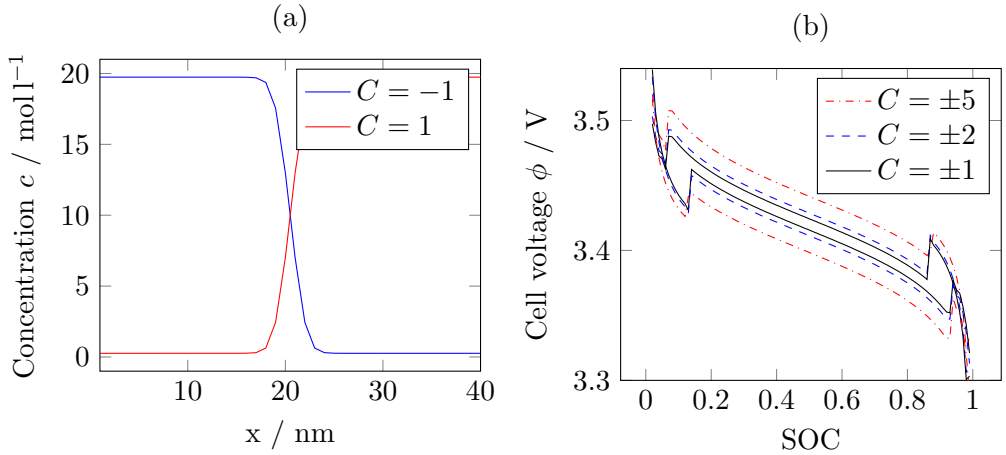

Figure 4.44: Lithium ion concentration and cell voltage for positive and negative C-rates. (a) Lithium ion concentration at SOC=0.5. (b) Cell voltage.

is charged. For $C = -1$, the lithium-poor phase originates at the cathode-electrolyte interface and a filled cathode particle is discharged.
Figure 4.44 (b) shows the cell voltage for different C-rates. For small C-rates, the difference between charging and discharging mostly disappears. The process is not totally symmetric. Phase separation happens at either SOC=0.13 (charging) or SOC=0.87 (discharging), but the reversal of the phase separation due to interface collision happens at either SOC=0.95 (charging) or SOC=0.05 (discharging).

4.5 Elastic coupling

In this section, the algorithm NWT is used for examples of the electro-chemo-mechanical model in 1D and 2D. The algorithm DD is used for examples of the electro-chemo-mechanical model in 3D. If not noted otherwise, the material parameters of Table 2.2 are applied as well as Model A for the exchange current density.
Effects of elastic coupling are investigated for structures in 1D in Subsection 4.5.1 and 2D in Subsection 4.5.2. The effect of an imposed eigenstrain is investigated in Subsection 4.5.3. Then 3D structures are analyzed, first on a spherical cathode particle in Subsection 4.5.4, then on a cathode built of multiple spheres in Subsection 4.5.5. Finally, the elastic properties of a spherical packing are analyzed in Subsection 4.5.6.

4.5.1 1D structure

Set $\Omega = (0, 100)$ with $\Omega_a = (0, 40)$, $\Omega_e = (40, 60)$ and $\Omega_c = (60, 100)$ with $C = 10$ $N_1 = 100$.
Figure 4.45 (a) shows the lithium ion concentration in the cathode particle at SOC=0.5. Figure 4.45 (b) and (c) show magnifications of interesting regions. The lithium ion concentration is shown for different values for the partial molar volume θ. As θ increases, different effects can be seen. The equilibrium concentrations change. The low equilibrium concentration gets higher and vice versa. For $\theta = 0$ cm^3 mol^{-1} they are $c_1 = 0.013 c_{\max,c}$ and $c_2 = 0.987 c_{\max,c}$, while for $\theta = 3$ cm^3 mol^{-1} they are $c_1 \approx 0.1 c_{\max,c}$ and $c_2 \approx 0.9 c_{\max,c}$. A second effect is the widening of the interface length L. For $\theta = 0$ cm^3 mol^{-1} it is $L = 3.3$ nm while for $\theta = 3$ cm^3 mol^{-1} it is $L \approx 4$ nm.
Figure 4.46 (a) shows the hydrostatic stresses in the cathode particle. First, θ is chosen as 0 cm^3 mol^{-1} and no stress occurs in the cathode material. For higher partial molar volumes, stress in both the lithium-rich phase and the lithium-poor phase occurs. At the interface a smooth transition between the two stress states can be observed that also widens according to a widening interface.
Figure 4.46 (b) shows the potential jump at the cathode-electrolyte interface. First, for higher values of θ the phase separation starts later and ends sooner. The phase-separated state is shorter compared to smaller values of θ. Second, for higher values of θ the electric potential during phase separation is lower.

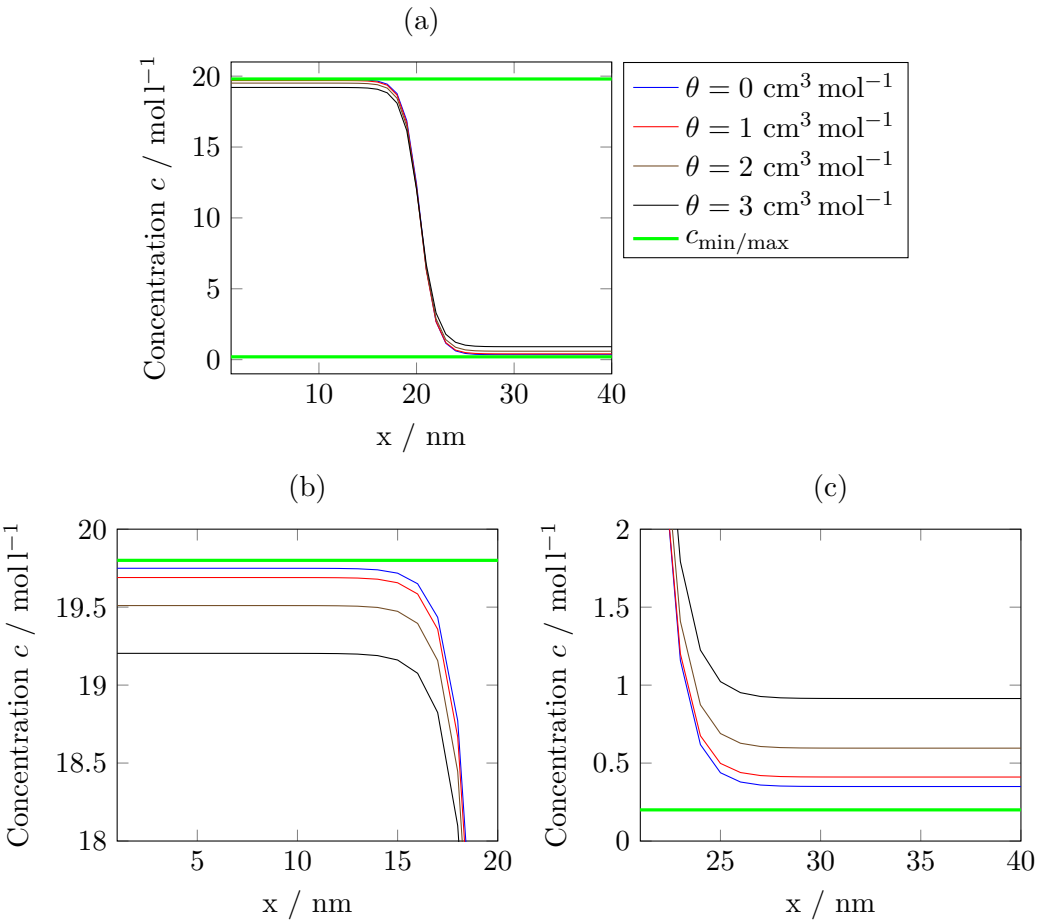

Figure 4.45: (a) Lithium ion concentration for different values of partial molar volume. (b)-(c) Magnifications of interesting regions.

4.5.2 2D structure

Set $\Omega = (0, 100)^2$, $C = 10$ and $N_1 = N_2 = 100$. Figure 4.33 introduces structures of different ellipsoidal particles. Choose an ellipsoidal cathode particle with axes 80 nm and 40 nm.
Figure 4.47 shows the voltage jump at the cathode-electrolyte interface. During phase separation, the electric potential is, similar to the 1D example, lower for higher values of θ. Additionally, numerical oscillations appear, as can be seen from the thick line for $\theta = 2$ cm^3 mol^{-1}.

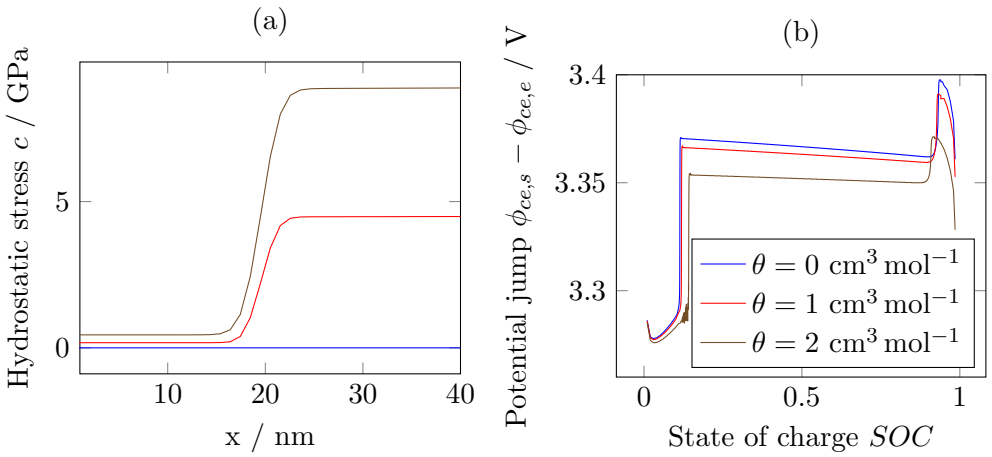

Figure 4.46: Hydrostatic Stress and cell voltage for different values of partial molar volume. (a) Hydrostatic stress. (b) Cell voltage.

4.5.3 Support of intercalation by eigenstrain

In this example, the effect of imposed eigenstrain on a battery particle is investigated. On a part of the domain Ω_c, a constant internal strain is added. The intercalation of lithium ions and the spinodal decomposition and nucleation of a lithium-rich phase is then supported in this domain. The expectation is that, compared to an example without interior strain, the lithium-rich phase prefers to expand in the part of the domain Ω_c with interior strain.
Set $\Omega = (0, 100)^2$, $C = 10$ and $N_1 = N_2 = 100$. Choose a half-circle shaped cathode particle. For the first example, the elastic strain $\boldsymbol{\varepsilon}_{\text{el}}$ is given as

$$\boldsymbol{\varepsilon}_{\text{el}} = \frac{1}{2}(\nabla \boldsymbol{u} + \nabla \boldsymbol{u}^T) - \frac{\theta}{3} c \boldsymbol{I}. \tag{4.47}$$

For the second example, the elastic strain $\boldsymbol{\varepsilon}_{\text{el}}$ is given as

$$\boldsymbol{\varepsilon}_{\text{el}} = \begin{cases} \frac{1}{2}(\nabla \boldsymbol{u} + \nabla \boldsymbol{u}^T) - \frac{\theta}{3} c \boldsymbol{I} + \boldsymbol{\varepsilon}^+_{\text{Eig}} \boldsymbol{I}, & x_1 < 50 \text{ nm}, \\ \frac{1}{2}(\nabla \boldsymbol{u} + \nabla \boldsymbol{u}^T) - \frac{\theta}{3} c \boldsymbol{I}, & x_1 > 50 \text{ nm}, \end{cases} \tag{4.48}$$

with $\boldsymbol{\varepsilon}^+_{\text{Eig}} = 0.1$. See Figure 4.48 for illustration.
Figure 4.49 shows the lithium ion concentration for different SOC with and without addition of eigenstrain. Row (a) shows a symmetric lithium ion concentration[9]. The phase separation starts at the cathode-electrolyte interface and two lithium-rich phases

[9] As has been shown in 4.4.1.

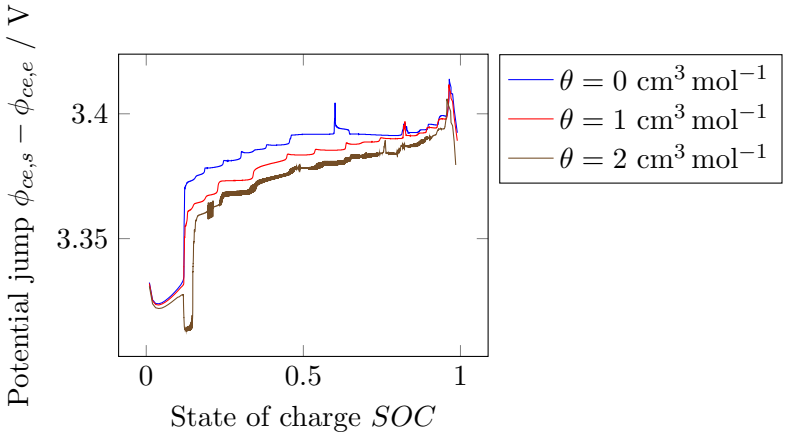

Figure 4.47: Potential jump at the cathode-electrolyte interface.

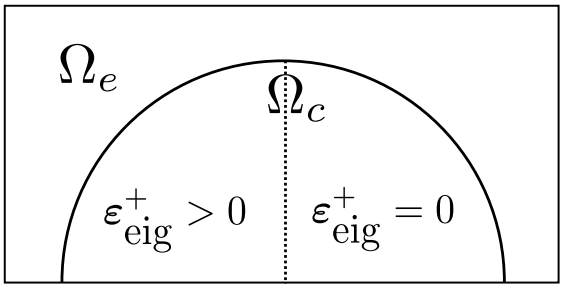

Figure 4.48: A cathode particle shaped like a half-circle with partially imposed eigenstrain.

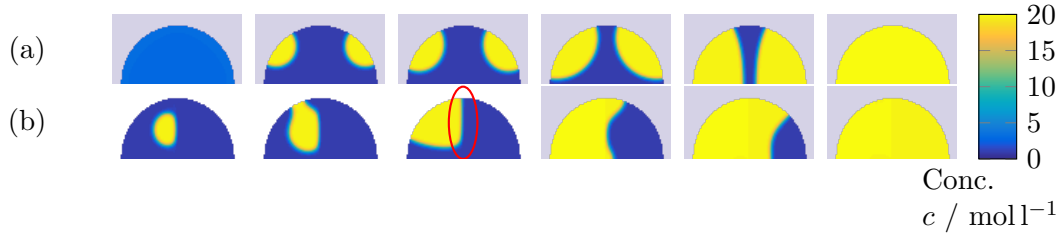

Figure 4.49: Lithium ion concentration for different eigenstrains. Row (a): Without additional eigenstrain. Row (b): With additional eigenstrain.

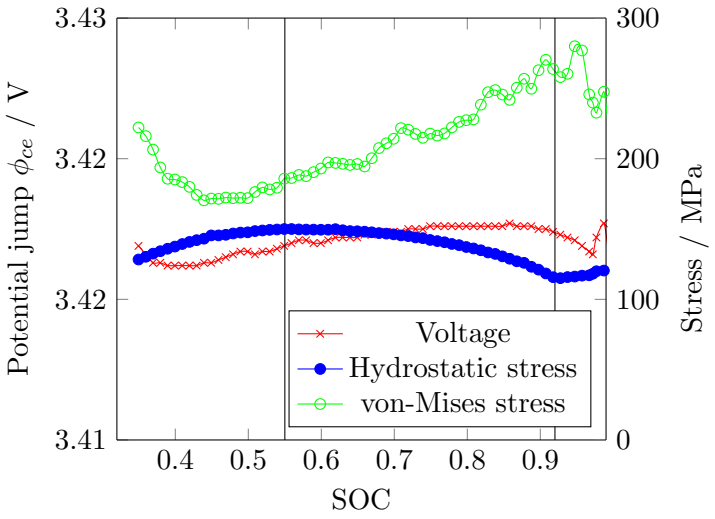

Figure 4.50: Cell voltage and stress invariants for a cathode built of a spherical particle

originate. Row (b) shows an asymmetric lithium ion concentration. The phase separation starts inside the particle at a lower SOC. The lithium-rich phase grows inside the domain with eigenstrain. The phase interface between lithium-rich and lithium-poor phase is built along the boundary between strained and unstrained domain.

4.5.4 Spherical particle

Set $\Omega = (0, 100) \times (0, 60) \times (0, 60)$, $C = 1$, $N_1 = 100$ and $N_2 = N_3 = 60$. The cathode is a spherical particle with radius $r = 30$ nm. The anode is a cuboid block.

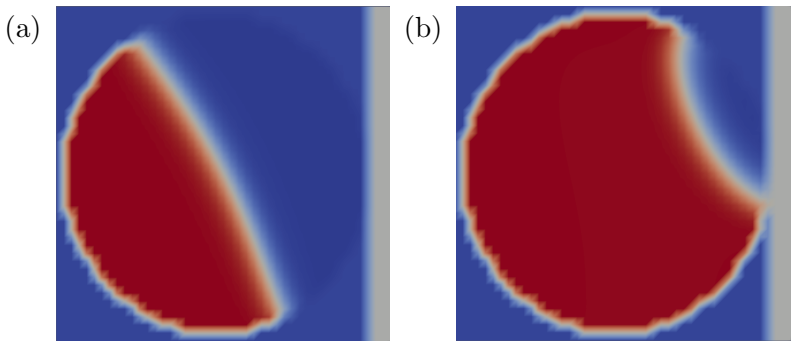

Figure 4.51: Lithium ion concentration for a cathode built of a spherical particle. (a) SOC=0.55. (b) SOC=0.92.

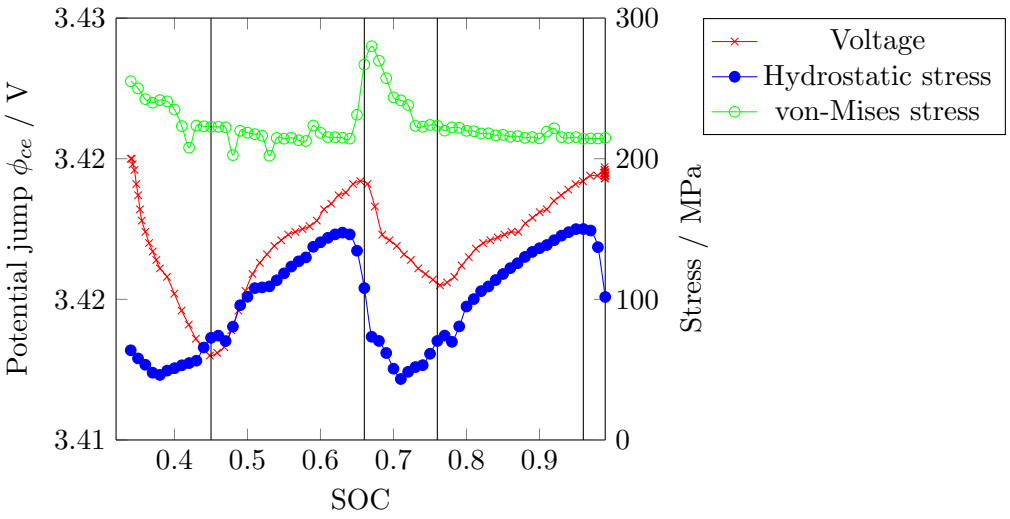

Figure 4.52: Cell voltage and stress invariants for a cathode built of multiple spherical particles

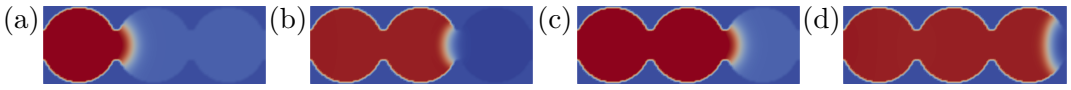

Figure 4.53: Lithium ion concentration for a cathode built of multiple spherical particles. (a)-(d) SOC $\in \{0.45, 0.66, 0.76, 0.96\}$.

Figure 4.50 shows the cell voltage as well as the maximum hydrostatic stress and the maximum von-Mises stress in the cathode particle. The plot is shown for SOC between 0.34 and 0.99 where phase separation is present. The hydrostatic stress attains its maximum around SOC=0.55 and its minimum around SOC=0.92. The von-Mises stress increases in this range.
Figure 4.51 shows the lithium ion concentration in the cathode particle at (a) SOC=0.55 and (b) SOC=0.92. The solution is rotationally symmetric and therefore a 2D projection is shown. At SOC=0.55 the particle is composed of approximately equally sized lithium-rich and lithium-poor phase.

4.5.5 Multiple spheres

Set $\Omega = (0, 320) \times (0, 60) \times (0, 60)$, $C = 1$, $N_1 = 320$ and $N_2 = N_3 = 60$. The cathode is built of three spherical particles touching each other. The parabola coating is applied between them. The anode is a cuboid block.
Figure 4.52 shows the cell voltage as well as the maximum hydrostatic stress and the maximum von-Mises stress in the cathode particle. The plot is shown for SOC between

0.32 and 0.99 where phase separation is present. Both the hydrostatic stress and the cell voltage are to some extent periodic. Local minima for the cell voltage are attained for SOC=0.45 and SOC=0.76, a local maximum for SOC=0.66. The hydrostatic stress attains its maximum at SOC=0.96.
Figure 4.53 shows the lithium ion concentration in the cathode particles at (a) SOC=0.45, (b) SOC=0.66, (b) SOC=0.76 and (d) SOC=0.96. (a) and (c) correspond to one or two completely filled particles, respectively, with small interfacial regions.

4.5.6 Spherical packings

Several spherical packings as introduced in 4.3 are applied for the generation of the microstructure of the cathode. For SC, BCC, and FCC, the simulation domain is $\Omega = (0, 200) \times (0, 100) \times (0, 100)$, $C = 1$, $N_1 = 200$ and $N_2 = N_3 = 100$. For HCP, the simulation domain is $\Omega = (0, 200) \times (0, 173) \times (0, 163)$, $C = 1$, $N_1 = 200$, $N_2 = 173$ and $N_3 = 163$. In both cases, the spatial discretization width is $h = 1$ nm. The cathode is built of one unit cell of the four spherical packings. The parabola coating is applied between them, see Figure 4.31. The anode is a cuboid block.
Figures 4.54 (a)-(b) and 4.55 (a)-(b) show the cell voltage as well as the maximum hydrostatic stress and the maximum von-Mises stress in the cathode particle. The plot is shown between SOC 0.32 and 0.99. In terms of the stresses, the simplest behavior is shown by the FCC packing. After the phase separation, both hydrostatic and von-Mises stress stay constant, although the lithium-rich phases are rearranged as can be seen from sudden shifts in the cell voltage. For SC and BCC the stresses rise constantly with the beginning of phase transformation and reach their maximum later for a high SOC. Both packings show sudden phase rearrangements, which are fewer for SC. The HCP packing shows very irregular behavior in the stresses as well as in the cell voltage. It seems that for all structures the evolution of hydrostatic and von-Mises stress are connected to each other as they show comparable progression during the charging.

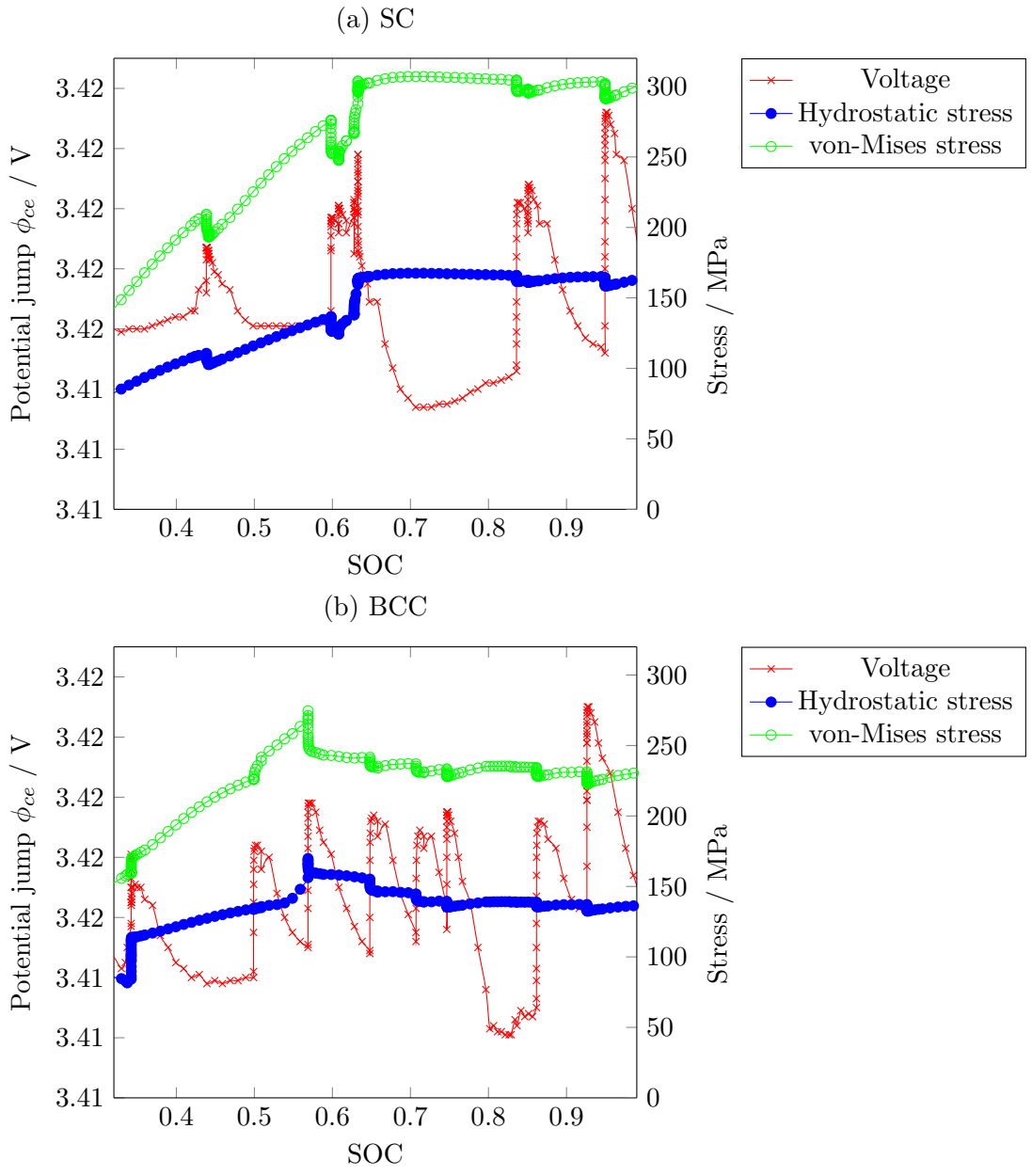

Figure 4.54: Cell voltage and stress invariants in a battery with a cathode built of spherical packings. (a) SC. (b) BCC.

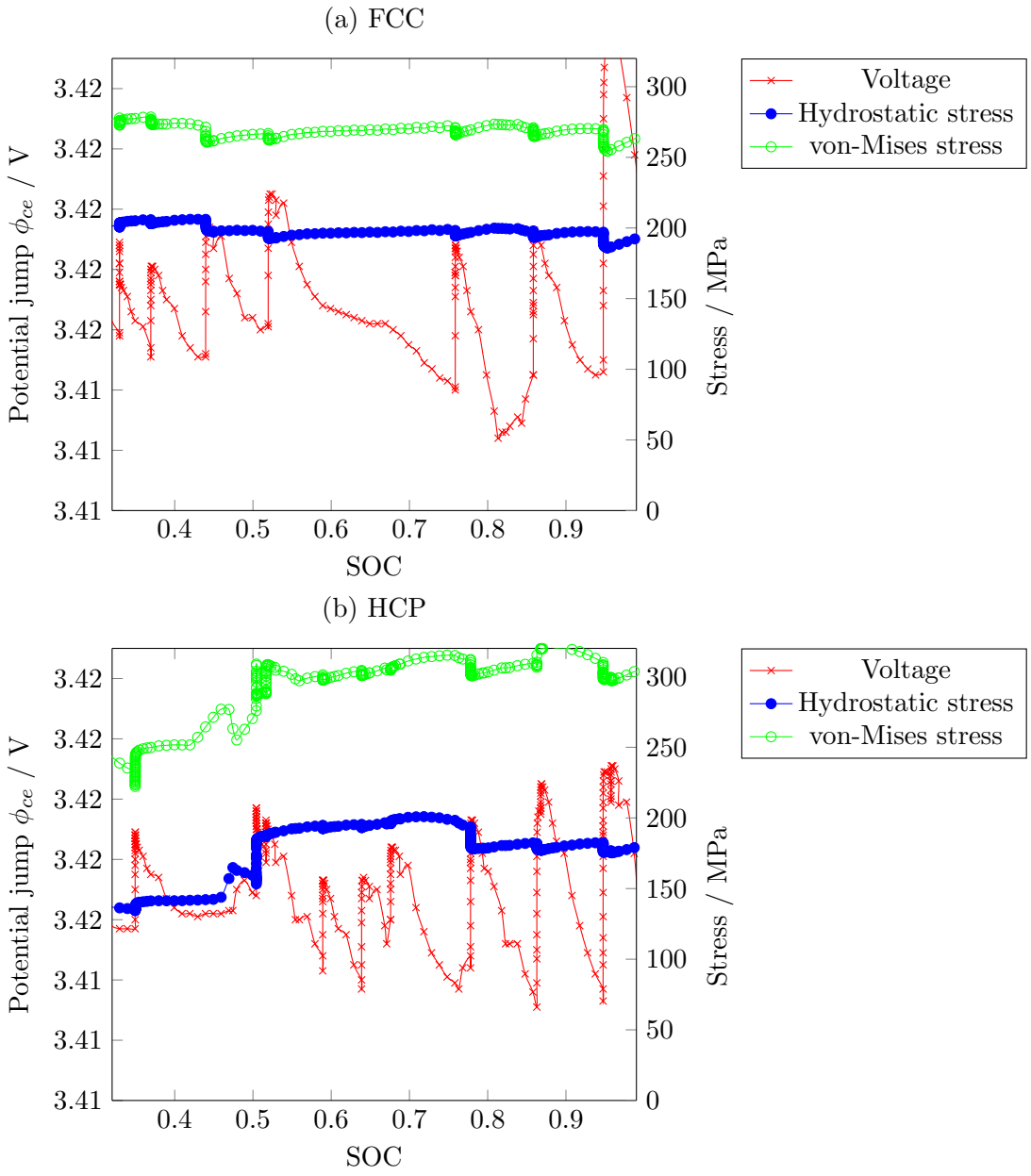

Figure 4.55: Cell voltage and stress invariants in a battery with a cathode built of spherical packings. (a) FCC. (b) HCP.

Chapter 5

Conclusion

First, a summary of the thesis is given in Section 5.1. Possible future work is discussed in Section 5.2.

5.1 Summary

In Chapter 2 an electro-chemo-mechanical model for the simulation of a lithium-ion battery on the microscale is given. The model is valid for a porous microstructure for both electrode domains. They can be generated by software or given by imaging. Several physical processes are described, including the transport of lithium ions inside each electrode and the intercalation from and into the liquid electrolyte and the combined transport of lithium ions and electrons in the liquid electrolyte. Furthermore, the electric field is modelled by a Laplace equation. The expansion of battery material is described by a chemical strain associated with the corresponding lithium ion concentration inside the electrode material. In anode and electrolyte, the mathematical model for the movement of the lithium ions is given by a classical diffusion equation with while in the cathode a model is given for the description of phase separation phenomena.
Section 2.2 deduces the multiphysics model. In Subsection 2.2.2, the governing equations are derived and the associated chemical potentials are given for anode, electrolyte and cathode. The formulation with a chemical potential in (2.15),(2.20), and (2.27) supports the dynamic analysis of charging and discharging of the battery in Section 4.1. The focus on consistent coupling conditions in (2.23) is important. Models with one-way coupling exist but their validity is diminished. Different models for the exchange current density have been introduced as Model A in (2.33) and Model B in (2.34) and compared in Subsection 4.4.2. While usually Model B is well-known and used, its validity is questionable for cathode materials showing phase separation. The interface current is channelled mainly through the phase interface region. Model A gives a better description. For the diffusion equation and the Poisson equation, both the homogeneous Neumann boundary condition may be justified as well as periodic boundary conditions. In the elastic model, periodic boundary conditions without macroscopic displacements have been prescribed.

In Chapter 3 different numerical methods are applied to the numerical solution of partial differential equations. A regular voxel mesh, a finite volume method and an implicit Euler scheme as introduced in [79] is used for the discretization of the microscale model on a cuboid domain. It is applied for both logarithmic (see [62]) and polynomial phase-field potentials.
The numerical simulation of phase separation requires very different sized time steps [149]. During the phase initiation small time steps in the range of microseconds are required. As soon as stable phases emerge, the time step can be enlarged again. In this work, an adaptive time step algorithm is presented in combination with a damped Newton scheme in Subsection 3.2.4 and demonstrated in Subsection 4.4.1.
The coupled electro-chemical model for the electrolyte (2.15) is decoupled. This requires rewriting of both the governing equations and the Butler-Volmer interface conditions. The decoupled model is given as (3.35) and (3.36). The logarithmic phase-field potential in (2.26) is replaced by the best polynomial approximation in (3.40). The Dirichlet boundary condition on the electric potential in (2.37) is replaced by a pure Neumann boundary condition in (3.42). Dirichlet boundary conditions require the application of a penalty method in the discretization. Their abundance simplifies the numerical solution. In 3.3.5 a fully decoupled algorithm is given that enables the parallel solution of the equations in the different domains. The information exchange is given by means of the Butler-Volmer interface currents.
The numerical solution of the Poisson equation and the diffusion equation in Section 3.4 by Fourier integration gives higher-order integration schemes for the periodic formulations in (3.69) and (3.71). On complex domains, first-order schemes are achieved by the immersed interface method in (3.77) and in (3.84). In space, finite difference approximations are applied, while in time, Gauss-Legendre methods are used. The higher-order convergence is demonstrated for the periodic Poisson equation in Subsection 4.2.1 and for the periodic diffusion equation in Subsection 4.2.2. For the Poisson equation in complex domains, the first-order discretization is compared to the second-order discretization given in [141]. All these convergence studies are performed by comparison with analytic, manufactured solutions.
While second-order time integration methods are mentioned for the Cahn-Hilliard equation in Subsubsection 4.2.5.7, the work is focused on the application of a semi-implicit first-order discretization in (3.86). The preconditioner in (3.94) reduces the number of iterations for the iterative solution of the problem as demonstrated in Subsubsection 4.2.5.2. The immersed interface is then applied to this equation and numerical first-order convergence is shown by comparison with a numerical reference solution in Subsubsection 4.2.5.1. Although not applied later in the electro-chemical model, surface-wetting can be included as demonstrated in Subsubsection 4.2.5.5. Neumann boundary conditions are applied to a porous microstructure in Subsubsection 4.2.5.6. These are later replaced by Butler-Volmer interface conditions in the domain decomposition algorithm.

In Section 4.3 the generation of microstructures composed of spherical packings is discussed. It is shown that the elastic properties of such microstructures are singular for grid refinement and not suitable for the prediction of internal stresses in Subsection 4.3.1. Subsection 4.3.2 introduces a mathematical model for the description of an additional coating on the spherical particles in order to give a well-posed elastic problem. Subsections 4.3.4 and 4.3.4 define two such coatings analytically. The volume fraction is derived dependent on the uncoated microstructure. The validity of the coating is then proven in 4.3.6. Using this, the coated microstructures can be applied for tests in Section 4.5.
In Section 4.4 several numerical tests show the electrochemical processes during the charging of a phase-separating cathode material. Between SOC 0.13 and 0.9, the cathode material undergoes phase separation into lithium-poor and lithium-rich phases in Subsection 4.4.1. Both lithium-rich and lithium-poor phase are shown to be present at the particle surface opposed to the core-shell model [5], where a spherically symmetric model predicts that either one of the phases is present at the particle surface. In Subsection 4.4.3 the electric potential difference at cathode-electrolyte interface is investigated. A discontinuity is observed as soon as the lithium-rich phase is initiated. During phase separation, a voltage plateau is observed. Size and shape of the cathode microstructure are shown to affect the emergence of lithium-rich phases in Subsection 4.4.4. Subsection 4.4.5 shows that the lithium-rich phases can grow independently in a complex microstructure.
In Section 4.5 the electro-chemo-mechanical model is applied. The equilibrium concentration in lithium-rich and lithium-poor phase is affected as well as the cell voltage in Subsection 4.5.1. Also, the emergence of lithium-rich phases is enforced by local eigenstrains in Subsection 4.5.3. For a cathode consisting of several spherical particles, the particles are charged one after another in Subsection 4.5.5. The maximum stress invariants show periodicity. For several spherical packings as a cathode microstructure, the maximum stress invariants are calculated during a charge cycle and compared to each other in Subsection 4.5.6.

5.2 Future work and outlook

The electro-chemical model in this work is given and analyzed for typical anode and cathode materials that work by intercalation of the lithium ions. Recently, with the rise of solid electrolytes, lithium metal anodes seem possible [145]. That would necessitate different models for both the lithium metal anode and a solid electrolyte. Furthermore, it is possible to combine several different cathode materials in a composite as, e.g., NMC (nickel manganese cobalt). The correct formulation of interface conditions between each of those materials for the intercalation of lithium ions (interface conditions for the lithium ion diffusion) as well as for the contact mechanics (interface conditions for the mechanical displacements) is up for discussion. Also, there are alternatives to a phase-field method

as a model for phase separation that is possibly faster or simpler in the implementation. The linear-elastic model can be just a first approach in understanding the ageing and degradation of electrode material during battery usage. A free energy including both elastic, chemical and interfacial parts may be given as a more general description. This way, the coupling conditions in (2.23) can be derived directly. Models including plasticity or even fracture and cycling effects can improve the value of the numerical simulation.
The Newton algorithm in this work relies heavily on a direct solver. This solver may be replaced by a general iterative scheme even though the structure of the Jacobian matrix is irregular and not symmetric. Direct solvers are restricted by the available memory and are also difficult to execute on parallel computing clusters. The optimum choice for the time step size can be decided by a line search [25] instead of simply multiplying or dividing it by a constant factor.
The domain decomposition algorithm needs linearized equations for its application. The removing of these restrictions would allow more complex applications. In [142], a method for the numerical solution of elliptic problems with two different material coefficients in two separate domains is discussed. It may be possible to solve the Poisson equation (or even the diffusion equation) in all three domains at the same time within one iterative scheme and arbitrary interface conditions. Right now the algorithm is split into six different loops, while the same may be achieved in two loops. The convergence of the algorithms may also be accelerated if predictors for the next jump variables are available by extrapolation from the last accepted time step.
The properties, advantages, and disadvantages of different phase-field potentials are not completely understood. Better approximations to the logarithmic potential may be found by higher-order polynomials. The nucleation properties in smaller electrode particles can be validated by experiments. The coatings, originally introduced for improved elastic properties in the spherical packings, may also be applied as a way to add carbon binder to the microstructure. The electro-chemical model describing the active cathode material as a simply connected intercalation domain which is only an approximation. The inclusion of a binder as a coating between electrode particles would heavily improve the modelling of the microstructure. The cell potentials as derived and simulated can be validated on experiments for different boundary conditions, different C-rates or different material parameters. Also, appropriate dimensions for the representative volume elements may be derived.

Bibliography

[1] A. Abdellahi et al. „The thermodynamic stability of intermediate solid solutions in LiFePO4 nanoparticles“. In: *Journal of Materials Chemistry A: Materials for energy and sustainability* 4 (2016), pp. 5436–5447.

[2] C. Andersson. „Phase-field Simulation of Dendritic Solidification“. PhD thesis. Royal Institute of Technology Stockholm, 2002.

[3] H. Arunachalam, S. Onori, and I. Battiato. „On Veracity of Macroscopic Lithium-Ion Battery Models“. In: *Journal of The Electrochemical Society* 162.10 (2015), A1940–A1951.

[4] P. Bai and M. Z. Bazant. „Charge transfer kinetics at the solid-solid interface in porous electrodes“. In: *Nature communications* 5 (2014), p. 3585.

[5] M. Z. Bazant. „Theory of Chemical Kinetics and Charge Transfer based on Nonequilibrium Thermodynamics.“ In: *Accounts of chemical research* 46.5 (2013), pp. 1144–1160.

[6] W. J. Boettinger et al. „Phase-Field Simulation of Solidification“. In: *Annual Review of Materials Research* 32 (2002), pp. 163–194.

[7] E. Bohn et al. „A Model for Lithium Diffusion and Stress Generation in an Intercalation Storage Particle with Phase Change“. In: *Journal of The Electrochemical Society* 160.10 (2013), A1638–A1652.

[8] J. Bosch. „Fast Iterative Solvers for Cahn-Hilliard Problems“. PhD thesis. Magdeburg: Otto-von-Guericke Universität Magdeburg, 2016.

[9] D. Braess. *Finite elements: Theory, fast solvers, and applications in solid mechanics*. Bochum: Cambridge University Press, 2007.

[10] M. Broussely et al. „Main aging mechanisms in Li ion batteries“. In: *Journal of Power Sources* 146.1-2 (2005), pp. 90–96.

[11] D. Burch. „Intercalation Dynamics in Lithium-Ion Batteries“. PhD thesis. Cambridge: Massachusetts Institute of Technology, 2009.

[12] D. Burch and M. Z. Bazant. „Size-dependent spinodal and miscibility gaps for intercalation in nanoparticles“. In: *Nano Letters* 9.11 (2009), pp. 3795–3800.

[13] J. W. Cahn. „Free Energy of a Nonuniform System. II. Thermodynamic Basis“. In: *The Journal of Chemical Physics* 30.5 (1959), pp. 1121–1124.

[14] J. W. H. Cahn John E. „Free Energy of a Nonuniform System. I. Interfacial Free Energy“. In: *The Journal of Chemical Physics* 28.2 (1958), pp. 258–267.

[15] C. Canuto et al. *Spectral Methods*. Springer Berlin Heidelberg, 2007, pp. 1–585.

[16] D. Chen et al. „In situ scanning electron microscopy on lithium-ion battery electrodes using an ionic liquid“. In: *Journal of Power Sources* 196.15 (2011), pp. 6382–6387.

[17] L. Q. Chen and J. Shen. „Applications of semi-implicit Fourier-spectral method to phase field equations“. In: 108 (1998), pp. 147–158.

[18] C.-K. ChiuHuang and H.-Y. Shadow Huang. „Stress Evolution on the Phase Boundary in LiFePO4 Particles“. In: *Journal of the Electrochemical Society* 160.11 (2013), A2184–A2188.

[19] Z. Choi, D. Kramer, and R. Mönig. „Correlation of stress and structural evolution in Li4Ti5O12-based electrodes for lithium ion batteries“. In: *Journal of Power Sources* 240 (2013), pp. 245–251.

[20] S.-M. Choo and S.-L. Chung. „Conservative nonlinear difference scheme for the Cahn-Hilliard equation“. In: *Computers & Mathematics with Applications* 39.1-2 (2000), pp. 229–243.

[21] W. C. Chueh et al. „Intercalation Pathway in Many-Particle LiFePO4 Electrode Revealed by Nanoscale State-of-Charge Mapping“. In: (2013).

[22] D. A. Cogswell. „Quantitative phase-field modeling of dendritic electrodeposition“. In: *Physical Review E - Statistical, Nonlinear, and Soft Matter Physics* 92.1 (2015), pp. 1–5.

[23] D. A. Cogswell and M. Z. Bazant. „Coherency strain and the kinetics of phase separation in LiFePO4 nanoparticles.“ In: *ACS nano* 6.3 (2012), pp. 2215–25.

[24] D. A. Cogswell and M. Z. Bazant. „Theory of coherent nucleation in phase-separating nanoparticles“. In: *Nano Letters* (2013), pp. 7–12.

[25] M. A. Crisfield. „An arc-length method including line searches and accelerations“. In: *International Journal for Numerical Methods in Engineering* 19.9 (1983), pp. 1269–1289.

[26] S. Dargaville and T. W. Farrell. „The persistence of phase-separation in LiFePO4 with two-dimensional Li+ transport: The Cahn-Hilliard-reaction equation and the role of defects“. In: *Electrochimica Acta* 94 (2013), pp. 143–158.

[27] A. Deb et al. „X-ray absorption spectroscopy study of the LixFePO4 cathode during cycling using a novel electrochemical in situ reaction cell“. In: *Journal of Synchrotron Radiation* 11.6 (2004), pp. 497–504.

[28] M. Dehghan and F. Fakhar-Izadi. „The spectral collocation method with three different bases for solving a nonlinear partial differential equation arising in modeling of nonlinear waves“. In: *Mathematical and Computer Modelling* 53.9-10 (2011), pp. 1865–1877.

[29] R. M. Dell and D. A. J. Rand. *Understanding Batteries: RSC (RSC Paperbacks)*. Royal Society of Chemistry, 2001.

[30] W. Dreyer, C. Guhlke, and R. Huth. „The behavior of many particle cathode in a lithium-ion battery“. In: *WIAS Preprint* 1423 (2009).

[31] W. Dreyer, C. Guhlke, and R. Müller. „Rational modeling of electrochemical double-layers and derivation of Butler-Volmer equations“. In: *WIAS Preprint* 1860 (2013).

[32] W. Dreyer et al. „The thermodynamic origin of hysteresis in insertion batteries“. In: *Nature Materials* 9.5 (2010), pp. 448–453.

[33] E. Hairer SP Norsett and G Wanner. *Solving ordinary differential equations I: Nonstiff problems*. Vol. 32. 3. Springer, 1990, pp. 485–486.

[34] M. Ebner et al. „Visualization and Quantification of Electrochemical and Mechanical Degradation in Li Ion Batteries“. In: *Science* 342.6159 (2013), pp. 716–720.

[35] C. Elliott and Z. Songmu. „On the Cahn-Hilliard equation“. In: *Archive for Rational Mechanics and Analysis* 96.4 (1986), pp. 339–357.

[36] C. Elliott and S. Luckhaus. *A generalised diffusion equation for phase separation of a multi-component mixture with interfacial free energy'*. 1991.

[37] A. B. Ellis. *Teaching General Chemistry : A Materials Science Companion*. An American Chemical Society Publication, 1993, p. 586.

[38] D. R. Ely, A. Jana, and R. E. Garcia. „Phase field kinetics of lithium electrodeposits“. In: *Journal of Power Sources* 272 (2014), pp. 581–594.

[39] L. Evans. *Partial Differential Equations*. American Mathematical Society, 1996, p. 672.

[40] D. Eyre. „An unconditonally stable one-step scheme for gradient systems“. 1998.

[41] D. Eyre. *An unconditonally stable one-step scheme for gradient systems*. Unpublished manuscript. 1998.

[42] D. Eyre. „Unconditionally Gradient Stable Time Marching the Cahn-Hilliard Equation“. In: *MRS Proceedings* 529 (1998).

[43] M. Farkhondeh et al. „Full-Range Simulation of a Commercial LiFePO4 Electrode Accounting for Bulk and Surface Effects: A Comparative Analysis“. In: *Journal of The Electrochemical Society* 161.3 (2014), A201–A212.

[44] M. Farkhondeh et al. „Mesoscopic modeling of Li insertion in phase-separating electrode materials: application to lithium iron phosphate.“ In: *Physical chemistry chemical physics : PCCP* 16.41 (2014), pp. 22555–65.

[45] T. R. Ferguson and M. Z. Bazant. „Nonequilibrium Thermodynamics of Porous Electrodes“. In: *Journal of the Electrochemical Society* 159.12 (2012), A1967–A1985.

[46] T. R. Ferguson and M. Z. Bazant. „Phase Transformation Dynamics in Porous Battery Electrodes“. In: *Electrochimica Acta* 146 (2014), pp. 89–97.

[47] B. Fornberg. „Generation of finite difference formulas on arbitrarily spaced grids“. In: *Mathematics of Computation* 51.184 (1988), p. 699.

[48] A. A. Franco. „Multiscale modelling and numerical simulation of rechargeable lithium ion batteries: concepts, methods and challenges“. In: *Rsc Advances* 3.32 (2013), pp. 13027–13058.

[49] M. Frigo and S. G. Johnson. „The design and implementation of FFTW3“. In: *Proceedings of the IEEE* 93.2 (2005), pp. 216–231.

[50] J. W. Gibbs. „Fourier's Series“. In: *Nature* 59.1539 (1899), pp. 606–606.

[51] GuidoB. *Alessandro Volta's electric battery (Tempio Voltiano in Como, Italy).* `https://commons.wikimedia.org/wiki/File:VoltaBattery.JPG`. cc-by-sa-3.0, accessed 08-June-2017. 2005.

[52] Y. Guo et al. „Li Intercalation into Graphite: Direct Optical Imaging and Cahn-Hilliard Reaction Dynamics“. In: *Journal of Physical Chemistry Letters* 7.11 (2016), pp. 2151–2156.

[53] M. E. Gurtin. „Generalized Ginzburg-Landau and Cahn-Hillard equations based on a microforce balance“. In: *Physica D* 92 (1996), pp. 178–192.

[54] E. Hairer and G. Wanner. *Solving Ordinary Differential Equations II: Stiff and Differential-Algebraic Problems (Springer Series in Computational Mathematics).* Springer, 2010.

[55] I. Harari and J. Dolbow. „Analysis of an efficient finite element method for embedded interface problems“. In: *Computational Mechanics* 46 (2010), pp. 205–211.

[56] P. Haupt. *Continuum Mechanics and Theory of Materials.* Springer, 2002.

[57] L.-P. He and Y. Liu. „A class of stable spectral methods for the Cahn-Hilliard equation“. In: *Journal of Computational Physics* 228.14 (2009), pp. 5101–5110.

[58] S. Hein and A. Latz. „Influence of local lithium metal deposition in 3D microstructures on local and global behavior of Lithium-ion batteries“. In: *Electrochimica Acta* 201 (2015), pp. 354–365.

[59] E. Hewitt and R. E. Hewitt. „The Gibbs-Wilbraham phenomenon: An episode in fourier analysis“. In: *Archive for History of Exact Sciences* 21.2 (1979), pp. 129–160.

[60] T. Hofmann, R. Müller, and H. Andrä. „A fast immersed interface method for the Cahn-Hilliard equation with arbitrary boundary conditions in complex domains“. In: *Computational materials science* 140 (2017), pp. 22–31.

[61] T. Hofmann, R. Müller, and H. Andrä. „Numerical simulation of phase separation in lithium ion batteries“. In: *Proceedings of the Young researchers symposium*. Fraunhofer Verlag, 2016, pp. 71–76.

[62] T. Hofmann et al. „Numerical simulation of phase separation in cathode materials of lithium ion batteries“. In: *International Journal of Solids and Structures* 100-101 (2016), pp. 456–469.

[63] M. E. Holtz et al. „Nanoscale imaging of lithium ion distribution during in situ operation of battery electrode and electrolyte“. In: *Nano Letters* 14.3 (2014), pp. 1453–1459.

[64] L. Hong et al. „Anisotropic Li intercalation in a LixFePO4 nano-particle: a spectral smoothed boundary phase-field model“. In: *Phys. Chem. Chem. Phys.* 18 (2016), pp. 9537–9543.

[65] L. Hu et al. „Scalable Coating and Properties of Transparent, Flexible, Silver Nanowire Electrodes“. In: *ACS Nano* 4.5 (2010), pp. 2955–2963.

[66] M. Huttin. „Phase-field modeling of the infuence of mechanical stresses on charging and discharging processes in lithium ion batteries“. In: (2014).

[67] T. Hutzenlaub et al. „Three-dimensional electrochemical Li-ion battery modelling featuring a focused ion-beam/scanning electron microscopy based three-phase reconstruction of a LiCoO2 cathode“. In: *Electrochimica Acta* 21 (2014), pp. 131–139.

[68] D. Jeong and J. Kim. „A practical numerical scheme for the ternary Cahn-Hilliard system with a logarithmic free energy“. In: *Physica A: Statistical Mechanics and its Applications* 442 (2016), pp. 510–522.

[69] S. G. Johnson and M. Frigo. „Implementing FFTs in Practice“. In: *Fast Fourier Transforms*. Ed. by C. S. Burrus. Rice University, Houston TX: Connexions, 2008. Chap. 11.

[70] B. S. Jovanović and E. Süli. *Analysis of Finite Difference Schemes: For Linear Partial Differential Equations with Generalized Solutions (Springer Series in Computational Mathematics)*. Springer-Verlag London, 2013, p. 58.

[71] J. Kim and H.-O. Bae. „An Unconditionally Gradient Stable Adaptive Mesh Refinement for the Cahn-Hilliard Equation“. In: *Journal of the Korean Physical Society* 53.2 (2008), p. 672.

[72] R. Kobayashi. „Modeling and numerical simulations of dendritic crystal growth“. In: 63 (1993), pp. 410–423.

[73] R. Kobayashi and J. a. Warren. „Modeling the formation and dynamics of polycrystals in 3D“. In: *Physica A: Statistical Mechanics and its Applications* 356 (2005), pp. 127–132.

[74] C. Kuhn and R. Müller. „A phase field model for fracture“. In: *Pamm* 8.1 (2008), pp. 10223–10224.

[75] C. Kuhn. „Numerical and Analytical Investigation of a Phase Field Model for Fracture“. PhD thesis. 2013.

[76] T. Küpper and K. Masbaum. „Simulation of particle growth and Ostwald ripening via the Cahn-Hilliard equation“. In: (1994).

[77] T. Küpper and N. Masbaum. „Simulation of Particle Growth and Ostwald Ripening via the Cahn-Hilliard Equation“. In: *Acta metallurgica materialia* 42.6 (1994), pp. 1847–1858.

[78] A. Latz and J. Zausch. „Multiscale modeling of lithium ion batteries: Thermal aspects“. In: *Beilstein Journal of Nanotechnology* 6.1 (2015), pp. 987–1007.

[79] A. Latz and J. Zausch. „Thermodynamic consistent transport theory of Li-ion batteries“. In: *Journal of Power Sources* 196.6 (2011), pp. 3296–3302.

[80] A. Latz and J. Zausch. „Thermodynamic derivation of a Butler-Volmer model for intercalation in Li-ion batteries“. In: *Electrochimica Acta* 110 (2013), pp. 358–362.

[81] H. G. Lee, J. W. Choi, and J. Kim. „A practically unconditionally gradient stable scheme for the N-component CahnHilliard system“. In: *Physica A: Statistical Mechanics and its Applications* 391.4 (2012), pp. 1009–1019.

[82] C. V. D. Leo, E. Rejovitzky, and L. Anand. „A Cahn-Hilliard-type phase-field theory for species diffusion coupled with large elastic deformations: Application to phase-separating Li-ion electrode materials“. In: *Journal of the Mechanics and Physics of Solids* 70 (2014), pp. 1–29.

[83] V. I. Levitas and H. Attariani. „Anisotropic compositional expansion in elastoplastic materials and corresponding chemical potential: Large-strain formulation and application to amorphous lithiated silicon“. In: *Journal of the Mechanics and Physics of Solids* 69.1 (2014), pp. 84–111.

[84] Y. Li, H. Geun Lee, and J. Kim. „A fast, robust, and accurate operator splitting method for phase-field simulations of crystal growth“. In: *Journal of Crystal Growth* 321.1 (2011), pp. 176–182.

[85] Y. Li et al. „A compact fourth-order finite difference scheme for the three-dimensional Cahn-Hilliard equation“. In: *Computer Physics Communications* 200 (2016), pp. 108–116.

[86] Y. Li et al. „A conservative numerical method for the Cahn-Hilliard equation with Dirichlet boundary conditions in complex domains“. In: *Computers and Mathematics with Applications* 65.1 (2013), pp. 102–115.

[87] Y. Li et al. „Current-induced transition from particle-by-particle to concurrent intercalation in phase-separating battery electrodes“. In: 13.September (2014), pp. 1149–1156.

[88] Z. Li. „A fast iterative algorithm for elliptic interface problems“. In: *SIAM Journal on Numerical Analysis* 35.1 (1998), pp. 230–254.

[89] J. Lim et al. „Origin and hysteresis of lithium compositional spatiodynamics within battery primary particles“. In: *Science* 27.2004 (2013).

[90] H. Liu et al. „Capturing metastable structures during high-rate cycling of LiFePO4 nanoparticle electrodes“. In: *Science* 344.6191 (2014), p. 1252817.

[91] Q. Liu et al. „Two-level methods for the Cahn-Hilliard equation“. In: *Mathematics and Computers in Simulation* 126.20130201120052 (2015), pp. 89–103.

[92] C. Mattiussi. „An Analysis of Finite Volume, Finite Element, and Finite Difference Methods Using Some Concepts from Algebraic Topology“. In: *Journal of Computational Physics* 133.2 (1997), pp. 289–309.

[93] M. T. McDowell et al. „Studying the Kinetics of Crystalline Silicon Nanoparticle Lithiation with In Situ Transmission Electron Microscopy“. In: *Advanced Materials* 24.45 (2012), pp. 6034–6041.

[94] C. Miehe et al. „A phase-field model for chemo-mechanical induced fracture in lithium-ion battery electrode particles“. In: *International Journal for Numerical Methods in Engineering* 106.9 (2016), pp. 683–711.

[95] S. Mitchell and M. Vynnycky. „Finite-difference methods with increased accuracy and correct initialization for one-dimensional Stefan problems“. In: *Applied Mathematics and Computation* 215.4 (2009), pp. 1609–1621.

[96] H. Moulinec and P. Suquet. „A numerical method for computing the overall response of nonlinear composites with complex microstructure“. In: *Computer Methods in Applied Mechanics and Engineering* 157.1-2 (1998), pp. 69–94.

[97] R. Müller et al. „Phase field simulation of domain structures in ferroelectric materials within the context of inhomogeneity evolution“. In: *International Journal of Fracture* 147.1-4 (2007), pp. 173–180.

[98] R. Müller. „A Phase Field Model for the Evolution of Martensite Microstructures in Metastable Austenites“. PhD thesis. TU Kaiserslautern, 2016.

[99] V. Müller et al. „Homogenization of linear elastic properties of short-fiber reinforced composites – A comparison of mean field and voxel-based methods“. In: *International Journal of Solids and Structures* 67-68 (2015), pp. 56–70.

[100] „Multi-component Cahn-Hilliard system with different boundary conditions in complex domains“. In: *Journal of Computational Physics* 323 (2016), pp. 1–16.

[101] I. N. Bronstein and K. A. Semendjajew. *Taschenbuch der Mathematik*. Ed. by G. Grosche and V. Ziegler. 19th ed. Leipzig, Moskau: BSB B. G. Teubner Verlagsgesellschaft, Nauka-Verlag, 1979.

[102] D. Neusius. „An advanced interpolation cut-cell method for numerically solving continuum granular flow equations“. PhD thesis. TU Kaiserslautern, 2016.

[103] J. Newman and K. Thomas-Alyea. *Electrochemical Systems*. John Wiley & Sons, 2004, p. 647.

[104] J. Nocedal and S. J. Wright. *Numerical Optimization*. Springer-Verlag New York, 1999, pp. 164–175.

[105] B. Orvananos et al. „Architecture dependence on the dynamics of nano-liFePO4 electrodes“. In: *Electrochimica Acta* 137 (2014), pp. 245–257.

[106] B. Orvananos et al. „Particle-Level Modeling of the Charge-Discharge Behavior of Nanoparticulate Phase-Separating Li-Ion Battery Electrodes“. In: 161.4 (2014).

[107] C. S. Peskin. „The immersed boundary method“. In: *Acta Numerica 2002* (2002), pp. 479–517.

[108] C. Plate. „Fracture Mechanical Analysis of Failure Processes in Antarctic Ice Shelves“. PhD thesis. TU Kaiserslautern, 2015.

[109] P. Popov and S. Margenov. „Microscale Modelling of Li-ion batteries“. In: *Berichte des Fraunhofer ITWM* 191 (2010).

[110] N. Provatas and K. Elder. *Phase-Field Methods in Materials Science and Engineering*. Wiley-VCH, 2010.

[111] V. Ramadesigan et al. „Modeling and Simulation of Lithium-Ion Batteries from a Systems Engineering Perspective“. In: *Journal of the Electrochemical Society* 159.3 (2012), R31–R45.

[112] A. K. Rao. „Stress Concentrations and Singularities at Interface Corners“. In: *ZAMM - Journal of Applied Mathematics and Mechanics / Zeitschrift fuer Angewandte Mathematik und Mechanik* 51.5 (1971), pp. 395–406.

[113] A. Rätz. „A benchmark for the surface Cahn-Hilliard equation“. In: *Applied Mathematics Letters* 56 (2016), pp. 65–71.

[114] D. Robert et al. „Multiscale Phase Mapping of LiFePO 4-Based Electrodes by Transmission Electron Microscopy and Electron Forward Scattering Diffraction“. In: *ACS nano* 7.12 (2013), pp. 10087–10894.

[115] R. Routledge. *A popular history of science*. G. Routledge and Sons, 1881.

[116] V. Rutka. „Immersed Interface Methods for Elliptic Boundary Value Problems“. PhD thesis. University of Kaiserslautern, 2005.

[117] M. Schneider, F. Ospald, and M. Kabel. „Computational homogenization of elasticity on a staggered grid“. In: *International Journal for Numerical Methods in Engineering* 105.9 (2016). nme.5008, pp. 693–720.

[118] D. Schrade. „Microstructural modeling of ferroelectric material behavior“. PhD thesis. TU Kaiserslautern, 2010.

[119] N. Sharma et al. „Direct evidence of concurrent solid-solution and two-phase reactions and the nonequilibrium structural evolution of LiFePO4“. In: *Journal of the American Chemical Society* 134.18 (2012), pp. 7867–7873.

[120] J. Shen and X. Yang. „An efficient moving mesh spectral method for the phase-field model of two-phase flows“. In: *Journal of Computational Physics* 228.8 (2009), pp. 2978–2992.

[121] J. Shin, D. Jeong, and J. Kim. „A conservative numerical method for the Cahn-Hilliard equation in complex domains“. In: *Journal of Computational Physics* 230.19 (2011), pp. 7441–7455.

[122] G. K. Singh, G. Ceder, and M. Z. Bazant. „Intercalation dynamics in rechargeable battery materials: General theory and phase-transformation waves in LiFePO4“. In: *Electrochimica Acta* 53.26 (2008), pp. 7599–7613.

[123] Y. C. Song et al. „Diffusion of lithium ions and diffusion-induced stresses in a phase separating electrode under galvanostatic and potentiostatic operations: Phase field simulations“. In: *Mechanics of Materials* 91 (2015), pp. 363–371.

[124] D. B. Stein, R. D. Guy, and B. Thomases. „Immersed boundary smooth extension: A high-order method for solving PDE on arbitrary smooth domains using Fourier spectral methods“. In: *Journal of Computational Physics* 304 (2016), pp. 252–274.

[125] P. Stein, Y. Zhao, and B. X. Xu. „Effects of surface tension and electrochemical reactions in Li-ion battery electrode nanoparticles“. In: *Journal of Power Sources* 332 (2016), pp. 154–169.

[126] J. D. Sugar et al. „High-resolution chemical analysis on cycled LiFePO4 battery electrodes using energy-filtered transmission electron microscopy“. In: *Journal of Power Sources* 246 (2014), pp. 512–521.

[127] M. Tang, J. F. Belak, and M. R. Dorr. „Anisotropic Phase Boundary Morphology in Nanoscale Olivine Electrode Particles“. In: (2011), pp. 4922–4926.

[128] M. Taralov. „Simulation of Degradation Processes in Lithium-Ion Batteries“. PhD thesis. TU Kaiserslautern, 2015.

[129] V. Taralova. „Upscaling Approaches for Nonlinear Processes in Lithium-Ion Batteries“. In: (2015).

[130] Tennen-Gas. *Nissan Leaf at the 2009 Tokyo Motor Show*. `https://commons.wikimedia.org/wiki/File:Nissan_Leaf_012.JPG`. cc-by-sa-3.0, accessed 08-June-2017. 2009.

[131] Timothy A. Davis. *Direct Methods for Sparse Linear Systems*. 2006, pp. 1–230.

[132] L. N. Trefethen. „Spectral Methods in Matlab“. In: *Lloydia Cincinnati* 10 (2000), p. 184.

[133] U. Trottenberg, C. W. Oosterlee, and A. Schuller. *Multigrid*. Academic Press, 2000.

[134] M. Ulbrich and S. Ulbrich. *Nichtlineare Optimierung (Mathematik Kompakt) (German Edition)*. Birkhäuser, 2012.

[135] H. Uzawa. „Iterative methods for concave programming“. In: *Studies in Linear and Nonlinear Programming* (1958), pp. 154–165.

[136] A. V. der Ven, J. Bhattacharya, and A. A. Belak. „Understanding Li Diffusion in Li-Intercalation Compounds“. In: *Accounts of Chemical Research* 46.5 (2013), pp. 1216–1225.

[137] T. Waldmann et al. „Post-Mortem Analysis of Aged Lithium-Ion Batteries: Disassembly Methodology and Physico-Chemical Analysis Techniques“. In: *Journal of The Electrochemical Society* 163.10 (2016), pp. 2149–2164.

[138] S.-L. Wang et al. „Thermodynamically-consistent phase-field models for solidification“. In: *Physica D: Nonlinear Phenomena* 69.1-2 (1993), pp. 189–200.

[139] R. Weiner. *Linear-implizite Runge-Kutta-Methoden und ihre Anwendung (German Edition)*. Vieweg+Teubner Verlag Wiesbaden, 2013.

[140] M. J. Welland et al. „Miscibility Gap Closure , Interface Morphology , and Phase Microstructure of 3D LixFePO4 Nanoparticles from Surface Wetting and Coherency Strain“. In: *ACS nano* 9(10) (2015), pp. 9757–9771.

[141] A Wiegmann, Z Li, and R. J. Leveque. „Crack jump conditions for elliptic problems“. In: *Applied Mathematics Letters* 12.6 (1999), pp. 81–88.

[142] A. Wiegmann. „The Explicit-Jump Immersed Interface Method and Interface Problems for Differential Equations“. PhD thesis. University of Washington, 1998.

[143] A. Wiegmann and K. P. Bube. „The Explicit-Jump Immersed Interface Method: Finite Difference Methods for PDEs with Piecewise Smooth Solutions“. In: *SIAM Journal on Numerical Analysis* 37.3 (2000), pp. 827–862.

[144] B. Y. M. L. Williams. „Stress Singularities Resulting Frolll Vari- ous Boundary Conditions in Angular Corners of Plates in Extension“. In: (), pp. 526–528.

[145] W. Xu et al. „Lithium metal anodes for rechargeable batteries“. In: *Energy Environ. Sci.* 7.2 (2014), pp. 513–537.

[146] X. Ye. „The Fourier collocation method for the Cahn-Hilliard equation“. In: *Computers and Mathematics with Applications* 44.1-2 (2002), pp. 213–229.

[147] Y. S. Yu et al. „Dependence on Crystal Size of the Nanoscale Chemical Phase Distribution and Fracture in LiFePO4“. In: *Nano Letters* 15.7 (2015), pp. 4282–4288.

[148] Y. Zeng et al. „Efficient Conservative Numerical Schemes for 1D Nonlinear Spherical Diffusion Equations with Applications in Battery Modeling“. In: *Journal of the Electrochemical Society* 160.9 (2013), A1565–A1571.

[149] Y. Zeng and M. Z. Bazant. „Phase Separation Dynamics in Isotropic Ion-Intercalation Particles“. In: *SIAM Journal on Applied Mathematics* 74.4 (2013), pp. 980–1004.

[150] X. Zhang, A. M. Sastry, and W. Shyy. „Intercalation-Induced Stress and Heat Generation within Single Lithium-Ion Battery Cathode Particles“. In: *Journal of The Electrochemical Society* 155.7 (2008), A542.

[151] X. Zhang, W. Shyy, and A. Marie Sastry. „Erratum: Numerical Simulation of Intercalation-Induced Stress in Li-Ion Battery Electrode Particles [J. Electrochem. Soc., 154, A910 (2007)]“. In: *Journal of The Electrochemical Society* 154.12 (2007), S21.

[152] X. Zhang et al. „Direct Observation of Li-Ion Transport in Electrodes under Nonequilibrium Conditions Using Neutron Depth Profiling“. In: *Advanced Energy Materials* 5.15 (2015), pp. 1–8.

[153] X. Zhang et al. „Rate-induced solubility and suppression of the first-order phase transition in olivine LiFePO4“. In: *Nano Letters* 14.5 (2014), pp. 2279–2285.

[154] Y. Zhu et al. „In Situ Atomic-Scale Imaging of Phase Boundary Migration in FePO4 Microparticles During Electrochemical Lithiation“. In: *Advanced Materials* 25.c (2013), pp. 5461–5466.

[155] A. Zygmund. *Trigonometric Series (Cambridge Mathematical Library)*. Cambridge University Press, 2003.

Appendix A

Solidification

Although the methods introduced in this thesis are mainly aimed at the efficient solution of Cahn-Hilliard phase-field methods in the context of electrochemical problems, phase-field methods can also be applied for a variety of other problems. The Cahn-Hilliard equation results from a conservation law, in this work conservation of the number and mass of lithium ions intercalated in the electrode material. This is called a *conserved* or *diffusive* model. Diffusive models are usually partial differential equations of fourth order. Other phase-field methods resulting from the Allen-Cahn equation describe phase-transformation without a conservation property are called *non-conserved* or *displacive*. Examples for displace phase transformations are the change of a material phase from liquid to solid with the formation of dendrites [2, 72, 73], the change of a material phase from gaseous to liquid or solid, called condensation or resublimation, the transformation of different martensites and austenite in steel [98], the occurence of fractures [75] or the coating of surfaces under the influence of surface tension. Also the buildup of metallic lithium dendrites in battery electrodes has been described with such models [38], [22].
This chapter features an application of a phase-field model for the phase-transformation during solidification. In a model introduced by [72] two fields are coupled by different parameters. The first field $p(\boldsymbol{x}, t)$ describes the state of the material as a phase-field order parameter. Two equilibrium values are defined, $p = 0$ being the liquid and $p = 1$ being the solid state. A value between the two equilibrium solutions $p \in (0, 1)$ describes an interface between the phases. The second field $T(\boldsymbol{x}, t)$ describes the temperature inside the material.
Section A.1 will introduce governing equations and shortly describe the boundary and initial conditions. It generalizes the model presented in [72] and uses ideas taken from [2]. Section A.2 then explains the addition to the already presented numerical methods in Chapter 3. In Section A.3 some numerical examples and parameter tests are shown.

A.1 Phase-field model

For the solidification a system of coupled partial differential equations is used. The phase-field parameter $p(\boldsymbol{x}, t)$ is described by a non-linear second-order equation called

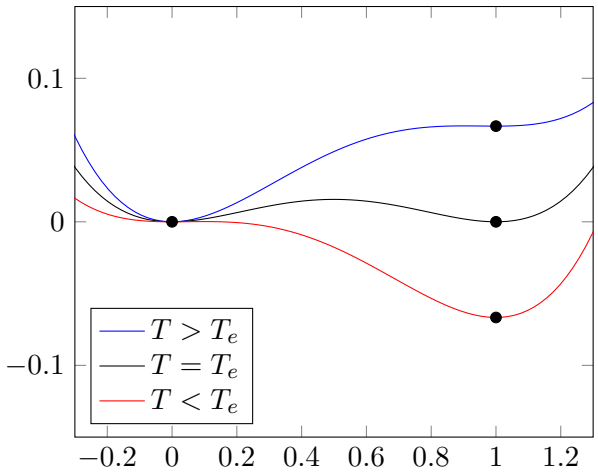

Figure A.1: A temperature-dependent double-well potential F for different temperatures. The minima are marked. For $T = T_e$ the energy content of both configurations solid and liquid is the same. There is no preferred state. For $T > T_e$ or $T < T_e$ the preferred state is liquid respectively solid.

Allen-Cahn equation deriving from a Ginzburg-Landau energy function [53]. The temperature is described by the heat equation. The equation system is fully coupled. The solidification process releases latent heat and results in a source term in the heat equation. At the same time, a higher temperature prevents further solidification.
Given an undercooled state where solidification is encouraged and a condensation nucleus, the solidification process starts at this nucleus and branches out, forming a fractal structure. This is a result from the opposing effects of the coupled equations.

A.1.1 Governing equations

A free energy density is given in [72] as

$$E = F(p,T) + \frac{1}{2}\epsilon^2 ||\nabla p||^2. \tag{A.1}$$

The bulk energy F is given as a temperature-dependent double-well potential,

$$F(p,T) = \frac{1}{4}p^4 - \left(\frac{1}{2} - \frac{1}{3}m(T)\right)p^3 + \left(\frac{1}{4} - \frac{1}{2}m(T)\right)p^2, \tag{A.2}$$

where $m(T)$ is a function acting as a coupling term to the temperature. The function m is required to be 0 at the equilbrium temperature such that no energetic distinction is made between the two physical states liquid and solid, $m(T_e) = 0$. Additionally

it needs to be monotonic in T such that for temperatures larger than the equilibrium concentration the liquid state is preferred and vice-versa. Here it is given as

$$m(T) = \alpha \frac{\arctan(-\gamma T)}{\pi}, \tag{A.3}$$

where α and γ are parameters.
Figure A.1 shows the function $F(\cdot; T)$ for different values of T. The minima of the energy mark the equilibrium states. For $T = T_e$ the energy content of both configurations solid and liquid is the same and there is no preferred state. For $T > T_e$ or $T < T_e$ the preferred state is liquid respectively solid.
In the presented model in Chapter 2, the phase-field parameter ϵ is constant and has been replaced by two constant phase-field parameters G and L denoting interfacial width and interfacial energy. In the model predented in this chapter, anisotropy is introduced into a phase-field model by a varying parameter ϵ. The value ϵ depends on the direction of the outer normal vector $\boldsymbol{n}$ at the phase interface, that is $\boldsymbol{n} = \frac{\nabla p}{||\nabla p||}$. In a two-dimensional domain, an angle θ is introduced as $\tan(\theta) = \frac{n_2}{n_1}$ with $\boldsymbol{n} = (n_1, n_2)$. Similar, in a three-dimensional domain, angles ϕ and θ are introduced as $\cos\theta = \frac{n_3}{\sqrt{n_1^2+n_2^2}}$ and $\tan\phi = \frac{n_2}{n_1}$. The parameter ϵ is then given as either $\epsilon(\theta)$ or $\epsilon(\phi, \theta)$, respectively.
The evolution equation for a displacive phase-field parameter is

$$\begin{aligned}
\frac{\partial p}{\partial t} &= -\frac{\delta E}{\delta p} = -\frac{\delta}{\delta p}(\epsilon^2 ||\nabla p||^2) + F'(p, T) \\
&= -\left(-\text{div}\left(\epsilon^2 \nabla p\right) + \text{div}\left(\epsilon \frac{\partial \epsilon}{\partial \boldsymbol{n}} ||\nabla p||^2\right)\right) \\
&+ p^3 - 3\left(\frac{1}{2} - \frac{1}{3}m(T)\right)p^2 + 2\left(\frac{1}{4} - \frac{1}{2}m(T)\right)p \\
&= \text{div}\left(\epsilon^2 \nabla p\right) - \text{div}\left(\epsilon \frac{\partial \epsilon}{\partial \boldsymbol{n}} ||\nabla p||^2\right) + p(1-p)(p - \frac{1}{2} + m(T))
\end{aligned} \tag{A.4}$$

In order to simplify the equation in a two-dimensional domain, the expression $\epsilon' := \frac{\partial \epsilon}{\partial \theta}$ is introduced. The partial derivative $\frac{\partial \epsilon}{\partial \boldsymbol{n}}$ is calculated as

$$\frac{\partial \epsilon}{\partial \boldsymbol{n}} = \frac{\partial \epsilon}{\partial \theta}\frac{\partial \theta}{\partial \boldsymbol{n}} = \epsilon' \begin{pmatrix} \frac{1}{1+\frac{n_2^2}{n_1^2}} \cdot \left(-\frac{n_2}{n_1^2}\right) \\ \frac{1}{1+\frac{n_2^2}{n_1^2}} \cdot \frac{1}{n_1} \end{pmatrix} = \epsilon' \frac{1}{n_1^2 + n_2^2} \begin{pmatrix} -n_2 \\ n_1 \end{pmatrix} \tag{A.5}$$

As $||\nabla p||^2 = n_1^2 + n_2^2$, the expression involving the partial derivative is further simplified

$$\begin{aligned}\operatorname{div}\left(\epsilon\frac{\partial\epsilon}{\partial\boldsymbol{n}}||\nabla p||^2\right) &= \begin{pmatrix}\frac{\partial}{\partial x_1} & \frac{\partial}{\partial x_2}\end{pmatrix}\left(\epsilon\epsilon'\frac{1}{n_1^2+n_2^2}\begin{pmatrix}-n_2\\ n_1\end{pmatrix}(n_1^2+n_2^2)\right)\\ &= -\frac{\partial}{\partial x_1}\left(\epsilon\epsilon'\frac{\partial}{\partial x_2}p\right)+\frac{\partial}{\partial x_2}\left(\epsilon\epsilon'\frac{\partial}{\partial x_1}p\right)\end{aligned} \tag{A.6}$$

This way A.4 is rewritten as

$$\frac{\partial p}{\partial t} = --\frac{\partial}{\partial x_1}\left(\epsilon\epsilon'\frac{\partial}{\partial x_2}p\right)+\frac{\partial}{\partial x_2}\left(\epsilon\epsilon'\frac{\partial}{\partial x_1}p\right)+\nabla(\epsilon^2\nabla p)+p(1-p)(p-\frac{1}{2}+m(T)) \tag{A.7}$$

In order to simplify the equation in a three-dimensional domain, the expressions $\epsilon_\theta := \frac{\partial\epsilon}{\partial\theta}$ and $\epsilon_\phi := \frac{\partial\epsilon}{\partial\phi}$ are introduced. Similar to the derivation in a two-dimensional domain, the partial derivative $\frac{\partial\epsilon}{\partial\boldsymbol{n}}$ is calculated as

$$\begin{aligned}\frac{\partial\epsilon}{\partial\boldsymbol{n}} &= \frac{\partial\epsilon}{\partial\theta}\frac{\partial\theta}{\partial\boldsymbol{n}}+\frac{\partial\epsilon}{\partial\phi}\frac{\partial\phi}{\partial\boldsymbol{n}}\\ &= -\epsilon_\theta\begin{pmatrix}-\frac{n_1n_3}{||\nabla p||^2\sqrt{n_1^2+n_2^2}}\\ -\frac{n_2n_3}{||\nabla p||^2\sqrt{n_1^2+n_2^2}}\\ \frac{\sqrt{n_1^2+n_2^2}}{||\nabla p||^2}\end{pmatrix}\\ &\quad+\epsilon_\phi\frac{1}{n_1^2+n_2^2}\begin{pmatrix}-n_2\\ n_1\\ 0\end{pmatrix}\end{aligned} \tag{A.8}$$

Using the abbreviation $r = ||\nabla p||$, A.4 is simplified to

$$\begin{aligned}\frac{\partial p}{\partial t} = -\operatorname{div}&\left(\epsilon^2\nabla p+\epsilon\epsilon_\theta r\begin{pmatrix}\cos(\theta)\cos(\phi)\\ \cos(\theta)\sin(\phi)\\ \sin(\theta)\end{pmatrix}+\epsilon\epsilon_\phi\frac{r}{\sin(\theta)}\begin{pmatrix}\sin(\phi)\\ \cos(\phi)\\ 0\end{pmatrix}\right)\\ &+p(1-p)(p-\frac{1}{2}+m(T))\end{aligned} \tag{A.9}$$

The coupling term m is either chosen as $m = \gamma(T_e - T)$ or $m = \frac{\alpha}{\pi}\arctan\gamma(T_e - T)$. T_e is the equilibrium temperature, γ and α are constants. The governing equation for the temperature is

$$\frac{\partial}{\partial t}T(\boldsymbol{x},t) = \Delta T(\boldsymbol{x},t)+K\frac{\partial}{\partial t}p(\boldsymbol{x},t), \quad \forall x\in\Omega. \tag{A.10}$$

This is a Laplacian heat diffusion equation with a heat source. The term $K\frac{\partial}{\partial t}p(\boldsymbol{x},t)$ models the latent heat release due to the solidification. The parameter K is the specific heat released by the material if it solidifies.

A.1.2 Anisotropic functions

The anisotropic function in two dimensions is chosen as

$$\epsilon(\theta) = \bar{\epsilon}\,(1 + \delta\cos(j\theta))\,. \tag{A.11}$$

Figure A.2 (a) shows this for several integer values of j. The plot is given in polar coordinates to highlight the result of anisotropic growth. The radius $r = \epsilon(\theta)$ is plotted against the polar angle θ given by the direction of the normal vector $\boldsymbol{n}$. For $j = 4$, the maxima are at $\theta = k\frac{\pi}{2}$ for $k \in \{0, 1, 2, 3\}$. In cartesian coordinates this holds for the vectors $\boldsymbol{n} = (n_1, n_2)$ being identical to $\pm\boldsymbol{e}_1$ and$\pm\boldsymbol{e}_2$. Application of trigonometric rules leads to

$$\cos(4\theta) = 4(\cos(\theta)^4 + \sin(\theta)^4) - 3 = 4(n_1^4 + n_2^4) - 3 \tag{A.12}$$

and rewritting (A.11) for $j = 4$ as

$$\epsilon(\boldsymbol{n}) = \bar{\epsilon}\left(1 + \delta(4(n_1^4 + n_2^4) - 3)\right). \tag{A.13}$$

The polynomial function $f_2(n_1, n_2) = n_1^4 + n_2^4$ attains maxima under valid definition range $||\boldsymbol{n}|| = 1$ for the four values $(\pm 1, 0)$ and $(0, \pm 1)$. This motivates to choose the polynomial function $f_3(n_1, n_2, n_3) = n_1^4 + n_2^4 + n_3^4$ for the three-dimensional case. Figure A.2 (b) shows a plot of this function in spherical coordinates. The radius $r = f_3(n_1, n_2, n_3)$ is plotted there against the spherical angles ϕ and θ, that define a normal vector $\boldsymbol{n}$ by e.g. spherical coordinates

$$(n_1, n_2, n_3) = (\sin(\theta)\cos(\phi), \sin(\theta)\sin(\phi), \cos(\theta)). \tag{A.14}$$

In order to control the magnitude of the anisotropy correctly with the parameters δ and $\bar{\epsilon}$, the function f in $\epsilon = \bar{\epsilon}\,(1 + \delta f)$ should map into the range $[-1, 1]$. The next paragraph will find the critical points of f_3 considering the appropriate constraint and study if they are maxima or minima.

The objective function $f_3(n_1, n_2, n_3) = n_1^4 + n_2^4 + n_3^4$ is searched for critical points under the constraint $n_1^2 + n_2^2 + n_3^2 = 1$, being equivalent to $||\boldsymbol{n}|| = 1$. Without loss of generality it may be assumed $0 \leq n_1 \leq n_2 \leq n_3$ due to symmetry. The corresponding Lagrange function

$$L(\lambda; n_1, n_2, n_3) = n_1^4 + n_2^4 + n_3^4 - \lambda(n_1^2 + n_2^2 + n_3^2 - 1) \tag{A.15}$$

has the gradient

$$\nabla_{n_i} L(\lambda; n_1, n_2, n_3) = 4n_i^3 - 2\lambda n_i. \tag{A.16}$$

Critical points are then given by the equation system $\nabla L = 0$. These system has the solution quadruplets $\boldsymbol{v}_1 = \left(\frac{2}{3}; \frac{1}{\sqrt{3}}, \frac{1}{\sqrt{3}}, \frac{1}{\sqrt{3}}\right)$, $\boldsymbol{v}_2 = \left(1; 0, \frac{1}{\sqrt{2}}, \frac{1}{\sqrt{2}}\right)$ and $\boldsymbol{v}_3 = (2; 0, 0, 1)$.

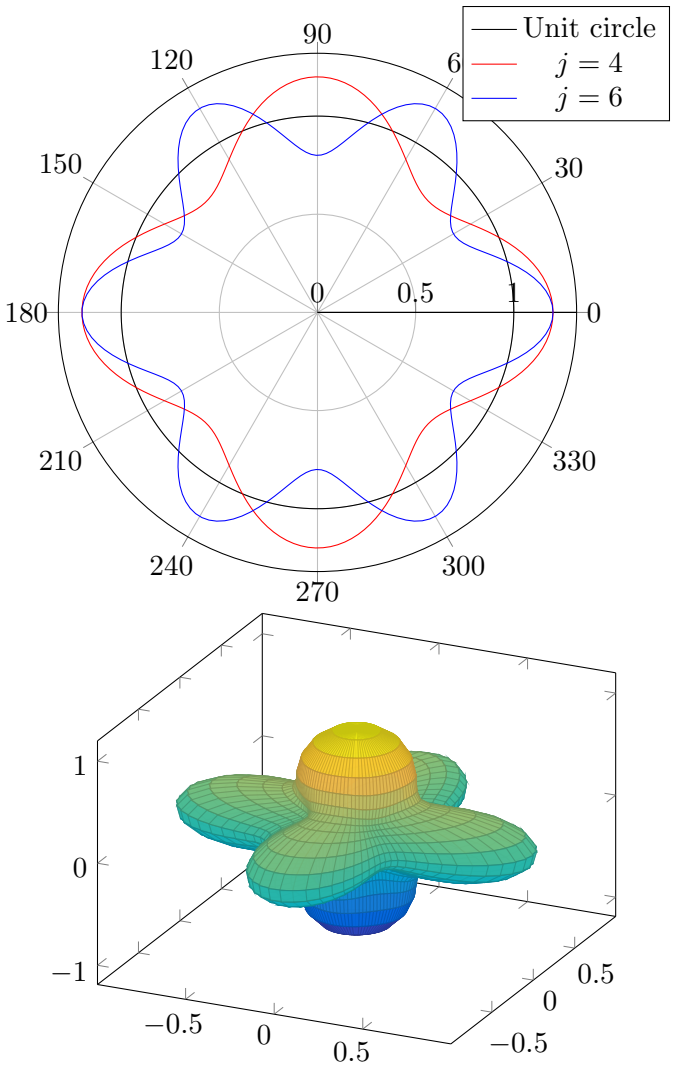

Figure A.2: (a) The anisotropic function $\epsilon(\theta)$ for a two-dimensional dendrite with integer symmetries $j = 4$ and $j = 6$. (b) The anistropic function $\epsilon(\theta, \phi)$ for a three-dimensional dendrite with octahedral symmetry

Function evaluation gives $L(\boldsymbol{v}_1) = \frac{1}{3}$,$L(\boldsymbol{v}_2) = \frac{1}{2}$ and $L(\boldsymbol{v}_3) = 1$. By application of regularity arguments it can be concluded that the range of f_3 is then $[\frac{1}{3}, 1]$. This can also be seen by calculating the sign of the minor determinants of the bordered Hessian [134],

$$\begin{aligned} H(\lambda; n_1, n_2, n_3) &= \nabla^2 L(\lambda; n_1, n_2, n_3) \\ &= \begin{pmatrix} 0 & -2n_1 & -2n_2 & -2n_3 \\ -2n_1 & 12n_1^2 - 2\lambda & 0 & 0 \\ -2n_2 & 0 & 12n_2^2 - 2\lambda & 0 \\ -2n_3 & 0 & 0 & 12n_3^2 - 2\lambda \end{pmatrix}. \end{aligned} \tag{A.17}$$

In the presented case, only two determinants have to be considered, the determinant of the minor consisting of the first three truncated rows and columns, $\det(H_{4,4}(\boldsymbol{v}))$ and the determinant of the complete Hessian $\det(H(\boldsymbol{v}))$. A sufficient condition for a local maximum is then that sign of the minors alternates starting with positive sign. A sufficient condition for a local minimum is that all minors have negative sign. Calculating the signs gives

$$\begin{aligned} \operatorname{sign}\det(H_{4,4}(\boldsymbol{v}_1)) &= 1, & \operatorname{sign}\det(H(\boldsymbol{v}_1)) &= -1, \\ \operatorname{sign}\det(H_{4,4}(\boldsymbol{v}_2)) &= 1, & \operatorname{sign}\det(H(\boldsymbol{v}_2)) &= 1, \\ \operatorname{sign}\det(H_{4,4}(\boldsymbol{v}_3)) &= -1, & \operatorname{sign}\det(H(\boldsymbol{v}_3)) &= -1. \end{aligned} \tag{A.18}$$

Therefore, a local maximum is present at $\boldsymbol{v} = \boldsymbol{v}_1$, a local minimum is present at $\boldsymbol{v} = \boldsymbol{v}_3$. Figure A.2 (b) gives evidence to support the assumption that f_3 has a saddle point at $\boldsymbol{v} = \boldsymbol{v}_2$.
Now that the range of f_3 is known, a simple linear map $x \mapsto 3x - 2$ is used to extend the range to $[-1, 1]$. The anisotropy function in three dimensions is then chosen as

$$\epsilon(\boldsymbol{n}) = \bar{\epsilon}\left(1 + \delta\left(3\left(n_1^4 + n_2^4 + n_3^4\right) - 2\right)\right), \tag{A.19}$$

which can be compared to (A.13).

A.1.3 Initial and boundary conditions

The governing equations are closed by periodic boundary conditions on both the phase-field parameter and the temperature,

$$\begin{aligned} p(\boldsymbol{x}, t) &= p(\boldsymbol{x} + L_i\boldsymbol{e}_i, t), & \boldsymbol{x}, \boldsymbol{x} + L_i\boldsymbol{e}_i \in \partial\Omega, t \in T, \\ \frac{\partial}{\partial \boldsymbol{n}} p(\boldsymbol{x}, t) &= -\frac{\partial}{\partial \boldsymbol{n}} p(\boldsymbol{x} + L_i\boldsymbol{e}_i, t), & \boldsymbol{x}, \boldsymbol{x} + L_i\boldsymbol{e}_i \in \partial\Omega, t \in T, \\ T(\boldsymbol{x}, t) &= T(\boldsymbol{x} + L_i\boldsymbol{e}_i, t), & \boldsymbol{x}, \boldsymbol{x} + L_i\boldsymbol{e}_i \in \partial\Omega, t \in T, \\ \frac{\partial}{\partial \boldsymbol{n}} T(\boldsymbol{x}, t) &= -\frac{\partial}{\partial \boldsymbol{n}} T(\boldsymbol{x} + L_i\boldsymbol{e}_i, t), & \boldsymbol{x}, \boldsymbol{x} + L_i\boldsymbol{e}_i \in \partial\Omega, t \in T. \end{aligned} \tag{A.20}$$

As initial conditions, the temperature is chosen as uniformly below the equilibrium temperature, an undercooled state,

$$T(x,0) = T_e - 1 \quad \forall x \in \Omega, \tag{A.21}$$

and the phase transformation is initiated by a small inclusion, a condensation nucleus in a small subset Ω_s of the domain Ω,

$$p(x,0) = \begin{cases} 1 & \forall x \in \Omega_s, \\ 0 & \forall x \in \Omega \setminus \Omega_s. \end{cases} \tag{A.22}$$

A.2 Numerical method

The phasefield equation is discretized in time explicit by a first order Eulerian scheme. In space, the Laplacian is calculated with finite differences. Note that here the Fourier derivation methods cannot be applied as the anisotropic function ε varies in space. The Laplacian operator is therefore not a constant-coefficient operator. The discrete linear equation system is

$$\begin{aligned} p_{n+1} = -\mathrm{div} \left(\epsilon^2 \nabla p_n + \epsilon \epsilon_\theta r \begin{pmatrix} \cos(\theta)\cos(\phi) \\ \cos(\theta)\sin(\phi) \\ \sin(\theta) \end{pmatrix} + \epsilon \epsilon_\phi \frac{r}{\sin(\theta)} \begin{pmatrix} \sin(\phi) \\ \cos(\phi) \\ 0 \end{pmatrix} \right) \\ + p_n(1-p_n)(p_n - \frac{1}{2} + m(T_n)). \end{aligned} \tag{A.23}$$

The equation for the temperature is discretized in time implicit by a first oder Eulerian scheme. In space, the Fourier integration method is used as introduced before.

$$T_{n+1} = \Delta T_{n+1} + K \frac{\partial}{\partial t} p_{n+1}. \tag{A.24}$$

This is a semi-implicit integration as p_{n+1} is given explicitly, while T_{n+1} is given implicitly. No linearization is needed as the equations are already linear. The solution of the linear equation system is given by explicit matrix-vector multiplication for p_{n+1} and the inverse Laplacian operator for T_{n+1}.

A.3 Numerical tests

The numerical parameters for the coupling terms are fixed in the presented numerical results as $\alpha = 0.9$, $\gamma = 10$ and $T_e = 0$.

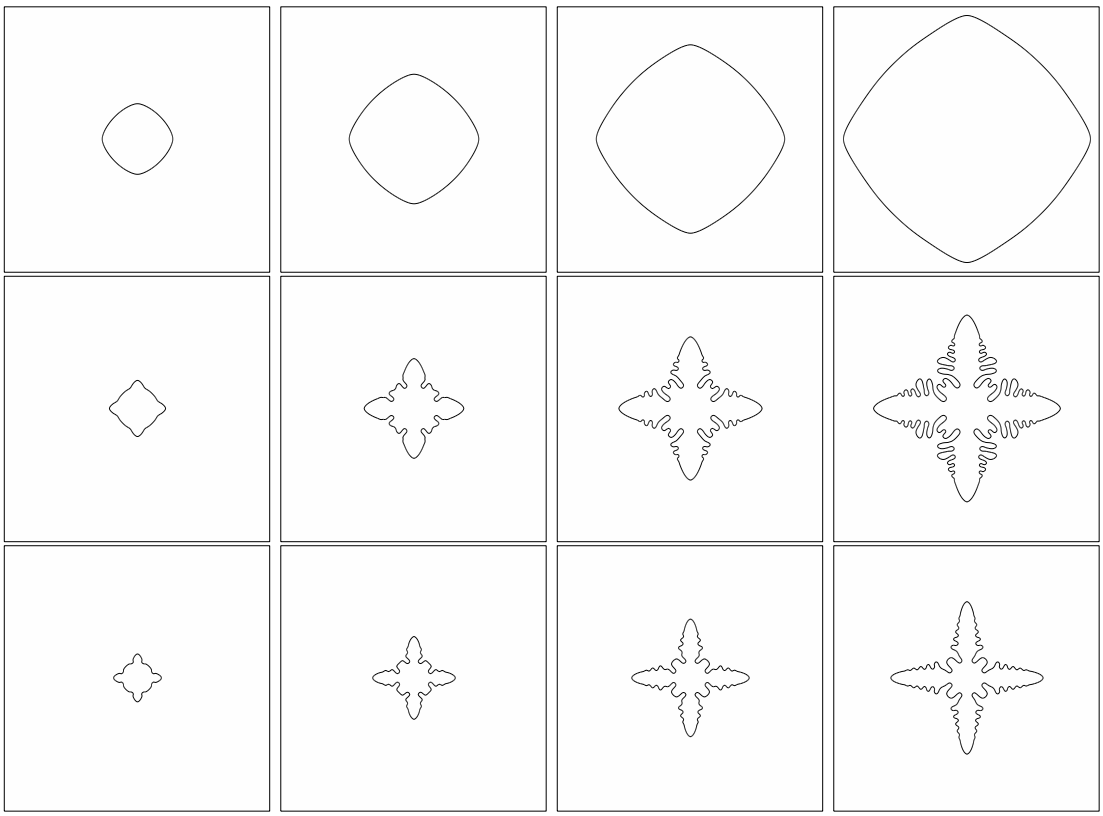

Figure A.3: Contour lines for different values of the temperature coupling parameter K. Each line depicts the time steps $t \in \{0.05, 0.1, 0.15, 0.2\}$. From top to bottom : $K = 1$, $K = 1.6$, $K = 2$.

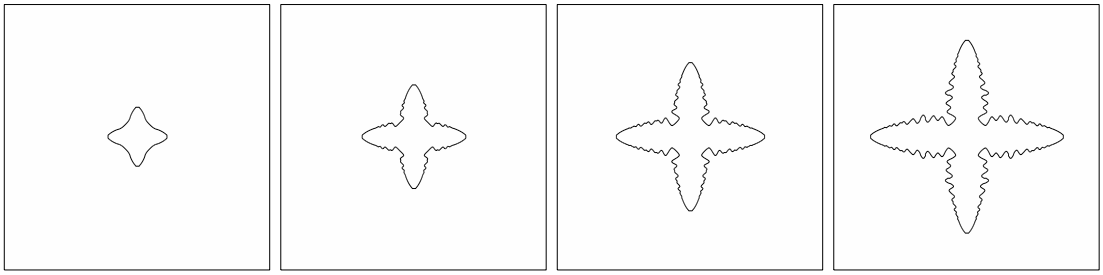

Figure A.4: Contour lines for a different value of the anisotropy parameter $\delta = 0.2$ The line depicts the time steps $t \in \{0.05, 0.1, 0.15, 0.2\}$.

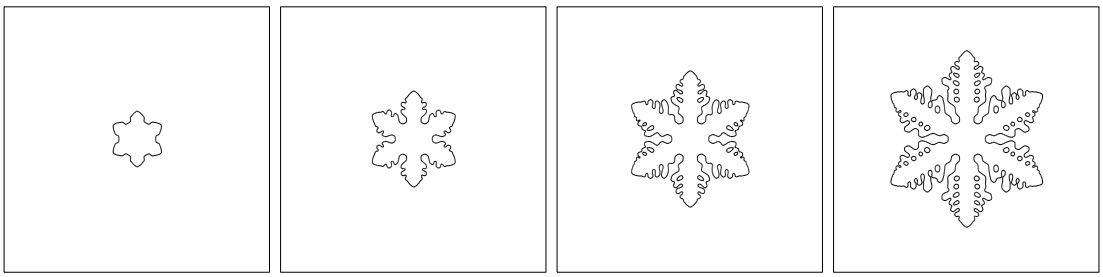

Figure A.5: Contour lines for a different value of the anisotropy parameter $j = 6$. The line depicts the time steps $t \in \{0.05, 0.1, 0.15, 0.2\}$.

A.3.1 Tests in two dimensions

The anisotropy parameter ist set to $\delta = 0.04$, the phase-field parameter is set to $\bar{\epsilon} = 0.01$ and the symmetry constant is $j = 4$ (fourfold symmetry). The temperature coupling parameters are $\alpha = 0.9$, $\tau = 3 \cdot 10^{-4}$ and $\gamma = 10$. The spatial discretization is set to $N_1 = N_2 = 256$ and the time step size is set to $\tau = 2 \cdot 10^{-4}$.
In the first example, the parameter K is varied. Figure A.3 shows the time evolution of the dendrite for three different values of $K \in \{1, 1.6, 2\}$. The contour lines are plotted along the level-set of the phase-field variable $\{p(\boldsymbol{x}) = 0.5\}$. It can be seen that for small temperature coupling values $K = 1$ the solidification is mainly temperature-driven as no dendrite evolves. The phase-change of the field p is only weakly influenced by the temperature field. For large temperature coupling values $K = 3$, the solidification is heavily anisotropy-driven and it only happens where the temperature is still small enough. The phase interface fastly progresses in the favoured solidification direction. For the value $K = 1.6$ both effects counteract each other and a complex branched microstructure evolves.
The second example is to be seen with respect to the previous figure. It is conducted for $K = 1.6$ but with a much larger anisotropic parameter $\delta = 0.2$. It can be seen that in this case, the anisotropic parameter behaves like the lower row of the previous figure. The solidification is mainly anisotropy-driven. Even fewer branches than for $K = 3$ evolve and a smooth fourfold star evolves.
The third and last example proves the correct implementation of the anisotropic function $\epsilon(j; \theta)$. For $j = 6$ a sixfold symmetry is expected. This example also shows that there are no artifacts from the voxel discretization as one might suspect. The growth of all six dendrite branches is uniform independent of their alignment with coordinate axes. Small bubbles of liquid material emerge in the last time step. This material takes a lot longer to solidify as a lot of latent heat has been released by the surrounding material at this point.

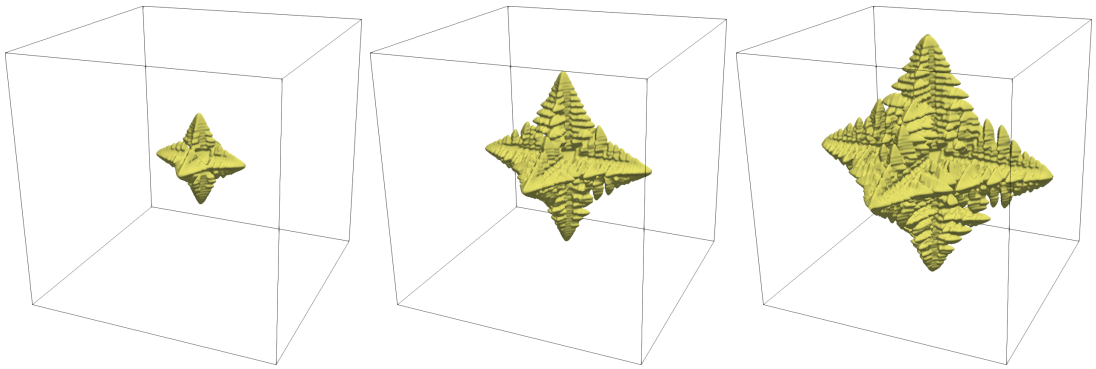

Figure A.6: Three-dimensional dendrite.

A.3.2 Test in three dimensions

In [6] numerical results of dendritic formation in three dimensions are given. Although computational simulation time is given, no more numerical details are given e.g. spatial or time discretization or the numerical methods or model parameters used. This example tries to reproduce the parameters for the simulation of the dendrites shown there.
The anisotropy parameter ist set to $\delta = 0.5$ and the phase-field parameter is set to $\bar{\epsilon} = 0.01$. The temperature coupling parameters are $K = 3$, $\alpha = 0.9$, $\tau = 3 \cdot 10^{-4}$ and $\gamma = 10$. The spatial discretization is set to $N_1 = N_2 = N_3 = 256$ and the time step size is set to $\tau = 10^{-4}$.

Appendix B

Multi-phase models

In this chapter a Cahn-Hilliard multi-phase model is introduced and numerically solved.

B.1 Phase-field model

First, the phase-field model given in Chapter 2 is put into a more general context and the introduction of a multi-phase model is motivated. Originally, a phase-field model for the distribution and development of two different phases, lithium-rich state and lithium-poor state, was introduced. Let $p_1(\boldsymbol{x}, t)$ the fraction of lithium-rich state and $p_2(\boldsymbol{x}, t)$ the fraction of lithium-poor state. Then follows $p_1(\boldsymbol{x}, t) + p_2(\boldsymbol{x}, t) = 1$ for all $\boldsymbol{x} \in \Omega$ and for all $t \in T$. Following this, p_2 was not calculated explicitly, but its energetic contribution it is included implicitly in the chemical potential, see the derivation of the phase-field energy in [66].
In this section, the governing equations for a multi-phase phase-field model are given. Assuming M phases are given, an equation system for a phase-field vector

$$\boldsymbol{p} = (p_1, \dots, p_M)(\boldsymbol{x}, t) \in \mathbb{R}^M$$

is given under the condition $\sum_{i=1}^{M} p_i = 1$. Appropriate boundary and initial conditions close the system.

B.1.1 Governing equations

In [8] the free energy density for a multi-phase phase-field model is given as

$$E(\boldsymbol{p}) = F(\boldsymbol{p}) + \frac{\epsilon^2}{2} \sum_{i=1}^{M} |\nabla p_i|^2, \tag{B.1}$$

where

$$F(\boldsymbol{p}) = \sum_{i=1}^{M} p_i^2 (1 - p_i)^2 \tag{B.2}$$

is the double-well potential. The chemical potential μ is then given as the variational derivative of the free energy density. This results in M evolution equations for the phase-field variables. Let Ω the spatial domain and $T = (0, t_0)$ the time domain. Following the derivations in [36] and considering the constraint $\sum_{i=1}^{M} p_i(\boldsymbol{x}, t) = 1$ the following system of equations is given

$$\frac{\partial}{\partial t} p_i(\boldsymbol{x}, t) = \Delta \left(F'(p_i(\boldsymbol{x}, t)) - \frac{1}{M} \sum_{j=1}^{M} F'(p_j(\boldsymbol{x}, t)) \right) - \epsilon^2 \Delta\Delta p_i(\boldsymbol{x}, t), \quad \boldsymbol{x} \in \Omega, t \in T. \tag{B.3}$$

After the discretization only $M - 1$ of those equations need to be solved. The remaining one is given by the constraint condition.

B.1.2 Initial and boundary conditions

The natural periodic boundary conditions from the previous chapters translate to the multi-phase model as

$$\begin{aligned} p_i(\boldsymbol{x}, t) &= p_i(\boldsymbol{x} + L_j \boldsymbol{e}_j, t), && \boldsymbol{x}, \boldsymbol{x} + L_j \boldsymbol{e}_j \in \partial\Omega, t \in T, \forall i \in \{1, \dots, M\}, \\ \frac{\partial}{\partial \boldsymbol{n}} p_i(\boldsymbol{x}, t) &= -\frac{\partial}{\partial \boldsymbol{n}} p_i(\boldsymbol{x} + L_j \boldsymbol{e}_j, t), && \boldsymbol{x}, \boldsymbol{x} + L_j \boldsymbol{e}_j \in \partial\Omega, t \in T, \forall i \in \{1, \dots, M\}. \end{aligned} \tag{B.4}$$

Additionally consistent initial conditions are required such that

$$p_i(\boldsymbol{x}, 0) = p_{i,0}(\boldsymbol{x}), \quad \forall i \in \{1, \dots, M\} \tag{B.5}$$

such that $\sum_{i=1}^{M} p_{i,0}(\boldsymbol{x}) = 1$.

B.2 Numerical method

In this section, the numerical method is shortly introduced and differences to the previously numerical methods are highlighted. While only $N - 1$ equations need to be solved, the discretization is given for all M equations and therefore the constraint condition is not needed for the solution.

B.2.1 Discretization

Let $\Omega = [0, L_1] \times [0, L_2] \times [0, L_3]$ a box domain. For the discretization in time, the implicit Euler method introduced in Section 3.2 is used for each scalar phase-field variables p_i. Here, a constant time step size τ is used. Then the already introduced finite volume discretization for a regular voxel discretization in space is applied. Let N_1, N_2, N_3 the

number of grid points in each dimension and $N = N_1 N_2 N_3$ the total number of grid points. The discretized equation system then involves NM equations. Given the notation for the discrete Laplacian operator and previous time steps introduced in Section 3.2, the equation system is written as

$$\frac{p_{i,h} - \check{p}_{i,h}}{\tau} = \Delta_h \left(F'(p_{i,h}) - \frac{1}{M} \sum_{j=1}^{M} F'(p_{j,h}) \right) - \epsilon^2 \Delta_h \Delta_h p_{i,h}, \forall i \in \{1, \dots, M\}. \quad \text{(B.6)}$$

B.2.2 Linearization

The non-linear equation system is solved with a Newton-Raphson algorithm. For this, it is rewritten in the form $\boldsymbol{f} = 0$,

$$f_i(\boldsymbol{p}_h) = \frac{p_{i,h} - \check{p}_{i,h}}{\tau} - \Delta_h \left(F'(p_{i,h}) - \frac{1}{M} \sum_{j=1}^{M} F'(p_{j,h}) \right) + \epsilon^2 \Delta_h \Delta_h p_{i,h} = 0, \quad \forall i \in \{1, \dots, M\}. \quad \text{(B.7)}$$

The Jacobian is then given by block matrices of the form

$$\frac{\partial}{\partial p_{j,h}} f_i(\boldsymbol{p}_h) = \frac{1}{\tau} \delta_{ij} \boldsymbol{E} - \Delta_h \left(F''(p_{i,h}) \delta_{ij} - \frac{1}{M} F''(p_{j,h}) \right) + \epsilon^2 \Delta_h \Delta_h \delta_{ij}, \quad \forall i, j \in \{1, \dots, M\}, \quad \text{(B.8)}$$

or rewritten

$$\frac{\partial}{\partial p_{j,h}} f_i(\boldsymbol{p}_h) = \begin{cases} \frac{1}{\tau} \boldsymbol{E} - \frac{M-1}{M} \Delta_h F''(p_{i,h}) + \epsilon^2 \Delta_h \Delta_h, & \text{if } i = j, \\ \frac{1}{M} \Delta_h F''(p_{j,h}), & \text{if } i \neq j. \end{cases} \quad \text{(B.9)}$$

B.2.3 Solution

Given an initial guess $\boldsymbol{p}_h^0$, an iteration is conducted as introduced in Subsection 3.2 with constant time step size. In the presented implementation in MatLab, the sparse matrix package UMFPACK is again used and the black-box solver is applied. The error tolerance of the algorithm TOL is set to 10^{-8} and a iteration maximum of $N_{\text{it}} = 1000$ is used.

B.3 Numerical tests

In this Section, short numerical tests are presented. Example in one and two dimensions with three different phases are presented. The phase-field parameter ϵ is set to 0.01.

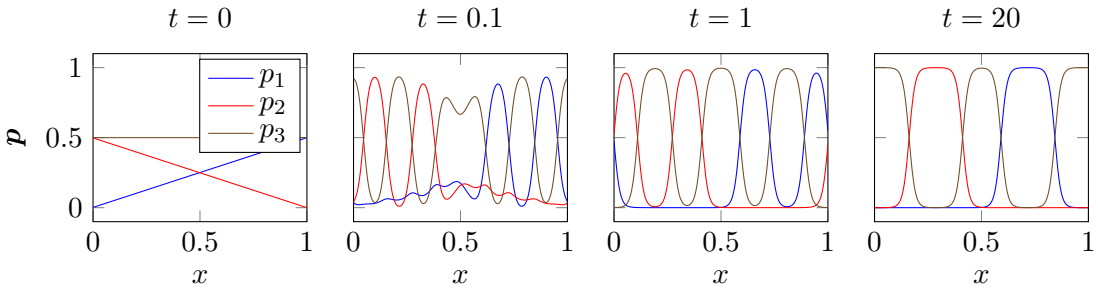

Figure B.1: Numerical solution for the phase-field variable vector $\boldsymbol{p}$ at different times.

B.3.1 Test in one dimension

A simulation of the spinodal decomposition of an alloy of three different phases in one dimension is given in this test. The domain is set to $\Omega = [0, 1]$. The initialization of the phase-field variable vector $\boldsymbol{p}_0$ is

$$\boldsymbol{p}_0 = \begin{pmatrix} p_1 \\ p_2 \\ p_3 \end{pmatrix} (0; x_1, x_2) = \begin{pmatrix} \frac{1}{2}x_1 \\ \frac{1}{2}(1 - x_1) \\ \frac{1}{2} \end{pmatrix}. \tag{B.10}$$

The spatial discretization is set to $N_1 = 256$ and the time step size is set to $\tau = 0.01$. Figure B.2 shows the phase separation of three different phases. The initial configuration is seen at $t = 0$. At $t = 0.1$ the phase separation starts and phases occur at several locations. Around $t = 1$ phase separation is complete and pure phases are seen where one of the three phase-field variables is near one while the other two are reduced to near zero. Then phase coarsening starts and at $t = 20$ several phase grains have merged to larger grains.

B.3.2 Test in two dimensions

A simulation of the spinodal decomposition of an alloy of three different phases in two dimensions is given in this test. The domain is set to $\Omega = [0, 1]^2$. The initialization of the phase-field variable vector $\boldsymbol{p}_0$ is

$$\boldsymbol{p}_0 = \begin{pmatrix} p_1 \\ p_2 \\ p_3 \end{pmatrix} (0; x_1, x_2) = \begin{pmatrix} \frac{1}{2}x_1 \\ \frac{1}{2}x_2 \\ 1 - \frac{1}{2}(x_1 + x_2) \end{pmatrix}. \tag{B.11}$$

The spatial discreitization is set to $N_1 = N_2 = 64$ and the time step size is set to $\tau = 0.01$. Figure B.2 shows the phase separation of three different phases. The differently hatched regions mark sets where a phase-field variable p_i is larger than 0.8 and therefore considered pure phase. For $i = 1, 2$ or 3 the hatching is either single-lined, crossed

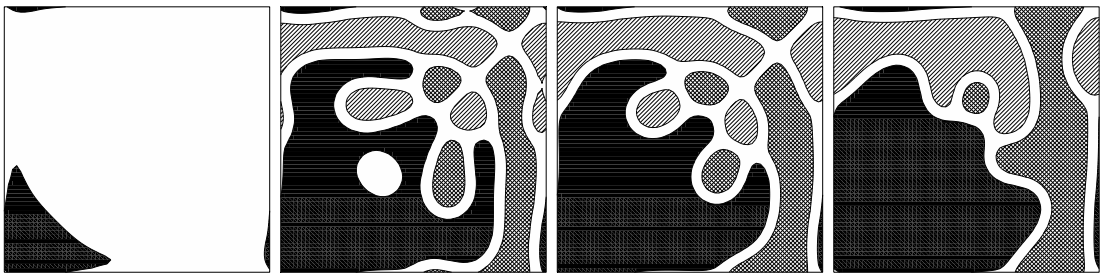

Figure B.2: Phase separation of an alloy of three different phases. The three differently hatched regions mark the sets $\{p_i > 0.8\}$. The remaining domain is considered interfacial region. Shown are four different solutions at times $t \in \{0, 0.2, 0.4, 0.6\}$.

or filled, respectively. In the beginning for $t = 0$, only p_3 is large enough in a small region to appear as a pure phase. For $t = 0.2$ the phase separation already started and phase grains can be seen. The interfacial regions appear as empty stripes separating the hatched regions. For $t = 0.4$ the branched region of p_3 starts to reshape into a more convex shape in order to minimize phase-interface length. For $t = 0.6$ several of the smaller grains disappeared. For p_1 and p_3 only one grain is left, while a small grain of p_2 is shrinking.

List of Figures

List of Tables

List of Abbreviations

1D ..... One-dimensional

2D ..... Two-dimensional

3D ..... Three-dimensional

BCC ..... Body centered cubic packing

C ..... Charge rate or C-rate

CFT ..... Continuous Fourier transform method

DD ..... Domain decomposition algorithm

DFT2 ..... Discrete Fourier transform method with convergence order 2

DFT4 ..... Discrete Fourier transform method with convergence order 4

DFT6 ..... Discrete Fourier transform method with convergence order 6

FCC ..... Face centered cubic packing

FD2 ..... Finite difference method with convergence order 2

FD4 ..... Finite difference method with convergence order 4

FD6 ..... Finite difference method with convergence order 6

HCP ..... Hexagonal closed packing

IIM ..... Immersed interface method

NWT ..... Newton algorithm

SC ..... Simple cubic packing

SOC ..... State of charge

List of Symbols

N_A ..... Avogadro constant

k ..... Butler-Volmer constant

$\boldsymbol{e}_i$ ..... Cartesian unit vector

μ ..... Chemical potential

c ..... Concentration

κ ..... Conductivity

$\boldsymbol{u}$ ..... Deformation

D ..... Diffusivity

N_i ..... Dimension of discretized domain

h ..... Discretization size

Ψ ..... Discretized delta matrix

Σ ..... Discretized facet mesh

Ω ..... Domain

$\boldsymbol{i}$ ..... Electric current

ϕ ..... Electric potential

Λ ..... Embedding domain

F ..... Energy density

F ..... Faraday constant

D ..... Finite difference matrix

T ..... Finite volume cell

$\mathcal{F}_h(\cdot)$ ..... Fourier transform

∇ ..... Gradient

I ..... Identity matrix

Γ ..... Interface between two domains

Δ ..... Laplacian operator

$\boldsymbol{f}$ ..... Lithium ion flux

t_+ ..... Lithium transference number

q ..... Mixing enthalpy

η ..... Nernst overpotential

ω ..... Newton line search step size

d ..... Newton search direction

σ ..... Newton line search reduction

$\boldsymbol{n}$ ..... Normal vector

e ..... Numerical error

U_0 ..... Open circuit potential

∂ ..... Partial derivative

θ ..... Partial molar volume

G ..... Phase-field energy density

L ..... Phase-field interface width

p ..... Phase-field parameter

L_0 ..... Reference length

$\bar{U}$ ..... Reference potential

$\mathbb{C}$ ..... Stiffness tensor

ε ..... Strain

$\boldsymbol{\sigma}$ ..... Stress

T ..... Temperature

τ ..... Time step size

R ..... Universal gas constant

δ ..... Variational derivative

ξ ..... Wave vector

E ..... Young's modulus

Lebenslauf

Name	Tobias Hofmann
2007	Allgemeine Hochschulreife Gymnasium bei St. Anna, Augsburg
2007 - 2008	Zivildienst Diakonisches Werk, Augsburg
2008 - 2011	Bachelor of Science Mathematik Nebenfach Physik Technische Universität München
2011 - 2013	Master of Science Mathematik Schwerpunkt numerische und technische Mathematik Technische Universität München
2013 - 2017	Doktorand am Fraunhofer ITWM Institut für Techno- und Wirtschaftsmathematik Kaiserslautern, Deutschland